Thermophysical and Structural Investigations of a CuTi- and a Zr-based Bulk Metallic Glass, the Influence of Minor Additions, and the Relation to Thermoplastic Forming

Dissertation

zur Erlangung des Grades

des Doktors der Ingenieurwissenschaften

der

Naturwissenschaftlich-Technischen Fakultät

der

Universität des Saarlandes

vorgelegt von

Benedikt Bochtler

Saarbrücken

2019

UNIVERSITÄT
DES
SAARLANDES

Tag des Kolloquiums:	27.05.2020
Dekan:	Prof. Dr. rer. nat. Guido Kickelbick
Berichterstatter:	Prof. Dr. rer. nat. Ralf Busch
	Prof. Dr.-Ing. Dirk Bähre
	Prof. Dr. rer. nat. Gerhard Wilde
Vorsitz:	Prof. Dr.-Ing. Frank Mücklich
Akad. Mitarbeiter:	Dr.-Ing. Florian Schäfer

Abstract

Bulk metallic glasses (BMGs) surpass the strength of steels and at the same time possess the elasticity and formability of thermoplastic polymers. These favorable properties make them interesting candidates for industrial applications.

In this work, the thermophysical properties and the structure of the CuTi-based BMG Vit101 ($Cu_{47}Ti_{34}Zr_{11}Ni_{8}$) and the Zr-based BMG Vit105 ($Zr_{52.5}Cu_{17.9}Ni_{14.6}Al_{10}Ti_{5}$) are investigated. Special focus lies on the influence of minor additions of sulfur and phosphorus, as they increase the thermal stability of the alloys in the supercooled liquid region. The thermodynamic functions of the alloys are determined, and viscosity and kinetic fragility are measured around the glass transition and in the stable liquid. In-situ synchrotron X-ray scattering experiments are performed, elucidating the crystallization sequence upon heating and cooling. Minor additions retard the formation of the primary crystalline phase upon heating. Based on the diffraction data, the temperature evolution of structural differences between the alloys is discussed.

Thermoplastic forming experiments on a variety of BMGs are performed and the deformation is discussed with respect to their thermophysical properties, leading to a description of the thermoplastic formability and the ideal processing region. These findings are transferred to thermoplastic consolidation experiments on amorphous powder, evaluating this technique for additive manufacturing. Finally, thermoplastic deformation experiments are conducted on the CuTi- and Zr-based alloys with minor additions. Minor additions can be used to significantly improve the thermoplastic formability and hence ease the industrial processability.

Zusammenfassung

Metallische Massivgläser (MMG) übertreffen Stähle in ihrer Festigkeit und besitzen gleichzeitig die Elastizität und Formbarkeit von thermoplastischen Polymeren. Diese vorteilhaften Eigenschaften machen sie für industrielle Anwendungen interessant.

In dieser Arbeit werden die thermophysikalischen Eigenschaften und die Struktur des CuTi-basierten MMG Vit101 ($Cu_{47}Ti_{34}Zr_{11}Ni_8$) und des Zr-basierten MMG Vit105 ($Zr_{52.5}Cu_{17.9}Ni_{14.6}Al_{10}Ti_5$) untersucht. Der Fokus liegt dabei auf dem Einfluss von geringen Schwefel- und Phosphorzusätzen, da diese die thermische Stabilität der Legierungen in der unterkühlten Schmelze erhöhen. Die thermodynamischen Funktionen der Legierungen werden bestimmt und Viskosität und kinetische Fragilität werden um den Glasübergang und in der stabilen Flüssigkeit gemessen. In-situ Synchrotron Röntgenstreuexperimente werden durchgeführt, um die Kristallisationssequenz beim Erhitzen und Abkühlen aufzuklären. Schwefel- und Phosphorzusätze verzögern die Bildung der primären kristallinen Phase beim Erhitzen. Basierend auf den Beugungsdaten wird auch die Temperaturentwicklung von Strukturunterschieden zwischen den Legierungen diskutiert.

Thermoplastische Umformversuche an verschiedenen MMG werden durchgeführt und die Verformung in Bezug auf die thermophysikalischen Kennwerte der Legierungen diskutiert, was zu einer Beschreibung der thermoplastischen Umformbarkeit und des idealen Verarbeitungsbereichs führt. Diese Erkenntnisse fließen in Konsolidierungsexperimente an amorphem Pulver ein und erlauben eine Bewertung dieser additiven Fertigungstechnik. Schließlich werden an den Legierungen auf CuTi- und Zr-Basis mit Schwefel- und Phosphorzusätzen thermoplastische Verformungsexperimente durchgeführt. Diese Zusätze können verwendet werden, um die thermoplastische Formbarkeit signifikant zu verbessern und damit die industrielle Verarbeitbarkeit zu erleichtern.

Danksagung

Diese Arbeit ist in den letzten vier Jahren am Lehrstuhl für Metallische Werkstoffe der Universität des Saarlandes entstanden, und ihre Umsetzung wäre nicht ohne die Unterstützung zahlreicher Personen möglich gewesen. Bei all diesen möchte ich mich an dieser Stelle ganz herzlich bedanken.

Mein besonderer Dank gilt zuerst Prof. Dr. Ralf Busch für die Betreuung dieser Arbeit. Er hat mich bereits seit meiner Bachelor- und Masterarbeit wissenschaftlich betreut und in der Entscheidung bestärkt in seiner Gruppe zu forschen. Seine Unterstützung und zugleich die Möglichkeit die eigenen Ideen frei umzusetzen sind wesentliche Grundlage für die Ergebnisse dieser Arbeit.

Ich bedanke mich ganz herzlich bei meinen Freunden und Mitdoktoranden (und inzwischen auch Doktoren) für das perfekte Arbeitsklima, die gegenseitige Unterstützung und Diskussionsbereitschaft. Meinem Büronachbarn Dr. Oliver Gross danke ich besonders für die herausragende Unterstützung bei den ersten Publikationen; Alexander Kuball für die vielen spannenden Stunden im Labor und Dr. Simon Hechler für die Einarbeitung bei der ersten Antragstellung. Natürlich gilt mein Dank auch den beiden „Jung-Doktoranden“ Maximilian Frey und Nico Neuber, die sich perfekt in die Gruppe eingefügt haben.

Mein Dank gilt allen Mitarbeitern am Lehrstuhl für Metallische Werkstoffe. Besonders möchte ich mich bei Dr. Frank Aubertin für die vielen Erklärungen, auch außerhalb des Themas amorphe Metalle, bedanken, sowie bei Dr. Isabella Gallino für viele konstruktive Diskussionen, vor allem im Bereich der Kalorimetrie. Ich bedanke mich auch besonders bei Hermann Altmeyer und Jörg Eiden, die jedes technische Problem im Handumdrehen behoben haben und immer eine pragmatische Lösung parat hatten. Vielen Dank auch an alle Hiwis und Studenten, die viele der arbeitsintensiven Experimente erst ermöglicht haben.

Zudem gilt mein Dank auch meinen ehemaligen Arbeitskollegen sowie externen Projektpartnern. Ich möchte mich bei Moritz Stolpe und Dr. William Hembree für die Einarbeitung zu Beginn meines Promotionsstudiums bedanken. Bei Nevaf Ciftci und Dr. Volker Uhlenwinkel vom Leibniz-IWT in Bremen bedanke ich mich für die produktive und angenehme Zusammenarbeit im Rahmen unseres gemeinsamen IGF Projektes. Ich bedanke mich bei den Mitarbeitern des DLR Institutes für Materialphysik im Weltraum von Prof. Dr. Andreas Meyer für die gute Zusammenarbeit. Besonderer Dank gilt dabei Dr. Fan Yang, der mir die Teilnahme an einer Synchrotron Messzeit in Grenoble ermöglicht hat und zudem alte Messdaten zur Verfügung gestellt hat.

Der größte Dank gebührt meiner Familie und meinen Freunden. Allen voran danke ich meinen Eltern Marlies und Heinz, die mich seit Beginn meines Studiums bedingungslos unterstützt und mich stets motiviert haben. Ohne eure Liebe wäre meine gesamte Laufbahn so nicht möglich gewesen. Zuletzt möchte ich mich bei meiner Freundin Jessica bedanken, die während meines gesamten Promotionsstudiums an meiner Seite stand. Vielen Dank für deine Geduld, dein offenes Ohr, dein Verständnis, und deine Liebe.

Publications and Contributions

In the following, a list of journal publications, patent applications, conference contributions, managed projects, accepted proposals, and supervised thesis projects that originate from the author's work of the last years, is presented.

Journal publications as first or corresponding author

- **B. Bochtler**, O. Gross, I. Gallino, R. Busch, *Thermo-physical characterization of the $Fe_{67}Mo_6Ni_{3.5}Cr_{3.5}P_{12}C_{5.5}B_{2.5}$ bulk metallic glass forming alloy*, Acta Mater. 118 (2016) 129-139. doi: 10.1016/j.actamat.2016.07.031

- **B. Bochtler**, O. Gross, R. Busch, *Indications for a fragile-to-strong transition in the high- and low-temperature viscosity of the $Fe_{43}Cr_{16}Mo_{16}C_{15}B_{10}$ bulk metallic glass-forming alloy*, Appl. Phys. Lett. 111 (2017) 261902. doi: 10.1063/1.5013108

- **B. Bochtler**, M. Stolpe, B. Reiplinger, R. Busch, *Consolidation of amorphous powder by thermoplastic forming and subsequent mechanical testing*, Mater. Des. 140 (2018) 188-195. doi: 10.1016/j.matdes.2017.11.058

- W. Hembree, **B. Bochtler***, R. Busch, *High-temperature rotating cylinder rheometer for studying metallic glass forming liquids*, Rev. Sci. Instrum. 89 (2018) 113904. doi: 10.1063/1.5039318 (* corresponding author)

Journal publications as co-author

- O. Gross, **B. Bochtler**, M. Stolpe, S. Hechler, W. Hembree, R. Busch, I. Gallino, *The kinetic fragility of Pt-P- and Ni-P-based bulk glass-forming liquids and its thermodynamic and structural signature*, Acta Mater. 132 (2017) 118-127. doi: 10.1016/j.actamat.2017.04.030

- O. Gross, S.S. Riegler, M. Stolpe, **B. Bochtler**, A. Kuball, S. Hechler, R. Busch, I. Gallino, *On the high glass-forming ability of Pt-Cu-Ni/Co-P-based liquids*, Acta Mater. 141 (2017) 109-119. doi: 10.1016/j.actamat.2017.09.013

- A. Kuball, O. Gross, **B. Bochtler**, R. Busch, *Sulfur-bearing metallic glasses: A new family of bulk glass-forming alloys*, Scr. Mater. 146 (2018) 73-76. doi: 10.1016/j.scriptamat.2017.11.011

- A. Kuball, **B. Bochtler**, O. Gross, V. Pacheco, M. Stolpe, S. Hechler, R. Busch, *On the bulk glass formation in the ternary Pd-Ni-S system*, Acta Mater. 158 (2018) 13-22. doi: 10.1016/j.actamat.2018.07.039

- A. Kuball, O. Gross, **B. Bochtler**, B. Adam, L. Ruschel, M. Zamanzade, R. Busch, *Development and characterization of titanium-based bulk metallic glasses*, J. Alloys Compd. 790 (2019) 337-346. doi: 10.1016/j.jallcom.2019.03.001

- O. Gross, N. Neuber, A. Kuball, **B. Bochtler**, S. Hechler, M. Frey, R. Busch, *Signatures of structural differences in Pt-P- and Pd-P-based bulk glass-forming liquids*, Comm. Physics. 2 (2019) 83. doi: 10.1038/s42005-019-0180-2

Articles without peer-review

- **B. Bochtler**, O. Gross, A. Kuball, R. Busch, *Titanium-Sulfur-Based Amorphous Metals - Stronger Than Steel, Elastic and Formable Like Plastic*, GIT Laboratory Journal - Business Web for Users in Science and Industry, (2018). www.laboratory-journal.com/science/material-science/titanium-sulfur-based-amorphous-metals (01.08.2019)

- A. Kuball, O. Gross, **B. Bochtler**, R. Busch, *Konstruktionswerkstoff für hochfeste Kleinteile*, Konstruktion - Zeitschrift fuer Produktentwicklung und Ingenieur-Werkstoffe, VDI Fachmedien GmbH & Co. KG (2018). www.konstruktion-online.de/2018/Ausgabe-04/Fachteil-Ingenieur-Werkstoffe/Konstruktionswerkstoff-fuer-hochfeste-Kleinteile (01.08.2019)

Patent applications

- Schwefelhaltige metallische Gläser bildende Legierungen
  WO2019038415A1, (08.2017)
  Inventors: **B. Bochtler**, R. Busch, O. Gross, A. Kuball

- Vorrichtung und Verfahren zur Herstellung eines aus einem amorphen oder teilamorphen Metall gebildeten Gussteils sowie Gussteil
  DE10 2018 115 815.7, (06.2018)
  Inventors: **B. Bochtler**, R. Busch, O. Gross, S. Hechler, A. Kuball

Conference contributions

- 04. – 09.09.2016:
  16th International Conference on Liquid and Amorphous Metals (LAM16), Bad Godesberg, Germany, **oral presentation**: *Characterization of the $Fe_{67}Mo_6Ni_{3.5}Cr_{3.5}P_{12}C_{5.5}B_{2.5}$ bulk metallic glass forming alloy*

- 19. – 24.03.2017:
  Tagung der Deutschen Physikalischen Gesellschaft (DPG) 2017, Dresden, Germany, **oral presentation**: *Characterization of the $Fe_{67}Mo_6Ni_{3.5}Cr_{3.5}P_{12}C_{5.5}B_{2.5}$ bulk metallic glass forming alloy*

- 27.08. – 01.09.2017:
  16th International Conference on Rapidly Quenched and Metastable Materials (RQ16), Leoben, Austria,
  oral presentation: *Characterization of the Fe-based bulk metallic glass forming alloys*
  poster contribution: *Consolidation of amorphous powder by thermoplastic forming and mechanical testing,* RQ16 - Best Poster Award

- 11. – 16.03.2018:
  Tagung der Deutschen Physikalischen Gesellschaft (DPG) 2018, Berlin, Germany, **oral presentation**: *Consolidation of amorphous powder by thermoplastic forming and subsequent mechanical testing*

- 26. – 30.08.2019:
  17th International Conference on Liquid and Amorphous Metals (LAM17), Lyon, France, **oral presentation**: *The influence of minor additions of sulfur in Zr- and Cu-based bulk metallic glass forming liquids*

Accepted proposals

- Industrielle Gemeinschaftsforschung (IGF) proposal in 2016:
  Herstellung, Charakterisierung und Thermoplastische Formung von glasbildenden Metallpulvern (IGF Vorhaben Nr. 19291 N),
  Authors: **B. Bochtler**, N. Ciftci, S. Hechler, V. Uhlenwinkel, R. Busch

- Deutsche Forschungsgemeinschaft (DFG) proposal in 2018:
  New sulfur-bearing Bulk Metallic Glasses: Thermophysical and mechanical properties (DFG Projekt BU 2276/10-1),
  Authors: A. Kuball, **B. Bochtler**, O. Gross, R. Busch

- Deutsche Forschungsgemeinschaft (DFG) proposal in 2018:
  Topological Frustration and Glass-Forming Ability of Sulfur-containing Metallic Glass-Formers (DFG Projekt BU 2276/11-1),
  Authors: **B. Bochtler**, R. Busch, F. Yang, A. Meyer, G. Wilde

- Deutsches Elektronen Synchrotron (DESY) beamtime I-20170938 in 2018 (48 h) , PETRA III, P02.1; O. Gross, **B. Bochtler**, A. Kuball, R. Busch; *Investigation of the compositional dependence of structural changes of Pt/Pd-Cu-Ni-P glass forming liquids and their connection to kinetic fragility.*

- Deutsches Elektronen Synchrotron (DESY) beamtime I-20180946 in 2019 (96 h), PETRA III, P10; O. Gross, I. Gallino, B. Ruta, A. Kuball, **B. Bochtler**, N.Neuber, R. Busch; *Dynamics on the medium range order length scale in a metallic glass-former.*

- EXIST-Forschungstransfer, Existenzgruendung aus der Wissenschaft, Bundesministerium fuer Wirtschaft und Energie, 05.2019:
  Industrielle Herstellung und Verarbeitung amorpher Metalle (IHVAM)
  Authors: **B. Bochtler**, O. Gross, S. Hechler, A. Kuball, P. Linek

- Deutsches Zentrum für Luft- und Raumfahrt (DLR)
  Parabolic flight campaigns:
  - 2015 (10 parabolas); O. Gross, W. Hembree, **B. Bochtler**, R. Busch; TEMPUS experiment proposal: *Melt viscosity of a the newly discovered* $Fe_{67}Mo_6Ni_{3.5}Cr_{3.5}P_{12}C_{5.5}B_{2.5}$ *bulk metallic glass-forming liquid*
  - 2016 (5 parabolas); **B. Bochtler**, O. Gross, R. Busch; TEMPUS experiment proposal: *Melt viscosity of the* $Fe_{43}Cr_{16}Mo_{16}C_{15}B_{10}$ *bulk metallic glass-forming liquid*
  - 2017 (5 parabolas); O. Gross, **B. Bochtler**, R. Busch; TEMPUS experiment proposal: *Melt viscosity and volume evolution in the undercooled liquid of the* $Pt_{42.5}Cu_{27}Ni_{9.5}P_{21}$ *bulk glass forming liquid*

- 2018 (5 parabolas); A. Kuball, **B. Bochtler**, O. Gross, R. Busch; TEMPUS experiment proposal: *Viscosity and surface tension of the melt of the novel bulk metallic glass-forming titanium alloy* $Ti_{65}Zr_{10}Cu_{15}Ni_2S_8$
- 2019 (5 parabolas); A. Kuball, **B. Bochtler**, O. Gross, R. Busch; TEMPUS experiment proposal: *Viscosity and surface tension of the melt of the bulk metallic glass-forming alloy* $Zr_{56.5}Ti_{13.3}Ni_{13.6}Cu_{9.6}S_7$

Managed externally funded projects

- 06.2016 – 10.2018 and 04.2019 – 09.2019:
  Industry research project with Heraeus Deutschland GmbH, *Process development for amorphous alloys*

- 01.2017 – 06.2019:
  Research project funded by Industrielle Gemeinschaftsforschung (IGF), *Herstellung, Charakterisierung und Thermoplastische Formung von glasbildenden Metallpulvern* (IGF Vorhaben Nr. 19291 N)

Supervised thesis projects

- Master thesis, Victor Pacheco, *Optimization and characterization of a novel Pd-Ni based bulk metallic glass forming alloy*, (12.2016) (co-supervised)

- EEIGM Master project (6 months), Marius Gipperich, *Processing of metallic glass powder*, (03.2017)

- EEIGM Master project (6 months), Thomas Zimmer, *Thermoplastic forming of bulk metallic glasses*, (04.2017)

- Bachelor thesis, Adrian Herges, *Fe- und Ni-basierte metallische Glaeser aus industriellen Vorlegierungen*, (09.2017)

- Bachelor thesis, Benedikt Reiplinger, *Thermoplastisches Formen Zirkonium basierter Metallischer Massivglaeser*, (07.2017)

- Bachelor thesis, Mathias Nicola, *Herstellung von Glasbildenden Zirkonium-Basis Legierungen und Optimierung eines Hochtemperaturviskosimeters*, (12.2017)

- Master thesis, Cristo Paulo, *Einfluss von Phosphor und Schwefel auf die thermoplastische Verformung und Oxidation von Zr- und Cu-basierten metallischen Glaesern*, (02.2019)

- Bachelor thesis, Oliver Kruse, *Thermoplastische Formbarkeit Metallischer Glaeser*, (08.2019)

Content

List of Abbreviations

3PB	three-point bending
AMZ4	$Zr_{59.3}Cu_{28.8}Al_{10.4}Nb_{1.5}$
BMG	bulk metallic glass
DSC	differential scanning calorimetry
DTA	differential thermal analysis
FSDP	first sharp diffraction peak
GFA	glass-forming ability
KWW	Kohlrausch-Williams-Watts
LLT	liquid-liquid transition
MRO	medium-range order
SCL	supercooled liquid
SEM	scanning electron microscopy
SF	strong-to-fragile
SRO	short-range order
STZ	shear transformation zone
T_g	glass transition temperature
T_x	crystallization temperature
TPF	thermoplastic forming
TTD	time-temperature-deformation
TTT	time-temperature-transformation
VFT	Vogel-Fulcher-Tammann
Vit101	$Cu_{47}Ti_{34}Zr_{11}Ni_8$
Vit101 P_1	$Cu_{46.53}Ti_{33.66}Zr_{10.89}Ni_{7.92}P_1$
Vit101 $S_{1.5}$	$Cu_{46.3}Ti_{33.5}Zr_{10.8}Ni_{7.9}S_{1.5}$
Vit105	$Zr_{52.5}Cu_{17.9}Ni_{14.6}Al_{10}Ti_5$
Vit105 P_2	$Zr_{51.45}Cu_{17.54}Ni_{14.31}Al_{9.8}Ti_{4.9}P_2$
Vit105 S_2	$Zr_{51.45}Cu_{17.54}Ni_{14.31}Al_{9.8}Ti_{4.9}S_2$
XRD	X-ray diffraction

Chapter 1

Introduction

Metallic glasses combine the favorable properties of conventional metals and polymers: they surpass the strength of steels and at the same time possess the elasticity and formability of polymers. Metallic glasses (MG), or amorphous metals, distinguish themselves from conventional metals due to their structure on the atomic scale. They do not display a crystalline long-range order, but an amorphous structure with short- and medium-range order, which is preserved when rapidly quenching a metallic liquid. This amorphous structure is responsible for their superior mechanical properties and unique characteristics.

The first metallic glass was produced in 1960, when Duwez and coworkers rapidly quenched a $Au_{75}Si_{25}$ melt [1]. The key to conserve the amorphous structure of the liquid is to cool it quickly enough to bypass crystallization. The governing crystallization kinetics are determined by the driving force for crystallization, the interfacial energy between the liquid and the crystal, and the atomic mobility in the melt. The interplay between crystallization times and temperature can best be visualized in a time-temperature-transformation (TTT) diagram, as schematically shown in Fig. 1.1. When casting the alloy, the melt is cooled rapidly from the stable liquid state, throughout the supercooled liquid (SCL) region, to temperatures below the glass transition temperature T_g, following the blue cooling curve. A glass is formed if the cooling curve bypasses the C-shaped crystallization "nose". The slowest feasible cooling rate is defined as the critical cooling rate and is directly connected to the position of the crystallization nose. It also defines the maximum casting thickness for fully amorphous samples, the critical casting diameter d_c, as the heat conduction in the material limits the cooling rate in the center of a sample.

Following this description, the achievable size of amorphous samples can be increased if the crystallization kinetics are retarded, and hence the glass-forming ability (GFA) is increased. Since the discovery of the first metallic glass, many efforts were made to find glass-forming metallic systems and systematically improve their GFA, resulting in a wide variety of alloys with a critical casting thickness of 1 mm and above [2–6], the so-called bulk metallic glasses (BMGs).

Throughout the years, elements from all over the periodic table were considered for the search for new glass-forming systems, even including toxic elements, e.g. beryllium [5]. But it was only in 2018, when we considered the element sulfur (S) for the first time as a main constituent in metallic glass-forming alloys and discovered various new alloy systems [7]. These include the Pd-Ni-S systems with high amounts of S [8], as well as the Ti-based system Ti-Zr-Cu-S with an intermediate percentage of S, which is highly promising for industrial applications [9].

In the context of alloy development, one strategy that evolved to improve the GFA of BMGs is to add minor amounts of an additional atom species, known as minor additions or also microalloying. Minor additions have a great impact on the formation and the properties of BMGs [10] and are a powerful tool to tailor the key properties of BMGs without starting alloy development from scratch in a new glass-forming system. This exact approach can also be applied for minor additions of sulfur, which was previously not considered as a desirable element in BMGs.

Preliminary results on the effect of minor additions of S in the Zr-based alloy system Vit105 ($Zr_{52.5}Cu_{17.9}Ni_{14.6}Al_{10}Ti_5$) [11] and the Cu-based system Vit101 ($Cu_{47}Ti_{34}Zr_{11}Ni_8$) [12] showed a significant increase in the thermal stability of the SCL region upon heating [7]. The stability of the SCL region is the key feature that allows for the thermoplastic forming of BMGs. Thermoplastic forming is commonly known from polymers, and in the case of metals, it is only possible for amorphous metals, allowing them to be formed like polymers. This advantage regarding formability in comparison to crystalline metals makes BMGs highly interesting candidates for small and complex structural parts, especially when considering their extraordinary strength.

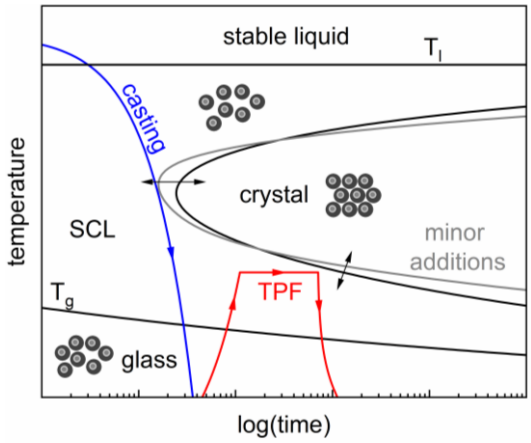

Figure 1.1: Schematic time-temperature-transformation (TTT) diagram. The stable liquid above the liquidus temperature, T_l, the supercooled liquid (SCL) region, the glass, and the crystal are indicated. The cooling curve of a typical casting process is shown as blue curve and the temperature profile of a TPF experiment as red curve. A glass is formed when the black T_g-line is crossed upon cooling, whereas crystallization starts when the crystallization "nose" is crossed. The shape and position of the nose can be changed by minor additions, as indicated by the double arrows.

A typical temperature protocol for the thermoplastic forming process is depicted as red curve in the TTT diagram in Fig. 1.1. The amorphous feedstock material is heated above the glass transition temperature and can then be deformed like a thermoplastic polymer, before it is cooled down again below the glass transition temperature. In order to avoid crystallization, the processing times need to remain below the crystallization time, which is visualized by the black border of the crystallization nose. As indicated by the grey line in the figure, the shape and position of this nose can be significantly altered by minor additions. As exemplarily shown, they can increase the SCL region at low temperatures, and at the same time decrease the GFA by pushing the tip of the nose to shorter times, e.g. by changing the primary crystallizing phases. In the end, the shape of the crystallization nose can be fine-tuned by minor additions in order to tailor the properties according to the needs of the intended process.

The mechanical properties of BMGs in comparison to other engineering materials are depicted in the qualitative stress-strain diagram in Fig. 1.2. There, the yield strength is shown over the elastic limit. Depending on the base element, a yield strength of up to 5 GPa can be reached. The commonly used Zr- or Cu-based alloys show a yield strength of around 2.5 GPa. In general, amorphous metals exceed the strength of steels and at the same time provide the elasticity of polymers, making them the perfect material for many structural applications, and especially for springs. However, the size of structural parts is limited by the previously mentioned critical casting thickness. Therefore, industrial applications can likely be found in medical engineering or precision mechanics, where small and complex parts have to withstand high mechanical loads.

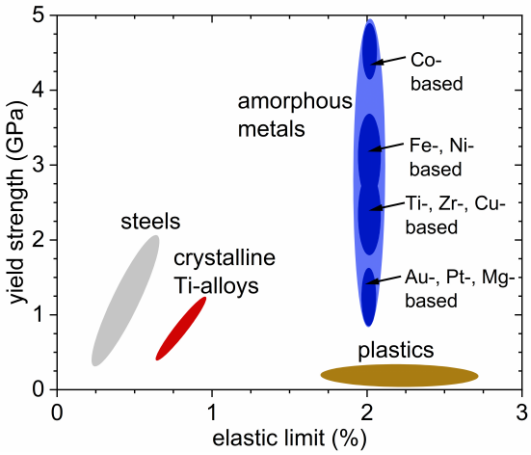

Figure 1.2: Qualitative stress-strain diagram for amorphous metals in comparison to other engineering materials. The yield strength is shown over the elastic limit. Amorphous metals exceed the strength of steels and at the same time provide the elasticity of polymers. Adapted from Ref. [13].

In this work, two of the discussed aspects regarding BMGs are investigated and the results are combined: Minor additions and thermoplastic forming.

First, the influence of minor additions of sulfur and also phosphorus on the thermophysical properties and the structure of Vit101 and Vit105 is extensively examined. The critical casting thickness of different compositions as well as the mechanical properties are evaluated. The thermodynamic functions are calculated based on the molar heat capacity and characteristic temperatures and enthalpies. TTT diagrams are obtained from isothermal calorimetric measurements. Viscosity of the alloys is measured at low temperatures around the glass transition and at high temperatures in the stable liquid. Based on these results, the kinetic fragility is determined and the course of viscosity over the whole temperature range is described by fitting functions and discussed in the context of a possible strong-to-fragile liquid-liquid transition. Finally, in-situ synchrotron X-ray scattering experiments are performed in the glassy, the supercooled liquid, and the stable liquid state. The crystallization behavior is investigated upon heating and cooling and the temperature evolution of structural differences is discussed.

Second, thermoplastic forming experiments on a variety of BMGs are performed and the observed deformation is discussed with respect to characteristic values of the alloys, leading to a description of the thermoplastic formability and the ideal TPF processing region. The findings from the deformation experiments are transferred to thermoplastic consolidation experiments on amorphous powder. This additive manufacturing technique is used in order to produce larger structural parts from powdery feedstock and the obtained samples are tested regarding their mechanical performance.

Finally, the two topics are brought together, when thermoplastic deformation experiments are conducted on the Vit101 and Vit105 alloy families with minor additions of S and P. Time-temperature-deformation maps are constructed and discussed with respect to the findings of the characterization of the alloys. Minor additions can ultimately be used to significantly improve the thermoplastic formability of the alloys and hence, ease their industrial processability.

Chapter 2

Background

In this chapter, the theoretical background on bulk metallic glasses (BMGs) in general, and on minor additions and thermoplastic forming (TPF) in particular, is presented. The relevant textbook knowledge on the glass formation in metallic systems, the nature of the supercooled liquid state, its thermodynamic and kinetic properties, as well as the structure and the mechanical properties of the glassy state are summarized. Some insights into the new class of sulfur-bearing BMGs are given, and the influence of minor additions in BMGs reported in literature is presented. In the end, a concise literature review on the state of the art regarding the processing of BMGs, especially by TPF, is offered to the reader.

2.1 Bulk Metallic Glasses (BMGs)

In terms of structure, BMGs, or rather amorphous metals, are frozen-in metallic liquids and their amorphous structure determines their principle properties. BMGs generally display an extraordinarily high yield strength (ca. 3 GPa) in combination with an elastic limit of around 2 % [14]. Their high strength is accompanied by a high hardness and good wear resistance. While these engineering properties are rather easy to measure, the properties intertwined with the nature of the glass transition are much harder to assess, as they strongly depend on time and temperature. The occurring relaxation processes constantly alter the observed properties, till eventually the metastable supercooled liquid (SCL) state is reached. However, shortly after, the formation of the stable crystalline phase starts. In the end, the thermodynamics and kinetics of the SCL phase determine the whole process of glass formation and define the glass-forming ability (GFA) of a system, as well as its thermal stability.

2.1.1 Glass Formation

When a metallic melt is cooled down from the stable equilibrium liquid, solidification will occur eventually. Two solidification pathways are conceivable, both of which are depicted in Fig. 2.1, where the molar volume is plotted over temperature. As soon as the liquidus temperature, T_l, is passed upon cooling, the metastable SCL is reached. After a certain undercooling, ΔT, pathway (1) is followed for all common crystalline

metals: Nuclei form and grow, and the whole system crystallizes. This crystallization process is accompanied by crystallization shrinkage, as the atoms rearrange from the amorphous liquid structure to the denser packed crystalline one. During this process the latent heat of crystallization is released. Amorphous metals however follow pathway (2): The SCL is cooled down further, while crystallization is avoided, until eventually the glass transition occurs and a glassy solid is formed. The glass transition is accompanied by a continuous change in the thermal expansion coefficient as can be seen by the change of slope of the volume curve. Upon further cooling, the glassy state shows a similar thermal expansion as the corresponding crystal, however, possesses a larger volume. The competition between crystallization and glass formation is further discussed in the context of the GFA in Chapter 2.1.5.

The glass formation can only occur if the system is quenched fast enough so that there is insufficient time for the nucleation and growth of crystals. The cooling rate dictates the temperature of the glass transition and hence defines the structural state that is frozen-in, which again effects the properties of the glass [15]. The glass transition temperature upon cooling is defined as the fictive temperature, T_{fic}, which is the most indisputable definition of the glass transition as it only depends on the cooling rate during vitrification. The temperature dependence of the glass transition underlines the kinetic nature of this phenomenon [16]. As can be seen in Fig. 2.1, at higher cooling rates the glass transition is shifted to higher temperatures: Glass 1 shows a higher fictive temperature than glass 2, and at the same time a larger volume is frozen-in.

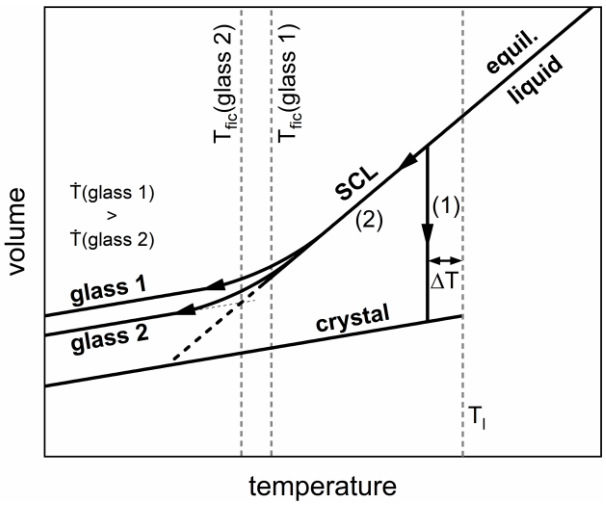

Figure 2.1: Schematic depiction of the volume of a metallic liquid and the corresponding solids as a function of temperature. When cooling the equilibrium liquid below the liquidus temperature T_l, it either crystallizes (1) after a certain undercooling ΔT or can be further undercooled (2) until the glass transition occurs at the fictive temperature T_{fic}. With the glass transition being a kinetic phenomenon, the fictive temperature depends on the cooling rate and is found to be higher for a faster cooling.

The underlying reason for the glass formation can be found in the rapidly increasing viscosity and relaxation time of the system, and hence the kinetic slowdown, as will be explained in Chapter 2.1.4. When the inherent time scale of the SCL surpasses the time scale of the experiment, which is directly linked to the applied cooling rate, the system falls out of equilibrium [17]. The dynamics in the liquid cannot follow anymore the changes forced upon the system by the change in temperature and the system leaves the metastable equilibrium, forming a glassy solid [18].

In the context of a kinetic slowdown, the glass transition is described as a purely kinetic phenomenon by Angell [19] and Turnbull and Cohen [20]. However, a thermodynamic component is still attributed to the transition, as discussed by Kauzmann [18], and later by Gibbs and DiMarzio [21]. Kauzmann arguments from an entropical point of view. The volume curves in Fig. 2.1 can also be interpreted as the entropy of the system. Due to a higher molar heat capacity in the SCL in comparison to the crystal, the higher entropy in the SCL declines faster and would eventually become the same as in the crystal (when following the dashed part of the SCL line). The temperature at which the entropy of the SCL reaches the one of the crystal is defined as the Kauzmann temperature, T_K, where the glass transition needs to occur at latest to prevent an entropic paradox, as the entropy of the disordered SCL would display a lower entropy as the ordered crystal.

2.1.2 Thermodynamics of the Supercooled Liquid

When undercooling the liquid down to the glass, crystallization must be avoided and the thermodynamics of the supercooled liquid state in comparison to the crystal play a decisive role that needs to be understood.

With the supercooled liquid being a metastable state, the system experiences a driving force for crystallization. This driving force can be described by the difference in Gibbs free energy between the liquid and the crystalline state. Schematic Gibbs free energy curves of the liquid and the crystalline state are shown in Fig. 2.2 a). Above the liquidus temperature T_l, the liquid state is stable due to its lower Gibbs free energy, which however increases faster as the one of the crystalline state with decreasing temperature. Consequently, the crystal is the energetically favored state below T_l. The driving force for crystallization, $\Delta G^{l\text{-}x}$, increases with increasing undercooling ΔT and it can be expressed as:

$$\Delta G^{l-x}(T) = \Delta H^{l-x}(\mathrm{T}) - T\,\Delta S^{l-x}(\mathrm{T})\,, \tag{2.1}$$

where H represents enthalpy, S entropy, and $\Delta^{l\text{-}x}$ indicates the difference between the supercooled liquid and the crystalline mixture. The excess enthalpy, $\Delta H^{l\text{-}x}$, and the excess entropy, $\Delta S^{l\text{-}x}$, arise from their discontinuity at the melting point (ΔH_f and ΔS_f) and the difference in molar heat capacity between the liquid and the crystal, $\Delta c_p^{l\text{-}x}$, and can be defined as:

$$\Delta H^{l-x}(\mathrm{T}) = \Delta H_f - \int_T^{T_f} \Delta c_p^{l-x}(T')dT' \tag{2.2}$$

$$\Delta S^{l-x}(\mathrm{T}) = \Delta S_f - \int_T^{T_f} \frac{\Delta c_p^{l-x}(T')}{T'} dT' \,, \tag{2.3}$$

where ΔH_f and ΔS_f are the enthalpy and entropy of fusion. T_f is the temperature of fusion, which here is defined as the peak position of the main melting peak. In the case of one-component monoatomic liquids, a driving force for crystallization is observed from T_l (= T_m) on and can be described precisely with the equations above, if T_f is replaced by T_l. In the case of complex multi-component melts, like BMGs, the situation is much more complicated. A different driving force for crystallization is present for the different crystalline phases that may form. The driving force for crystallization of the primary crystallizing phase might not be well represented by an estimation based on the averaged difference in molar heat capacity between the liquid and the crystalline mixture, when the liquidus temperature of the highest melting component is used. Hence, in this case, the temperature of fusion, T_f, is used as a representative average value to estimate ΔH^{l-x} and ΔS^{l-x}, and hence ΔG^{l-x} between the liquid and the crystalline mixture.

At the equilibrium point between liquid and crystal, where the difference in Gibbs free energy vanishes, Eq. 2.1 can be rewritten, taking into account Eq. 2.2 and 2.3, as:

$$0 = \Delta H^{l-x}(T_f) - T_f\, \Delta S^{l-x}(T_f) \;\Rightarrow\; 0 = \Delta H_f - T_f\, \Delta S_f \;\Rightarrow\; \boldsymbol{\Delta S_f = \frac{\Delta H_f}{T_f}}. \tag{2.4}$$

Hence, the entropy of fusion can be calculated from a single calorimetric measurement, where the enthalpy and temperature of fusion are determined. For small undercoolings up to around 100 K [22], the driving force for crystallization can be estimated by the Turnbull approximation [23]:

$$\Delta G^{l-x}(T) \approx \Delta H_f - T\,\frac{\Delta H_f}{T_f} = -\frac{\Delta H_f}{T_f}(T - T_f) = -\Delta S_f\, \Delta \mathrm{T}\,. \tag{2.5}$$

For the Turnbull approximation it is assumed that the difference in molar heat capacity between the liquid and the crystal is neglectable ($\Delta c_p^{l-x}(\mathrm{T}) = 0$). The corresponding geometrical interpretation is visualized by the dashed tangent lines in Fig. 2.2 a), where $S_l(T_f)$ and $S_x(T_f)$ correspond to the slope of the G-curves at T_f.

In conclusion, the driving force for crystallization can be estimated based on the molar heat capacity data of the liquid and the crystal, the characteristic temperatures, and the latent heat of fusion. As ΔS_f corresponds to the slope of the ΔG^{l-x}-curve at T_f, knowledge of ΔH_f and T_f is sufficient to estimate the driving force for crystallization when applying the Turnbull approximation.

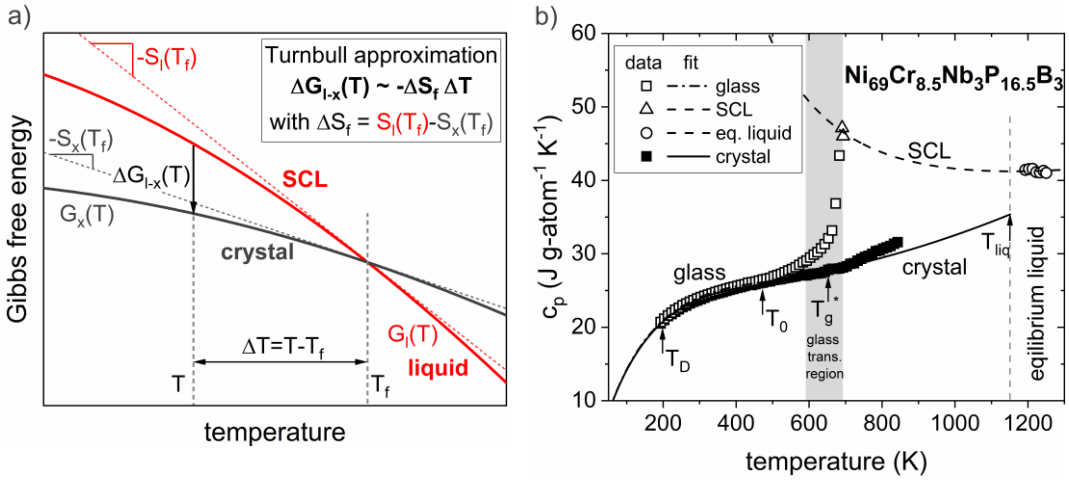

Figure 2.2: a) Schematic Gibbs free energy curves of the crystal, $G_x(T)$, and the liquid, $G_l(T)$, as a function of temperature. Liquid and crystal are in thermodynamic equilibrium at the temperature of fusion, T_f, and a driving force for crystallization, $\Delta G^{l\text{-}x}$, forms upon undercooling by ΔT. According to the Turnbull approximation, the driving force for crystallization can be estimated by the difference in slope of the G(T)-curves, which corresponds to the entropy of fusion ΔS_f. **b)** Molar heat capacity of the crystalline mixture, the glassy state, the SCL, and the equilibrium liquid as a function of temperature. The data for the $Ni_{69}Cr_{8.5}Nb_3P_{16.5}B_3$ alloy exemplarily illustrates the difference in heat capacity between the (supercooled) liquid and the crystal. Data taken from Ref. [24].

The course of the molar heat capacity as a function of temperature is exemplarily shown in Fig. 2.2 b) for the bulk metallic glass-forming system $Ni_{69}Cr_{8.5}Nb_3P_{16.5}B_3$. Measurement data for the molar heat capacity of the crystalline mixture, the glassy state, the SCL, and the equilibrium liquid is shown. The difference in heat capacity between the (supercooled) liquid and the crystal is clearly visible, and the glass transition region corresponds to a step in the c_p-curve. The fitting functions used for the mathematical description of the data are introduced later in Chapter 3.3.4. $\Delta c_p^{l\text{-}x}$ can be calculated from the fitting functions and then be used for the calculation of the $\Delta G^{l\text{-}x}(T)$-curve according to Eq. 2.1 and Eqs. 2.2 and 2.3. Thermodynamic functions calculated from the measured c_p data can be found later in Fig. 4.8 on page 84.

All the previous considerations regarding the driving force for crystallization are true for a single-component system. Bulk metallic glass-forming alloys, however, are complex multi-component systems (compare to the Ni-based alloy above) where the differences in chemical potential, $\Delta\mu$, upon nucleation and crystallization of a phase with a different chemical composition need to be considered. In this case, the quantity $\Delta G^{l\text{-}x}$ only corresponds to the Gibbs free energy difference between the liquid and the crystalline phase mixture. This difference however, is not necessarily equivalent to the driving force for nucleation of the primary crystallizing phase (e.g. α) which displays

a different chemical composition than the liquid [25]. The driving force for nucleation of the primary phase is given by the difference in chemical potential between the liquid and the primary crystalline phase upon formation of a nucleus, $\Delta\mu^{l-\alpha}$. The composition of said nucleus can be defined by a parallel tangent construction on the Gibbs free energy curves in the compositional space, as the parallel tangent construction allows to find the composition with the maximum driving force. In this case, the value of ΔG^{l-x} can be understood as a lower limit for the driving force for nucleation, $\Delta\mu^{l-\alpha}$ [25]. However, in order to determine $\Delta\mu^{l-\alpha}$, the Gibbs free energy curves for all phases as a function of temperature and composition would need to be known, which is almost impossible in a complex multi-component system. Consequently, ΔG^{l-x} can be seen as the best possible approximation of the driving force for crystallization in a multi-component system. A profound explanation of this topic can be found in Refs. [25,26].

While these considerations describe the driving force for crystallization, they do not yet include the kinetics of the crystallization process, which is discussed in the context of viscosity in Chapter 2.1.4, nor do they include the nucleation energy barrier, which is introduced in Chapter 2.1.5.

2.1.3 Relaxation in the Glassy State

Once the supercooled liquid is traversed upon cooling, the glass transition occurs, the system falls out of its metastable equilibrium and reaches a thermodynamically unstable state. This unstable glassy state strives to relax into the metastable SCL or to form the stable crystalline mixture. At temperatures far below the glass transition, the relaxation kinetics are so slow that the system is virtually frozen-in. At temperatures in the vicinity of the glass transition however, the so-called α-relaxation takes place and the system structurally relaxes, which is also called physical aging. A comprehensive review of the relaxation behavior can be found in Refs. [27,28].

Relaxation is commonly investigated during either isothermal experiments or during experiments with a constant heating rate, so-called scans. The effects of relaxation can for example be observed in the heat flow of calorimetric measurements, in the entropy of the system, in its volume, and in the viscosity or relaxation time. All these quantities are exemplarily depicted as a function of temperature in Fig. 2.3 in vicinity of the glass transition. Figure 2.3 a) shows the heat flow during a calorimetric measurement as a function of temperature. Upon heating and approaching the glass transition, exothermic α-relaxation is observed. The dashed area corresponds to the released amount of enthalpy during the relaxation process. Subsequently, the glass transition starts at T_g^{onset} and at the SCL region is reached at T_g^{end}. The hump shortly before the end of the glass transition corresponds to the endothermic enthalpy recovery event. Upon further heating, the crystallization process starts at T_x.

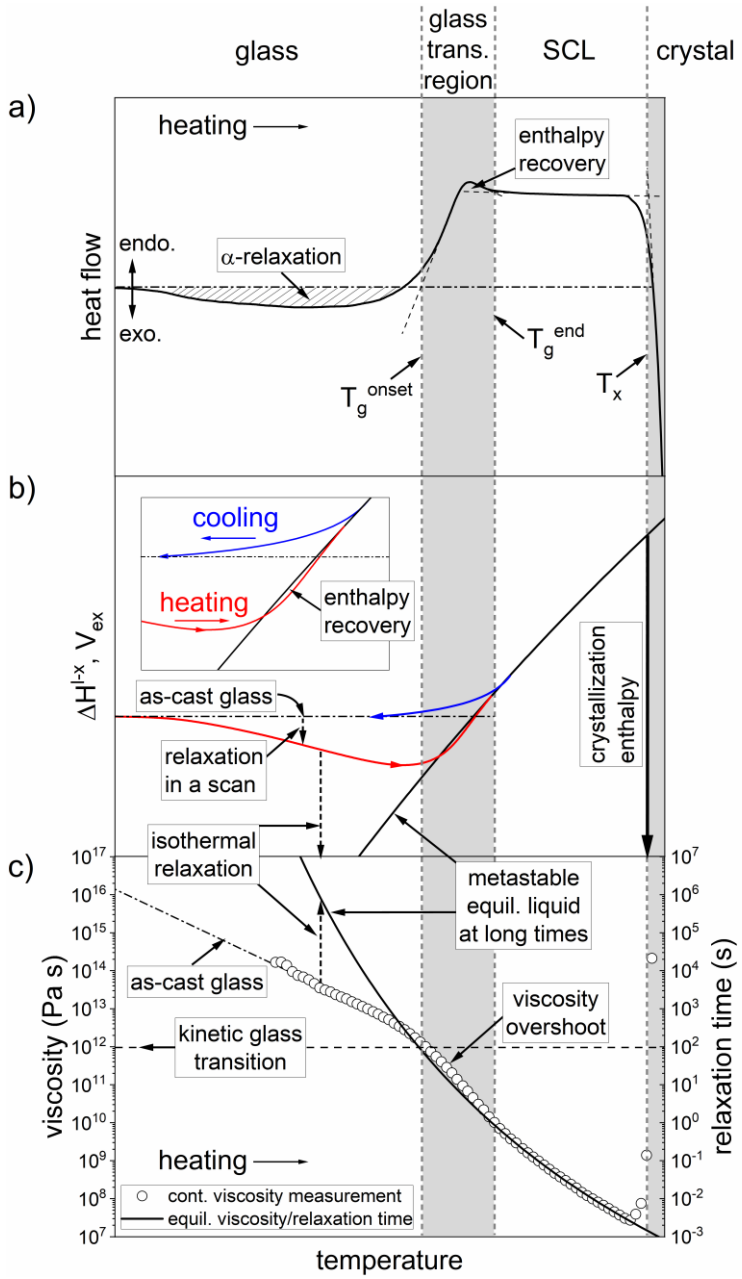

Figure 2.3: Thermophysical properties of a metallic glass upon heating in vicinity of the glass transition. **a)** Heat flow as a function of temperature. The characteristic temperatures are indicated, as well as the exothermic relaxation event and the endothermic enthalpy recovery. **b)** Enthalpy or volume difference between the liquid (or glass) and the crystal (excess enthalpy ΔH^{l-x} or excess volume V_{ex}) upon heating and cooling. The horizontal dash-dotted line represents the as-cast state and the dashed arrow indicates an isothermal relaxation pathway. **c)** Viscosity (or relaxation time) upon heating. The solid black line indicates the viscosity of the metastable equilibrium liquid. Figure and caption adapted from Ref. [29].

Figure 2.3 b) displays the enthalpy (or volume) difference between the liquid or glass and the crystal (excess enthalpy $\Delta H^{l\text{-}x}$ or excess volume V_{ex}) upon heating and cooling. Upon cooling (blue curve), the SCL falls out of equilibrium and a glass is formed, resulting in the as-cast state which is represented by the horizontal dash-dotted line. Upon heating (red curve), relaxation occurs, constantly lowering the enthalpic state of the system. The loss in enthalpy corresponds to the dashed area in panel a). During the glass transition, an enthalpy undershoot below the enthalpy of the equilibrium SCL is observed, as the kinetics of the system are still too slow to follow the enthalpy increase due to the continuous increase in temperature [30]. This leads to the phenomenon of enthalpy recovery towards the end of the glass transition [31]. The long vertical dashed arrow indicates one possible isothermal relaxation pathway. The process of isothermal relaxation will be discussed shortly. Upon further heating, the crystallization temperature is reached eventually, and the crystallization enthalpy is released, reaching the lower enthalpy level of the crystalline mixture.

Viscosity and relaxation time are depicted in Fig. 2.3 c). The open dots represent viscosity as measured during a scan with a constant heating rate. In the glassy state, viscosity decreases exponentially with temperature. Within the glass transition region, a viscosity overshoot is observed which corresponds to the enthalpy undershoot. The viscosity of the metastable equilibrium liquid is described by the Vogel-Fulcher-Tammann equation (black line) which will be introduced in Chapter 2.1.4. The vertical dashed arrow represents a possible isothermal relaxation pathway. During relaxation, viscosity increases until the higher viscosity of the metastable equilibrium liquid at long time scales is reached.

As mentioned above, relaxation can also be observed during isothermal experiments, and in this case at temperatures below the calorimetric glass transition. At the end of the relaxation process, the metastable equilibrium liquid state at long time scales is reached. The temporal evolution of this isothermal relaxation pathway can best be described by a stretched exponential function, as proposed by Kohlrausch, Williams, and Watts (KWW) [32]:

$$\phi(\mathrm{t}) = \phi_a + \Delta\phi\left(1 - exp\left[-\left(\frac{t}{\tau_{KWW}}\right)^{\beta_{KWW}}\right]\right), \tag{2.6}$$

where $\phi(t)$ is the relaxing quantity, ϕ_a its value in the amorphous sample before relaxation at $t = 0$, and $\Delta\phi$ the amplitude during relaxation. The equilibrium value of the relaxing quantity is $\phi_{eq} = \phi_a + \Delta\phi$. The characteristic relaxation time is τ_{KWW}, and β_{KWW} is the stretching exponent.

For a single relaxation process, a plain exponential relaxation behavior with $\beta_{KWW} = 1$ would be expected. Structural relaxation, however, can be understood as many relaxation processes occurring in different structural units at the same time [33]. Theses relaxation processes possess different superimposed relaxation times. This wide

distribution of superimposed relaxation processes can be described by a stretched exponential equation [27].

For metallic glasses, the temporal pathways of the quantities viscosity, enthalpy, and volume during relaxation can all be described by the KWW equation. Typical datasets from isothermal viscosity measurements at different temperatures in metallic glasses are depicted in the results chapter in Fig. 4.11 on page 89. It can clearly be seen how the KWW fit describes the stretched exponential relaxation behavior.

2.1.4 Viscosity and the Fragility Concept

The glass transition upon cooling is caused by a kinetic slowdown of the system. Therefore, the atomic mobility in the liquid plays a crucial role for the formation of a glass and is also a key factor influencing the glass-forming ability, together with the thermodynamic properties.

The atomic mobility can be represented by three quantities: viscosity, diffusivity, and relaxation time. All these quantities are interconnected as will be briefly discussed in the following. Viscosity is the most easily accessible quantity in laboratory experiments. It describes the resistance of a liquid against deformation at a certain rate. The dynamic viscosity, η, is connected with the diffusivity, D, via the Stokes-Einstein relation [34]:

$$D(T) = \frac{k_B T}{6\pi\, r\, \eta(T)}, \tag{2.7}$$

where k_B is the Boltzmann constant, T the absolute temperature, and r the particle radius, corresponding to the average atomic radius in the metallic liquid. The Stokes-Einstein relation holds true in the stable liquid and for intermediate undercoolings [35]. In the deeply undercooled liquid, when approaching the glass transition, however, a breakdown of the Stokes-Einstein relation is reported in many bulk metallic glass-forming liquids [36], as supposedly, the diffusivities of the different atomic species in a multicomponent alloy decouple.

The structural α-relaxation time, τ_α, is linked to the viscosity by the Maxwell relation:

$$\eta = G_\infty\, \tau_\alpha\,, \tag{2.8}$$

where G_∞ is the high frequency shear modulus. τ_α corresponds to the rearrangement time of atoms in the equilibrium liquid state [37].

With the knowledge that atomic mobility can be described by all three quantities, viscosity, diffusivity, and relaxation time, the focus is now laid upon viscosity, as it is the main property that is assessed within this work.

Many efforts have been made to adequately describe the viscosity behavior in the supercooled liquid state over the whole temperature range from the equilibrium liquid

down to the glass transition. For some liquids, the temperature-induced change in viscosity can be described by a classical Arrhenius equation [38]. However, in undercooled liquids the activation barrier for translational atomic movements is often found to be temperature dependent, making a different description necessary. One of the earliest models developed to describe the temperature dependence of viscosity in undercooled liquids was presented by Vogel [39], Fulcher [40], and Tammann and Hesse [41]. This so-called VFT equation can be written as [19]:

$$\eta(T) = \eta_0 \exp\left(\frac{D^* T_0}{T - T_0}\right), \tag{2.9}$$

where D* is the fragility parameter, which describes how much the temperature-induced change in viscosity departs from Arrhenius behavior. T_0 is the VFT-temperature, where viscosity diverges. The pre-exponential factor, η_0, represents the viscosity at infinite temperature and can be estimated by the following equation [42]:

$$\eta_0 = N_A \cdot h/V\,, \tag{2.10}$$

with N_A being Avogadro's constant, h Planck's constant, and V the molar volume.

In 1995, Angell presented a concept to categorize glass-forming liquids according to their temperature dependence of the kinetic properties (e.g. viscosity), the so-called fragility concept [19]. In order to compare liquids with different glass transition and liquidus temperatures, the temperature scale is normalized to the kinetic glass transition temperature, T_g*, which is defined as the temperature where the system reaches a viscosity of 10^{12} Pa s. This definition of the glass transition is based on the concept of a kinetic slowdown that causes said transition. Following this idea, viscosity is plotted on a logarithmic scale over inverse temperature normalized to T_g* in the so-called Angell plot, as shown in Fig. 2.4. Due to the used scaling, all systems meet in the upper right corner of the plot and their temperature-induced change in viscosity can easily be compared.

The kinetic fragility of a liquid describes the temperature dependence of viscosity. Liquids that display a fast change in viscosity around T_g* are called kinetically fragile, while kinetically strong liquids show a rather Arrhenius like behavior, which implies that their structure is less sensitive to changes in temperature. When using the VFT equation (Eq. 2.9) to describe the course of viscosity, a large fragility parameter D* corresponds to a strong liquid, while a small D* corresponds to a fragile liquid. A common example for a kinetically strong liquid is SiO_2, with a D* of around 100 [43], where an Arrhenius like behavior can be observed due to its network structure with strong directional bonds. For the most fragile liquids however, e.g. for o-terphenyl, a D* of around two is observed, indicating a strong temperature dependence of viscosity around T_g*.

When not taking thermodynamics into consideration, strong liquids tend to be better glass formers, as the glass formation is based on the kinetic slowdown around T_g. Their

viscosity only changes slowly with temperature and is several orders of magnitude higher than the one of fragile liquids above T_g.

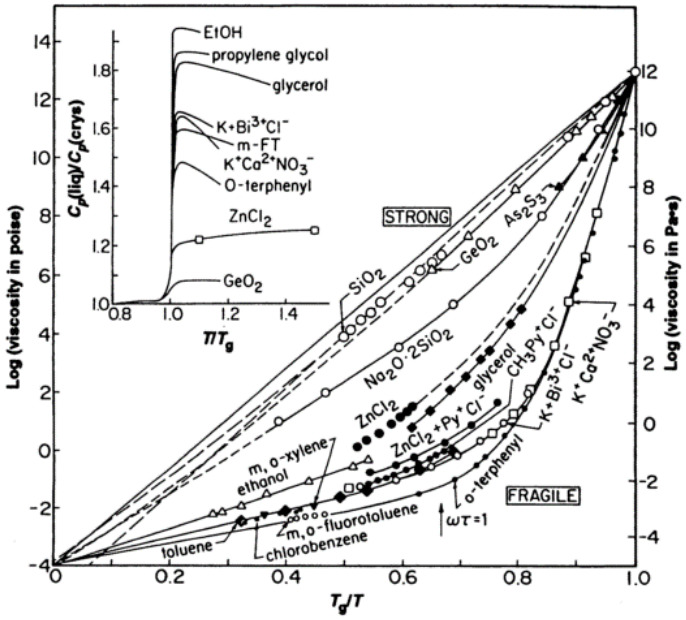

Figure 2.4: Angell plot, showing viscosity on a logarithmic scale over inverse temperature normalized to T_g*, which corresponds to the kinetic glass transition temperature where a viscosity of 10^{12} Pa s is reached. The display format allows for a comparison of the temperature dependence of viscosity between various liquids with different T_g, with fragile liquids showing a strong temperature dependence of viscosity around T_g* and strong liquids almost showing an Arrhenius like behavior. The inset shows the increase in molar heat capacity, c_p, at the glass transition, which is commonly larger for fragile liquids. Figure taken from Ref. [19].

Within the framework of kinetic fragility, metallic glass-forming liquids are found in the range of intermediate D*-values. The kinetically stronger metallic glasses display D*-values in between 25 and 35 [44–46], the intermediate ones have a D* around 20 [44,47,48], and the most fragile ones show values below 15 and even down to 10 [8,24,49].

When interpreted as an activation energy, the kinetic fragility of the liquid can also be described by the slope of the viscosity curve in the Angell plot at T_g*, leading to the so-called fragility index, m, which can be calculated as [50–52]:

$$m = \left.\frac{d\log_{10}\eta}{d(T_g^*/T)}\right|_{T=T_g^*}. \tag{2.11}$$

This fragility index, or steepness index, can be calculated directly from the fitting parameters of the VFT equation (Eq. 2.9):

$$m = \frac{D^* T_0 T_g^*}{\ln(10)\,(T_g^* - T_0)^2}. \tag{2.12}$$

While the VFT model can describe the course of viscosity for many glass-forming liquids, it is only an empirical model and there are systems that are not well fitted by this model. Hence, many more viscosity models were developed [17,53,54], and some of the more recent ones are used in this work and are presented in the following. The models are used to describe the course of viscosity over the whole experimental temperature range and the corresponding results are discussed in Chapter 4.7.

The MYEGA (Mauro, Yue, Ellison, Gupta, Allan) equation was first reported in 2009 [55] and is based on the Adam-Gibbs model [53]. The physical foundation of their model is based on the temperature dependence of the configurational entropy and the model provides an improved prediction of the low-temperature viscosity without a singularity at a finite temperature (compare to T_0 in the VFT equation), hence contradicting the existence of an ideal glass transition as implied by Kauzmann [18].

According to the MYEGA model, viscosity can be described as [55]:

$$\eta(T) = \eta_0 \exp\left[ln(10)\frac{B}{T}exp\left(\frac{C}{T}\right)\right], \tag{2.13}$$

where B and C are the fitting parameters, and η_0 represents the viscosity at infinite temperature, as in the VFT equation. The corresponding m-fragility index can be calculated according to:

$$m = \frac{B}{T_g^*}\left(1 + \frac{C}{T_g^*}\right)\exp\left(\frac{C}{T_g^*}\right). \tag{2.14}$$

Another viscosity model is the cooperative shear model which was developed by Demetriou et al. in 2006 [56]. It is based on the idea that flow in metallic glasses is accommodated by "shear transformation zones" (STZ) (compare to Chapter 2.1.7) where a cooperative shearing of atomic clusters takes place [57]. Within the cooperative shear model, an exponential dependence of viscosity on the activation barrier for shear flow is assumed, which itself again depends exponentially on temperature. The mathematical formulation of the model is the following [56,58]:

$$\begin{aligned}\eta = \eta_0 \exp\left\{\frac{W}{kT}\right\} &= \eta_0 \exp\left\{\frac{W_g}{kT}\exp\left[2n\left(1 - \frac{T}{T_g^*}\right)\right]\right\} \\ &= \eta_0 \exp\left\{\frac{T_g^*}{T}\log\left(\frac{\eta_g}{\eta_0}\right)\exp\left[2n\left(1 - \frac{T}{T_g^*}\right)\right]\right\},\end{aligned} \tag{2.15}$$

where W is the activation energy barrier for shear flow, which displays an exponential temperature dependence and k the Boltzmann constant. n is the elastic softening index and can be interpreted as effective fragility parameter. $W_g = k\, T_g^* \log(\eta_g/\eta_0)$ is the

equilibrium activation energy barrier at the glass transition and η_g is the viscosity at the glass transition, which is 10^{12} Pa s by definition. The estimated corresponding STZ volume is roughly 5 nm^3 or around 250 atoms [58]. In the end, the cooperative shear model makes use of only three fitting parameters.

For a profound explanation of the nature of the activation energy barrier for shear flow, the reader is referred to Ref. [58]. In short, it depends on the shear modulus and the effective STZ volume, which both are temperature dependent and connected via the elastic softening index n, thus resulting in the formulation written above.

The m-fragility index for the cooperative shear model can be calculated as [58]:

$$m = (1 + 2n) \log\left(\frac{\eta_g}{\eta_0}\right). \tag{2.16}$$

The last viscosity model introduced in this work is the extended MYEGA model [59]. It was developed by Mauro and coworkers in 2010, and accounts for a strong and a fragile contribution in metallic glass-forming systems that display a strong-to-fragile transition in their fragility behavior upon heating. This extended MYEGA model reproduces the scaling of dynamics across the strong and the fragile regime. The model uses two constraint onset temperatures and can be expressed as [59]:

$$\ln \eta = \ln \eta_0 + \frac{\ln(10)}{T\left[W_1 \exp\left(-\frac{C_1}{T}\right) + W_2 \exp\left(-\frac{C_2}{T}\right)\right]}, \tag{2.17}$$

where C_1 and C_2 are two different onsets at which different structural mechanisms cause floppy-to-rigid transitions. W_1 and W_2 are weighting factors for the two contributions. An m-fragility steepness index can now be calculated for the strong and the fragile contribution individually, after determining their respective T_g*-values:

$$m_n = \frac{1}{W_n T_{g\,n}^*}\left(1 + \frac{C_n}{T_{g\,n}^*}\right)\exp\left(\frac{C_n}{T_{g\,n}^*}\right), \tag{2.18}$$

where n is 1 or 2 for the strong or the fragile part.

As the extended MYEGA equation already implies, a crossover from a strong to a fragile fragility behavior is observed in several bulk metallic glass-forming alloy compositions [60,61]. In Zr-based glass-forming liquids, a change in the temperature dependence of viscosity is well documented [62,63] and was further investigated by Wei and Stolpe et al. [64,65]. In their work, the changes in fragility are caused by structural changes resulting from a temperature induced strong-to-fragile (SF) liquid-liquid transition (LLT) upon heating. These structural changes can be seen as an abrupt shift in the first peak position of the total structure factor in in-situ synchrotron X-ray diffraction experiments without a pronounced change in density. The rather disordered and fragile high temperature liquid (HTL) transforms into a more ordered and stronger low temperature liquid (LTL). In the corresponding real-space data, the

LLT involves changes in the short- and medium-range order. Given the importance of the kinetics of the melt, and even more its structure, on the crystallization process and hence the glass-forming ability, the existence of such a transition is of great importance to the glass-forming behavior of a BMG.

A typical example for the indication of a SF LLT in high- and low-temperature viscosity measurements can be seen in the Angell plot in Fig. 2.5 for two Fe-based BMGs from our publications [48,66]. The lines correspond to VFT fits of the datapoints that clearly indicate a mismatch between the high- and the low-temperature behavior. The red dots only indicate a possible course of such a transition and do not result from measurements.

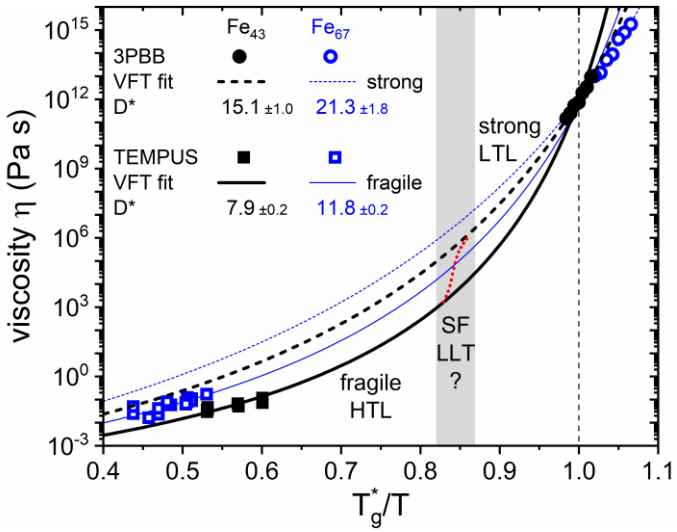

Figure 2.5: Angell viscosity plot of the bulk metallic glass-forming alloys $Fe_{43}Cr_{16}Mo_{16}C_{15}B_{10}$ (black) and $Fe_{67}Mo_6Ni_{3.5}Cr_{3.5}P_{12}C_{5.5}B_{2.5}$ (blue thin lines). The lines correspond to VFT fits of the datapoints. The viscosity measurements at low and high temperatures indicate a strong-to-fragile (SF) liquid-liquid transition (LLT) in between the low temperature liquid (LTL) and the high temperature liquid (HTL). The red dots only indicate a possible course of such a transition and do not result from measurements. Figure adapted from Ref. [48].

Such LLTs have been observed in many more metallic glass-forming systems, e.g. in an Au-based BMG where a LLT occurs just around the glass transition, as observed by synchrotron XRD and X-ray photon correlation spectroscopy (XPCS) measurements [67,68], and also in a Pd-Ni-P alloy [69] and a La-Al-Ni alloy [70]. Even binary metallic and metalloid melts can display LLTs, as experimentally proven by Wei et al. for the Ge-Te system [71], and also found for the Cu-Zr system in molecular dynamics simulations [72] and later in experiments [73,74]. However, not only metallic liquids display LLTs, but a wide variety of other systems show similar phenomena, e.g. water [75], silicon [76], Al_2O_3-Y_2O_3 [77], and triphenyl phosphite [78].

As a last comment on the fragility concept for metallic liquids, it should be mentioned that the fragility behavior can also be directly correlated to temperature-induced structural changes in the liquid. Based on their in-situ synchrotron X-ray diffraction experiments, Wei and Stolpe et al. found a correlation between a structural metric and the kinetic fragility [65,79], leading to the so-called structure-fragility concept. The synchrotron diffraction data obtained in this work is also evaluated with respect to this metric and the theoretical concept is introduced directly in the context of the discussion of the data in Chapter 4.6.3, starting with Eq. 4.2.

2.1.5 Glass-Forming Ability

The glass-forming ability (GFA) of a liquid describes the ease at which crystallization can be avoided upon cooling and a glass can be formed. It can be measured in terms of a critical maximal casting diameter d_c, or by a critical minimum cooling rate for a fully amorphous sample. The crystallization kinetics that determine the GFA of a liquid are governed by the driving force for crystallization, the interfacial energy between the liquid and the crystal, and the atomic mobility in the melt. The resulting temperature-dependent crystallization times can best be visualized in a time-temperature-transformation (TTT) diagram (compare to Fig. 1.1).

The driving force for crystallization, $\Delta G^{l\text{-}x}(T)$, as well as the atomic mobility in terms of the melt viscosity, $\eta(T)$, were already discussed in the previous chapters. The interfacial energy between the liquid and the crystal, however, causes a nucleation energy barrier for the formation of a supercritical crystalline nucleus. In the end, all three factors influence the nucleation and growth of crystals in an undercooled melt. While here only a short summary of nucleation theory and crystal solidification can be presented, a detailed explanation can be found in Refs. [80,81].

From a thermodynamic point of view, both, the driving force for crystallization and the interfacial energy between the liquid and the crystal, determine if a crystalline nucleus is stable. The change in Gibbs free energy, ΔG, upon the formation of a crystalline nucleus can be expressed as:

$$\Delta G = -V_S \, \Delta G^{l-x}(T) + A_{SL} \, \gamma^{l-x} \,, \tag{2.19}$$

where $\Delta G^{l\text{-}x}(T)$ is the volumetric difference in Gibbs free energy between the liquid and the crystal, as given by Eq. 2.1. V_S is the volume of the solid phase, A_{SL} is the area of the interface between the solid and the liquid, and $\gamma^{l\text{-}x}$ is the interfacial energy between the liquid and the solid. For a spherical crystallin nucleus with radius r, Eq. 2.19 can be rewritten as:

$$\Delta G = -4/3 \, \pi \, r^3 \, \Delta G^{l-x}(T) + 4\pi \, r^2 \, \gamma^{l-x} \,, \tag{2.20}$$

and the corresponding contributions in Gibbs free energy as a function of r are depicted in Fig. 2.6. Due to the cubic contribution of the volume term and the quadratic

contribution of the surface term, the Gibbs free energy curve displays a maximum for a cluster with the critical radius r*. Below this radius, the cluster remains an unstable embryo and energy is gained by dissolving the cluster, however, above the critical radius a supercritical nucleus is formed that gains energy upon growth. The critical radius r* corresponds to the point where $d\Delta G/dr = 0$, and the Gibbs free energy value at the critical radius, ΔG^*, is referred to as the nucleation barrier. This barrier needs to be overcome to form a supercritical nucleus that leads to crystallization of the system. As for small undercoolings the Turnbull approximation (Eq. 2.5) can be applied, both r* and ΔG^*, can be expressed as a function of the undercooling ΔT:

$$r^* = \frac{2\,\gamma^{l-x}\,T_f}{\Delta H_f\,\Delta T} \tag{2.21}$$

$$\Delta G^* = \frac{16\pi\,\gamma^{l-x^3}\,T_f^2}{3\,\Delta H_f^2\,\Delta T^2}, \tag{2.22}$$

where ΔH_f is the enthalpy of fusion, and T_f the fusion temperature. The influence of undercooling is also visualized in Fig. 2.6. The dashed grey line corresponds to a higher undercooling, which lowers the critical radius and the nucleation barrier, thus increasing the nucleation probability.

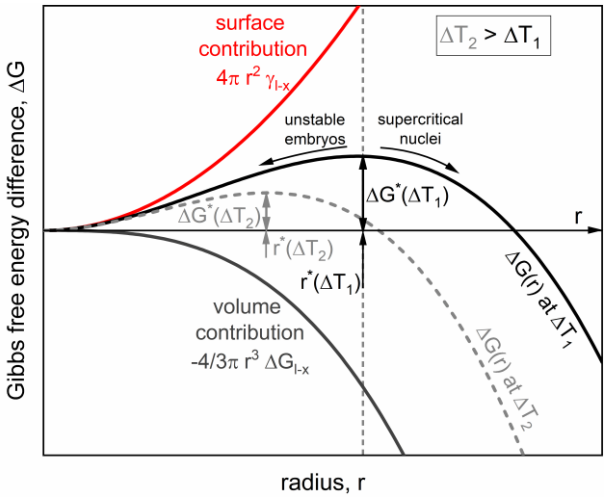

Figure 2.6: Gibbs free energy difference ΔG in a liquid when a spherical crystalline nucleus with the radius r is formed. The ΔG-curve contains a volume- (grey) and a surface- (red) contribution, leading to a maximum for a cluster with the critical radius r* and a nucleation barrier ΔG^*. Clusters larger than r* are supercritical and gain energy upon growth.

With the knowledge of the nucleation barrier and the atomic mobility of the system, the homogeneous nucleation rate, I(T), can be caluclated:

$$I(T) = A\,\upsilon(T)\exp\left(-\frac{\Delta G^*}{k_B\,T}\right), \tag{2.23}$$

where A is a constant pre-factor, $\upsilon(T)$ the atomic jump frequency, and k_B the Boltzmann constant. The atomic jump frequency corresponds to the attachment frequency of atoms to a supercritical cluster and represents the atomic mobility. It is directly connected to the average atomic diffusion coefficient, D, which again relates to the viscosity via the Stokes-Einstein relation (Eq. 2.7).

Once a supercritical nucleus was formed, the growth velocity of its surface can be described by the growth rate u(T) [82]:

$$u(T) = \frac{f}{a_0} D\left[1 - \exp\left(-\frac{\Delta G^{l-x}}{R\,T}\right)\right], \tag{2.24}$$

where f is a constant influenced by the roughness of the interface between the crystal and the liquid, a_0 corresponds to the average atomic diameter, and D is the atomic diffusivity. Both, the nucleation rate and the growth rate, depend on a thermodynamic contribution in terms of a Gibbs free energy difference, and a kinetic contribution in terms of the atomic diffusivity.

Finally, the crystallization process upon undercooling is governed by the combined influence of I(T) and u(T). For a given temperature T, the volume fraction X of the system that has crystallized in the time t, can be modelled by the Johnson-Mehl-Avrami-Kumogorov (JMAK) equation [80]:

$$X(t) = 1 - \exp[\pi/3\ I(T)\,u(T)^3\,t^4]\,. \tag{2.25}$$

When rearranging this equation for a given volume fraction of crystals, it directly describes the shape of the crystallization nose in a TTT diagram. At high temperatures, thus small undercoolings, the contribution of the growth rate u(T) dominates, due to a small driving force for crystallization and a high atomic mobility. At low temperatures and high undercoolings however, the large driving force for nucleation triggers nucleation but the low atomic mobility limits the growth of the nuclei. Therefore, the crystallization process is nucleation controlled at small undercoolings and growth controlled at high undercoolings. Consequently, the minimum waiting time for crystal formation, τ_x^*, is found at the temperature T*, where growth and nucleation rate superimpose most constructively. τ_x^* corresponds to the time where the tip of the crystallization nose is located in the TTT diagram and can be translated into a critical casting thickness [83].

Figure 2.7 displays three schematic TTT diagrams in order to visualize the influence of the previously discussed quantities (driving force for crystallization, interfacial energy, and atomic mobility) on the crystallization time in the JMAK equation. The influence of the interfacial energy between liquid and crystal is considered directly via

$\gamma^{l\text{-}x}$, the driving force is considered via the entropy of fusion ΔS_f, according to the Turnbull approximation (Eq. 2.5), and the atomic mobility is considered via the kinetic fragility that determines the viscosity.

System 1) in Fig. 2.7 corresponds to a bad glass-former with a low GFA. The minimum waiting time for crystal formation, τ_x^*, is only 1.7×10^{-8} s which roughly corresponds to a critical casting thickness of only 7.5 µm. Such properties are expected for alloys with a low interfacial energy, a high driving force, and a kinetically fragile liquid. System 2) describes a better glass-former with intermediate values for the three properties, and system 3) corresponds to an excellent glass-former with a critical casting thickness of 63 mm. Such a high GFA can be observed in systems with a high interfacial energy, a kinetically strong liquid behavior and a driving force for crystallization that is not too high.

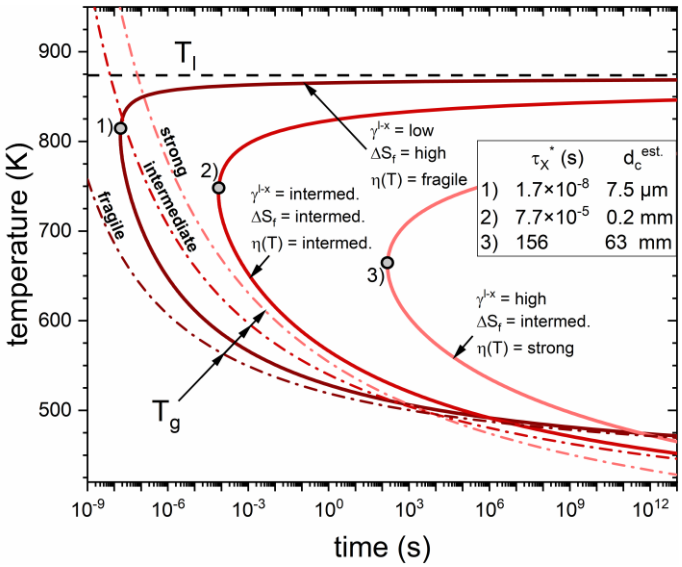

Figure 2.7: Effect of the interfacial energy, $\gamma^{l\text{-}x}$, the Gibbs free energy difference between the liquid and the crystal (represented by the entropy of fusion, ΔS_f) $\Delta G^{l\text{-}x}$, and the kinetic fragility of a liquid on the crystallization nose in a TTT diagram. The GFA improves systematically from system 1) to 3) by changing the parameters. Figure taken and caption adapted from Ref. [29].

Within the context of minor additions, and also impurities, the topic of heterogeneous nucleation plays an important role. In a system with a high GFA, e.g. system 3), the GFA can be drastically reduced if heterogeneous nucleation occurs and the resulting TTT diagram could resemble the one of system 2), or even system 1). The nucleation barrier ΔG^* is reduced due to the presence of crystalline surfaces that act as initial nucleation sites. These heterogeneous nucleation sites can for example be oxide particles due to impurities that do not dissolve at the casting temperature [11,84,85], but also the walls of the mold the alloy is cast into [86].

When the alloy composition is changed, e.g. by minor additions, this can also result in a change of the primary crystallizing phase. This goes along with a change in the interfacial energy between this new phase and the liquid, as well as with a possible change in the driving force for nucleation of this phase. Consequently, minor additions can shift the nose in the TTT diagram in different directions, either improving or deteriorating the GFA.

Theoretical considerations aside, there are many empirical correlations and models that can be used to estimate the GFA of BMGs.

In 1969, Turnbull presented the concept of the reduced glass transition temperature, $T_{rg} = T_g/T_l$ [87] (Turnbull initially used the solidus temperature T_m instead of the liquidus temperature T_l, which was however later found to correlate better with the GFA [88]). A high T_{rg}-value indicates a better GFA, as only a small temperature range between the stable liquid and the glass needs to be passed, and good glass formers often show T_{rg}-values above 2/3. This is the case for deep eutectic compositions, where the liquid phase is stable down to low temperatures.

Another criterion for good glass-formers is the confusion principle [89]. The chance that a melt easily forms a stable crystalline structure diminishes with an increasing number of elements, as complicated crystal structures hamper the crystallization process. This effect is increased if the constituent elements possess different atomic sizes, which allows for a more efficiently packed structure. This densely packed structure displays retarded kinetics and slows down crystallization. According to Miracle and his efficient cluster packing model [90,91], the atomic structure can be used to predict the GFA, with an efficient packing being highly beneficial. An efficient packing goes along with a small amount of free volume in the liquid, which again indicates a pronounced short range order [92]. Systems with a pronounced order in the liquid state typically display a small entropy of fusion, which following the Turnbull approximation indicates a small driving force for crystallization [93].

In 1997, Inoue proposed three empirical rules to predict the GFA. Necessary for a high GFA are: "(1) a multicomponent system consisting of more than three elements, (2) significantly different atomic size ratios above about 12% among the main constituent elements, and (3) negative heats of mixing among the elements." [94]. These rules can be understood as a combination of some of the previously mentioned criteria, with (1) referring to the confusion principle, and (2) and (3) to the efficient cluster packing, due to atomic size and atomic bonding. Inoue also proposed that the length of the supercooled liquid region upon heating correlates with the GFA, as a thermally stable supercooled liquid region indicates sluggish kinetics and a high resistance against crystallization and is therefore often observed in strong liquids [95]. This criterion is however often not followed, as will also be shown by the results of this work.

2.1.6 Structure

In crystalline metals the structure is well defined by the atomic lattice. In metallic liquids and glasses however, the structural order is much more complicated, and no long-range order is found. Hence, no sharp Bragg diffraction peaks are found in X-ray diffraction experiments, which was already proven for the first metallic glass in 1960 [1]. Metallic liquids and glasses are often considered disordered, which is not completely true as a distinct short-range order (SRO) and even medium-range order (MRO) exists. When taking into consideration that a metallic glass is a frozen-in metallic liquid, structural similarities are apparent. However, an increase in structural order is still observed upon cooling a metallic liquid from high temperatures down to the glassy state.

Till the 1960s, liquids were mostly seen as dense gases or disordered solids. At this time, the works of Bernal contributed to a profound understanding of the structure of liquids and the idea of random packing [96]. For a better understanding, simple monoatomic liquids were considered, where the atoms can be seen as hard spheres. These spheres form a dense randomly packed structure with irregular polyhedra, which are the structural unit defining the SRO in the liquid [97–99].

In the 1970s, review articles by Cargill [100] and Finney [101] summarized the progress made so far in the investigation of the structure of amorphous metals and alloys. These solid amorphous structures were found to show structural features similar to the ones of the liquid state. New experimental diffraction techniques were described, the structure of alloys (and not only monoatomic liquids) was investigated and the dense random packing model of hard spheres was refined [100]. In this context, the concept of icosahedral arrangements as local structural units (clusters) was introduced, where twelve atoms surround a center atom. Around the same time, Gaskell proposed trigonal prisms that connect via edge sharing as local structural units in metal-metalloid glasses [102].

Only few years ago, local icosahedral order in metallic glasses was experimentally imaged for the first time [103]. Hirata et al. used Angstrom-beam electron diffraction (ABED) to obtain two-dimensional images of distorted icosahedral clusters. As shown in Fig. 2.8 a), the electron diffraction images resemble the images predicted by simulations. The models on the right visualize the distorted icosahedra from two different viewing angles.

Depending on the alloy system, the constituent elements, their size distribution, and their chemical interactions, different local representative structural units or clusters are conceivable. The size ratio of the different constituent elements for example determines which coordination number (Z) around a central solute atom leads to an efficient filling of space. Figure 2.8 b) displays six different Kasper polyhedra [104] corresponding to the different coordination numbers. While the size ratio of atoms defines the topological SRO, a strong chemical affinity between the constituent elements causes chemical SRO, leading to the formation of a cluster where a metalloid

atom is surrounded by metallic atoms [105]. Just recently we found experimental evidence for a change in the local representative structural unit upon a change in alloy composition. In Pt-P based liquids, trigonal prisms are the dominant representative structural unit, whereas the influence of icosahedral SRO increases upon gradually replacing Pt by Pd, thus diminishing the presence of trigonal prisms [93].

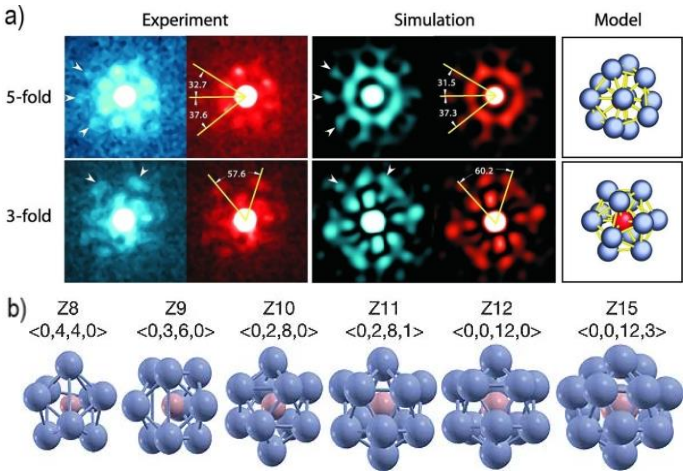

Figure 2.8: Short-range order (SRO) in metallic liquids and glasses. **a)** Experimental and simulated electron diffraction patterns of icosahedral clusters in a $Zr_{80}Pt_{20}$ metallic glass, confirming the presence of icosahedral clusters as local representative structural units. Taken from Ref. [103]. **b)** Kasper polyhedra corresponding to the different possible cluster structures depending on the coordination number Z. Taken from Ref. [105].

The medium-range order (MRO) in metallic liquids and glasses is defined by the connection scheme between the local representative structural units that define the SRO. In 2004, Miracle proposed the so-called efficient cluster packing (ECP) model [91] and further elaborated the model in 2006 [106], where efficiently packed solute-centered atomic clusters act as local representative structural element (RSE). The model combines the random positioning of solvent atoms with an atomic order of the solutes. The clusters can be idealized as spheres that are again efficiently packed to fill space, hence resulting in a quasi-periodic arrangement similar to a face-centered cubic or hexagonal close-packed structure, which explains the MRO. Neighboring clusters can overlap in the first coordination shell, thus reducing internal strains. Furthermore, the solvent atoms are located on random positions, as there is no orientational order in between the clusters. And finally, all solute atoms have a specific preferred size ratio in relation to the solvent atoms, which are the majority species, to satisfy the conditions for topological SRO within the cluster.

The Miracle model does not take chemical effects into account and is purely based on geometrical considerations. In 2006, Ma and coworkers further elaborated on the idea of efficient cluster packing by including the effects of chemical affinity on the SRO [105]. Figure 2.9 a) displays one of their simulated assemblies of clusters in the $Zr_{84}Pt_{16}$

metallic glass. Their results show the presence of fragments of icosahedra, indicating an icosahedral-type MRO or cluster ordering. The dominant type of MRO in a metallic glass can change for systems with a high solute concentration. At one point, solute-solute contacts cannot be avoided, and the solute atoms arrange in string-like structures that are surrounded by solvent atoms. These so-called extended clusters connect via edge-, vertex- or face sharing and lead to a different type of MRO [105].

The structure in metallic glasses is typically investigated by diffraction methods, e.g. by synchrotron X-ray diffraction experiments. The underlying principle is introduced in Chapter 3.5, and a typical diffraction pattern of an amorphous metallic solid can be seen in Fig. 3.11 a). The structural information is contained in the structure function, S(Q), as well as in its Fourier transform, the pair distribution function, g(r). Simply spoken, the pair distribution function shows the probability of finding an atom in the distance r from the reference atom. A typical g(r)-curve for a metallic glass is shown in Fig. 2.9 b), together with a schematic 2D depiction of the atom arrangement. The first peak in g(r) corresponds to the first coordination shell around a central atom, whereas the second peak corresponds to the second nearest-neighbor shell.

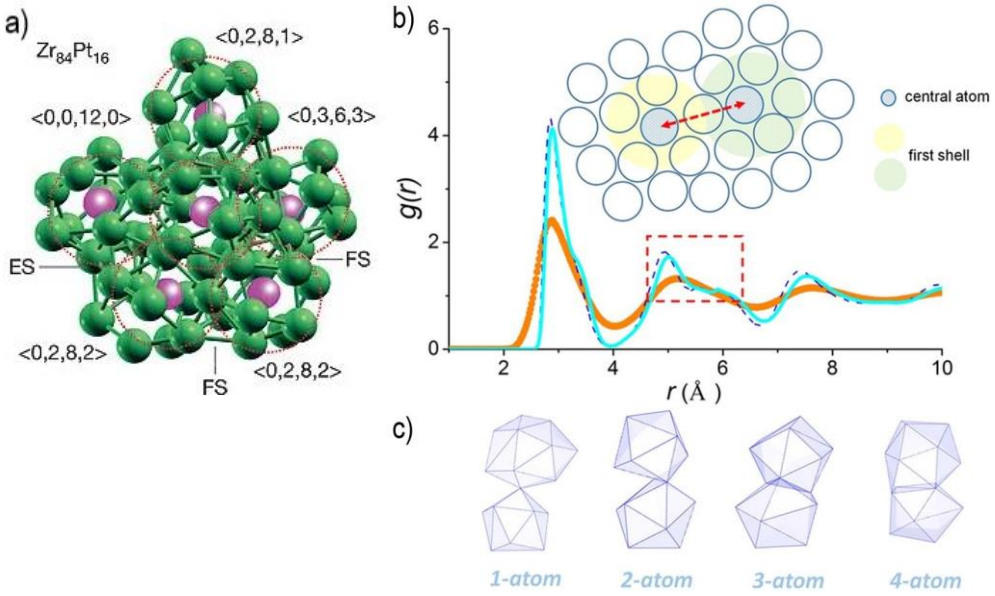

Figure 2.9: Medium-range order (MRO) in metallic liquids and glasses. **a)** 3D model of an assembly of clusters in the $Zr_{84}Pt_{16}$ metallic glass. The SRO is dominated by solute (Pt) centered clusters, as indicated by the dashed circles. For each cluster, the Voronoi index is given in triangular brackets. The combination of edge sharing (ES) and face sharing (FS) between the clusters determines the MRO. Taken from Ref. [105]. **b)** Pair distribution function, g(r), of a metallic liquid (orange line) and the corresponding glass (blue dashed line). The inset displays a schematic 2D representation of the atom arrangement with shells around a central atom. The second peak in g(r) corresponds to the second nearest neighbor distance. **c)** Schematic representation of different cluster connection schemes, for the sharing of one to four atoms between neighboring clusters. b) and c) taken from Ref. [107].

The shape and position of the second peak in g(r) reveals information on the MRO and the dominant cluster connection schemes [107]. A splitting of the peak indicates different cluster connection schemes, e.g. the sharing of edges, faces and vertices. Such connection schemes are schematically depicted in Fig. 2.9 c), for the sharing of one to four atoms between neighboring clusters. A more detailed interpretation of the g(r)-curve with respect to the connection schemes and implications regarding icosahedral SRO is presented later on in the discussion in Chapter 4.6.3.

2.1.7 Mechanical Properties and Deformation

Their extraordinary strength and elasticity are what makes BMGs interesting candidates for structural applications and explains the large interest in BMGs from industry. A qualitative stress-strain diagram (yield strength vs. elastic limit) for BMGs in comparison to common structural engineering materials was already shown in the introduction in Fig. 1.2. In general, amorphous metals exceed the strength of steels and at the same time provide the elasticity of polymers. Their compressive fracture strengths range from 2 GPa for Zr-based glasses up to 5 GPa for Co-Fe-based glasses, thus approaching the theoretical strength limit. In combination with a yield strain of typically 2 %, BMGs display an extraordinary high resilience σ_y^2/E, which makes them an ideal spring material [108]. Based on their high yield strength, they also show high hardness values (up to 1100 HV for iron-based alloys) and excellent wear resistance [109].

Their unique mechanical properties in comparison to crystalline metals result from their different microstructure, or rather the lack of it. As amorphous metals do not show any long-range order and crystalline lattice, the well-known vehicles of plastic deformation in crystalline metals, the dislocations, cannot be formed. This results in new deformation mechanisms that explain the increased strength and elasticity. Plastic deformation at temperatures well below the glass transition (e.g. at room temperature) in amorphous metals is carried by so-called shear bands [110].

Two possible atomistic mechanisms for shear band formation were already proposed in the late 1970s by Argon [57] and by Spaepen [111], both of which describe a local rearrangement of atoms that can accommodate shear strain. Figure 2.10 a) depicts a two-dimensional schematic of the mechanism proposed by Argon, the shear transformation zone (STZ). A STZ is basically a cluster of atoms where an inelastic shear event occurs, transferring the cluster from one energetically low configuration to a different one, while a configuration of higher energy and volume needs to be crossed in the process. Simulations predict such STZ to contain few to roughly 100 atoms [112]. Contrary to dislocations in crystalline metals, STZ are not structural defects in the amorphous structure. They cannot be distinguished from the rest of the structure and are rather defined by the shear event itself, leading from one configuration to another one.

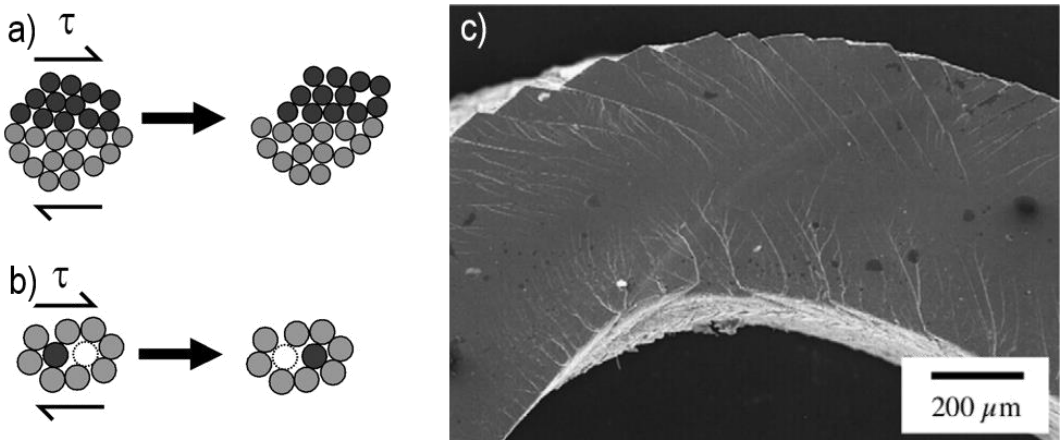

Figure 2.10: a) and **b)** Schematic depictions of atomistic mechanisms for plastic shear deformation in BMGs. a) shows a shear transformation zone (STZ), after Argon [57], and b) a local atomic jump, after Spaepen [111]. **c)** Scanning electron image showing surface offsets due to shear bends in a metallic glass deformed by bending. Figures a) and b) taken from Ref. [112], c) taken from Ref. [113].

The second deformation model by Spaepen is schematically depicted in Fig. 2.10 b). Spaepen describes plastic flow as a series of discrete atomic jumps, which are favored near sites of high free volume. Consequently, this diffusive-jump-type model is based on the ideas of the free volume concept by Cohen and Turnbull [17,20,114]. The free volume is defined as the part of the excess volume that can be redistributed without changing the energy of the system [20]. The excess volume describes the difference in volume between the observed structure and the "ideal glass", which would be the glass with the lowest possible energetic state [20].

The process of shear band formation determines the macroscopic mechanical properties of BMGs. While the term "glass" often implies a brittle behavior, many BMGs display a large ductility and plasticity, e.g. as in Ref. [115]. Figure 2.10 c) shows a BMG sample after strong plastic deformation by three-point flexural bending. Surface offsets due to shear bands are clearly visible and accommodate the plastic deformation. Typical stress-strain curves corresponding to bending tests on ductile BMGs can be found later in the results section in Fig. 4.3 on page 74.

However, as in crystalline materials, the mechanical properties, and especially the ductility, strongly depend on the processing conditions during production of the sample or the sample history in general. As the atomistic deformation mechanism is largely influenced by the excess volume and free volume of the structure, the amount of free volume that is frozen-in upon quenching influences the ductility. The influence of the sample cooling rate on the excess volume and at the same time on the fictive temperature was already visualized in Fig. 2.1. In 2013, Kumar et al. for the first time showed experimental evidence for a brittle-to-ductile transition based on the fictive

temperature of the system [116] and just recently the concept was further elaborated in the context of a toughening transition [117].

Kumar proposed that there is a critical fictive temperature $T_{fic,crit}$ below which a brittle fracture behavior is observed. When the fictive temperature T_{fic} falls below $T_{fic,crit}$, the amount of excess volume that is frozen-in is too low to allow for the activation of multiple STZ which would be necessary for plastic deformation. This idea leads to many more implications. First, if a sample is cooled too slowly, the fictive temperature falls below the threshold. As large samples experience a lower cooling rate in the center, they tend to embrittle. The slow cooling of smaller samples also causes embrittlement. Second, the fictive temperature is also linked to the relaxational state of a sample. Relaxation lowers T_{fic} (and decreases the excess volume), hence causing embrittlement. Third and last, increasing the excess volume of a sample can make initially brittle samples ductile. The process of increasing the excess volume is typically called rejuvenation and can be achieved by various methods. A thermoplastic forming process (compare to Chapter 2.3) can be used to heat a sample to the desired fictive temperature with a higher excess volume and then rapidly quench the sample to conserve the obtained structure. Furthermore, the excess volume can be increased by mechanical deformation, e.g. by cold rolling [118–120] and by shot peening [121], or even by cryogenic cycling [122].

To this point, only the mechanical properties and deformation behavior at temperatures far below the glass transition were discussed. Approaching the glass transition however, the mechanical behavior of BMGs changes drastically and different deformation mechanisms come into play. The deformation behavior dependent on temperature as well as the applied stress and the deformation rate is schematically visualized in Fig. 2.11. This deformation map is taken from a review by Schuh et al. [112] and is based on the ideas of Spaepen [111].

Figure 2.11. displays the dominant deformation mechanism on a temperature scale normalized to T_g. On the left ordinate, the shear stress normalized to the shear modulus is shown and on the right one, absolute stress values are shown for a typical Zr-based BMG. At low temperatures and low stresses, the system shows an elastic response where flow can be neglected (white area). When increasing temperature, homogeneous deformation sets in. The temperature at which homogeneous flow can be observed largely depends on the applied strain rate, which is indicated by the dashed black lines in the bottom right corner. At slow strain rates for example, homogeneous flow can already be detected at lower temperatures (and hence higher viscosities). At increased stresses, the homogeneous Newtonian deformation behavior changes to a non-Newtonian one.

The whole area of homogeneous flow corresponds to the processing area for thermoplastic forming (compare to Chapter 2.3). In this region the softening of the amorphous structure due to the glass transition can be used to accommodate large deformations in a homogenous manner. The process is equivalent to the one known

for thermoplastic polymers. Homogeneous flow itself is thermally activated and allows for deformation that is evenly distributed throughout the whole sample.

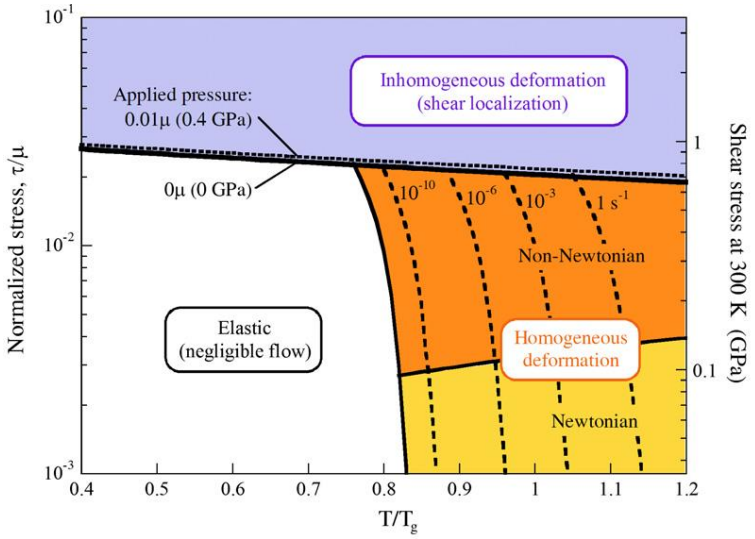

Figure 2.11: Schematic deformation map for BMGs. The dominant deformation mechanism is shown on a temperature scale normalized to T_g and depending on the shear stress normalized to the shear modulus. At low temperatures and low stresses, the system shows an elastic response where flow can be neglected. At high temperatures, homogeneous flow is observed, and the starting temperature depends on the strain rate (dashed black lines). At high stresses, inhomogeneous deformation occurs due to a shear localization in shear bands. Taken from Ref. [112].

When the stress is increased, a transition from homogeneous steady-state flow (or elastic behavior) to inhomogeneous deformation (blue area) occurs. The thick black almost horizontal line separates the regime at high temperatures and low stresses, where homogeneous deformation occurs, from the regime at low temperatures or high stresses where inhomogeneous deformation and shear localization occur. The regime of shear localization, or rather shear band formation, corresponds to the inhomogeneous deformation mechanisms that are depicted in Fig. 2.10 a) and b).

For an in-depth discussion of the mechanical properties and the deformation behavior of amorphous metals, the interested reader is referred to literature. The review article by Schuh et al. [112] is recommended for an overview with a specific focus on fundamentals and mechanisms of deformation and fracture. For a general review of mechanical properties of BMGs the reader is referred to the work of Trexler and Thadhani [123], and for a review on shear bands to the work of Greer et al. [110]. Different publications on fatigue and fracture behavior can be found from Kruzic and coworkers [120,124–126].

2.1.8 Sulfur-Containing BMGs

To date there are hundreds or even thousands of BMGs that have been discovered. However, there is a vast variety of alloy compositions that have never been investigated so far, and the number of potential BMG compositions is estimated to be more than three million [127]. This estimation is based on a combinatory approach that considers 32 elements to be practical for the formation of BMGs, excluding toxic or radioactive metals and elements that have not been used in BMGs before. The number of possible combinations can even be significantly increased if additional elements can be considered, and within the scope of this work, sulfur (S) is considered as a new constituent element in BMGs.

In late 2015, Kuball, Gross, Busch, and I for the first time discovered a bulk metallic glass-forming alloy with sulfur as a major constituent. This discovery was made in the Pd-Ni-S system and inspired the attempt to try sulfur as a constituent element in many other metallic systems. Throughout 2016 and 2017, hundreds of alloy compositions were produced and tested regarding their GFA, leading to the discovery of more than 500 different and new sulfur-containing glass-forming compositions. Finally, in 2017 a patent for S-containing BMGs was filed [128] and the first paper was published [7].

Three general classes of S-containing BMGs were found: alloys with high S-contents above 20 at%, alloys with intermediate S-contents around 8 at%, and alloys with minor additions of S (between 1 and 2 at%). The S-containing alloys were found in systems with distinctly different constituents, e.g. in Pd-Ni-S, in Ti-(Zr)-Ni-S, in Ti-(Zr)-Cu-S, in Ti-(Zr)-Pd-S, in Zr-Cu/Ni-Al-S, in Zr-(Ti)-Ni-S, in Cu-Ti-Zr-Ni-S, and in Ni-Nb-S. A publication on the bulk glass formation in the initially discovered Pd-Ni-S system was released in 2018 [8], and the first paper on Ti-based alloys in the Ti-(Zr)-Cu/Ni-S system was published in 2019 [9]. An in-depth investigation on the properties of S-containing BMGs in the Pd-Ni-S and the Ti/Zr-Cu/Ni-S system can be found in the doctoral thesis of Alexander Kuball, which is written simultaneously with this work [129].

Especially in the Cu-Ti-Zr-Ni-S and the Zr-Cu/Ni-Al-S system, minor additions of S drastically change the properties. The supercooled liquid region of the Zr-based alloy Vit105 ($Zr_{52.5}Cu_{17.9}Ni_{14.6}Al_{10}Ti_5$) [11] and the Cu-based alloy Vit101 ($Cu_{47}Ti_{34}Zr_{11}Ni_8$) [12] can significantly be enhanced [7]. These findings inspired the first part of this work on the effect of minor additions in these two systems. The observations made for S suggested to also evaluate the influence of minor additions of phosphorus (P) in the same alloy families, as P is the neighboring element of S in the periodic table and is already known as an important constituent element in many BMGs.

2.2 Minor Additions

Minor additions of certain elements are commonly used in the whole field of metallurgy. In fact, the most used structural metal, steel, owes its excellent properties to minor additions of carbon in iron. In the case of aluminum, minor additions of copper can be used to significantly strengthen the material, based on the phenomenon of precipitation hardening [130]. Minor additions also provide an effective way to control the nucleation process in a melt and hence fine-tune the microstructure during solidification. Instead of the term minor additions, sometimes the term microalloying is used synonymously. As microalloying tendentially refers to additions of far below 1 at%, in this work the term minor additions is used preferentially, as additions up to some at% are considered.

2.2.1 Minor Additions in BMGs

As for conventional alloys, the properties of BMGs can also be adapted and fine-tuned by minor additions. There is a large number of publications on different effects of such additions, and for a deeper insight the reader is referred to a well-written review article by Wang [10], as well as two other review articles in Refs. [131,132].

In general, the functions of minor additions in BMGs can be summarized as the following [10]: Enhance (but also deteriorate) the GFA [133,134], explore new BMGs [135], scavenging the oxygen in elements and processing environment [136,137], improve the castability, induce the formation of BMG-based composites [133], enhance the thermal stability [133,134,138], strengthen the BMG, enhance the ductility [139–141], improve the magnetic properties, or even change the corrosion behavior [142].

The mechanisms causing these changes are not so easy to reveal. One possible influence is that the liquid behavior of an alloy is changed by minor additions. The kinetic fragility behavior can for example be altered, whereas a kinetically stronger behavior causes a slowdown in the atomic mobility above the glass transition temperature, thus slowing down the crystallization process and increasing the GFA. Another possibility is a stabilization of the liquid state by minor additions, where the liquidus temperature is lowered by alloying. Minor additions can also suppress the formation of the crystalline phases competing with the liquid phase. And finally, they can act as oxygen scavenger, e.g. yttrium, and bind harmful oxygen impurities [137].

Typically, different types of atoms for minor additions can be distinguished. Metalloid elements, like Si, C, and B show small atomic diameters and also a high chemical affinity to the typical constituents of BMGs, like Zr, Ti, Cu, etc. While the metalloids tend to form high-melting compounds with the other metals, which should trigger heterogeneous nucleation, they also significantly increase the packing density in the liquid state and hence stabilize the melt against crystallization. Therefore, the effect of metalloid additions can be both beneficial and unfavorable for the GFA. A positive effect on the GFA cannot only be achieved by adding small atoms, but also by large

ones. Therefore, minor additions of Hf, Zr, or Sn are often found. Additions of rare earth elements mostly act as oxygen scavengers, improving the GFA by removing heterogeneous nucleation sites [10].

The Cu-Ti-Zr-Ni alloy system, with its industrially interesting alloy composition Vit101 ($Cu_{47}Ti_{34}Zr_{11}Ni_8$) [12], has often been modified by minor additions. Vit101 itself displays a critical casting thickness of 4 mm and shows virtually no stable supercooled liquid region upon heating [12]. Experiments with SiC particles for the production of BMG composites revealed the beneficial influence of Si on Vit101 [133]. A Si addition of only 1 at% results in a critical casting thickness of 7 mm, thus 3 mm larger than for the base alloy. Additionally, the length of the SCL region upon heating can be extended by 20 K. Subsequent investigations by Park et al. revealed that both, the critical casting thickness and the length of the SCL region, can further be increased in the $Cu_{47}Ti_{33}Zr_{11}Ni_8Si_1$ alloy by adding 2 at% of Sn [134]. The influence of minor additions of Si and Sn in Vit101 on the toughness was later investigated by Johnson and coworkers [143]. They found that both elements sharply decrease the toughness. This might be associated to a small increase in shear modulus, glass transition temperature, yield strength, and a decrease in Poisson's ratio, which implies a negative correlation between toughness and the shear flow barrier. Eckert and coworkers however discussed, that the Si-containing alloys might not be fully amorphous and contain nanocrystals [144].

While minor additions are typically added on purpose, oxygen impurities or other impurities can also be considered as minor additions. In most cases, an increased amount of oxygen has a detrimental effect on the GFA and often also on the toughness or ductility. In the case of Vit105 ($Zr_{52.5}Cu_{17.9}Ni_{14.6}Al_{10}Ti_5$) the effect of oxygen on the crystallization behavior of the undercooled melt was investigated by electrostatic levitation (ESL) [11]. A drastic shift of the crystallization nose in the TTT diagram upon cooling is reported, demonstrating a reduced GFA. An oxygen related embrittlement in a Zr-Cu-Al BMG was reported by Inoue and coworkers [145]. The influence of oxygen on the mechanical properties of Vit105 was shortly after investigated by Liu et al. [146]. There, they also report that the impurities dramatically embrittle the alloy and also decrease the GFA. They identified Zr_4Ni_2O particles by electron diffraction and suggest that these particles trigger crystallization. The strong influence of oxygen impurities is a general phenomenon in Zr-based alloys and explain the necessity to use high purity Zr instead of industrial grade material.

2.2.2 Minor Additions of Sulfur and Phosphorus

Minor additions of different metalloids like Si, C, and B are well known in BMGs. These elements are typically added due to their small atomic radius, leading to an increased packing density in the melt. The neighboring elements of Si when going to higher atomic numbers are phosphorus (P) and sulfur (S), which are considered as reactive nonmetals. While P is commonly found in BMGs, e.g. in the Pd-Ni-P system [2], in Pt-P alloys [147], in Ni-based alloys [49] and in many Fe-based BMGs [109];

S was never considered as constituent element in BMGs before 2018 [7]. However, it should be noted that the P-containing alloys typically contain significant amounts of P, above 10 at%, and not only minor additions.

In our work from Ref. [7], the influence of minor additions of S on the thermal stability upon heating in three different alloy systems was presented, as shown in Fig. 2.12. In Vit101 and Vit105, additions of 1.5 % and 2 % of S, respectively, shift the glass transition to higher temperatures and at the same time increase the length of the SCL region. In the Ni-Nb system, the glass transition temperature stays unaffected upon the addition of 3 % of S, while the SCL region gets significantly extended. In all three cases, the extended SCL region indicates an improved thermoplastic formability [138], as will be evaluated later in this work.

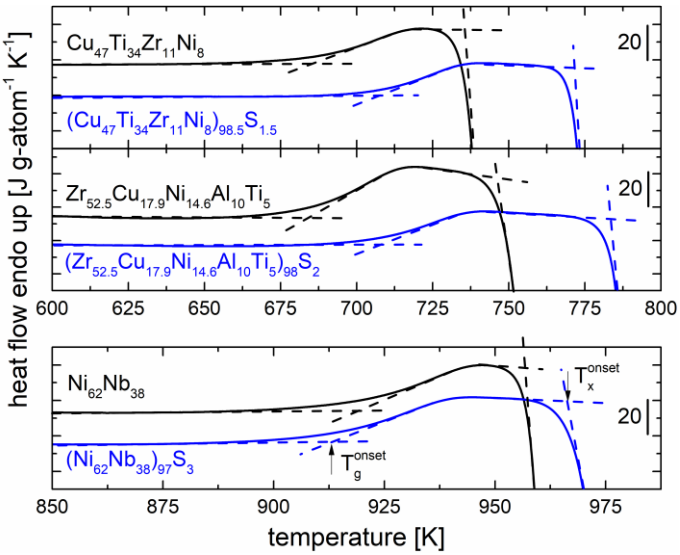

Figure 2.12: Influence of minor additions of sulfur on the thermal stability of three different BMGs. DSC scans with a heating rate of 1 K/s are displayed, with the base alloys shown in black and the sulfur-bearing compositions in blue, which have an extended supercooled liquid region. Taken from Ref. [7].

When only considering topological aspects regarding the constitution of an alloy, Si, P, and S can play the same role due to their similar atomic diameter, which are 110 pm for Si, 106 pm for P, and 103 pm for S [90]. The discovery of S as an element for minor additions in BMGs directly suggested to also try P, especially as Si was already successfully used, e.g. in Vit101 [133]. Hence, in this work the influence of minor additions of both S and P are investigated and compared for the Vit101 and Vit105 system.

One case where small amounts of P, around 5 at%, are known to be beneficial to the GFA is the binary Ni-Nb system. Kawashima et al. investigated the corrosion resistance of $Ni_{55}Nb_{40}P_5$ upon the substitution of Nb with Ta [135]. Related to the alloy development efforts for the filing of the S-BMG patent, we also considered

additions of P in the Ni-Nb system. Some promising preliminary results of this work are shown in the outlook in the very end of this thesis.

2.3 Thermoplastic Forming

One of the great advantages of polymers, especially thermoplastic polymers, in comparison to conventional metals, is the way they can be shaped. Thermoplastics become moldable above their glass transition temperature and can be brought into complex shapes without too much force or at too high temperatures. Typical processing techniques for thermoplastics are injection molding, blow molding, extrusion, and thermoforming and the corresponding products are found in our everyday lives. These advantages regarding formability are based on the amorphous structure of thermoplastics and can therefore be transferred to amorphous metals. As long as crystallization can be avoided, amorphous metals can be formed like thermoplastics in their supercooled liquid (SCL) region. Consequently, the possibilities of thermoplastic forming (TPF) are one of the great advantages of BMGs in comparison to crystalline metals.

2.3.1 Casting of BMGs

Before BMGs can be thermoplastically formed, an amorphous feedstock material needs to be produced. However, this amorphous feedstock material can be produced by different techniques and does not need to have a shape similar to the desired final product, thus decoupling the initial casting process from the subsequent forming process. This decoupling eases the boundary conditions regarding a rapid cooling of the melt and the resulting limited time for the filling of complex molds.

Amorphous feedstock material can typically be obtained by mold casting techniques where a rapid cooling of the melt can be achieved. Alternatively, amorphous powder can be produced by melt atomization, which will however be discussed in Chapter 2.3.3. On a laboratory scale, copper mold suction casting is one of the most common techniques and is established since 1994 [148,149]. The solid master alloy is placed in an arc melting furnace, on top of a copper mold with a small opening. An electric arc is ignited between the master alloy and a tungsten electrode and used to melt the alloy. The liquid metal is then sucked into the copper mold by a vacuum pump that is connected to the bottom of the mold. Upon entering the mold, the alloy is rapidly quenched and forms a glassy solid. Yet, this technique only allows for rather simple casting geometries, as the mold filling is only based on the force of the vacuum and gravity.

However, when using an injection molding technique, complex molds can be filled. The forming abilities of such an injection casting process were recently described by Liu et al. [150]. During the casting process, amorphous metals do not behave like conventional crystalline metals. They do not show crystallization shrinkage and can

therefore even reproduce microscopic features in the mold, allowing for near-net-shape casting. Additionally, no subsequent heat-treatment after the casting process is necessary, as amorphous parts already possess their superior mechanical properties in the as-cast state. Crystalline alloys, in contrast, typically need a heat-treatment for hardening.

Within the last two years, an industrial casting process as well as the corresponding device were designed and built in the laboratory of Ralf Busch. The advantages of the laboratory suction casting process were transferred to an automized process and combined with a newly invented injection technology. A patent application was filed for both, the functional principle and the device (DE10 2018 115 815.7). This technology allows the production of large quantities of amorphous feedstock material for thermoplastic forming. Furthermore, the process is capable of the near-net-shape casting of complex amorphous parts, similar to the possibilities of an injection molding process for thermoplastics. Hence, the thermoplastic formability of amorphous metals cannot only be used as a second processing step, but already in the supercooled liquid region during the initial casting process.

2.3.2 Thermoplastic Forming of BMGs

In this section, a short literature review on the state of the art of thermoplastic forming of BMGs is presented. The concept of homogeneous flow in the SCL region was already introduced in Chapter 2.1.7, and the implementation of the TPF process regarding devices and parameters will be discussed in Chapter 3.6. A comprehensive review on the processing of BMGs, especially regarding TPF, was published by Schroers in 2010 [151].

Soon after the discovery of the first amorphous metals, the possibility to shape them like a thermoplastic in the SCL region was already considered [152]. It was however not before 1978, when Patterson et al. reported on the hot forming (or thermoplastic forming) of amorphous metals near the glass transition [153]. In the following years, BMGs with a significantly higher thermal stability were developed, e.g. the Be-containing Zr-based alloys of the Vitreloy family [5], or later the alloys in the Pt-P system [154]. These compositions had a sufficiently high thermal stability to allow for superplastic forming in the SCL region, which was reported for the first time in 2005 by Schroers [155]. In the following years, many more thermoplastic forming techniques were investigated, mimicking the processes known from thermoplastics. Figure 2.13 shows a variety of parts and products that were produced from amorphous metals by different thermoplastic forming techniques.

Miniature Fabrication, Nanomolding, and Surface Patterning

One of the possible applications for thermoplastic forming of BMGs is the fabrication of microstructures and micro-electromechanical systems (MEMS) [156]. Such products are difficult to produce from metallic materials by conventional fabrication techniques, and complex methods based on lithography, electroplating, and molding are in use.

BMGs however, can simply be forged by reusable micro-dies, resulting in three-dimensional MEMS structures, as first demonstrated by Saotome et al. [157]. A review article on TPF micro-forming can be found in Ref. [158]. Examples for such structures are depicted in Fig. 2.13 a)-f), with a) showing micro tweezers, b) micro scalpels with a radius of curvature of 1 µm, c) a gear wheel, and d) a membrane with 50 µm pores [159]. Figures 2.13 e) and f) display more complex MEMS, where the teeth are only 5 µm wide. Both devices are comb-drive actuators that move when an AC voltage is applied [160].

A decisive advantage of BMGs in comparison to crystalline metals is also the lack of microstructure. When forming parts on the nanoscale, the size of grains and the grain boundaries in-between cause problems. In BMGs however, the material is homogeneous down to the scale of the atomic short-range order and can easily reproduce features of only few nanometers. This structural homogeneity allows for the patterning of surfaces, even for optical applications. Kumar at al. demonstrated that holograms can perfectly be reproduced by the thermoplastic patterning of BMGs [160], and that feature sizes as small as 13 nm can be reproduced [159]. Consequently, the TPF process of BMGs cannot only be used to create functional surfaces, but also to obtain a surface finish with the roughness of a chemically polished silicon surface [160].

Furthermore, BMGs replicas can also be used as mold material themselves to shape materials with a lower softening temperature [159]. Kumar and coworkers also showed that the patterning of BMGs with a rather low glass transition temperature is possible using flexible and reusable polymer templates, which eases the demolding process [161].

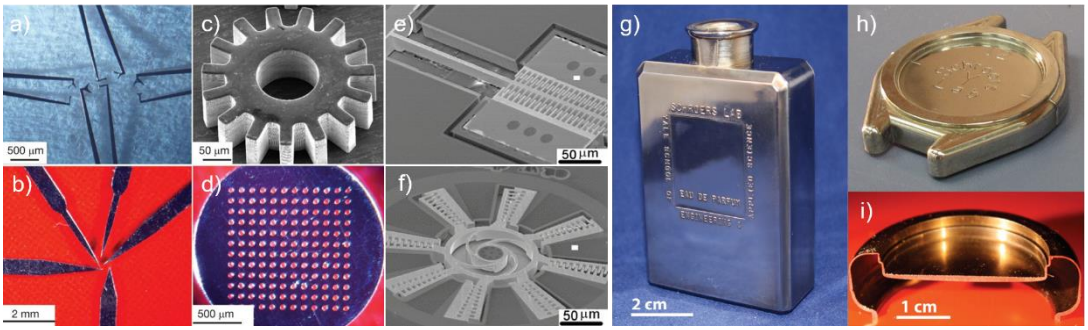

Figure 2.13: Amorphous metal parts and products produced by different thermoplastic forming techniques. **a)** micro tweezers, **b)** micro scalpels with a radius of curvature of 1 µm, **c)** gear wheel, **d)** membrane with 50 µm pores, **e)** linear and **f)** gyro comb-drive actuators that move when an AC voltage is applied, **g)** rectangular shaped bottle with surface imprinting, **h)** watch casing and **i)** its cross-section. a)-d) taken from Ref. [159], e), f) taken from Ref. [160], and g)-i) taken from Ref. [162].

Blow Molding

A different approach to exploit the formability of BMGs is blow molding. BMGs can be formed by this technique, which is commonly used for example to produce plastic bottles. Shapes that cannot be realized by any other metal processing method can be achieved. The blow molding of BMGs was reported for the first time in 2007 by Schroers et al. [163]. They succeeded in obtaining a strain of around 400 % for the free expansion of a disk during blow molding. Only some years later, they presented a significantly refined process where actual product shapes could be achieved [162].

Figure 2.13 g)-i) shows the corresponding samples, where g) is a rectangular shaped bottle with surface imprinting and h) and i) are a watch casing and its cross-section.

Extrusion

The formability of BMGs can also be used for extrusion processes, where products with a high aspect ratio are created. Early works on extrusion of amorphous metals focused on the consolidation of amorphous powder [164–166] (compare to Chapter 2.3.3). Later, Chiu et al. reported that they successfully extruded a 50 cm long wire from an initially only 15 mm long rod [167]. However, the dimensional accuracy in the cross-section is limited due to a strong swelling of the sample after exiting the die.

Flash-Heating Techniques

The formability of BMGs is limited due to the looming onset of crystallization in the supercooled liquid region. As the highest formability is expected at high temperatures [168], an ultra-fast heating of the sample is beneficial to reach the deformation temperature as fast as possible and achieve the highest possible deformation. In 2011, Johnson et al. published an article on the millisecond heating and processing of BMGs [169]. There, they used a capacitive discharge heating method to heat samples with rates of 10^6 K/s to temperatures in the SCL region. With such high rates, the critical heating rate for crystallization can be bypassed and the complete SCL region, even above the so-called crystallization nose, is accessible. Subsequently, the sample is injected into a cold steel mold, where it rapidly vitrifies. The process is similar to the injection molding process of polymers, however, takes into account the very limited processing times available for BMGs at high temperatures. While this process opens many new forming possibilities, it still requires amorphous feedstock material.

In 2014, the group around Johnson reported on new insights on their capacitive discharge heating technology [170]. They determined a TTT diagram for their process, including a critical heating rate, which was found to lie around 1000 K/s. Furthermore, they not only used an injection technique to shape the BMG in the SCL region, but also used a forging operation, where the heated sample is shaped by forging dies that approach from the outside and also quench the sample. Finally, the heating current itself can be used to deform the sample, when the whole process is performed within a strong electromagnetic field. The current induces a magnetic body force that plastically shapes the sample and external molds can be used to apply desired contours [171].

Processing Window and Formability

While the thermoplastic forming of BMGs offers multiple new forming possibilities, only a limited processing window is available. Processing temperatures and times need to be exactly known and controlled in order to exploit the potential of this technology. The reason for this lies in the metastable nature of the SCL region and hence the limited time till the onset of crystallization. Therefore, a profound understanding of the time-temperature-transformation (TTT) diagrams of each alloy is crucial.

The fundamental shape of a TTT diagram and a typical temperature profile of a TPF process were already displayed in Fig. 1.1. The TPF temperature protocol needs to be chosen such that crystallization is avoided, meaning that with increasing temperatures a decreasing amount of time remains for the process. At the same time, the viscosity of the alloy drops drastically with increasing temperature, and hence formability increases. A depiction of two TPF processing temperatures with different processing times can later be found in Fig. 5.9 b) on page 154, shown in red and labeled as A) and B).

The formability of BMGs is strongly temperature dependent, due to the interplay between viscosity and crystallization time. Schroers elaborated different concepts to evaluate and estimate the formability of BMGs [172]. This formability concept will be presented and discussed together with the results from this work in Chapter 5.1.3. In advance, it can be said that the highest formability is expected at the highest possible processing temperatures where crystallization can still be avoided [168]. Within the frame of this work, time-temperature-deformation (TTD) diagrams are used to relate the accessible TPF processing window with the achievable deformation under given experimental conditions. Such a TTD diagram can later be found in Fig. 5.5 on page 147, where the information regarding crystallization times at certain temperatures (TTT diagram), is superimposed by a color-coded contour plot that indicates the deformation.

The formability of a BMG can best be increased by increasing the thermal stability and hence the accessible processing temperatures and times. Within the context of minor additions, different works already showed that the thermoplastic formability of alloys can be increased by purposeful minor additions. Wiest et al. optimized alloys in the Zr-Ti-Be system by additions of Cu, Co, and Fe [173]; Hu et al. improved the formability in the Zr-Cu/Ni-Al system by additions of Er [138], and Gong et al. the Ti-Zr-Be system by Fe additions [174].

Mechanical Properties and Embrittlement

The mechanical properties of BMGs were already discussed in Chapter 2.1.7. At this point only the direct correlation between TPF and the mechanical properties, or rather an undesired embrittlement should be mentioned. In BMGs, embrittlement can typically be caused by either relaxation [126,175–177] or beginning crystallization [178–180]. Relaxation phenomena correspond to the idea of a critical fictive temperature [116], below which a brittle fracture behavior is observed. The fictive

temperature, however, can be manipulated by the TPF process. If a sample is heated above its initial fictive temperature (obtained during the casting process), and then rapidly cooled, a higher fictive temperature can be set. Wakeda et al. showed that such a thermal processing can be used to rejuvenate samples and regain their ductility [181]. On the other hand, a prolonged heat treatment close to the crystallization temperature causes nanocrystallization. While nanocrystals also cause embrittlement, this process cannot be reversed by thermal processing in the SCL region.

2.3.3 Consolidation of Amorphous Powder

One of the severest limitations of BMGs for structural applications is their critical casting thickness, and hence a size limit for structural parts. One way to overcome this size limitation are additive manufacturing techniques, were in a first step a powder feedstock material is produced and then consolidated in a second step.

Amorphous powder can be produced by different powder atomization techniques, e.g. by close-coupled hot gas atomization [182]. One way to consolidate the resulting powder is the thermoplastic forming process. Early works on the consolidation of amorphous powder used methods like explosive consolidation, high hydrostatic pressure, and warm extrusion [164–166] where the powder was encapsulated in Cu-cans. Later, Schroers et al. showed that granules from precious metal BMGs can be used as feedstock material for a TPF consolidation process [147]. Some years ago, Geissler et al. used amorphous granules from different BMG alloy classes to produce bulk samples by hot isostatic pressing in the SCL region [183]. Recently, we published a work on the consolidation of amorphous powder by thermoplastic forming, also assessing the ideal processing region, as well as the mechanical properties of the consolidated powder samples [184]. The results of this publication are also part of this thesis and will be presented and discussed later on.

An alternative additive manufacturing technology for the consolidation of powder into amorphous bulk samples is selective laser melting, often also called 3D printing. While this method is not part of this work, it is shortly mentioned for the sake of completeness. A general review on additive manufacturing of metals can be found in Ref. [185] and a more specific one on amorphous metals in Ref. [186].

Selective laser melting of amorphous metals is a rather new process which also starts with powder as feedstock material and allows for the fabrication of parts with complex geometries [187–189]. During the SLM process, a thin layer of powder particles is rapidly and locally melted with a laser. The liquid phase fuses with the layer underneath and cools down rapidly when the laser moves on. Due to the very localized heat input, fine structures can be built, and high heating and cooling rates are achieved. As the powder is melted during the process, the feedstock material does not necessarily need to be amorphous. It forms an amorphous structure due to the high cooling rates. However, this exact re-melting, as well as the powder atomization process itself, causes an increased oxygen content in the material. The high oxygen

content is often thought to cause embrittlement and the mechanical performance of 3D printed BMGs is still under investigation [190,191]. Additional difficulties are a fully dense consolidation, and crystallization and relaxation in the heat-affected zone. Only now, researchers are starting to understand the influence of the processing parameters on the structure and develop first models [192], or even investigate the structural heterogeneity across the build-planes by synchrotron X-ray microdiffraction [193].

Chapter 3

Experimental Methods

In this chapter, the applied methods are explained regarding their theoretical background and the exact experimental procedure, including data evaluation. As a wide variety of methods are used, only a brief explanation of each can be given and the reader is referred to several textbooks for further reading throughout the chapter.

3.1 Sample Preparation

All samples examined in this work were prepared according to the subsequently presented procedure, starting with the alloying of the raw materials, the casting of amorphous samples and a quality inspection using X-ray diffraction.

Alloy Synthesis

Alloys were synthesized from high purity raw elements with purities ranging from 99.95 wt% to 99.9995 wt%. For alloys containing sulfur (S) and phosphorus (P), $Ni_{55}S_{45}$ and $Ni_{67}P_{33}$ prealloys were produced by inductively melting the two raw elements in a silica tube in a high purity argon atmosphere (see also Ref. [8]). Subsequently, the prealloys were fluxed by re-melting them in dehydrated B_2O_3 in a silica tube in order to remove heterogeneous nucleation sites [194]. The raw elements and the prealloys were alloyed by melting quantities according to the desired composition in an arc-melting furnace under a high purity Ti-gettered argon atmosphere. In order to obtain homogeneous master alloys, samples were flipped and remelted at least three times. The main alloy compositions used in this work are shown in Table 3.1.

Casting

The master alloys were cast into samples of different shapes using an arc melting furnace with a suction casting inset. There, the alloy was melted in a high purity Ti-gettered argon atmosphere on top of a water-cooled copper mold and then sucked into the mold cavity, thus rapidly cooling the melt and forming an amorphous sample. Samples with the following geometries were produced: rods with a length of 50 mm and a diameter between 3 and 9 mm; plates with dimensions of 50 x 12 x 2 mm^3, and 30 x 4 x 0.8 mm^3; and beams with a length of 50 mm and a rectangular cross-section of 2 x 2.8 mm^2.

Table 3.1: Alloy compositions.

Alloy Name	Composition [at%]
Vit101	$Cu_{47}Ti_{34}Zr_{11}Ni_{8}$
Vit101 P_1	$Cu_{46.53}Ti_{33.66}Zr_{10.89}Ni_{7.92}P_1$
Vit101 $S_{1.5}$	$Cu_{46.3}Ti_{33.5}Zr_{10.8}Ni_{7.9}S_{1.5}$
Vit105	$Zr_{52.5}Cu_{17.9}Ni_{14.6}Al_{10}Ti_5$
Vit105 P_2	$Zr_{51.45}Cu_{17.54}Ni_{14.31}Al_{9.8}Ti_{4.9}P_2$
Vit105 S_2	$Zr_{51.45}Cu_{17.54}Ni_{14.31}Al_{9.8}Ti_{4.9}S_2$

Cutting and Quality Inspection

After casting, the samples were cut according to the needs of the envisaged characterization or processing method, using a Buehler IsoMet 1000 high precision saw. The amorphous structure of the samples was checked by X-ray diffraction (XRD) with a PANalytical X'Pert Pro diffractometer using Cu K_α-radiation ($\lambda = 0.15406$ nm) within an angular range of $20° < 2\theta < 80°$ and a resolution of 0.02°. An in-depth overview of the methods of X-ray diffraction can be found in Ref. [195].

3.2 Mechanical Testing

Three-point Beam Bending

Three-point beam bending tests are performed to evaluate the mechanical performance of different amorphous alloys. The measurements provide stress-strain curves that allow to determine, among others, the yield strength, the fracture stress and strain, and the elastic modulus. Beam bending experiments were preferred to tensile testing as the necessary samples are easier to cast and no additional machining is necessary.

Amorphous beams with a rectangular cross-section of of 2 x 2.8 mm^2 were cut to a length of 30 mm and polished on the four side faces. Three-point bending (3PB) flexural tests were conducted using a Shimadzu universal testing machine with a support span of L = 20 mm. The beams were loaded with a testing speed of v = 5 µm/s up to the point of fracture. The acquired load-displacement curves were transformed into stress-strain curves using the following equations:

$$\sigma_f = \frac{3\,F\,L}{2\,b\,h^2} \tag{3.1}$$

$$\varepsilon_f = \frac{6\,D\,h}{L^2}, \tag{3.2}$$

where σ_f is the stress in the outer fiber at midpoint, ε_f is the strain in the outer surface, F is the applied load, L the support span, b the width of the sample, h the height of the sample, and D the displacement at the center of the beam.

3PB tests were also conducted on consolidated amorphous powder samples that were produced as described in Chapter 3.6.2. Here, the fracture surfaces of the beams were examined in a Zeiss Sigma VP scanning electron microscope in secondary electron contrast.

Hardness

Hardness measurements are a quick and easy method to compare the mechanical properties of different materials, where the resistance of a material against plastic deformation caused by an indenter is measured.

Vickers hardness tests (HV5) were carried out with a Wolpert Wilson 930N universal hardness tester on the polished surfaces of the same samples that were used for the 3PB experiments. Microscopic images of the indents were taken with an Olympus BH-2 optical microscope and were used to measure the indent diameter and then calculate the Vickers hardness.

3.3 Calorimetric Measurements

Calorimetric measurements allow to determine the heat within a sample due to physical changes, reactions, or phase transitions. The obtained data provides information about melting and crystallization enthalpies, molar heat capacities, and the characteristics of the glass transition in amorphous samples.

In this work, two calorimetric measurement methods, namely, differential scanning calorimetry (DSC) and differential thermal analysis (DTA) are used. Their functional principle is shortly explained in the following, while the reader is referred to Ref. [196,197] for a comprehensive overview on calorimetry. For all calorimetric methods it should be noted that a calibration with standard materials is necessary to guarantee accurate measurements.

Differential scanning calorimetry (DSC)

During a DSC measurement, the heat required to change the temperature of a sample is measured in comparison to a reference. In a power-compensated DSC, both, sample and reference, undergo the same temperature program in two identical micro furnaces and heat flow is recorded as a function of time or temperature. A power-compensated DSC operates according to the so-called "null principle", where the temperature difference between the sample and the reference is kept zero by adapting the heating power of each individual furnace. Hence, the heat flow $\dot{Q}$ is directly proportional to the difference in heating power ΔP measured in mW. For an empty reference furnace, the heat flow $\dot{Q}$ can be written as:

$$\Delta P \sim \dot{Q} = \mathrm{m}\, c_p \frac{dT}{dt}, \tag{3.3}$$

where m is the mass of the sample and c_p the specific heat capacity at constant pressure, and dT/dt the heating rate. With a power-compensated DSC, highly accurate heat flow measurements are possible up to temperatures of around 1000 K.

In this work, a power-compensated Perkin-Elmer HyperDSC 8500 with a three-stage Intracooler III was used. This device allows for a measurement range from 173 K to 1023 K (-100 to 750 °C) with heating and cooling rates up to 3 K/s (180 K/min). Temperature and heat flow calibrations were performed for different scanning rates under a constant flow of 20 ml/min ultra-high-purity Ar gas (≥ 99.9999%), using the melting transitions of In, Sn, Zn and the phase transition of K_2SO_4. Al-pans were used as crucibles for measurements up to 853 K and Cu-pans for measurements up to 1023 K. Samples were sanded on one side to have a flat surface in order to achieve good thermal contact with the pan and weighed with an accuracy of ± 0.01 mg.

Differential thermal analysis (DTA)

Similar to DSC, DTA measurements allow to determine the heat flow into a sample during a given temperature program. The measurement head consists of a sample and a reference holder which are placed in a single furnace. The holders are connected to a thermocouple and the temperature difference between them is measured while sample and reference undergo the same thermal program. An exothermic (e.g. crystallization) or endothermic (e.g. melting) reaction causes a detectable temperature difference ΔT_{SR} between the sample and the reference. The heat flow which is according to Newton's law of cooling directly proportional to ΔT_{SR} can be described using the following equation:

$$\dot{Q}\, R = \Delta T_{SR} = \mathrm{m}\, c_p\, \mathrm{R} \frac{dT}{dt}, \tag{3.4}$$

where m and c_p are the mass and the specific heat capacity of the sample, dT/dt the heating rate, and R the thermal resistance that is dependent on the experimental setup and the DTA instrument. While DTA analysis allows for less accurate measurements than DSC, it can be used up to temperatures of around 1900 K.

For the high temperature DTA measurements shown in this work, a NETZSCH STA 449 Jupiter DTA was used. This device allows for measurements up to 1873 K (1600 °C) with heating and cooling rates up to 0.833 K/s (50 K/min). A temperature and heat flow calibration were performed for a heating rate of 0.333 K/s, using the melting transitions of In, Sn, Zn, Al, Ag, Au, and Cu. Measurements took place under a constant purge gas flow of 50 ml/min ultra-high-purity Ar gas (≥ 99.9999%) and a protective gas flow of 20 ml/min Ar gas. Graphite crucibles and Y_2O_3 coated graphite crucibles were used.

3.3.1 Standard Scans

For all samples, DSC and DTA standard scans with a constant heating rate of q_h= 0.333 K/s (20 K/min) were performed. In the DSC, samples were heated in Cu-pans from room temperature to 993 K, then cooled and reheated with the same rate in order to obtain the baselines scan of the crystalline sample. Samples with a mass of around 40 mg were used and multiple scans were done to obtain reliable statistics. In the DTA, the same procedure was applied, however samples were heated from room temperature to a maximum temperature of 1573 K and graphite as well as Y_2O_3 coated graphite crucibles were used. Additionally, each sample was melted several times.

A typical DSC/DTA standard scan is shown in Fig. 3.1, with the insets showing magnifications of the glass transition region and the melting peak. During the first heating the amorphous sample passes through the glass transition region, crystallizes, and melts. The glass transition temperature T_g, crystallization temperature T_x, melting temperature T_m, and liquidus temperature T_l are assessed using the tangent method. The temperature of fusion T_f corresponds to the peak position of the main melting peak. The enthalpy of crystallization ΔH_x results from an integration of the area between the first heating curve and the baseline. For the enthalpy of fusion ΔH_f, a feasible baseline has to be defined, as the melting also occurs during the second heating. The DSC and DTA scans provide a raw heat flow signal in mW that is transformed into units of J g-atom^{-1} K^{-1}, using the molar mass of the alloy, the sample mass, and the heating rate.

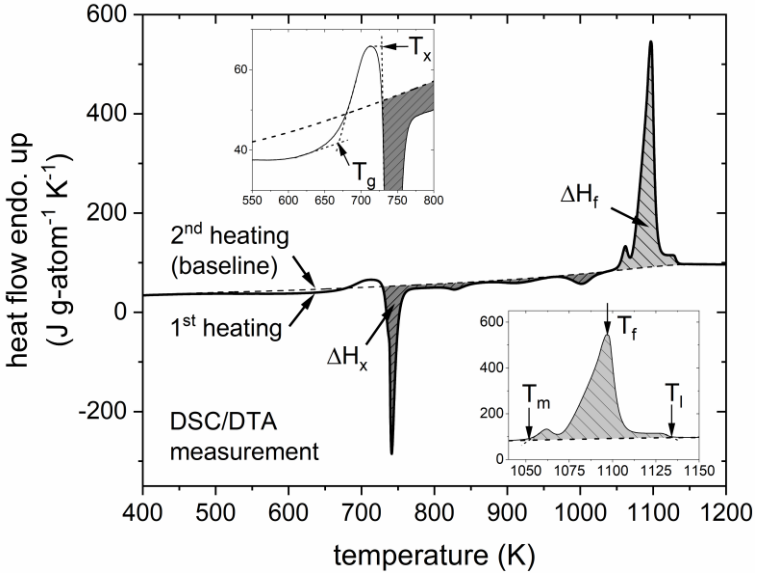

Figure 3.1: DSC/DTA standard scan and baseline. The characteristic temperatures and enthalpies that can be obtained from a standard scan are indicated. The insets show magnifications of the glass transition region and the melting peak. Data for Vit105 at 0.333 K/s.

The influence of the crucible material on the DTA measurements at high temperatures is visualized in Fig. 3.2. For highly reactive melts with a high Zr- or Ti-content, crucible reactions are observed for all standard crucible materials, e.g. Al_2O_3, or graphite, thus making it difficult to determine the true liquidus temperature. Within the framework of this thesis, alternative crucible materials were tested, with Y_2O_3 turning out to be the most feasible one. While pure Y_2O_3 crucibles are very costly, graphite crucibles can easily be coated with an Y_2O_3 spray (e.g. Y aerosol from ZYP Coatings), yielding the same result. The coated graphite crucibles were burned out in high vacuum (HV) at 1473 K and then used for measurements. The upper curve in Fig. 3.2 shows the DTA curve for Vit 105 S_2 measured in graphite, while the lower curve shows the measurement for the same material in Y_2O_3 coated graphite. It can clearly be seen that no severe crucible reactions occur in the coated crucibles.

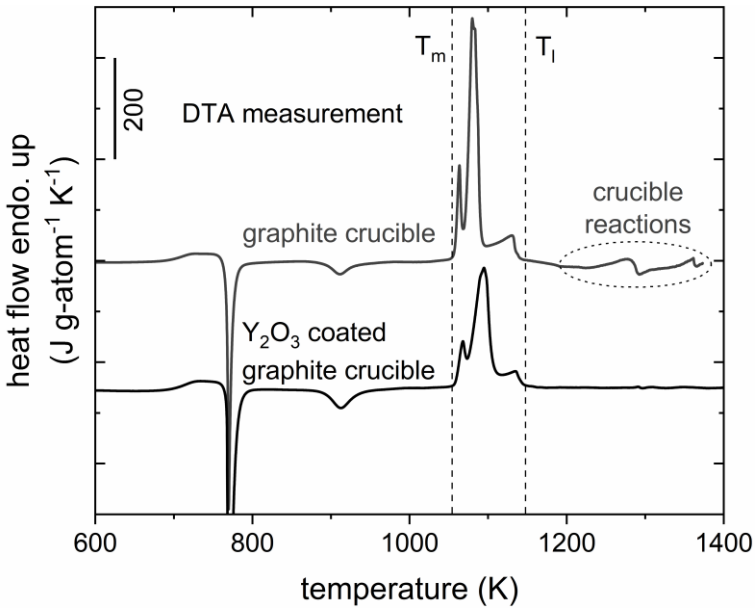

Figure 3.2: DTA curves of Vit 105 S_2 in different crucibles with a heating rate of 0.333 K/s. The measurements in graphite crucibles show reactions at high temperatures, whereas Y_2O_3 coated graphite crucibles show no severe reactions.

3.3.2 T_g-Shift Experiments

The T_g-shift method is used to assess the heating rate dependence of the glass transition temperature. With the glass transition being a kinetic phenomenon (compare to Chapter 2.1.1), T_g is shifted to higher temperatures with higher heating and cooling rates. This rate dependence also reflects the kinetic fragility (see Chapter 2.1.4) of an alloy, as it is connected to the intrinsic relaxation time τ_α of the liquid. More fragile systems tend to show a smaller rate dependence of T_g. The transition

time τ_{trans} that the system needs to pass through the glass transition region can be calculated as:

$$\tau_{trans} = \frac{\Delta T_g}{q_h}, \tag{3.5}$$

where $\Delta T_g = T_g^{end} - T_g^{onset}$ is the width of the glass transition region and q_h is the heating rate. τ_{trans} is also proportional to the total relaxation time measured in isothermal viscosity measurements [198]. When the transition time τ_{trans} is attributed to the fictive temperature T_{fic} of the corresponding heating rate, the temperature dependence of τ_{trans} can be described by a VFT equation (see Eq. 2.9) and the kinetic fragility parameter D* can be calculated.

According to Ref. [52], the fictive temperature T_{fic} coincides with the onset of the glass transition temperature T_g^{onset} if the sample is heated with the same rate at which it was vitrified ($q_h = q_c$). If this condition is satisfied, T_g-shift measurements provide a correct description of the kinetic fragility, as shown by Evenson et al. [199]. An adequate method to meet these requirements is illustrated in Fig. 3.3.

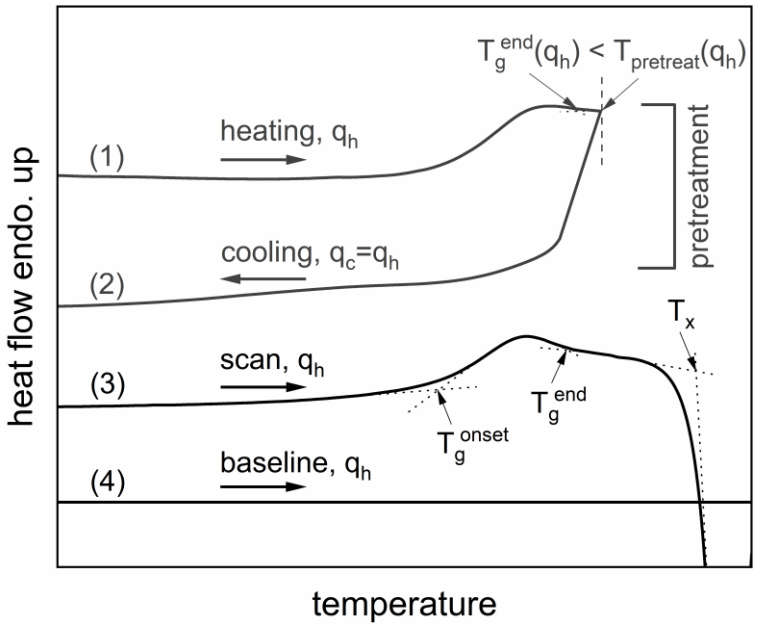

Figure 3.3: DSC traces for a T_g-shift measurement at one heating rate q_h. The curves (1) and (2) show the pretreatment, where the sample is heated to $T_{pretreat}$, a temperature above T_g^{end} of the selected heating rate q_h (1) and then cooled with the same rate q_c (2). The actual measurement is performed during the scan with $q_h = q_c$ (3) and T_g^{onset} and T_g^{end} are determined. Here, T_g^{onset} coincides with the fictive temperature. After crystallization of the sample, a baseline scan is performed, and the baseline is subtracted from the previous scans.

An as-cast amorphous sample is first heated to a pretreatment temperature $T_{pretreat}$ that is higher than T_g^{end} of the chosen heating rate q_h (1). Then, the sample is cooled and vitrified with the rate q_c (2). After this pretreatment, the sample is heated with the same rate ($q_h = q_c$) above the crystallization temperature T_x (3) and the onset and end of the glass transition can be determined. Finally, a baseline scan is performed with the same rate (4). For alloys with a large SCL region, a single pretreatment temperature above T_g^{end} of the highest heating rate is chosen and samples are initially heated (1) with a single heating rate, independent of the subsequent measurement rate, as described in Ref. [199]. For alloys with a less pronounced SCL, an adaptation to this method was developed within the framework of this thesis, to avoid crystallization of the sample during pretreatment. T_g^{end} of as-cast samples is previously determined for all used heating rates, and the pretreatment temperature is adjusted for each heating rate. The initial heating (1) is then performed with the same rate as the subsequent cooling (2), meeting the condition of $q_h = q_c$ for all runs. In this work, scans were performed with heating rates of 0.025; 0.083; 0.333; 1; 1.5; 2; and 3 K/s (1.5 to 180 K/min) from 303 K to 853 K in Al-pans.

3.3.3 Time-Temperature-Transformation (TTT) Diagram

The crystallization behavior of bulk metallic glass-forming alloys in relation to time and temperature can be visualized in a time-temperature-transformation (TTT) diagram. Crystallization can occur when cooling the melt below the liquidus temperature, and it also occurs when heating an amorphous sample above its crystallization temperature. Crystallization upon cooling can be observed by containerless electrostatic levitation (ESL) [200] (compare to the second part of Chapter 3.5.2), or in a DTA setup with sufficiently high cooling rates for the characterized alloy [201,202].

In this work, the focus lies on the time and temperature dependent crystallization behavior of the amorphous phase upon heating, thus assessing the lower side of the C-shaped crystallization curve. Knowledge about this part of the crystallization curve is crucial in order to adjust times and temperatures for all further thermoplastic forming experiments (see Chapter 3.6 and Chapter 5) and to determine a processing window.

Isothermal TTT diagrams were measured as visualized in Fig. 3.4. Figure 3.4 b) shows a schematic TTT diagram where the 1%, 50%, and 99% crystallization transformation, as well as the glass transition (T_g) are shown. The red curves represent the thermal protocol of the DSC measurements, as shown for a single isothermal temperature in Fig. 3.4 a). First, the sample was heated with q_h= 2 K/s to the isothermal holding temperature T_{iso} and the crystallization process was monitored in the heat flow signal, where the release of crystallization enthalpy is visible. Temperature was kept constant until the heat flow signal equilibrated and crystallization was clearly completed. Peaks in the heat flow signal were integrated as visualized by the grey shaded area in Fig. 3.4 a). The integration results were used to determine the times for 1%, 50% and 99%

of the crystallization transformation for each temperature. For the measurement of the TTT diagram, as cast samples with a mass of 100 to 200 mg were used in order to provide a sufficiently large heat flow signal.

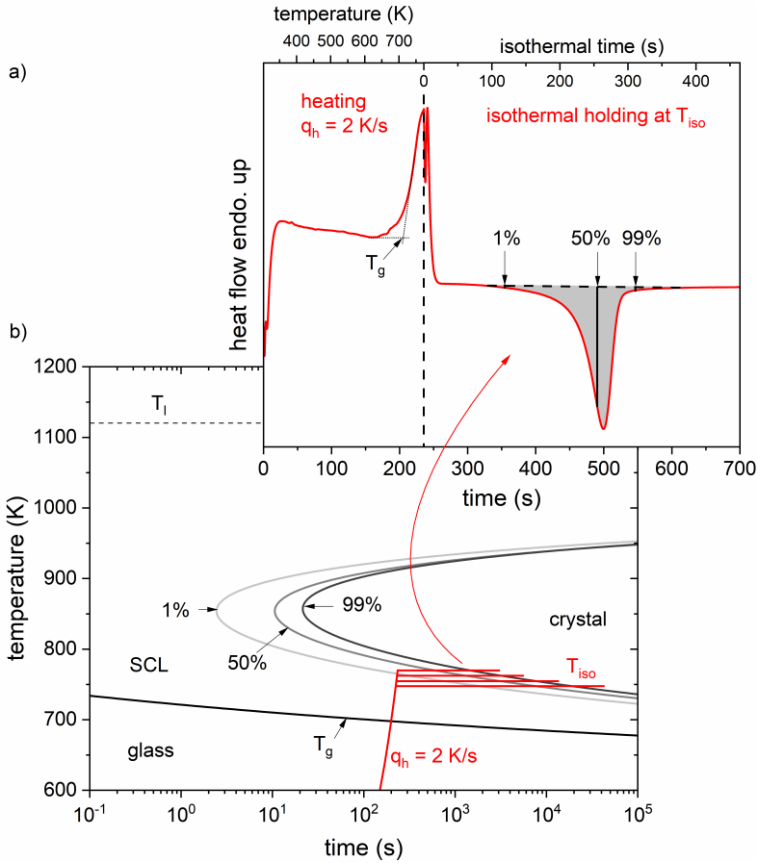

Figure 3.4: Measurement procedure for an isothermal time-temperature-transformation (TTT) diagram in a DSC. **b)** Schematic TTT diagram where the 1%, 50%, and 99% crystallization transformation, as well as the glass transition (T_g) are shown. The red curves represent the thermal protocol of the DSC measurements, as shown in **a)**. Samples are heated with q_h= 2 K/s to the isothermal holding temperature T_{iso} and the crystallization is monitored in the heat flow signal. Integration of the heat flow results in the 1%, 50%, and 99% crystallization times for each temperature.

3.3.4 Molar Heat Capacity

The molar heat capacity of a system is a crucial property in order to calculate its thermodynamic functions (compare to Chapter 2.1.2) and can be measured by calorimetric methods. In theory, it can simply be obtained by the relation given in Eq. 3.3. In practice however, this relation is not applicable for measuring an exact heat capacity value as a function of temperature, due to an additional heat flow term caused by the measurement pans. The influence of the pans can be eliminated by

measuring the heat capacity in comparison to a sapphire standard. The molar isobaric heat capacity can then be calculated according to [45]:

$$c_p(T)_{sample} = \frac{\dot{Q}_{sample} - \dot{Q}_{pan}}{\dot{Q}_{sapphire} - \dot{Q}_{pan}} \cdot \frac{m_{sapphire}\,\mu_{sample}}{m_{sample}\,\mu_{sapphire}} \cdot c_p(T)_{sapphire}\,, \qquad (3.6)$$

where $\dot{Q}$ is the heat flow, m the mass, μ the molar mass, and $c_p(T)_{sapphire}$ the known molar heat capacity of sapphire. Three measurement runs are needed to calculate c_p: a measurement with empty pans to receive $\dot{Q}_{pan}$, a reference run with a sapphire standard ($\dot{Q}_{sapphire}$) and a sample run with the actual sample ($\dot{Q}_{sample}$), all with the exact same thermal protocol.

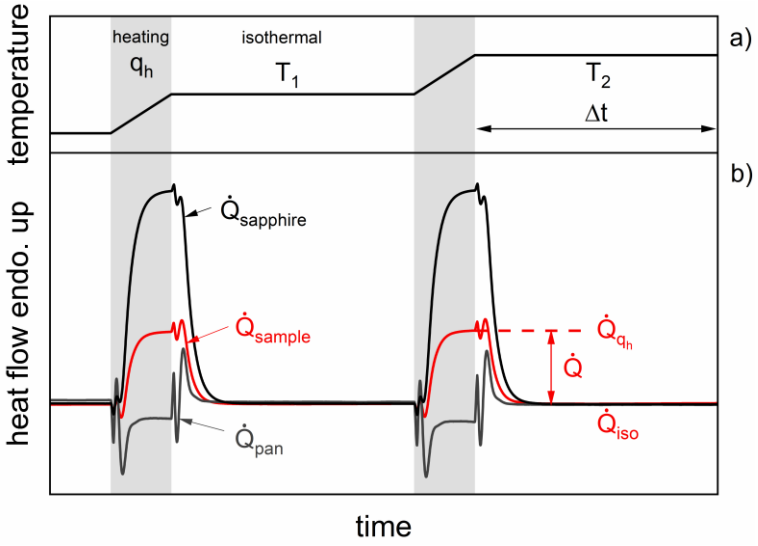

Figure 3.5: Temperature profile and heat flow curves from a DSC heat capacity measurement using the step method. **a)** Steplike temperature profile. The shaded grey areas indicate the heating period while the white sections correspond to isothermal holding for the time Δt. **b)** Heat flow signals from the sample (red), the sapphire (black), and the empty pan (grey).

The molar heat capacity of the glassy, supercooled liquid, and crystalline state was measured by DSC, using Eq. 3.6 in combination with a "step method". The procedure of the step method is visualized in Fig. 3.5. The sample was heated to a temperature T_1 with a constant heating rate of q_h = 0.333 K/s (shaded grey area) and then held isothermally for Δt = 120 s until the equilibration of the heat flow signal. In the next step, the sample was heated by 10 K to T_2 and held again, thus providing a c_p value at a higher temperature. The heat flow of a single temperature results from:

$$\dot{Q} = \dot{Q}_{q_h} - \dot{Q}_{iso}\ \left(= \dot{Q}_{\dot{T}\neq 0} - \dot{Q}_{\dot{T}=0}\right), \qquad (3.7)$$

where $\dot{Q}_{qh}$ is the heat flow at the end of the heating interval and $\dot{Q}_{iso}$ is the equilibrium heat flow during the isothermal interval, as indicated in Fig. 3.5. A detailed explanation of the step method can be found in Ref. [203].

Molar heat capacity was measured for a temperature range from 193 K to 923 K, always using the same pans and performing all four runs (empty pans, sapphire, amorphous sample, crystalline sample) on the same day to minimize experimental errors.

In order to calculate the thermodynamic functions of each alloy, the obtained c_p data was then fitted by the following equations, as proposed by Kubaschewski [204]:

liquid $$c_p^{liquid}(\mathrm{T}) = 3R + a\,T + b\,T^{-2} \tag{3.8}$$

crystal $$c_p^{xtal}(\mathrm{T}) = 3R + c\,T + d\,T^2\,, \tag{3.9}$$

where R is the universal gas constant and T the temperature. a, b, c, and d are the fitting parameters in the appropriate units.

With molar heat capacity data only being available in the supercooled liquid, and not in the stable high-temperature liquid, Eq. 3.8 cannot be used for fitting without further data input. However, the method applied in Ref. [66] can be used, and according to the relation:

$$\Delta H_f - \Delta H_x = \int_{T_x}^{T_f} \Delta c_p^{l-x} dT\,, \tag{3.10}$$

the difference in molar heat capacity between the supercooled liquid and the crystal $\Delta c_p^{l\text{-}x}$ is linked to the difference between the heat of fusion ΔH_f and the heat of crystallization ΔH_x. T_x is the crystallization temperature and T_f the temperature of fusion. Hence, these previously measured enthalpies can be used to estimate the temperature dependence of the molar heat capacity in the (supercooled) liquid.

3.4 Viscosity Measurements

Viscosity measurements provide information about the flow behavior of a liquid. Viscosity itself is connected to the kinetics of the system and its temperature dependence is described by the kinetic fragility (compare to Chapter 2.1.4).

As the viscosity of a metallic liquid typically increases over roughly 14 orders of magnitude from the stable high-temperature liquid to the supercooled liquid around the glass transition, rather different measurement techniques are used for both regimes. In this work, high-temperature viscosity measurements are performed using Couette rheometry and viscosity around the glass transition is measured by three-point beam bending in a thermomechanical analyzer, as explained in the following.

3.4.1 Viscosity around the Glass Transition

The most common method to measure viscosity around the glass transition is three-point beam bending (3PBB) in a thermomechanical analyzer (TMA). Thermo-mechanical analysis is a characterization method that allows to measure the mechanical response of a sample to a defined temperature program. In the 3PBB setup, which is schematically shown in the inset in Fig. 3.6, the deflection of a thin beam is recorded. The beam is placed on two sharp bearings on both ends and a wedge-shaped head is used to apply a load in the center and measure the deflection, or rather the deflection rate. Viscosity, η, can then be calculated according to [205,206]:

$$\eta = -\frac{gL^3}{144\,\nu\,I_c}\left(M + \frac{\rho AL}{1.6}\right), \tag{3.11}$$

where g is the gravitational acceleration constant, L the length of the beam, ν the midpoint deflection rate, I_c the cross-section moment of inertia, M the loading mass, ρ the density of the sample, and A its cross-sectional area. The cross-section moment of inertia with respect to the neutral fiber is $I_c = bh^3/12$, where b is the width and h is the thickness of the beam. 3PBB in combination with Eq. 3.11 can be used to calculate viscosities in the range from 10^7 to 10^{14} Pa s.

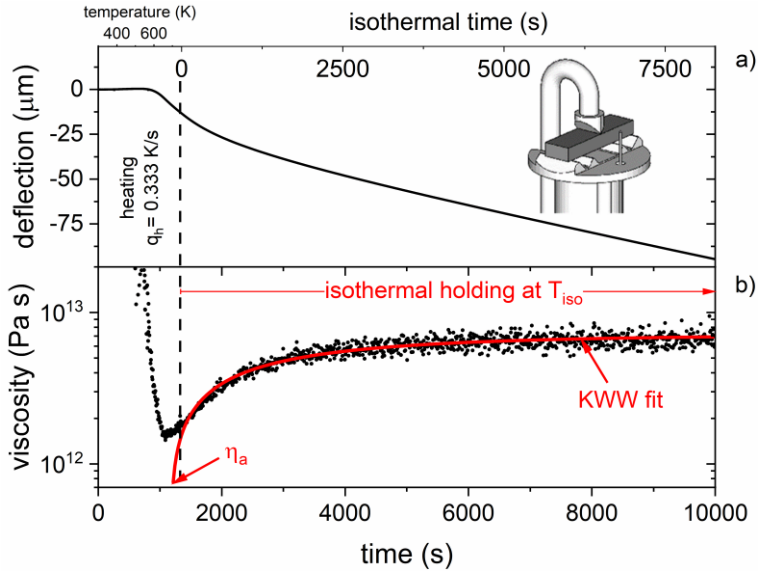

Figure 3.6: a) Deflection curve of an isothermal equilibrium viscosity measurement around the glass transition. After the initial heating, the sample is hold isothermally at the desired temperature T_{iso}. The inset schematically shows the measurement head used for 3PBB [207]. **b)** Viscosity, calculated from the deflection curve according to Eq. 3.11. The red line represents the KWW fit (compare to Eq. 2.6) that is used to determine the equilibrium viscosity value.

3PBB viscosity measurements were performed in a Netzsch TMA 402 F3 Hyperion. Beams with rectangular cross-sectional areas of 0.3 to 1.1 mm² and a length of 13 mm were used, and a force of 0.1 N was centrally applied. For equilibrium viscosity measurements in the vicinity of the glass transition, samples were heated with a constant heating rate of $q_h = 0.333$ K/s to the desired temperature T_{iso} and held isothermally till the onset of crystallization. A typical deflection curve from an isothermal 3PBB viscosity measurement is shown in Fig. 3.6 a). Figure 3.6 b) shows the resulting viscosity curve as calculated according to Eq. 3.11. The red line represents the KWW fit (compare to Eq. 2.6) that is used to determine the equilibrium viscosity value. Additionally, continuous scans from room temperature to 873 K with a heating rate of $q_h = 0.333$ K/s were also performed.

3.4.2 High-Temperature Viscosity

The viscosity of metallic melts at high temperatures in the equilibrium liquid is a quantity difficult to measure. The main challenges result from the rather high measurement temperatures, mostly above 1200 K, and the high reactivity of metallic glass-forming liquids containing Zr or Ti. Different techniques are known and used, providing different advantages and drawbacks.

In this work, a custom-built Couette rotating concentric cylinder rheometer is used. A detailed description of said device and the methodology can be found in our recently published article in Ref. [208]. Alternative measurement principles are the oscillating cup technique [209,210], which is typically used for the measurement of pure metals, and the oscillating drop technique [211], where the damping behavior of a levitating droplet is analyzed to calculate its viscosity. Levitation can either be achieved by an electrostatic field (electrostatic levitation, ESL) [212–215] or an electromagnetic field (electromagnetic levitation, EML), whereas EML viscosity measurements need to be performed under microgravity conditions [216,217].

In Couette rheometry, the liquid sample is stirred between rotating concentric cylinders and the reaction torque due to viscous shear stresses is measured [210,218]. The device uses custom machined graphite Mooney-Ewart coni-cylinder shear cells with a cup and a bob, as shown in Fig. 3.7 a), that satisfy the narrow-gap DIN/ISO standards. For these shear cells, viscosity can be calculated according to [219]:

$$\eta = \frac{M}{\omega} \frac{\left(R_e^2 - R_i^2\right)}{4\pi L R_e^2 R_i^2} \frac{1}{c}, \tag{3.12}$$

where M is the reaction torque measured on the cup, ω is the angular velocity of the bob, R_e is the radius of the cup ("external radius"), R_i is the radius of the bob ("internal radius"), L is the length of the cylindrical section of the bob that is immersed, and c is a correction length that accounts for the shear contribution of the conical end of the bob. The cup and the bob of the shear cell are mounted on the

viscosimeter, as shown in the cross-section view in Fig. 3.7 b) where all main components of the device are labeled.

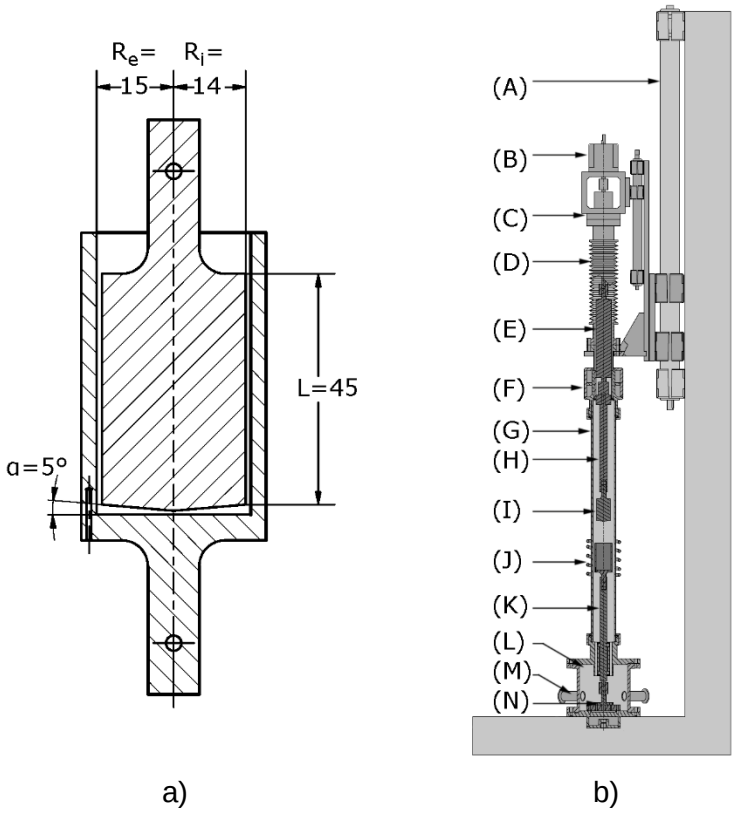

Figure 3.7: a) Section view of the shear cell with the relevant dimensions labeled, where $R_e = 15$ mm is the radius of the cup, $R_i = 14$ mm is the radius of the bob, $L = 45$ mm is the immersion length of the bob, and $\alpha = 5°$ is the taper angle. **b)** Partial section view of the viscometer with the main components labeled: (A) schematic apparatus frame and large linear manipulator, (B) DC stepper motor, (C) ferrofluid rotary feedthrough, (D) edge welded vacuum bellows, (E) spindle bearing, (F) water cooled bearing housing, (G) quartz glass tube, (H) bob shaft, (I) bob (raised position shown), (J) cup and inductive coil, (K) cup shaft, (L) lower vacuum chamber, (M) vacuum feedthrough, and (N) torque sensor. Figure and description taken from Ref. [208].

Before each experiment, the vacuum chamber was evacuated to 10^{-4} mbar and subsequently filled with 0.5 bar of high purity argon (Ar 6.0). The graphite shear cell was heated inductively with a high frequency generator and a type K thermocouple embedded in the crucible was used to measure the temperature, which was controlled by a Labview program. Ingots of a crystalline master alloy with a volume of ~ 6 cm^3 were heated to 1423 K in the rheometer and a stepwise shear rate profile with a shear rate of 456 s^{-1} was applied. To investigate the temperature dependent rheological behavior, the liquid was cooled and reheated various times at a rate of $q = 0.333$ K/s. The minimum temperature was chosen just at the onset of crystallization and then

the sample was immediately reheated to prevent overloading of the sensor. Additionally, isothermal measurements with various shear rates between 274 s^{-1} and 456 s^{-1} were performed in order to investigate the shear rate dependence of viscosity.

The raw data from a typical measurement is visualized in Fig. 3.8. Here, the signal of the torque sensor in mV (Fig. 3.8 a)), the motor rotation speed in Hz (Fig. 3.8 b)), and the shear cell temperature in K (Fig. 3.8 c)) are shown for two shearing steps. The inset displays a typical temperature profile of a single experiment. Viscosity is calculated according to Eq. 3.12 from the stationary torque signal between the dashed lines (t_1 to t_2) where a constant rotation speed is applied.

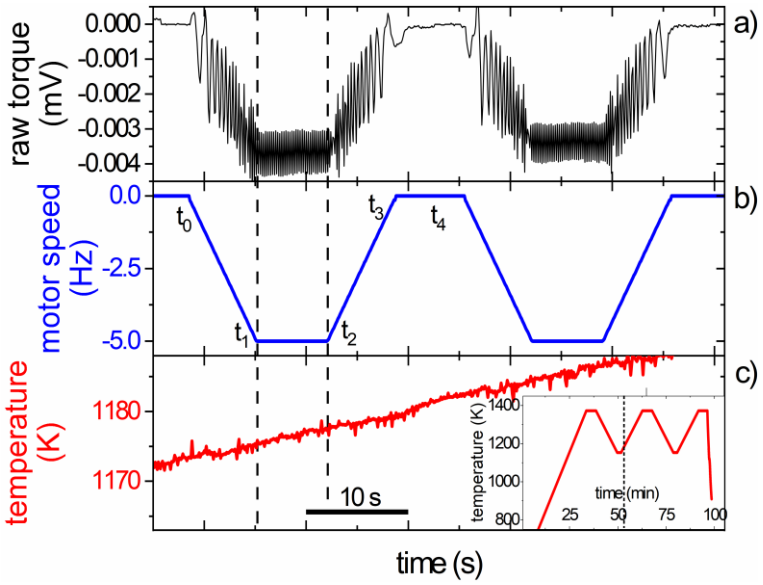

Figure 3.8: Excerpt from the raw measurement data of the rotating cylinder viscosity measurement. **a)** shows the signal of the high precision torque sensor in mV, and **b)** shows the corresponding motor rotation speed in Hz. **c)** displays the crucible temperature during those measurements with the inset showing the overall temperature profile of the whole experiment. The dashed line in the inset indicates the region that is magnified in the main plot. Viscosity data are calculated from the stationary torque signal between the dashed lines (t_1 to t_2) where a constant rotation speed is applied, according to Eq. 3.12. Figure and description taken from Ref. [208].

Furthermore, viscosity measurements with free cooling of the sample were performed. Due to the fast cooling rate and the short measurement time, the typically used stepwise shear rate profile could not be applied, as only very few data points would be measured before the onset of crystallization. For the free cooling experiments, the bob was constantly rotated at a frequency of 5 Hz to provide a continuous measurement, however not allowing for a zeroing of the torque value throughout the measurement. During the stepwise shear rate profile, the zeroing was performed to account for temperature drifts of the torque sensor.

3.5 In-situ Synchrotron X-ray Scattering

In-situ synchrotron X-ray scattering experiments were used to analyze structural changes on an atomic scale while the sample was exposed to a defined temperature profile. Special focus was laid on the crystallization behavior upon heating and cooling. Two distinctly different experimental setups were used to apply the temperature profile: One with a simple resistive furnace to heat samples in the solid state, and another one where the sample was electrostatically levitated (ESL) in the liquid state and heating was achieved by laser.

3.5.1 Functional Principle of Synchrotron X-ray Scattering

In this chapter, the functional principle of a synchrotron source, generating hard X-rays, as well as the basic principle of X-ray scattering are outlined.

Synchrotron X-ray sources

In the laboratory, X-rays are typically generated in an X-ray tube where they are obtained from the characteristic radiation of the target anode. A common X-ray tube with a copper anode generates characteristic Cu K_α radiation with a wavelength of 1.544 Å.

In contrast to laboratory X-ray tubes, large scale synchrotron facilities can produce much more energetic X-rays (with a shorter wavelength) with a brilliance that is about nine orders of magnitude higher. Brilliance is a typically used quantity to evaluate the quality of a light source. It evaluates the number of photons per second, the cross-sectional area of the beam, the angular divergence of the photons, and the amount of photons within a bandwidth of 0.1% of the central wavelength. Hence, the unit of brilliance is [photons/(s mm^2 mrad^2 0.1%BW)] [220].

The functional principle of a synchrotron is based on the fact that an accelerated charge emits energy. In a synchrotron, electrons that were accelerated to almost the speed of light are forced on a circular path by bending magnets in a so-called storage ring. One section of such a storage ring is schematically depicted in Fig. 3.9. The focusing magnets are used to keep the electrons close to the ideal orbital path. The storage ring also includes an accelerating cavity where electrons are re-accelerated every turn to compensate for their energy loss due to radiation.

While synchrotron radiation is emitted every time the electrons are deflected, the high-energy X-rays used for experiments are generated in insertion devices called undulators (see Fig. 3.9). The undulators consist of an array of magnets that force the electrons to follow a defined undulating path. Due to constructive interference a very brilliant and focused beam of radiation with a specific wavelength is generated and guided to a so-called beamline that is tangentially attached to the storage ring. Before

being used for experiments, the synchrotron radiation passes through an optics hutch where the beam is focused, shaped, and made monochromatic.

A more detailed explanation of the production and properties of synchrotron radiation can be found in Refs. [220,221].

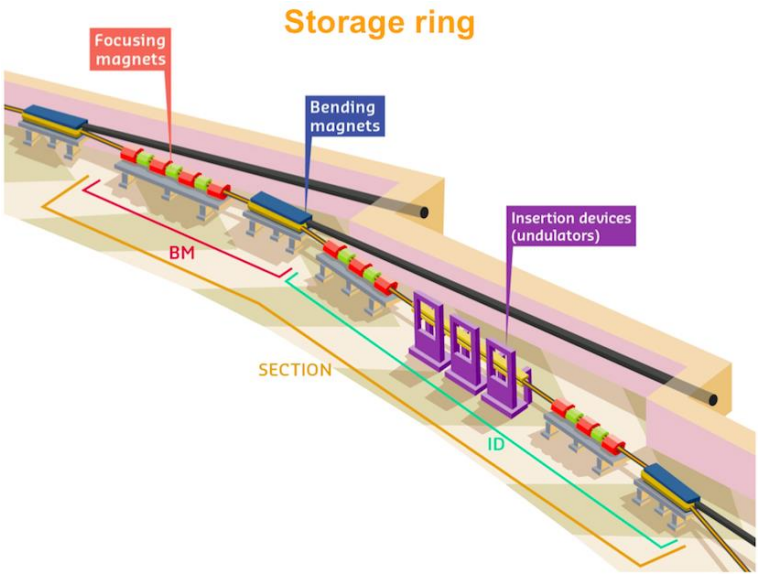

Figure 3.9: Schematic depiction of a section of a synchrotron storage ring. Bending magnets and focusing magnets are used to force the electrons on a circular path and to keep them focused. The insertion devices (undulators) generate the synchrotron radiation used for experiments. Taken from Ref. [221].

X-ray scattering

An extensive explanation of the theoretical background of total X-ray scattering and related data analysis procedures and corrections can be found in the book "Underneath the Bragg Peaks" by T. Egami and S.J.L. Billinge (Ref. [222]). Here, only a short summary with the most important points is presented.

The interaction of X-rays with single atoms can best be understood when the X-ray photons are described as a wave with the wavevector $|k| = 2\pi/\lambda$, where λ is the wavelength. This wave interacts with the electronic shells of the atom and contributions arise from the scattering with all electrons in the shell. The different locations in the shell of all scattering electrons are taken into account in the atomic form factor b, which is an integral over the volume of the shell. Now, if scattering not only takes place with a single atom, the influence of an ensemble of atoms has to be taken into account. The scattering on an ensemble of atoms can be calculated similar to the case of the atomic form factor. However, here, the discrete sum over the scattering contributions from all atoms is calculated, considering their different locations [220].

The resulting sample scattering amplitude is:

$$\Psi(Q) = \frac{1}{\langle b \rangle} \sum_{c} b_\nu \, e^{i \, Q \, R_\nu} \,, \tag{3.13}$$

where $\langle b \rangle$ is the averaged atomic form factor over all atoms, b_ν is the atomic form factor of atom ν, R_ν is the atomic position, and Q is the scattering vector, defined as:

$$Q = k_{init} - k_{final} \,, \tag{3.14}$$

with k being the wavevector of the incoming (init) and the scattered (final) beam. For elastic scattering, the wavelength of the incoming and scattered beam are equivalent, resulting in:

$$|Q| = \frac{4\pi \sin\theta}{\lambda} \,, \tag{3.15}$$

where 2θ is the scattering angle between k_{init} and k_{final}. The scattering amplitude $\Psi(Q)$ from Eq. 3.13 is the Fourier transform of the atomic position R_ν, and hence provides the information on the atomic structure of the sample that is intended to be resolved in the X-ray scattering experiments. However, the only quantity that can be measured directly in experiments is the intensity $\mathrm{I}(Q)$ of the scattered wave, which relates to $\Psi(Q)$ according to:

$$\mathrm{I}(Q) = \frac{\langle b \rangle^2}{N} |\Psi(Q)|^2 + \langle b \rangle^2 - \langle b^2 \rangle \,, \tag{3.16}$$

where N is the number of atoms in the sample and $\langle b \rangle^2 - \langle b^2 \rangle$ is called the Laue monotonic scattering term. Now, the scattering intensity $\mathrm{I}(Q)$ can be transformed into the total scattering structure function $\mathrm{S}(Q)$ (often called structure function or structure factor) which approaches unity at large Q:

$$\mathrm{S}(Q) := \frac{\mathrm{I}(Q)}{\langle b \rangle^2} = \frac{1}{N} |\Psi(Q)|^2 + \frac{\langle b \rangle^2 - \langle b^2 \rangle}{\langle b \rangle^2} \,. \tag{3.17}$$

$\mathrm{S}(Q)$ is a continuous function of Q and only depends on the magnitude of Q for isotropic scattering, as in liquids and glasses. The structure function contains all local structural information of the sample in the Fourier space and can be calculated from the scattering intensities measured in X-ray scattering experiments.

In order to obtain structural information in the real space, a direct Fourier transform of the structure function is performed, resulting in the reduced pair distribution function (PDF):

$$\begin{aligned} G(r) &= 4\pi r[\rho(r) - \rho_0] = 4\pi r\rho_0[g(r) - 1] \\ &= \frac{2}{\pi}\int_0^\infty Q\,[S(Q) - 1]\sin(Qr)dQ\,, \end{aligned} \tag{3.18}$$

where $\rho(r)$ is the atom pair density function, ρ_0 is the average number density, r is the distance to the reference atom, and g(r) is the pair distribution function. As the PDF provides real space structural information, it shows the probability of finding an atom in the distance r from the reference atom. It has to be kept in mind that the PDF represents an average over all pairs of atoms in the sample, which makes its interpretation especially challenging in the case of multicomponent alloys (as for BMGs), where many different pairs of atom species are present. In this context, it has also to be considered that the atomic form factors of all these atom species are very different, resulting in large differences in the weighting factors of the partial structure factors. In general, atoms with a higher atomic number are stronger X-ray scatterers and therefore contribute more to the total scattering intensity than atoms with a low atomic number.

As can be seen from Eq. 3.18, G(r), g(r), and ρ(r) all provide the same structural information. However, there are some advantages to using G(r) in this work. First, G(r) is directly calculated from the Fourier transform of S(Q), without assuming any value for ρ_0, and second, the uncertainties of G(r) are constant with r, whereas the ones of g(r), and ρ(r) decrease with r^{-1}.

In Chapter 3.5.3, dealing with the data analysis of synchrotron X-ray scattering experiments, the reader will again be referred to the scattering intensity I(Q), the structure function S(Q), and the reduced pair distribution function G(r), as these are the main quantities obtained and calculated from the experiments.

3.5.2 Experimental Setup

As mentioned in the beginning of the Chapter, different experimental setups were used for the in-situ X-ray diffraction experiments. In the first one, solid samples were heated with a resistive furnace, and in the second one samples were processed by electrostatic levitation (ESL) in the liquid state. Both experimental setups are explained in the following.

Furnace heating experiments

In-situ synchrotron X-ray scattering experiments with solid samples were carried out on the PETRAIII high-resolution beamline P02.1 at DESY (Deutsches Elektronen-Synchrotron) in Hamburg [223]. As-cast samples that were cut to a thickness of around 300 µm were analyzed in transmission mode using a Perkin Elmer XRD 1621 CsI bonded amorphous silicon flat-panel detector (2048 × 2048 pixels, pixel size 200 µm × 200 µm). A beam size of 0.5 × 0.5 mm^2 with a wavelength of 0.207 Å

(60 keV) was used. The samples were heated from room temperature to 823 K with a constant heating rate of 0.333 K/s in a Linkam THMS 600 furnace under a constant flow of high-purity Ar. Additionally, isothermal experiments at elevated temperatures were conducted where the samples were initially heated with a rate of 2 K/s. Two-dimensional raw diffraction patterns were collected in 10 s intervals.

Electrostatic levitation experiments

In-situ synchrotron X-ray scattering experiments with liquid samples were carried out on the materials science beamline ID11 at ESRF (European Synchrotron Radiation Facility) in Grenoble, France. Samples were processed in an electrostatic levitation (ESL) device [212–215] in collaboration with the Institute of "Materials Physics in Space" at the German Aerospace Center (DLR, Deutsches Zentrum für Luft- und Raumfahrt).

The ESL technology uses Coulomb forces to levitate and position a positively charged sample in an electrostatic field. The used electrode assembly is schematically shown in Fig. 3.10 a). The levitation force is applied by two vertically positioned high voltage levitation electrodes (+/- 20 kV) and the horizontal sample position is controlled by four side electrodes. At low temperatures, sample charge is maintained by ultraviolet (UV) radiation from an UV lamp and by thermionic emission at high temperatures. As no stable equilibrium position exists for an electrostatically positioned point charge, the horizontal position needs to be actively controlled. This control feedback loop is based on the information obtained from a setup of two position sensitive photodetectors (PSDs) and two positioning lasers, that detects the position of the sample, as shown in Fig. 3.10 b). The sample can be heated and melted by two 75 W infrared (λ = 808 nm) heating lasers and temperature is measured by two two-color pyrometers. Cooling of the sample is limited by radiative heat transfer when completely switching off the lasers. The whole setup is placed in a vacuum chamber and levitation takes place under high vacuum, roughly around 10^{-7} mbar. The mass of a typical sample processed by ESL is around 100 mg to 150 mg for the X-ray diffraction experiments.

The main advantages of the ESL technique are the following: Highly reactive samples can be processed containerless in the liquid and the solid state in a high vacuum, thus avoiding reactions. In contrast to electromagnetic levitation techniques [216,224], heating is decoupled from the levitation itself, allowing for all kinds of temperature protocols. Furthermore, there are no induced electromagnetic currents, that disturb the sample. And finally, ESL samples are not limited to electrically conductive materials.

For the in-situ synchrotron X-ray scattering experiments, an X-ray beam with a size of 0.5 × 0.5 mm^2 and a wavelength of 0.124 Å (100 keV) was used. The diffraction patterns were recorded by a two-dimensional FReLoN detector (2048 × 2048 pixels, pixel size 50 µm × 50 µm) and raw diffraction patterns were collected every second. Samples were heated to several hundred Kelvin above the liquidus temperature and

then cooled freely. The heating and cooling cycle was repeated several times for each sample. The temperature calibration of the pyrometer was obtained from the melting point upon heating.

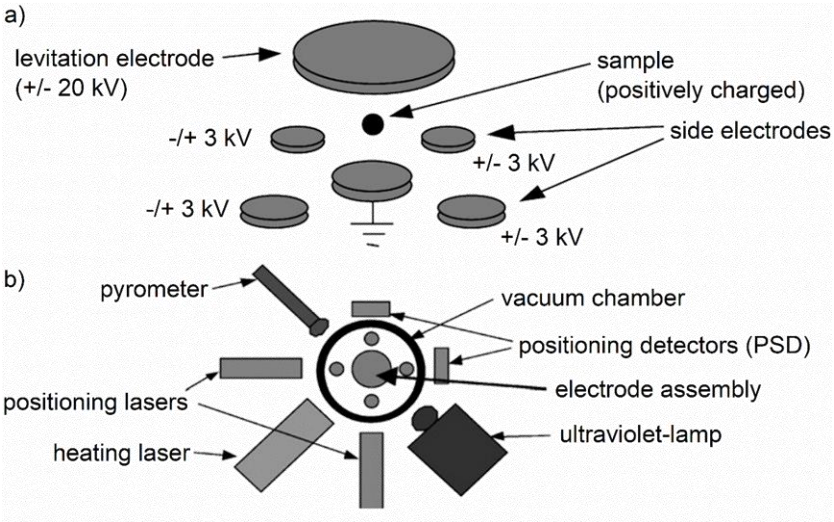

Figure 3.10: a) Schematic diagram of the electrode assembly with the levitating sample in the center. **b)** Schematic diagram of the electrostatic levitator, including the positioning and heating systems. Taken from Ref. [214].

3.5.3 Data Analysis

The raw data obtained from the synchrotron X-ray scattering experiments consists in two-dimensional diffraction patterns, as shown in the top-right corner of Fig. 3.11. These diffraction patterns first need to be integrated in order to obtain the raw intensity as a function of Q. Furthermore, each pattern needs to be correlated with the measured temperature.

For the experiments performed at DESY, an azimuthal integration of the diffraction patterns was performed after subtraction of the dark image, using the software DAWN Science [225,226]. The azimuthal integration of the diffraction patterns recorded at ESRF was performed using the software package PyFAI (Python Fast Azimuthal Integration) [227]. In both cases, information on the exact wavelength and the sample detector distance from calibration measurements were used for the integration. A typical raw intensity diffraction pattern of an amorphous sample is shown as red line in Fig. 3.11 a) and in the inset. At very low Q-values, no intensity was measured due to the shading of the beamstop. A background image was recorded at room temperature and the appropriate background subtraction resulted in the scattering intensity I(Q) (black line in Fig. 3.11 a)).

The resulting scattering intensity I(Q) was then used to calculate the structure function S(Q), using the software PDFgetX2 [228], according to Eq. 3.17, and taking

into account corrections for sample absorption, multiple scattering, fluorescence, and Compton scattering. The typical shape of S(Q), approaching unity for large Q-values, is displayed in Fig. 3.11 b). The reduced pair distribution function G(r) was calculated from the Fourier transformation of S(Q) according to Eq. 3.18, also using PDFgetX2. The maximum Q-value used for the transformation was 16.5 Å for the experiments performed at DESY and 9 Å for the ones at ESRF. The optimization algorithm of PDFgetX2 was used to obtain the parameters for fluorescence and energy dependence of the Compton scattering in order to optimize G(r) in the low r-range (0 to 2 Å). One of the calculated G(r) curves is shown in Fig. 3.11 c). For the determination of peak positions, both S(Q) and G(r) curves were interpolated with a cubic spline. A more detailed explanation of the complete data analysis procedure can be found in Ref. [222].

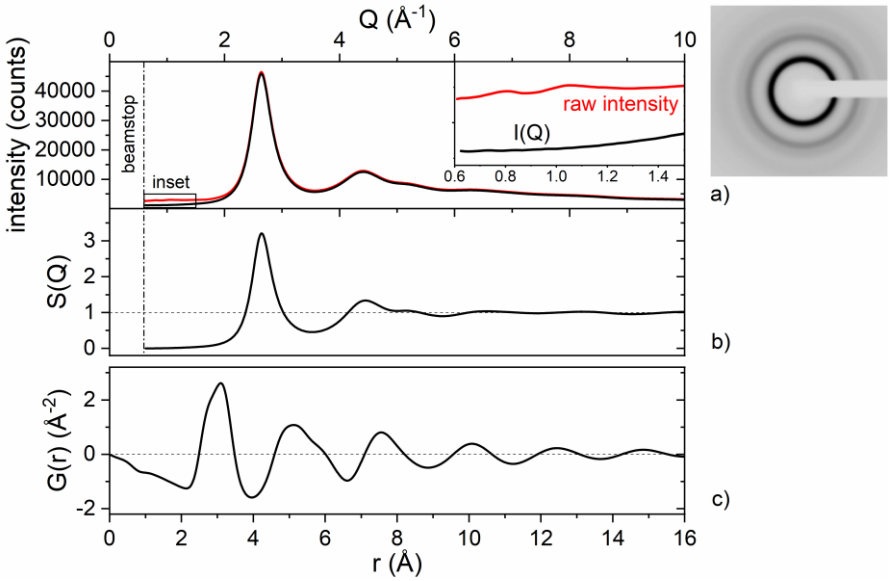

Figure 3.11: a) Integrated intensity from synchrotron X-ray scattering experiments as a function of Q. The red line shows the raw intensity and the black line the scattering intensity I(Q) after background subtraction. The image on the right shows the diffraction pattern before azimuthal integration. **b)** Structure function S(Q) as calculated from I(Q). **c)** Reduced pair distribution function G(r), resulting from the Fourier transform of S(Q).

For the analysis of the crystallization behavior, the scattering intensity I(Q) was considered. For the different alloy compositions, the relevant binary phase diagrams were evaluated, and possible crystalline phases were listed. A literature search for the crystal structures of these phases was performed, e.g. using "Springer Materials", and the idealized diffraction patterns of these crystalline phases were simulated using the software "PowderCell 2.3", as described in Ref. [229]. The simulated patterns were then compared to the measured diffraction data. For this analysis, equilibrium phases were considered, as only for these reliable data is available. However, it should be

pointed out that in the fast quenched, multicomponent BMG alloys strong deviations of the diffraction patterns from the idealized equilibrium values are likely to occur. Peak shifts and changes in intensity are for example caused by a distortion of the lattice due to the substitution of one atom species by another one and by the different atomic form factors of different atoms.

3.6 Thermoplastic Forming

Different thermoplastic forming (TPF) experiments were performed to assess the thermoplastic formability of the amorphous alloys. Similar to the temperature profiles known from the DSC experiments, deformation experiments with a constant heating rate and isothermal ones were conducted. Besides deformation experiments on bulk samples, thermoplastic consolidation experiments with amorphous powder were performed, evaluating this additive processing route as an alternative way to obtain larger amorphous structures.

For all TPF experiments, a custom-built machine was used that allows for rapid heating, pressing, and cooling of samples in a high purity Ar-atmosphere (also see Ref. [230]). The experimental setup is depicted in Fig. 3.12.

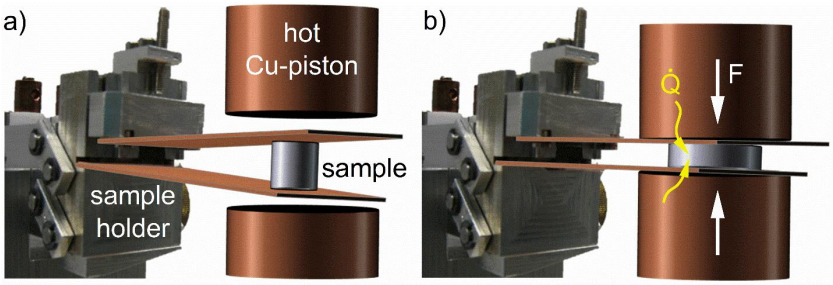

Figure 3.12: Visualization of the experimental setup for TPF. A sample holder carries the sample to the combined heating and pressing station between two hot Cu-pistons. The temperature of the pistons can be precisely controlled, and the pistons are brought in contact with the sample, causing a rapid heating. The desired pressing force is then also applied by the Cu-pistons. **a)** Initial position before the pistons are brought into contact with the sample. **b)** Final position after deformation of the sample.

Figure 3.12 a) shows the initial position while b) shows the final position after deformation of the sample. On the left-hand side the sample holder is displayed, including two thin Cu-plates that carry the sample. The sample is fixated by a slight pretension of the Cu-plates. Within the TPF machine, eight of these sample holders are attached to a rotatable mount, placed inside a vacuum chamber. Prior to each experiment, the sample holder is rotated to the combined heating and pressing station between two hot Cu-pistons, as shown in Fig. 3.12 a). The temperature of the pistons can be precisely controlled, and the pistons are brought in contact with the sample, causing a rapid heating due to heat conduction. The desired pressing force is then also

applied by the Cu-pistons. After reaching the programmed pressing time, the pistons return to their initial position and the sample holder rotates immediately to the next position where the sample is rapidly cooled between cold Cu-pistons.

3.6.1 Bulk Deformation

Bulk deformation experiments were performed with a single, standardized sample geometry in order to allow for comparison between different alloys. Cylindrical samples with a diameter of 3 mm and a length of 7 mm were used. The majority of experiments was performed on the alloys listed in Table 3.1, as well as on the Zr-based alloy AMZ4 ($Zr_{59.3}Cu_{28.8}Al_{10.4}Nb_{1.5}$) and the Fe-based alloy FeMoPCB ($Fe_{67.5}Mo_{7.5}P_{10}C_{10}B_5$).

Constant Heating Rate

Deformation experiments with a constant heating rate were used to assess the maximum deformability of an alloy in a single scan (compare to the experiments shown in Ref. [172]).

The sample was positioned as shown in Fig. 3.12 a) and prior to heating the Cu-pistons, the Cu-pistons were lowered to press on the sample with a constant load of 500 N. The temperature of the Cu-pistons was now adjusted to a temperature 50 K below the glass transition temperature of the sample (T_g - 50 K). After equilibrating, the whole setup (Cu-pistons and sample) was heated with a constant heating rate of 0.333 K/s up to a temperature at least 10 K above the crystallization temperature of the chosen rate (T_x + 10 K). During the experiment, the displacement of the upper piston as well as the temperature of the pistons were recorded. A typical dataset of one experiment is shown in Fig. 3.13. The blue curve displays said piston displacement, showing the deformation of the sample in the supercooled liquid. The red curve shows the temperature-time profile and the black curve is a DSC scan with the same heating rate where the characteristic temperatures are indicated by dashed lines as a reference.

After each experiment, the sample was cooled to room temperature and its mean diameter and its exact thickness were measured with a micrometer screw.

Isothermal Experiments

Isothermal deformation experiments were used to measure the deformability of an alloy as a function of time and temperature, thus resulting in a TPF TTD (thermoplastic forming time-temperature-deformation) diagram. The applied temperature protocol was very similar to the one used for the measurement of the TTT diagram in DSC (see Chapter 3.3.3). The main advantage of this experimental procedure over the one with a constant heating rate is that here the amorphous structure of the sample can be preserved, thus maintaining the advantageous properties of the metallic glass.

The geometrical setup of the experiment was the same as described for the constant heating rate experiment. However here, the Cu-pistons were preheated to the desired

pressing temperature before getting into contact with the sample. The pistons were then lowered and pressed on the sample with a constant load of 500 N. Due to the fast conductive heating through the Cu-pistons, the sample quickly reached the temperature of the pistons and was held isothermally for the programmed time. After each experiment, the sample was rapidly cooled between cold Cu-pistons and its mean diameter and its exact thickness were measured with a micrometer screw. Selected samples were also analyzed by DSC scans (compare to Chapter 3.3.1) and XRD measurements (compare to end of Chapter 3.1).

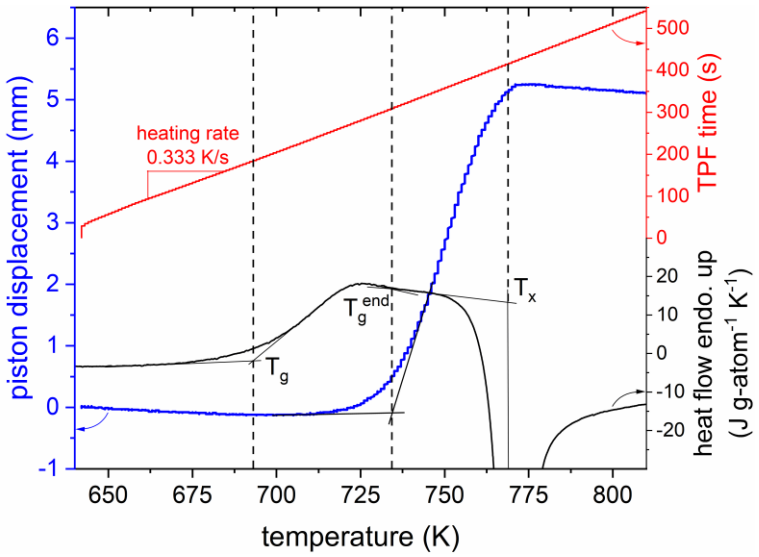

Figure 3.13: Process diagram for TPF bulk deformation experiments with a constant heating rate. The blue curve displays the displacement of the pressing piston, showing the deformation of the sample in the supercooled liquid. The red curve shows the temperature-time profile of the TPF experiment with a heating rate of 0.333 K/s. The black curve is a DSC scan with the same heating rate where the characteristic temperatures are indicated by dashed lines.

3.6.2 Powder Consolidation

TPF consolidation experiments with amorphous powder were conducted additionally to the bulk deformation experiments. The focus of these experiments was to evaluate this processing route as one possible additive manufacturing method to produce large amorphous structures that cannot be obtained by casting methods.

Amorphous powder of three different alloy compositions, namely AMZ4 ($Zr_{59.3}Cu_{28.8}Al_{10.4}Nb_{1.5}$), CuTi ($Cu_{47}Ti_{33}Zr_{11}Ni_6Si_1Sn_2$), and FeMoPCB ($Fe_{67.5}Mo_{7.5}P_{10}C_{10}B_5$), was used. The amorphous powder was produced at the "Leibniz-Institut für Werkstoff-orientierte Technologien – IWT" in Bremen within the framework of a cooperative AiF/IGF research project (IGF Nr. 19291 N). Additionally, amorphous AMZ4 powder

was provided by the Heraeus Additive Manufacturing GmbH [231]. Different powder fractions between 25-45 µm and 150-180 µm were used.

The consolidation experiments were performed similar to the isothermal deformation experiments described in the previous chapter and the interested reader is also referred to our recent publication on the same topic [184]. In contrast to bulk deformation experiments, the powder needed to be enclosed in some kind of container to allow for heating and pressing of the sample. Hence, permanent steel molds consisting of an outer frame with an interior rectangular hole of 3 x 20 mm and two tight fitting rectangular punches that seal the frame from top and bottom, were used. A typical mold is schematically depicted in the inset in Fig. 3.14 a). A force applied onto the two punches compacts the powder in the middle which on the sides is enclosed by the frame. Quantities of 0.5 to 1.5 g of powder were filled into the molds and the mold bundle was placed on the TPF sample holder as previously explained.

A typical process diagram for the TPF powder consolidation experiments is displayed in Fig. 3.14, with a) showing the pressing force as a function of time, b) the piston displacement, and c) the temperature profile. The blue curve shows the sample temperature, measured with a thermocouple, and the black and red curves show the lower and upper Cu-piston temperatures, respectively. In the inset, a magnification of the pressing interval can be seen.

The TPF procedure started at t = 0 s, where the hot Cu-pistons were lowered and pressed on the powder filled mold with an initial force of 500 N. During the next 20 s the sample was heated until the desired process temperature was reached. Then the consolidation process started when a pressing force of maximally 4500 N was applied by the pistons. After reaching the desired pressing time, the pistons went back to their initial position and the sample was rapidly cooled between cold Cu-pistons. For AMZ4, pressing temperature was varied between 703 K and 743 K, and pressing times ranged from 10 s to 150 s. A maximum pressing stress of 75 MPa was reached.

All selected process parameters were evaluated regarding powder compaction and the conservation of the amorphous structure. The degree of compaction, or rather the remaining porosity, was evaluated by optical microscopy with an Olympus BH-2 optical microscope on polished cross-sections. The amorphous structure of the samples after consolidation was checked by XRD with a PANalytical X'Pert Pro diffractometer as described in Chapter 3.1, as well as DSC.

The samples obtained from the TPF consolidation process were beam shaped samples with a rectangular cross section of 1-2 x 3 mm^2 and a length of 20 mm. These samples were used for three-point beam bending tests as described in Chapter 3.2, in order to evaluate their mechanical performance. The fracture surfaces of the beams were examined in a Zeiss Sigma VP scanning electron microscope in secondary electron contrast.

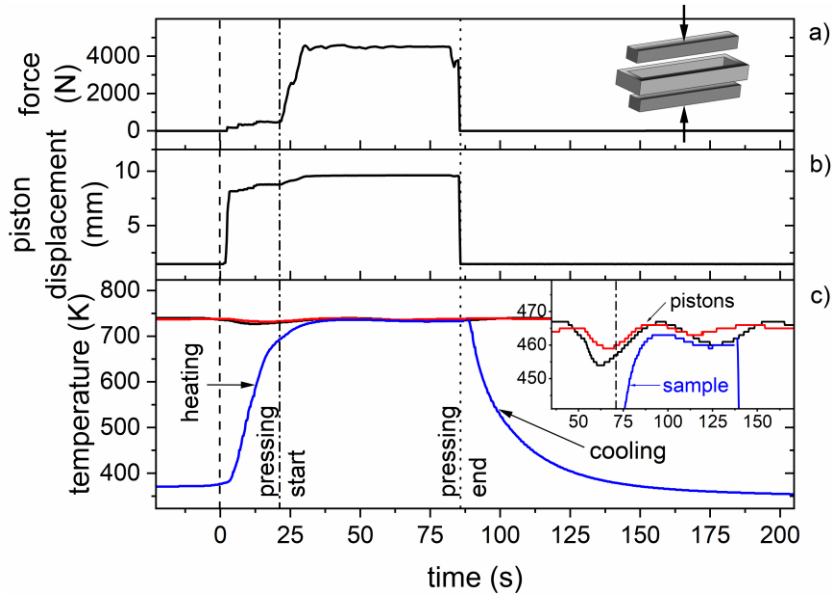

Figure 3.14: Process diagram for TPF powder consolidation experiments. The dashed line indicates the beginning of the heating phase, the dash-dotted line the start of the pressing process, and the dotted line the end of pressing. **a)** Pressing force as a function of time, with the inset schematically showing the permanent steel molds used for the powder pressing. **b)** Piston displacement. **c)** Temperature profile. The blue curve shows the sample temperature, measured with a thermocouple in the center of the sample, and the black and red curves show the lower and upper Cu-piston temperatures, respectively. In the inset, a magnification of the pressing interval can be seen.

Chapter 4

Thermophysical and Structural Investigation

In this Chapter, the thermophysical properties and the structure of the CuTi-based bulk metallic glass (BMG) Vitreloy 101 ($Cu_{47}Ti_{34}Zr_{11}Ni_8$) [12] and the Zr-based BMG Vitreloy 105 ($Zr_{52.5}Cu_{17.9}Ni_{14.6}Al_{10}Ti_5$) [11] are investigated. Special focus is laid on the influence of minor additions of sulfur (S) and phosphorus (P) on the two alloy systems, as it was found that already minor additions of S drastically change the properties. This work is motivated by the discovery of S-containing BMGs in the research group of R. Busch in 2016, which resulted in the filing of a patent in 2017 and the first publication [7].

The critical casting thickness of the different compositions, the mechanical properties, and the crystallization behavior are evaluated. The thermodynamic functions are determined, and viscosity and kinetic fragility are measured around the glass transition and in the stable liquid. In-situ synchrotron X-ray scattering experiments are performed, elucidating the crystallization sequence upon heating and cooling. Based on the diffraction data, the temperature evolution of structural differences between the alloys is discussed.

4.1 Modifications of CuTi- and Zr-based Alloys by Minor Additions

Minor additions of S and P were added to the well know bulk metallic glass-forming alloys $Cu_{47}Ti_{34}Zr_{11}Ni_8$ (Vit101) and $Zr_{52.5}Cu_{17.9}Ni_{14.6}Al_{10}Ti_5$ (Vit105). Both alloys are of industrial interest due to their rather cheap constituent elements (Vit101) or their rather high GFA (Vit105), and are already used in industrial production, e.g. by the Heraeus Deutschland GmbH [232]. However, both alloy compositions do not show a pronounced SCL region upon heating, thus hampering their use for thermoplastic forming processes or selective laser melting. Hence, the initial goal of the microalloying efforts was to enhance their thermal stability.

The measured data for the initial optimization process regarding the thermal stability of the alloys and the influence of microalloying is depicted exemplarily for Vit105 S in Fig. 4.1. Samples with increasing S-content were produced and standard DSC scans were performed. Additions of S shift T_g to higher temperatures and significantly

increase the length of the SCL, reaching its maximum for the compositions with a S-content between 1.75 and 2.25 at%, with $\Delta T_x = T_x - T_g = 85$ K for a heating rate of $q_h = 1$ K/s. The measurements also show that the length of the SCL is not too sensitive to changes in the S-content in the region between 1.5 and 2.25 at%, as shown in the right window of Fig. 4.1. For all further investigations the composition $(Vit105)_{98}S_2$ was selected. Additionally, other element ratios of the S-containing alloy were changed (Cu-Ni, Zr-Ti, and Cu-Al) and the length of the SCL was evaluated, however not resulting in any significant improvements.

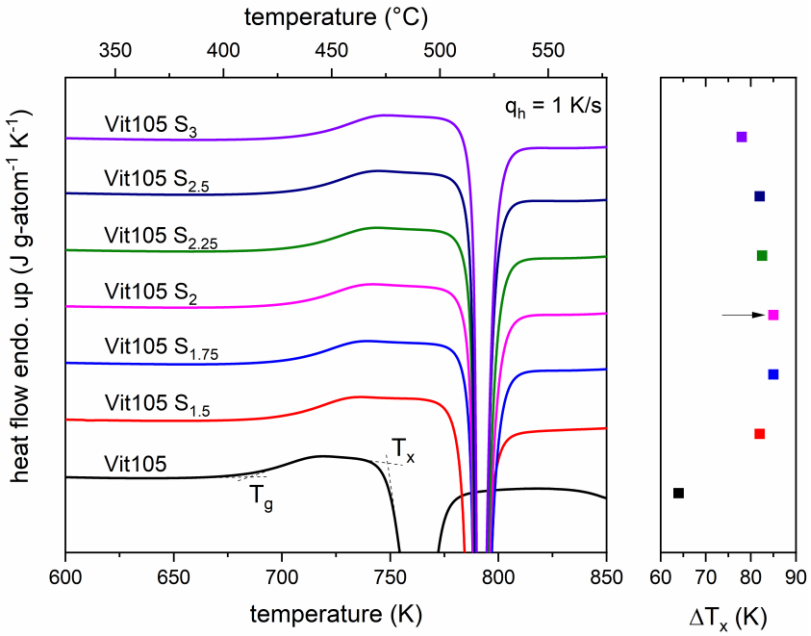

Figure 4.1: DSC scans of Vit105 S alloy compositions with a heating rate of $q_h = 1$ K/s. Vit105 is compared to its S-bearing counterparts with S-contents between 1.5 and 3 at%. The length of the SCL region is indicated in the right window.

The previously described initial selection process for the appropriate S- and P-content was performed in the same manner for Vit105 P and Vit101 P/S, resulting in the following compositions that were thoroughly characterized in this work: Vit101 P_1 ($Cu_{46.53}Ti_{33.66}Zr_{10.89}Ni_{7.92}P_1$), Vit101 $S_{1.5}$ ($Cu_{46.3}Ti_{33.5}Zr_{10.8}Ni_{7.9}S_{1.5}$), Vit105 P_2 ($Zr_{51.45}Cu_{17.54}Ni_{14.31}Al_{9.8}Ti_{4.9}P_2$), and Vit105 S_2 ($Zr_{51.45}Cu_{17.54}Ni_{14.31}Al_{9.8}Ti_{4.9}S_2$). The base alloys Vit101 and Vit105 were also characterized in the same way to allow for a consistent comparison of the properties.

4.1.1 Critical Casting Thickness

The XRD results for all six alloys for rod-shaped samples produced by Cu-mold casting are shown in Fig. 4.2 and the resulting critical casting thickness d_c for fully amorphous rods is summarized in Table 4.1. Figure 4.2 a) shows the diffraction patterns for the

Vit101 alloys, where fully XRD amorphous samples are obtained up to a thickness of 5 mm for Vit101 and Vit101 P_1 and up to 6 mm for Vit101 $S_{1.5}$. Hence, the addition of P does not significantly improve the GFA, while the addition of 1.5 at% S improves the critical casting thickness by one millimeter. A similar improvement is observed for the addition of 1 at% Si to Vit101 [133], as well as for 2 at% Sn [134,143]. It should also be noted that the critical casting thickness of Vit101 was reported as $d_c = 4$ mm in the original publication [12], whereas in this work a 5 mm rod was XRD amorphous.

Figure 4.2 b) shows the diffraction patterns for the Vit105 alloys. The critical casting thickness is found to be 8 mm for Vit105, 3 mm for Vit105 P_2, and 6 mm for Vit105 S_2. Here, minor additions result in a decreasing GFA, especially for the P addition. In literature, the critical casting thickness of Vit105 is estimated as 18 mm in the supplementary information of Ref. [83], however without specifying the casting method.

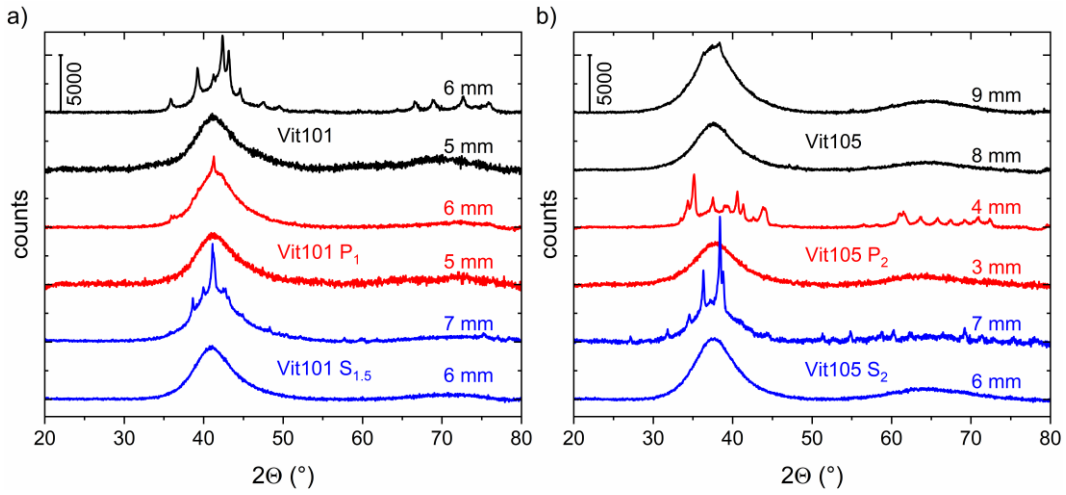

Figure 4.2: XRD patterns of rods for the evaluation of the critical casting thickness. **a)** Vit101 alloys. **b)** Vit105 alloys. The composition and the diameter of the samples is given in the figure.

Experiments to determine the critical casting thickness were additionally performed with industrial grade raw materials, where Zr crystal bar[1] was replaced by Zr702[2], and Ti 99.995%[3] by Ti CP grade 1[4]. Using industrial grade raw materials significantly increases the oxygen content of the master alloys and is known to decrease the GFA of many Zr-containing alloys [11,84,146]. Surprisingly, for the Vit101 alloys it was found that the critical casting thickness of industrial grade Vit101 and Vit101 $S_{1.5}$ is at least 5 mm, and hence is not diminished. For the Vit105 alloys the experiments showed that the critical casting thickness of both, industrial grade Vit105 and Vit105 S_2 is reduced to 5 mm, and therefore the same as for the Vit101 alloys.

[1] Zr crystal bar: 30 wt. ppm oxygen
[2] Zr702: 1600 wt. ppm oxygen
[3] Ti 99.995%: 200 wt. ppm oxygen
[4] Ti CP grade 1: 1800 wt. ppm oxygen

Table 4.1: Critical casting thickness d_c for fully amorphous rods in Cu-mold casting.

Alloy	d_c [mm]	Alloy	d_c [mm]
Vit101	5	Vit105	8
Vit101 P_1	5	Vit105 P_2	3
Vit101 $S_{1.5}$	6	Vit105 S_2	6

4.1.2 Mechanical Properties

The mechanical properties were assessed by three-point bending (3PB) flexural tests and by Vickers hardness measurements. The results of the 3PB tests are depicted in Fig. 4.3. For the Vit101 alloys in Fig. 4.3 a), it can clearly be seen that minor additions of P and S result in an embrittlement of the alloy as no more plasticity is observed in bending. As for the influence on the GFA, these results are very similar to the ones reported for minor additions of Si and Sn to Vit101 [143].

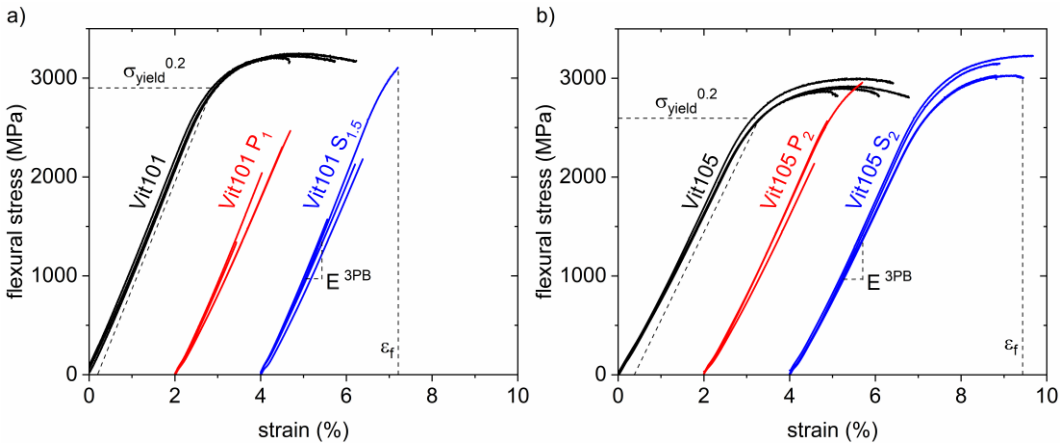

Figure 4.3: Stress-strain diagram of **a)** the Vit101 alloys and **b)** the Vit105 alloys resulting from the three-point bending flexural test. The characteristic properties are indicated by dashed lines.

In Ref. [143] the authors report on a significant drop in toughness that seems to be related to an increase in glass transition temperature, yield strength, and shear modulus. Due to the decrease in toughness, small defects already cause sample fracture under bending load before the nominal yield strength is reached. The measurement curve of Vit101 $S_{1.5}$ reaching a flexural stress above 3 GPa indicates that the yield strength for defect-free samples lies above the one for Vit101. The characteristic mechanical properties obtained from 3PB of the Vit101 alloys and the standard deviation of the measurements are summarized in Table 4.2. E^{3PB} is the elastic modulus, $\sigma_{yield}^{0.2}$ is the 0.2 % offset yield point, or rather the fracture stress for the alloys with minor additions, and ε_f is the strain to fracture in %.

The 3PB measurements for the Vit105 alloys are shown in Fig. 4.3 b). For Vit105 P_2, a slight increase in the elastic modulus and an embrittlement of the alloy are observed. For Vit105 S_2 however, there is no significant embrittlement and the strain to fracture ($\varepsilon_f = 5.2$ %) is similar to the one for Vit105 ($\varepsilon_f = 6.1$ %). The 0.2 % offset yield point is increased by almost 200 MPa in comparison to the base alloy, hence showing a strengthening of the alloy without a decrease in ductility. All characteristic values are also shown in Table 4.2.

Hardness measurements showed an increase in hardness for all alloys with minor additions in comparison to their base alloys (576 HV for Vit101 and 506 HV for Vit105). While for the Vit101 alloys an increase of roughly 15 HV is observed, the Vit105 alloys show an increase of around 25 HV. The results of the hardness measurements are also summarized in Table 4.2.

Table 4.2: Characteristic mechanical properties of the amorphous alloys and the standard deviation of the measurements. HV5 indicates Vickers hardness values, E^{3PB} the elastic modulus as determined in three-point bending, $\sigma_{yield}{}^{0.2}$ the 0.2 % offset yield point, and ε_f the strain to fracture.

Alloy	HV 5	E^{3PB} [GPa]	$\sigma_{yield}{}^{0.2}$ [MPa]	ε_f [%]
Vit101	576 ± 5	108 ± 0.5	2900 ± 10	5.5 ± 0.6
Vit101 P_1	588 ± 3	103 ± 3	2040 ± 430	2.15 ± 0.5
Vit101 $S_{1.5}$	590 ± 6	105 ± 3	2240 ± 550	2.35 ± 0.6
Vit105	506 ± 6	89 ± 1	2600 ± 45	6.1 ± 0.6
Vit105 P_2	538 ± 8	94 ± 2	2510 ± 240	3.0 ± 0.4
Vit105 S_2	527 ± 2	92 ± 2	2770 ± 95	5.2 ± 0.4

4.2 Thermodynamic Properties

The thermodynamic properties discussed in this work include characteristic temperatures, transformation enthalpies, molar heat capacity, and the derived quantities enthalpy, entropy, and Gibbs free energy. All these properties can be determined from calorimetric measurements and allow, among others, an estimation of the driving force for crystallization in the supercooled melt.

In the first section, the characteristic temperatures and enthalpies determined from standard DSC and DTA scans are discussed, and in the second one the thermodynamic functions are calculated from the molar heat capacity measurements and discussed.

4.2.1 Characteristic Temperatures and Enthalpies

Figure 4.4 shows the DSC scans of all alloys with a heating rate of $q_h = 0.333$ K/s, where the glass transition temperature T_g and the crystallization temperature T_x are indicated by arrows. The obtained characteristic temperatures are summarized in Table 4.3 on page 78, where also the fictive temperature T_{fic} for a heating and cooling rate of $q = 0.333$ K/s is shown. T_{fic} results from the T_g-shift measurements discussed in Chapter 3.3.2 and 4.4. Furthermore, the integrated crystallization enthalpy upon heating ΔH_x is given in Table 4.4.

For the Vit101 alloys, shown in Fig. 4.4 a), the minor additions cause the glass transition temperature to increase by around 20 K (from 674 K for Vit101 to 691 K for Vit101 P_1 and 695 K for Vit101 $S_{1.5}$). At the same time, the crystallization temperature increases even further, resulting in an increase of the SCL region ΔT_x of around 15 K. The crystallization enthalpies upon heating, ΔH_x, were determined to be rather similar and lie between 7 and 8 kJ g-atom^{-1} for the three alloys, where Vit101 $S_{1.5}$ shows the lowest enthalpy and one less crystallization peak.

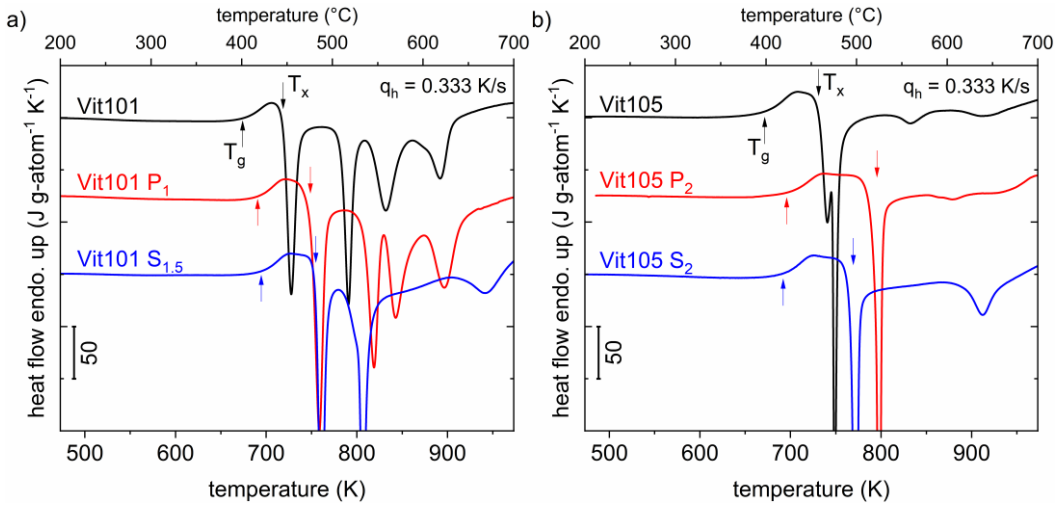

Figure 4.4: DSC scans of **a)** the Vit101 alloys and **b)** the Vit105 alloys with a heating rate of $q_h = 0.333$ K/s. The glass transition temperature T_g and the crystallization temperature T_x are indicated by arrows. In both alloy families, minor additions of P or S increase T_g and significantly enlarge the SCL region.

The DSC scans of the Vit105 alloys are displayed in Fig. 4.4 b). The influence of minor P and S additions described for Vit101 generally holds true for Vit105. T_g increases by roughly 20 K and the SCL region is enlarged. Microalloying seems to inhibit the first crystallization event occurring in Vit105 which is visible as a shoulder, or rather a small peak, in the heat flow signal before the main crystallization event occurs. For both, Vit105 P_2 and Vit105 S_2, only a single sharp crystallization peak is visible. While for Vit105 S_2, ΔT_x is increased by 17 K to a value of 77.4 K, Vit105 P_2 shows an even

larger SCL region with $\Delta T_x = 100$ K, and hence a pronounced thermal stability upon heating. The crystallization enthalpies are smaller than for Vit101 and are determined to lie between 4.82 kJ g-atom^{-1} for Vit105 P_2 and 5.86 kJ g-atom^{-1} for Vit105 S_2.

In summary, for the Vit101 and the Vit105 alloys, minor additions of P and S increase T_g and significantly enlarge the SCL region, thus causing an enhanced thermal stability upon heating.

The DTA melting curves are depicted in Fig. 4.5. For each alloy composition, an amorphous and a crystalline sample were heated up to 1373 K with a heating rate of $q_h = 0.333$ K/s. The obtained characteristic temperatures are displayed in Table 4.3 and the enthalpy ΔH_f, and entropy of fusion ΔS_f, in Table 4.4. For all compositions, various measurements were performed and the values in the tables represent mean values for the first melting of an initially amorphous sample.

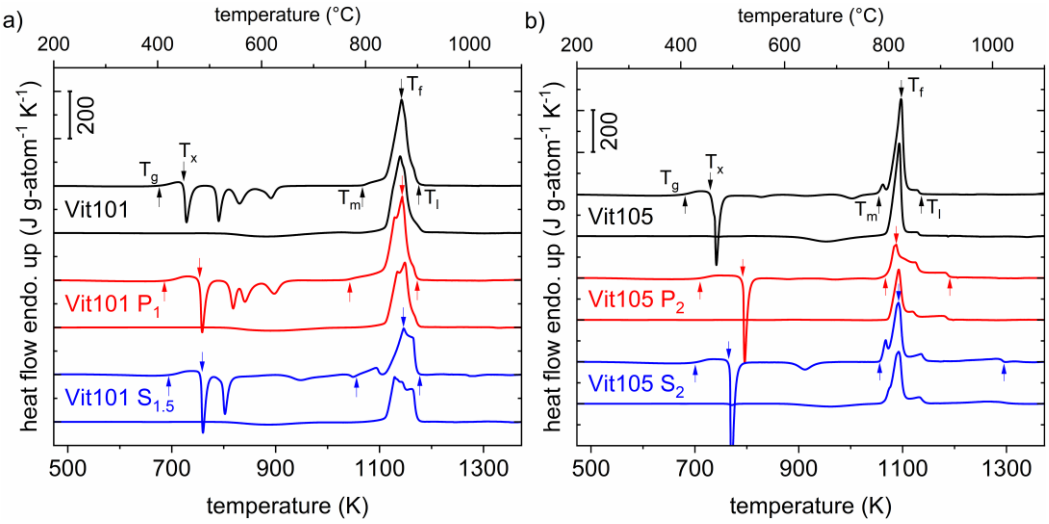

Figure 4.5: DTA scans of **a)** the Vit101 alloys and **b)** the Vit105 alloys with a heating rate of $q_h = 0.333$ K/s. For each alloy composition, an amorphous and a crystalline sample were heated up to 1373 K. For the amorphous samples, the glass transition temperature T_g, the crystallization temperature T_x, the melting temperature T_m, the temperature of fusion T_f, and the liquidus temperature T_l, are indicated by arrows. Especially for the Vit101 alloys it can be noted that the melting of initially amorphous samples starts at lower temperatures than for their crystalline counterparts, whereas the liquidus temperature stays the same.

The Vit101 alloys in Fig. 4.5 a) show a distinct difference in the melting curves for initially amorphous and initially crystalline samples. The melting (or eutectic) temperature of the amorphous samples T_m^{am} is roughly 60 K lower than the one of crystalline samples (T_m^{xtal}) during the first melting in the DTA. The temperature of fusion T_f however, which corresponds to the peak position of the main melting peak, is around 1140 K for the three Vit101 compositions. The liquidus temperature T_l lies around 1170 K and the alloys show a close to eutectic composition. The enthalpy of

fusion ΔH_f is approximately 11.3 kJ g-atom^{-1} for Vit101 and Vit101 P_1 and only 10 kJ g-atom^{-1} for Vit101 $S_{1.5}$. Given a similar value of T_f, the entropy of fusion $\Delta S_f = \Delta H_f/T_f$ of the alloys shows the same proportionality, with ΔS_f (Vit101) = 9.9 J g-atom^{-1} K^{-1}. The reduced glass transition temperature $T_{rg} = T_g/T_l$ increases from 0.577 for Vit101, over 0.590 for Vit101 P_1, to 0.594 for Vit101 $S_{1.5}$.

The phenomenon that the melting point of the initially amorphous sample is lower than the one of the slowly cooled crystalline sample might be related to the findings presented in Refs. [233–235]. There, a significant decrease in the melting temperature is reported for very small and nanocrystalline samples. The same effect could occur in the initially amorphous samples that form a nanocrystalline structure upon heating during the DTA measurement. This structure shows a high amount of grain boundaries, is less stable and hence displays a higher Gibbs free energy. Therefore, the liquid structure is already energetically preferred at lower temperatures, initiating the melting process, as observed in Ref. [236].

The DTA scans of the Vit105 alloys are shown in Fig. 4.5 b). These alloys also show a slightly earlier onset of melting for the initially amorphous samples, however less pronounced as Vit101. The temperature of fusion T_f lies around 1090 K for all three compositions. While Vit105 almost shows a eutectic composition (T_l = 1134 K), Vit105 P_2 shows a larger melting shoulder (T_l = 1189 K), and Vit105 S_2 an even more pronounced one (T_l = 1295 K). The existence of a crystalline phase in Vit105 S_2 up to high temperatures will also be discussed later in the context of the in-situ synchrotron X-ray scattering experiments at high temperatures in Chapter 4.6.2.

Table 4.3: Characteristic temperatures, determined by DSC and DTA measurements at a heating rate of $q_h = 0.333$ K/s. Glass transition temperature T_g, crystallization temperature T_x, length of the SCL region ΔT_x, fictive temperature T_{fic}, Kauzmann temperature T_K, melting (or eutectic) temperature for an amorphous sample T_m^{am}, a crystalline sample T_m^{xtal}, temperature of fusion T_f, liquidus temperature T_l, and reduced glass transition temperature T_{rg}.

Alloy	T_g [1)] [K]	T_x [1)] [K]	ΔT_x [1)] [K]	T_{fic} [1)] [K]	T_K [K]	T_m^{am} [K]	T_m^{xtal} [K]	T_f [K]	T_l [K]	T_{rg}
Vit101	674.0	718.7	44.7	674.0 [2)]	553	1067	1112	1139	1168	0.577
Vit101 P_1	690.5	748.7	58.2	688.7	577	1036	1113	1146	1171	0.590
Vit101 $S_{1.5}$	694.5	754.7	60.2	696.3	599	1049	1112	1144	1170	0.594
Vit105	671.4	731.1	59.7	670.3	591	1055	1071	1095	1134	0.592
Vit105 P_2	695.7	795.6	99.9	690.3	634	1068	1074	1089	1189	0.585
Vit105 S_2	691.9	769.3	77.4	690.8	603	1057	1065	1093	1295	0.534

1) for 0.333 K/s
2) T_g from standard scan without pre-treatment

Table 4.4: Characteristic enthalpy, entropy and Gibbs free energy values, as measured by DSC and DTA, or calculated from the molar heat capacity functions of the liquid and the crystal. Crystallization enthalpy upon heating ΔH_x, enthalpy of fusion ΔH_f, and entropy of fusion ΔS_f. Enthalpy ($\Delta H^{l\text{-}x}$), entropy ($\Delta S^{l\text{-}x}$), and Gibbs free energy ($\Delta G^{l\text{-}x}$) difference between the liquid and the crystal at the fictive temperature T_{fic}.

Alloy	ΔH_x [kJ g-atom^{-1}]	ΔH_f [kJ g-atom^{-1}]	ΔS_f [J g-atom^{-1} K^{-1}]	$\Delta H^{l\text{-}x}(T_{fic})$ [kJ g-atom^{-1}]	$\Delta S^{l\text{-}x}(T_{fic})$ [J g-atom^{-1} K^{-1}]	$\Delta G^{l\text{-}x}(T_{fic})$ [J g-atom^{-1}]
Vit101	7.46	11.3	9.92	6.70	4.41	3.72
Vit101 P_1	7.98	11.4	9.95	6.85	4.49	3.76
Vit101 $S_{1.5}$	6.97	10.0	8.74	5.87	3.75	3.26
Vit105	5.24	8.8	8.04	4.24	2.53	2.54
Vit105 P_2	4.82	6.9	6.34	3.15	1.76	1.94
Vit105 S_2	5.86	8.7	7.96	4.52	2.95	2.49

The enthalpy of fusion ΔH_f is approximately 8.7 kJ g-atom^{-1} for Vit105 and Vit105 S_2 and only 6.9 kJ g-atom^{-1} for Vit105 P_2, and the entropy of fusion ΔS_f of the alloys shows the same trend (compare to Table 4.4). The reduced glass transition temperature T_{rg} ranges from 0.592 for Vit105, over 0.585 for Vit105 P_2, to 0.534 for Vit105 S_2.

At this point it should be noted that for the evaluation of the data only the first heating cycle of each sample was analyzed. As described in Chapter 3.3.1, each sample was melted several times. However, the DTA melting signal changes with every melting cycle when heating to temperatures high above the liquidus temperature, as visualized in Fig. 4.6 a). There, three subsequent melting and two cooling cycles of the same sample are shown. The first heating and cooling are shown in black, the second one in red, and the third one in blue. First, it can be noted that the enthalpy of fusion decreases with every cycle, from initially 11.1 to 7.9 J g-atom^{-1} K^{-1} for the third run, even though the sample mass stays constant. Second, the initially eutectic alloy composition shows a pronounced melting shoulder in the third heating run at around 1500 K, as indicated by the blue arrow. A similar but less pronounced effect can already be observed during the second heating. The existence of this shoulder is supported by the exothermic crystallization events upon cooling between 1400 K and 1300 K, as indicated by the black and the red arrow.

These results indicate that oxidation of the alloy occurs at high temperatures, even though the measurement is performed in a high-purity Ar atmosphere, thus forming an oxygen-stabilized phase with a higher melting point [85]. Hence, the percentage of the initial alloy composition decreases, lowering the enthalpy of fusion in the initial

temperature range, and increasing the percentage of the oxygen-stabilized phase that causes the shoulder at high temperatures.

In order to confirm this assumption, the DTA sample was analyzed by XRD and SEM/EDX on a polished cross-section after the three heating and cooling cycles. The black line in Fig. 4.6 b) shows the obtained X-ray diffraction pattern of the crystalline sample. The inset in the figure shows a backscattered electron SEM image where large crystals (dark grey), with an on average lower atomic number than the remaining sample, are visible. EDX analysis of these crystals predicts an atomic composition of 54.4 at% Ti, 29.5 at% Cu or Ni, and 16.1 at% O. This ratio fits well to the oxygen-stabilized phase Ti_4Cu_2O (or Ti_4Ni_2O) which was previously found in other glass-forming alloy compositions [85,146,237]. The red line in Fig. 4.6 b) shows the X-ray diffraction pattern of Ti_4Cu_2O calculated with PowderCell 2.3 [229] according to the structural data from Ref. [238]. The diffraction peaks of the Ti_4Cu_2O phase are, among others, clearly found in the pattern of the analyzed sample, confirming the formation of this oxygen-stabilized phase.

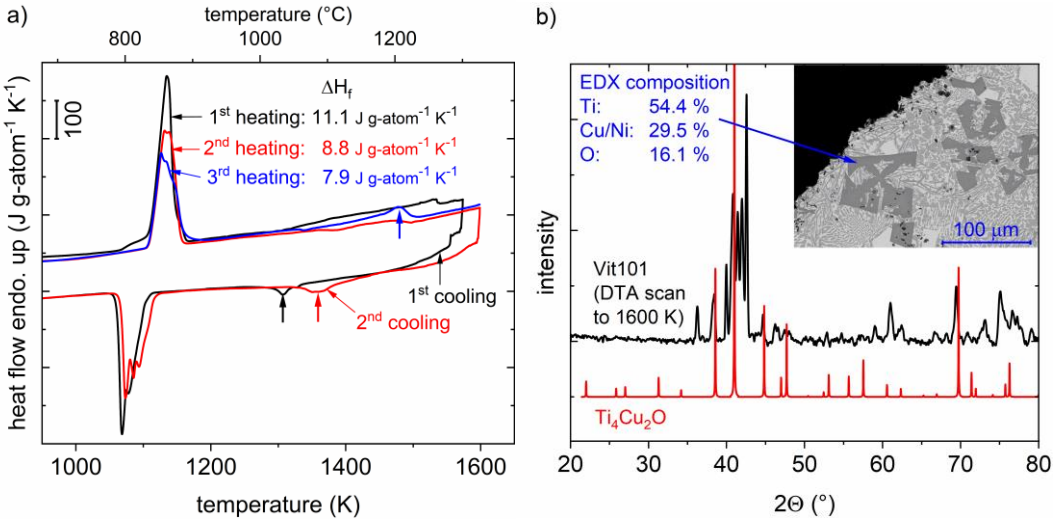

Figure 4.6: a) DTA heating and cooling curves for Vit101. The heating curves show a decreasing enthalpy of fusion in the main peak for subsequent scans of the same sample. In the third scan, a pronounced shoulder at around 1500 K becomes visible (blue arrow) and the cooling curves show an exothermic crystallization event above the nominal liquidus temperature of the alloy. **b)** X-ray diffraction pattern of the Vit101 sample after the DTA measurement (black line). The red line represents the calculated diffraction pattern of a crystalline Ti_4Cu_2O phase. The inset shows a SEM image of the same sample and the results of the EDX analysis of the indicated phase are presented.

In summary, samples of highly reactive metallic melts, containing Ti or Zr, experience oxidation during DTA measurements at temperatures several hundred degrees above the liquidus temperature. The remaining oxygen content in the high-purity Ar atmosphere is sufficient to form an oxygen-stabilized phase, e.g. Ti_4Cu_2O, with a

higher liquidus temperature. The existence of such a phase was confirmed by EDX and XRD analysis, in agreement with Refs. [85,146,237]. Consequently, for DTA measurements of highly reactive melts, only the first melting event should be evaluated, and excessive overheating should be avoided when looking at cooling curves.

4.2.2 Molar Heat Capacity and Thermodynamic Functions

In this Chapter, the results of the molar heat capacity measurements are presented and the thermodynamic functions for enthalpy H, entropy S, and Gibbs free energy G, are calculated on this basis.

The data points from the molar heat capacity measurements for the six alloy compositions are presented in Fig. 4.7 a)-f). On the left-hand side, the Vit101 alloys are shown and on the right-hand side the Vit105 alloys. For all alloys, the c_p measurements of the glassy state are displayed as red dots and the data points in the supercooled liquid state are displayed as blue circles. c_p of the crystalline sample is shown as black squares. The arrows indicate the characteristic temperatures (T_g, T_x, T_m, and T_f from Table 4.3) for each composition. The black line represents a fit of the molar heat capacity of the crystal according to Eq. 3.9, and the dashed blue line represents the liquid state according to Eq. 3.8.

No reliable c_p measurements could be performed in the stable liquid state, due to the temperature limitations of the DSC and the reactions occurring at high temperatures in the DTA. Hence, the fitting of the molar heat capacity of the liquid state needs additional data to complement the data points measured around T_g. The relation presented in Eq. 3.10 is used to roughly estimate the course of c_p in the liquid state, using the difference between the enthalpy of fusion and crystallization. The value of c_p at the liquidus temperature was assumed such, that the integral in Eq. 3.10 equals the enthalpy difference. The resulting fitting parameters for the Kubaschewski equations (Eq. 3.8 and Eq. 3.9) are written down in Table. 4.5.

The Vit101 alloys (Fig. 4.7 a), c), e)) show rather similar c_p values in the crystalline state, and Vit101 P_1 and Vit101 $S_{1.5}$ also show similar values in the glassy state. For each of these two compositions, two data points in the supercooled liquid state were obtained before crystallization occurred during the step method (compare to Chapter 3.3.4). For Vit101, the c_p curve is shifted to lower temperatures by about 20 K according to the shift in T_g. Furthermore, due to the short and unstable SCL region, no reliable data point in the SCL was obtained and a value similar to the ones for Vit101 P_1 and Vit101 $S_{1.5}$ was assumed for the fitting.

A similar situation is found for the Vit105 alloys. c_p in the crystalline and the glassy state resembles one another for the three compositions, with a shift to lower temperatures for Vit105. While for Vit105 P_2 and Vit105 S_2 several data points in the SCL region were obtained, for Vit105 only a single reliable data point in the SCL

could be measured, due to the rather short SCL region. The c_p measurements for the Vit105 alloys are shown in the Figs. 4.7 b), d), and f).

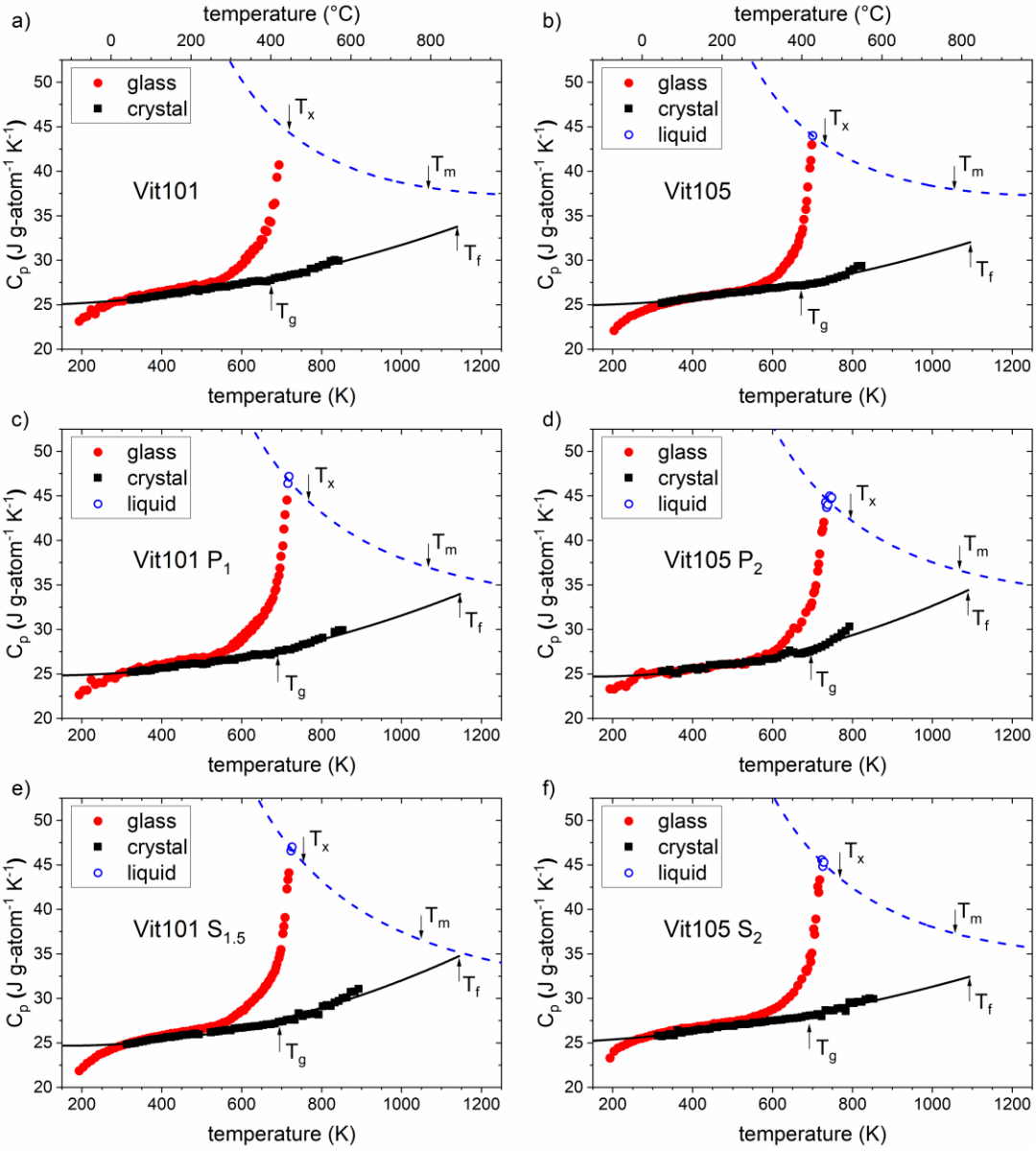

Figure 4.7: Molar heat capacity c_p in [J g-atom^{-1} K^{-1}] as measured with the DSC step method. The black squares represent the crystalline state, the red dots the glassy state, and the blue circles represent c_p values in the supercooled liquid state. The black line corresponds to a fit according to Eq. 3.9, describing c_p in the crystalline state, whereas the dashed blue line describes c_p of the liquid state (Eq. 3.8). As no c_p values are available in the stable high temperature liquid state, Eq. 3.10 was used to calculate c_p. The arrows indicate the characteristic temperatures (T_g, T_x, T_m, and T_f). In **a)**, **b)**, **c)**, **d)**, **e)**, and **f)**, the same depiction is shown for the six alloys discussed.

Table 4.5: Fitting parameters of the Kubaschewski functions (Eq. 3.8 and Eq. 3.9), describing the molar heat capacity in the liquid and the crystalline state as a function of temperature.

Alloy	**a** [$\times 10^{-3}$] [J g-atom^{-1} K^{-2}]	**b** [$\times 10^{6}$] [J g-atom^{-1} K]	**c** [$\times 10^{-3}$] [J g-atom^{-1} K^{-2}]	**d** [$\times 10^{-6}$] [J g-atom^{-1} K^{-3}]
Vit101	5.9616	7.8161	-0.1549	6.9447
Vit101 P_1	2.8887	10.1619	-1.9621	8.5986
Vit101 $S_{1.5}$	1.7231	10.8112	-3.2852	10.3694
Vit105	6.1935	7.2205	-0.8554	6.7032
Vit105 P_2	3.2428	9.3593	-3.2134	10.9324
Vit105 S_2	3.8825	9.2005	1.1879	5.1906

Based on the c_p fitting functions, describing c_p of the liquid and the crystalline state as a function of temperature, the difference in enthalpy, entropy, and Gibbs free energy between the liquid and the crystal are calculated according to Eq. 2.2, Eq. 2.3, and Eq. 2.1. The results for the six alloy compositions are plotted in Fig. 4.8, with the Vit101 alloys on the left and the Vit105 alloys on the right. The characteristic temperatures are indicated on the crystalline reference line. The horizontal dashed lines represent the enthalpic and entropic state of a glass frozen in at $q = 0.333$ K/s and the dashed arrows indicate the corresponding fictive temperature T_{fic}. Vertical double arrows indicate the enthalpy of crystallization and the enthalpy and entropy of fusion. The values for the Enthalpy ($\Delta H^{l\text{-}x}$), entropy ($\Delta S^{l\text{-}x}$), and Gibbs free energy ($\Delta G^{l\text{-}x}$) difference between the liquid and the crystal at T_{fic} are given in Table 4.4.

Figure 4.8 a) and b) show the enthalpy difference $\Delta H^{l\text{-}x}$ between the liquid and the crystal. In general, the liquids (and the glasses) of the Vit101 alloys are in a higher enthalpic state than the ones of the Vit105 alloys, as they show a higher crystallization enthalpy and enthalpy of fusion. The enthalpy of fusion defines the enthalpy difference at the temperature of fusion T_f, whereas the crystallization enthalpy defines it at the crystallization temperature T_x. Vit101 and Vit101 P_1 have a very similar course of their enthalpy curve, whereas Vit101 $S_{1.5}$ lies a bit lower. For the Vit105 alloys, Vit105 P_2 lies below the other two compositions, which behave very similarly.

The difference in entropy $\Delta S^{l\text{-}x}$ between the liquid and the crystal is presented in Fig. 4.8 c) and d). The relations between the alloy compositions are similar to the ones for $\Delta H^{l\text{-}x}$. The temperature at which $\Delta S^{l\text{-}x}$ vanishes defines the Kauzmann temperature T_K (compare to Chapter 2.1.1), where the glass transition needs to occur at latest from a thermodynamic point of view. The Kauzmann temperatures of all compositions are given in Table 4.3.

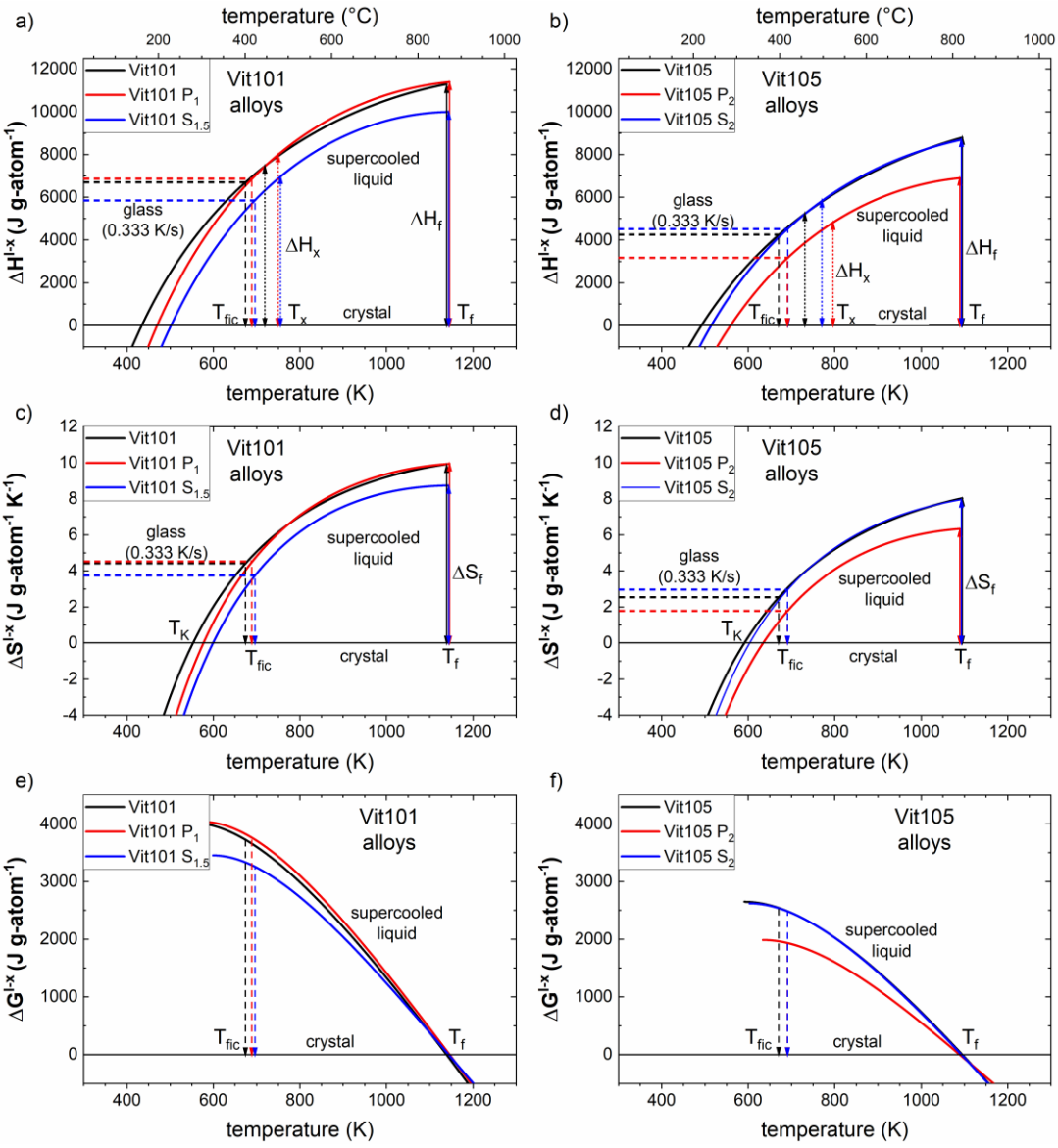

Figure 4.8: Thermodynamic functions of the supercooled liquid with respect to the crystalline state as a function of temperature. **a), b)** Enthalpy $\Delta H^{l\text{-}x}$, **c), d)** Entropy $\Delta S^{l\text{-}x}$, **e), f)** Gibbs free energy $\Delta G^{l\text{-}x}$, with the Vit101 alloys being displayed on the left and the Vit105 alloys on the right. The characteristic temperatures are indicated on the crystalline reference line. The horizontal dashed lines represent the enthalpic and entropic state of a glass frozen in at q = 0.333 K/s. Vertical double arrows indicate the enthalpy of crystallization and the enthalpy and entropy of fusion.

The Gibbs free energy difference between the liquid and the crystal, $\Delta G^{l\text{-}x}$, is presented in Fig. 4.8 e) and f). $\Delta G^{l\text{-}x}$ correlates with the driving force for crystallization and increases upon undercooling a melt. For many glass-forming alloy systems, a low $\Delta G^{l\text{-}x}$ corresponds to a higher glass-forming ability (GFA) within the same alloy family [92]. Hence, good glass-formers tend to show a smaller value for $\Delta c_p{}^{l\text{-}x}$ and ΔS_f, where the latter one is the slope of the $\Delta G^{l\text{-}x}$ curve at T_f [239]. A small entropy of fusion indicates a small amount of free volume and a pronounced short range order in the liquid [45].

The Vit101 alloys all show a higher $\Delta G^{l\text{-}x}$ value around the fictive temperature than the Vit105 alloys (see Table 4.4), which is roughly in line with the lower GFA of the Vit101 alloys. Within the Vit101 alloys, Vit101 $S_{1.5}$ shows the smallest difference in Gibbs free energy, which correlates well with its slightly higher GFA or critical casting thickness. This trend cannot be confirmed for the Vit105 alloys, where Vit105 P_2 displays the lowest $\Delta G^{l\text{-}x}$ value while at the same time it has the lowest GFA. However, $\Delta G^{l\text{-}x}$ can only be used as a rough estimate of the GFA, as other factors like the primary crystallizing phase and the kinetics of the alloy also determine its GFA. Hence, these results might suggest a change in the primary crystallizing phase for the Vit105 P_2 composition, causing the reduced GFA.

4.3 TTT-Diagrams

Time-temperature-transformation (TTT) diagrams are typically used to visualize the temperature dependence of transformation times, e.g. the time to crystallization as a function of temperature in a metallic glass-forming melt. In this Chapter, isothermal TTT diagrams are presented for the low temperature regime above the glass transition temperature (compare to Chapter 3.3.3). This data is especially valuable for thermoplastic forming experiments, as will be presented in Chapter 6.

The isothermal TTT diagrams for the six alloy compositions are shown in Fig. 4.9. The Vit101 alloys are on the left and the Vit105 alloys on the right, all on the same scale. The black triangles pointing to the right represent the 1 % crystallization transformation, the black squares the 50 % transformation, and the black triangles pointing to the left the 99 % transformation[5]. Red dots are used to indicate the peak position of the crystallization peak in the isothermal DSC heat flow curve. In the case of Vit105, two different dots are used, corresponding to the two crystallization events. The insets show the heat flow curve of a single measurement, always displaying the curve of the temperature where the main crystallization peak is located roughly at 500 s. The same symbols as in the main plot are used to indicate the crystallization transformation percentages for this temperature, as determined from the integration of the heat flow.

[5] The „%“ of transformation correspond to the percentage of crystallization enthalpy released up to the corresponding time.

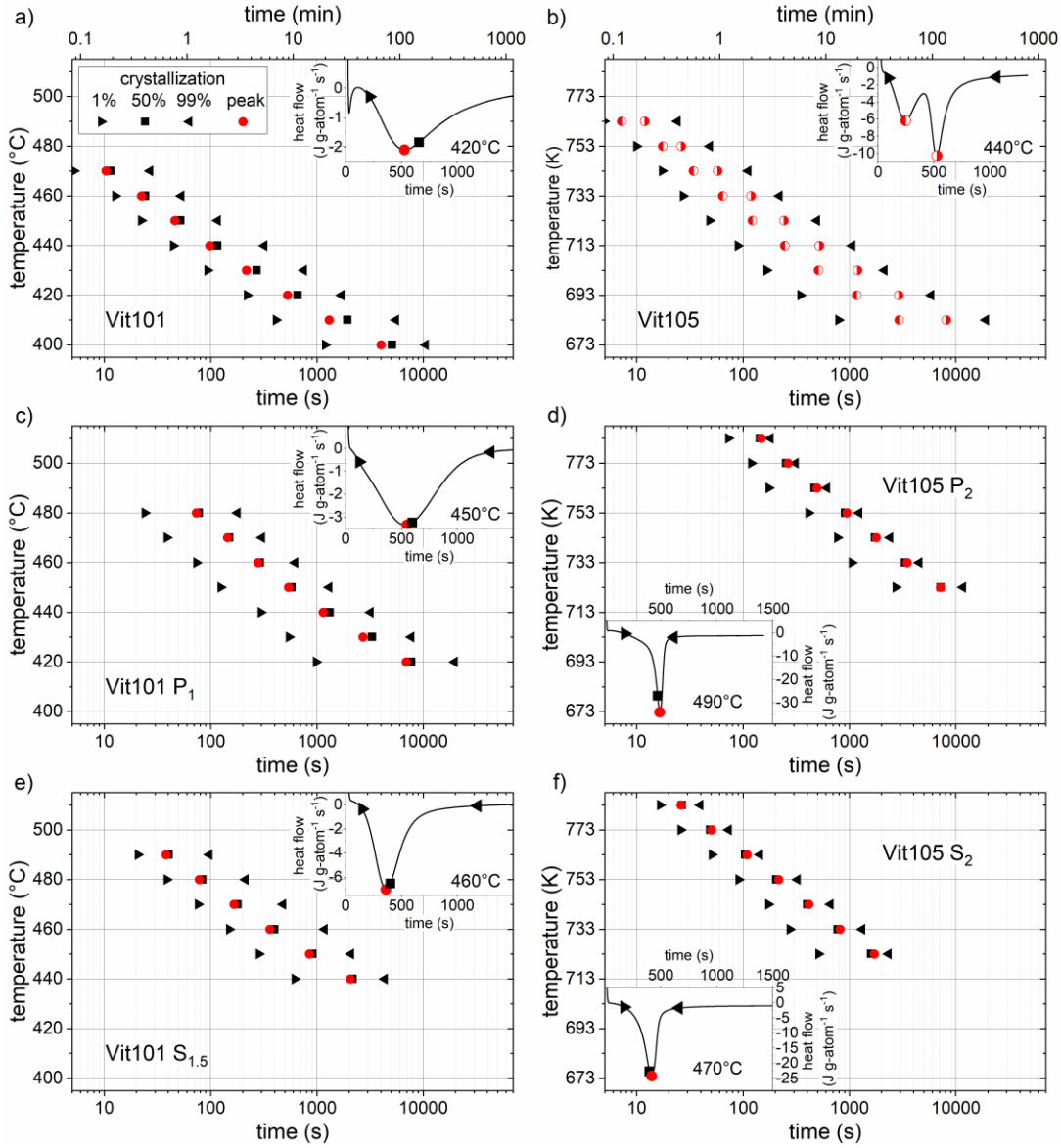

Figure 4.9: Isothermal TTT diagrams. The black symbols indicate the 1 % (►), the 50 % (■), and the 99 % (◄) crystallization transformation and the red dot represents the peak position of the main crystallization peak. The insets show the heat flow curve of a single measurement and the same symbols are used to indicate the crystallization transformation for this temperature. **a)**, **c)**, and **e)** show the Vit101 alloys and **b)**, **d)**, and **f)** the Vit105 alloys, all on the same time and temperature scale.

For the Vit101 alloys (Fig. 4.9 a), c), e)), the TTT diagrams show that Vit101 crystallizes at lower temperatures and/or shorter times than its modifications with minor additions. Vit101 P_1 and Vit101 $S_{1.5}$ show a similar crystallization behavior with the main crystallization peak occurring at the same times for the same temperatures. However, it should be noted that Vit101 $S_{1.5}$ shows a temporally much sharper

crystallization peak, thus causing the 1 % crystallization to happen closer to the main peak and shifting the onset of crystallization to longer times in comparison to the Vit101 P_1 composition.

Vit105 (Fig. 4.9 b)) shows a different crystallization behavior than its modifications. Crystallization takes place in two separated events, as indicated by the half-filled red dots. The first event starts without a noticeable incubation time when the isothermal temperature is reached, indicating a low thermal stability of the alloy upon heating. Crystallization is shifted to lower temperatures and/or times than in the modified compositions. Vit105 S_2 and Vit105 P_2 only show a single sharp crystallization event. Hence, the minor additions of P and S suppress or at least delay the first crystallization event observed in Vit105 and significantly increase the thermal stability. Comparing the two micro-alloyed Vit105 compositions, Vit105 S_2 crystallizes at shorter times than Vit105 P_2. At the same temperature, crystallization in the P-containing alloy only starts after it is already finished in Vit105 S_2.

The results of the TTT diagrams are in good agreement with the previously measured DSC scans with a constant heating rate, shown in Fig. 4.4. There, a first estimate of the thermal stability of the alloys was provided by the length of the SCL (ΔT_x), given in Table 4.3. A DSC scan with a constant heating rate represents a specific line profile in the TTT diagram that cannot provide the whole time and temperature information, however, allows a quick estimate of the thermal stability of an alloy. As in the TTT diagram, Vit101 P_1 and Vit101 $S_{1.5}$ show almost the same ΔT_x value, 15 K higher than the one of Vit101. For the Vit105 alloys, ΔT_x increases from 60 K for Vit105 up to 100 K for Vit105 P_2 in the same order as the crystallization times increase in the TTT diagram.

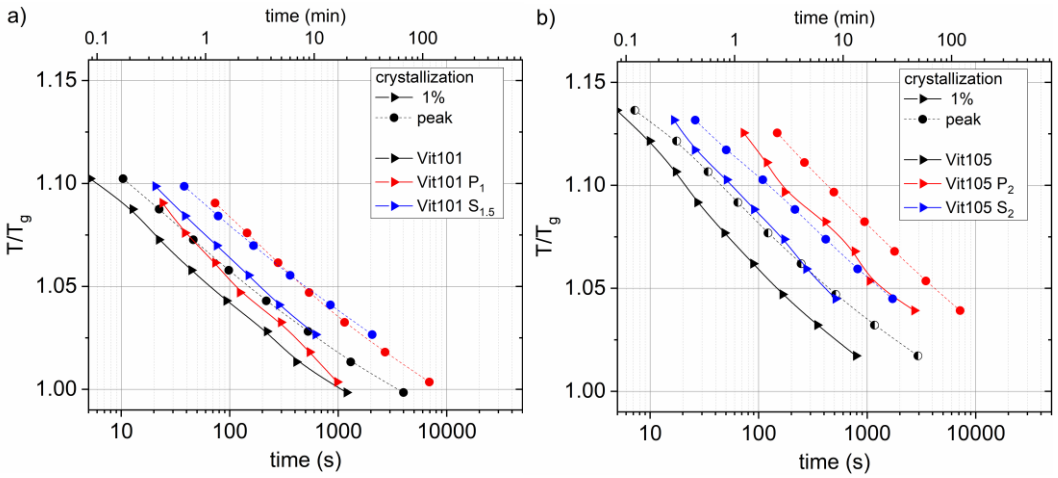

Figure 4.10: T_g-scaled isothermal TTT diagrams. The 1 % (►) crystallization transformation is shown as solid line and the peak of the crystallization event as round dots (●), connected with a dashed line. The base alloy is shown in black, the P-containing alloy in red, and the S-containing alloy in blue. **a)** Vit101 alloys. **b)** Vit105 alloys.

Figure 4.10 shows the isothermal TTT diagrams on a T_g-scaled temperature axis. The T_g-scaling allows a better comparison of the alloys, especially regarding their estimated viscosity, as at T_g a viscosity of about 10^{12} Pa s can be assumed. Hence, this depiction is advantageous when evaluating the thermoplastic formability of an alloy. The topic of thermoplastic formability, also in connection with measured viscosity data (see Chapter 4.4), will be discussed later on in Chapter 6.

Figure 4.10 a) confirms the results previously discussed for the Vit101 alloys, even on a T_g-adjusted temperature scale. The thermal stability, or rather the time till the onset of crystallization, increases from Vit101 over Vit101 P_1 to Vit101 $S_{1.5}$. The Vit105 alloys all show a higher thermal stability, with Vit105 being the least stable alloy in this family. Vit105 S_2 has a much higher thermal stability and Vit105 P_2 again is significantly more stable. Only based on this information, the thermoplastic formability of these alloys is supposed to increase from Vit101 to Vit105 P_2 in the previously discussed order.

4.4 Viscosity and Fragility around T_g

In this Chapter, viscosity and its temperature dependence around the glass transition, thus the kinetic fragility of the alloy, are assessed. In order to complete the picture of kinetic fragility, the viscosity measurements are supplemented by the temperature dependence of the transition times obtained from the T_g-shift measurements. Later on, in Chapter 4.7, the kinetic fragility around T_g will be discussed in relation to the fragility at high temperatures in the stable liquid. Furthermore, the viscosity values together with the TTT diagrams from the previous chapter will be connected to the thermoplastic deformation experiments in Chapter 6.

The results of the isothermal three-point beam bending (3PBB) viscosity measurements in the thermomechanical analyzer (TMA) around the glass transition for the six alloy compositions are shown in Fig. 4.11. Viscosity is shown on a logarithmic scale as a function of time during the relaxation process, where the glass relaxes into the metastable supercooled liquid state. A time of zero seconds corresponds to the start of the isothermal holding after the initial heating phase. The measurement curves are color-coded from blue to red for increasing temperatures and the temperature values are written next to the curves. The dashed black lines represent the KWW fits (compare to Eq. 2.6) that are used to determine the equilibrium viscosity value.

Here, it should be noted that the Vit101 and Vit105 alloys exhibit deviations from the equilibrium viscosity for higher temperatures and longer annealing times, as also reported in Refs. [44,63]. This behavior can be observed in Fig. 4.11 when viscosity increases quicker as predicted by the stretched exponential KWW function. The phenomenon is caused by phase separation and/or primary crystallization in the supercooled liquid region [240–243]. For the KWW fitting, only the data points up to the onset of crystallization, as roughly estimated by the TTT diagrams, are used.

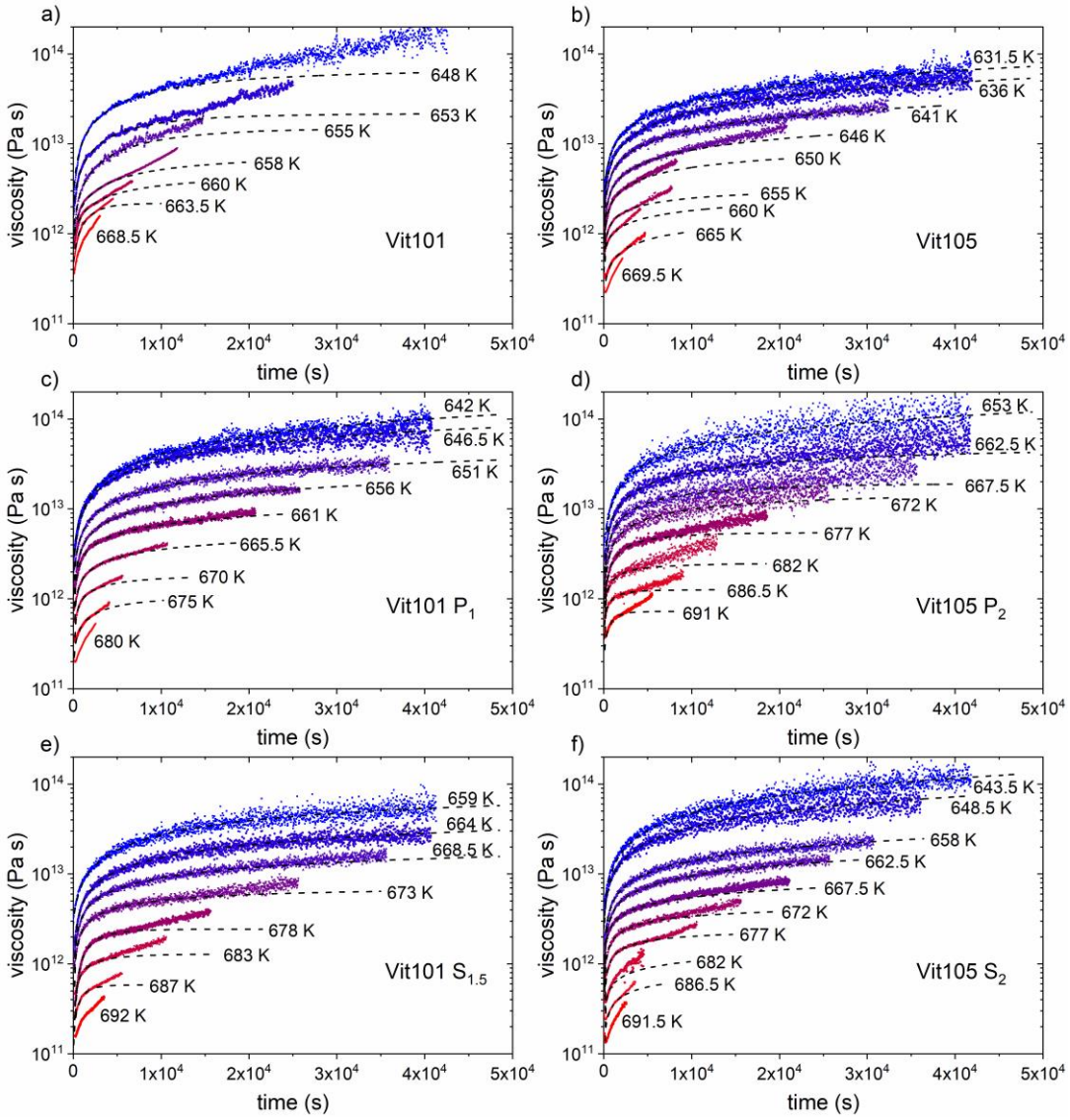

Figure 4.11: Viscosity values from isothermal three-point beam bending (3PBB) measurements around T_g. Viscosity is shown as a function of time during the relaxation process. The measurement curves are color-coded from blue to red for increasing temperatures and the temperature values are written next to the curves. The dashed black lines represent the KWW fits (compare to Eq. 2.6) used to determine the equilibrium viscosity value. **a)**, **c)**, and **e)** show the Vit101 alloys and **b)**, **d)**, and **f)** the Vit105 alloys, all on the same time and viscosity scale.

The resulting equilibrium viscosity values are shown later in Fig. 4.13 when the temperature dependence of viscosity is discussed.

A complementary way to assess the kinetic fragility of an alloy are the T_g-shift measurements (see Chapter 3.3.2) that provide the transition times of the system as a function of temperature, according to Equation 3.5. The measurement curves of the T_g-shift experiments are depicted in Fig. 4.12.

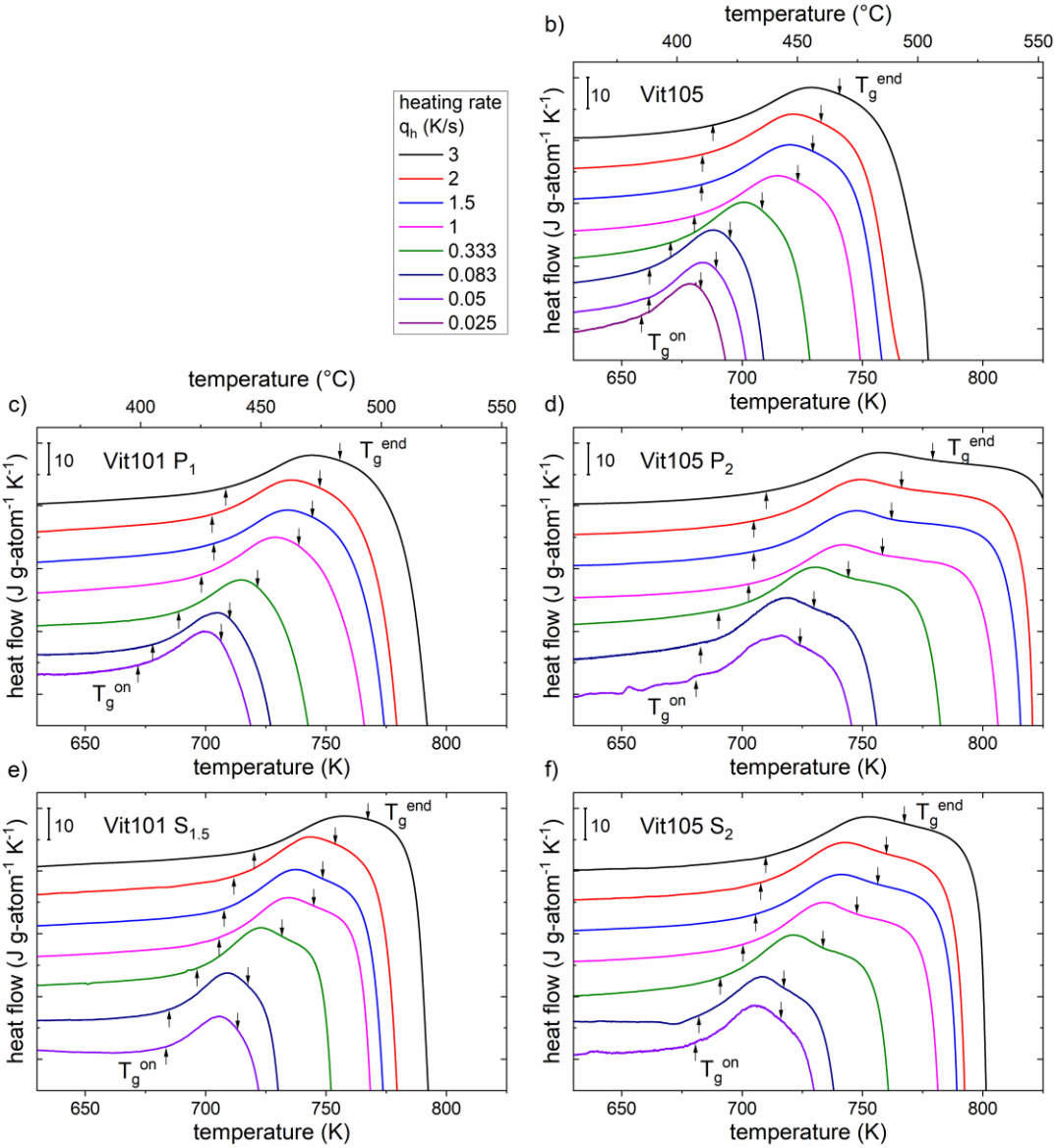

Figure 4.12: DSC scans from T_g-shift experiments, resulting from the heating after the pretreatment and after baseline subtraction. Scans for heating rates between 0.025 and 3 K/s are shown in different colors. T_g^{on} and T_g^{end}, used to calculate ΔT_g, are indicated by arrows. **c)**, and **e)** show Vit101 P_1 and Vit101 $S_{1.5}$, respectively. Vit101 could not be analyzed by this method due to the small SCL region and the onset of crystallization during the pretreatment. **b)**, **d)**, and **f)** show the Vit105 alloys.

The presented DSC scans correspond to the heating after the pretreatment and after baseline subtraction (compare to scan (3) in Fig. 3.3). Scans for heating rates between 0.025 and 3 K/s are shown, all on the same temperature scale. As the pretreatment requires a rather stable SCL region to avoid decomposition and crystallization during the pretreatment, T_g-shift measurements could not be performed for Vit101, the composition with the smallest SCL region. For all other alloy compositions, the experiments could be performed successfully. The onset of the glass transition T_g^{on} and the end of the glass transition T_g^{end}, used to calculate ΔT_g, are indicated by arrows. A clear shift of both values to higher temperatures can be observed for increasing heating rates. The calculated transition times τ_{trans} are shown as blue dots in Fig. 4.13.

As mentioned, Fig. 4.13 shows the isothermal equilibrium viscosity values from the 3PBB experiments as black squares and the transitions times from the T_g-shift experiments as blue dots, both on the same temperature scale. The equilibrium viscosity values are fitted by the VFT equation (see Eq. 2.9) which is shown as dashed black line and the obtained fitting parameters are summarized in Table 4.6. The parameters D* and T_0 are also written into the figure. The grey line represents viscosity as measured by 3PBB in a scan with a continuous heating rate of q_h= 0.333 K/s. Additionally, a DSC scan with the same heating rate is shown below as a temperature reference and T_g and T_x are indicated.

For all alloys, the isothermal equilibrium viscosity values align well with the VFT fit, not showing significant outliers. The infinite temperature limit of viscosity η_0, is calculated according to Eq. 2.10 and was fixed for each VFT fit. The errors of the fitting parameters D* and T_0 from the VFT fits are given (±) in Table 4.6.

The transition times τ_{trans} from the T_g-shift measurements can be converted into viscosity (η) values according to the relation $\eta = G_{\tau-\eta} \cdot \tau_{trans}$ (compare to Eq. 2.8). The obtained values for the proportionality constant $G_{\tau-\eta}$ are given in Table 4.6. This conversion determines the alignment of the transition time axis with respect to the viscosity ordinate. It can be seen that the temperature dependence of the transition times corresponds very well to the VFT fit obtained from the viscosity values. Due to the nature of the transition time measurements, the obtained datapoints reach to higher temperatures than the equilibrium viscosity measurements, confirming the course of the viscosity values predicted by the VFT fit.

At even higher temperatures, when the system reaches the metastable equilibrium above T_g^{end} (not indicated in the DSC scan) during a scan with a constant heating rate, the VFT fit also aligns well with the viscosity data from the continuous scan, supporting the accuracy of the VFT fit. Around T_x, a sudden increase of viscosity in the scan can be observed, as can be expected when crystallization occurs. This verifies the temperature calibration of the TMA. For Vit105 P_2 and Vit105 S_2, the alloys with the largest SCL, a stepwise increase of viscosity is observed before crystallization occurs. This step is related to the deflection limit of the TMA device, when the sample touches the bottom of the sample holder and does not imply a real increase in viscosity.

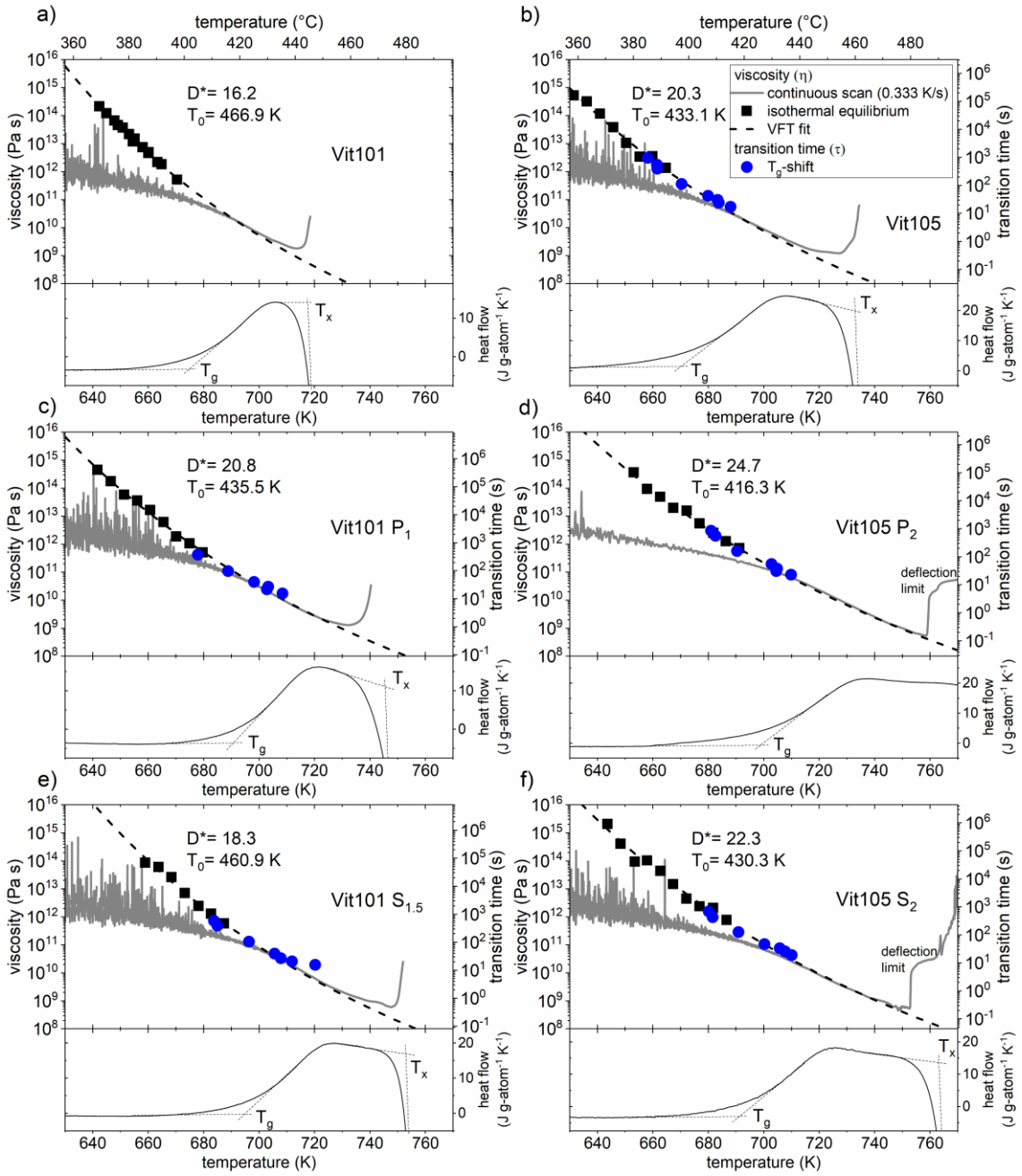

Figure 4.13: Viscosity and transition time as a function of temperature. Black squares indicate equilibrium viscosity values which are fitted with the VFT equation (dashed black line). The grey line results from a viscosity scan with a constant heating rate of 0.333 K/s, and below, a DSC scan with the same heating rate is shown as reference. The blue dots are transition times obtained from T_g-shift experiments. **a)**, **c)**, and **e)** show the Vit101 alloys and **b)**, **d)**, and **f)** the Vit105 alloys, all on the same temperature and viscosity scale.

Table 4.6: VFT fitting parameters and related values. Fragility parameter D*, VFT temperature T_0, infinite temperature limit of viscosity η_0, fragility index m, kinetic glass transition temperature T_g*, and the proportionality factor ("shear modulus") between relaxation time and viscosity $G_{\tau-\eta}$. For D* and T_0 the errors of the VFT fitting are also presented (±).

Alloy	D*	T_0 [K]	η_0 [10^{-5} Pa s]	m	T_g* [K]	$G_{\tau-\eta}$ [MPa]
Vit101	16.19 ± 1.04	466.86 ± 8.66	4.419	54.38	667.6	
Vit101 P_1	20.76 ± 0.95	435.53 ± 6.65	4.395	46.03	675.6	1.12
Vit101 $S_{1.5}$	18.26 ± 1.56	460.90 ± 12.19	4.374	50.12	684.3	1.24
Vit105	20.33 ± 1.76	433.11 ± 12.25	3.585	47.09	665.6	3.22
Vit105 P_2	24.76 ± 1.40	416.30 ± 8.83	3.567	41.60	688.5	3.55
Vit105 S_2	22.34 ± 1.72	430.31 ± 11.50	3.558	44.34	684.1	2.27

For a better comparison of the temperature dependence of viscosity or rather the kinetic fragility of the different alloys, all VFT fits are plotted together as a function of inverse temperature scaled to T_g* in Fig. 4.14. T_g* corresponds to the kinetic glass transition temperature, where an equilibrium viscosity of 10^{12} Pa s is reached. In this depiction, commonly known as the "Angell plot", all curves coincide at the temperature T_g* and the viscosity 10^{12} Pa s. The curves showing a steeper slope at T_g* are kinetically more fragile than the more gently inclined ones. The T_g*-values for all alloys are also given in Table 4.6.

In Fig. 4.14 it can be seen that for both, the Vit101 and the Vit105 families, the base alloys show the most fragile behavior, whereas the P-containing alloys are the strongest ones. For the Vit101 family, the kinetic fragility parameter D* increases from 16.2 for Vit101, over 18.3 for Vit101 $S_{1.5}$ to 20.8 for Vit101 P_1. For the Vit105 family, D* increases from 20.3 for Vit105, over 22.3 for Vit105 S_2 to 24.8 for Vit105 P_2. Besides the D* values, the m-fragility values (compare to Eq. 2.12) are also given in Table 4.6.

Commonly, a kinetically stronger behavior is associated with a higher GFA due to more sluggish kinetics throughout the entire SCL region [47,92]. However, for the Vit105 alloy family this relation obviously does not hold true, with Vit105 P_2 showing the kinetically strongest behavior while having the lowest GFA. This observation will further be discussed in Chapter 4.7, where other aspects like the primary crystallizing phase, heterogeneous nucleation, or the presence of a liquid-liquid transition will be considered.

On the other hand, the kinetic fragility of the alloys correlates well with the length of the SCL region ΔT_x upon heating from the glassy state. For example, in the Vit105 family, ΔT_x increases from 59.7 K for Vit105, over 77.4 K for Vit105 S_2 to 99.9 K for Vit105 P_2. This behavior indicates that the more sluggish kinetics upon heating delay the beginning of the crystallization process and hence increase the thermal stability.

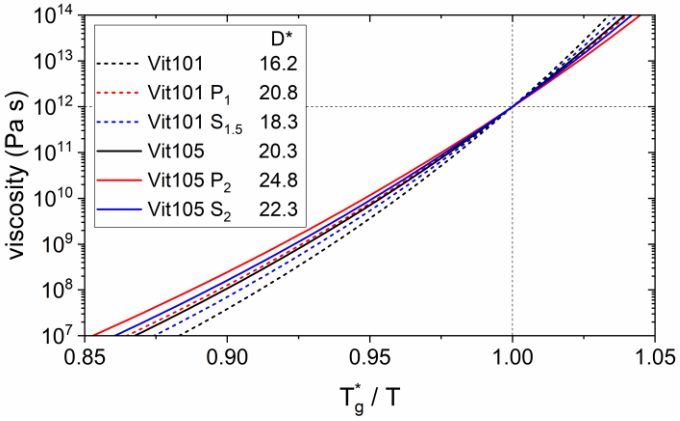

Figure 4.14: "Angell plot" – viscosity as predicted by the VFT fits, shown on an inverse temperature axis scaled to the kinetic glass transition temperature T_g*. Kinetic fragility corresponds to the slope of the VFT fit at T_g* (see m-fragility) where curves with a steeper slope are kinetically more fragile than the more gently inclined ones.

4.5 High-Temperature Viscosity

The results and implications of the high-temperature viscosity measurements are presented and discussed in this chapter. Couette rotating concentric cylinder rheometer measurements were performed for all alloys. First, results from different measurement procedures are exemplarily presented and compared for Vit105 S_2, and then viscosity data for all compositions are shown.

A representative temperature profile for a single viscosity measurement experiment is presented in Fig. 4.15, where the black line shows the temperature and the blue line the motor rotation speed in Hz. Initially, the sample is heated, melted, and the bob is lowered into the melt at the end of the heating phase (1). Phase (2) represents the first measurement phase, where viscosity is measured during cooling and heating with a rate of q = 0.333 K/s, first in counterclockwise direction (ccw, 5 Hz), and then in clockwise direction (cw, -5 Hz). The two cooling and heating cycles provide the same information and are simply used to verify the reproducibility of the measurement, also regarding the cw and ccw rotation direction. During phase (3), viscosity is measured in cooling and the minimum temperature is chosen such that the onset of crystallization is observed. When viscosity increases drastically due to the onset of crystallization, the sample is again quickly heated to the starting temperature. In

phase (4), isothermal measurements with different motor rotation speeds and hence different shear rates between 274 s^{-1} and 456 s^{-1} are performed at three isothermal temperatures. Phase (5) corresponds to free cooling experiments where a constant shear rate is applied, and phase (6) is the final free cooling of the melt where the recalescence during solidification of the alloy can be observed (compare to the right part of Fig. 4.15).

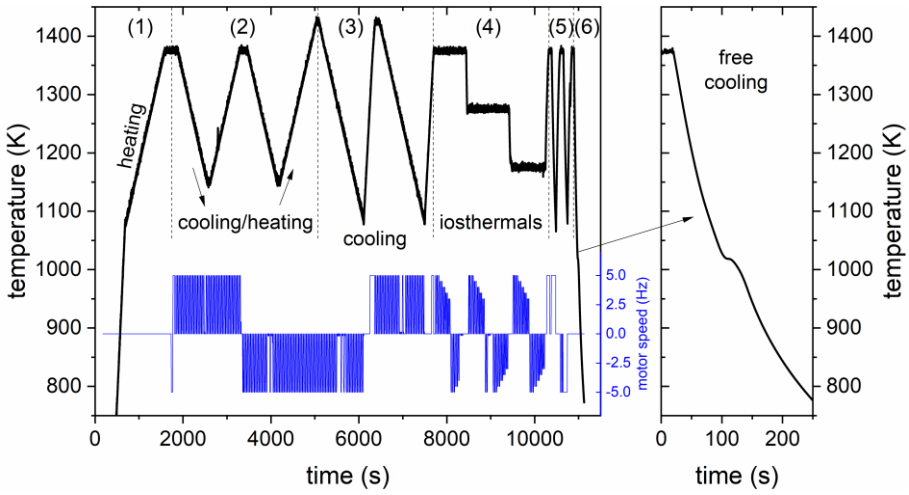

Figure 4.15: Typical temperature profile of a Couette rotating concentric cylinder viscosity measurement experiment. The black line shows the temperature and the blue line the motor rotation speed in Hz. The experiment consists of 6 phases ((1) to (6)) where different temperature and shearing profiles are applied. The right part of the figure shows the final free cooling of the melt after the measurement.

The full range of results from the different measurement phases are exemplarily shown for the Vit105 S_2 alloy composition. Figure 4.16 a) displays all data points obtained during phase (2) and (3). This includes the first cooling and subsequent heating in both counterclockwise and clockwise direction, as well as the second cooling cycle in both directions during phase (3). The viscosity data points of all six measurements coincide perfectly, demonstrating the reproducibility of the measurement. This proves that viscosity does not change over time and that no reactions occur that interfere with the measurement. While the data points obtained in phase (2) only reach down to around 1150 K, the points measured in phase (3) reach down to 1100 K, where the onset of crystallization is observed, and viscosity increases drastically.

Figure 4.16 b) shows the results of the free cooling viscosity measurements in phase (5) as black dots. As a reference, viscosity values from Fig. 4.16 a) with a controlled cooling rate of q = 0.333 K/s are also shown. The blue line indicates the cooling rate during free cooling. Initially, a cooling rate of 4.5 K/s is measured at high temperatures, which decreases down to 2.5 K/s before the onset of crystallization at around 1100 K.

At high temperatures, the viscosity data from the free cooling measurement perfectly coincides with the reference values. However, at around 1240 K, a sudden stepwise and reproducible increase of viscosity is observed. On closer examination, the reference data points also show a change in slope at roughly 1200 K which could be attributed to the same event. Considering that the temperature is already below the liquidus temperature, the increase in viscosity could be explained by the onset of crystallization of the primary crystallizing phase. The sharp increase in viscosity at 1100 K then corresponds to the main crystallization event, as also observed in the reference data.

Without further investigations, the increase in viscosity cannot certainly be attributed to crystallization effects. However, in Chapter 4.6.2 the crystallization behavior upon cooling during levitation is investigated by in-situ synchrotron X-ray diffraction experiments. In Chapter 4.7, the results of the diffraction experiments and the viscosity measurements are combined, supporting the picture of an increase in viscosity due to the beginning of crystallization.

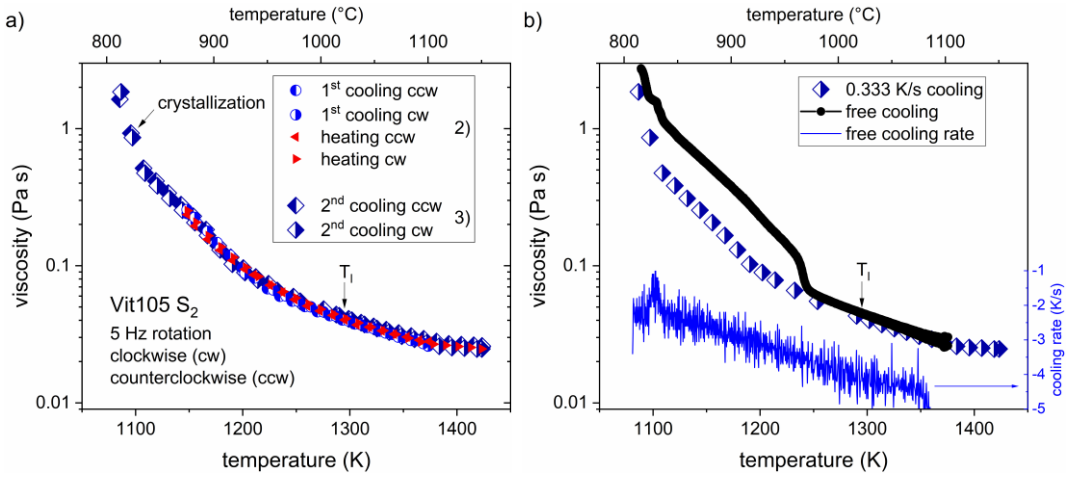

Figure 4.16: a) Viscosity of Vit105 S_2 as a function of temperature. Six different measurement runs of the same experiment are shown, including cooling and heating procedures in counterclockwise (ccw) and clockwise (cw) direction, all with a motor rotation frequency of 5 Hz. The data points from all measurement runs coincide perfectly. **b)** Data from a free cooling viscosity measurement (black) and one dataset from a) as a reference. The blue line indicates the cooling rate during free cooling.

The results of the isothermal viscosity measurements during phase (4) are displayed in Fig. 4.17. Measurements were performed at 1373 K (1100 °C), 1273 K (1000 °C), and 1173 K (900 °C), with the isothermal holding time being roughly 15 min for each temperature. Figure 4.17 a) shows the isothermal viscosity values as a function of shear rate, with shear rates between 274 s^{-1} and 456 s^{-1}, corresponding to a motor rotation frequency between 3 Hz and 5 Hz. The results prove that viscosity in this system is independent of the shear rate and that no shear thinning is observed. This is in agreement with the observations of Evenson et al. for Vit101 and Vit105 [63].

Earlier works on Vitreloy 1 found shear thinning slightly above the liquidus temperature [244]. This effect was attributed to a pronounced short- and medium-range order above T_l which can be destroyed by mechanical shearing and an increase in temperature. This transition from a more ordered state to a less ordered one is accompanied by a transition from a kinetically strong to a kinetically fragile state, and also includes a rapid change in viscosity [62].

Figure 4.17 b) displays the data points of the isothermal viscosity measurements on a temperature scale, together with the reference data from Fig. 4.16. The measurements coincide very well, with only the data points at 1173 K showing a minor deviation to higher values from the reference points. If the theory of a beginning crystallization of the primary crystallizing phase below 1200 K holds true, a prolonged isothermal treatment at 1173 K could cause a slight increase in viscosity, above the value reached during continuous cooling.

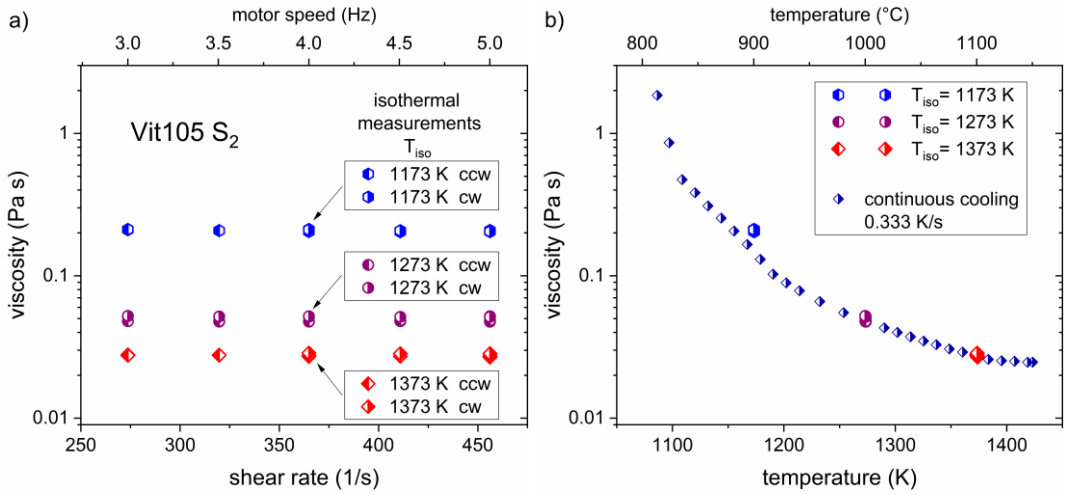

Figure 4.17: Isothermal viscosity measurements of Vit105 S_2 at three temperatures. **a)** Viscosity as a function of shear rate. **b)** Results of the isothermal measurements in reference to the continuous cooling experiments with a rate of q = 0.333 K/s.

While the different viscosity measurement procedures were only discussed for Vit105 S_2, they were performed for all alloys. The obtained results are in good agreement with the ones for Vit105 S_2, thus not making it reasonable to display all measured curves. In the investigated systems, viscosity is found to be independent of the shear rate or the measurement time. Hence, only one single, representative viscosity measurement curve for each alloy is shown in Fig. 4.18 a) and b). The same data is also shown in the appendix in Fig. A1 on a linearly scaled plot.

The melt viscosity values for the Vit101 family are shown in Fig. 4.18 a). The liquidus temperature of each composition is indicated by an arrow. The alloys show a relatively low melt viscosity of roughly 30 mPa s at T_l. Many other Zr- and also Fe-based bulk metallic glass-forming alloys show a viscosity of above 100 mPa s at T_l [63,66]. However, the viscosity data points for Vit101 coincide very well with literature data

from Jonas [245]. These values were obtained from electrostatic levitation (ESL) measurements based on the oscillating drop technique. The fact that the Couette measurements are confirmed by a completely different measurement technique is a strong argument for their validity. The compositions Vit101 and Vit101 $S_{1.5}$ display almost the exact same viscosity behavior and no influence of the minor sulfur additions on viscosity are visible. Vit101 P_1 has a slightly higher viscosity when approaching the liquidus temperature upon cooling.

Figure 4.18 b) shows the viscosity of the Vit105 alloys. As for Vit101, the viscosity of Vit105 coincides perfectly with the ESL literature values of Jonas [245]. Vit105 has a viscosity of around 120 mPa s at T_l, which resembles other Zr-based glass-forming liquids and is significantly higher than the value found for Vit101. At high temperatures, Vit105 S_2 shows very similar values as Vit105, however below the previously discussed change in slope at around 1200 K, the viscosity of Vit105 S_2 increases more quickly as the one of Vit105 upon cooling. Vit105 P_2 shows a steeper increase of viscosity upon cooling throughout the whole temperature range, resulting in slightly higher viscosity values. There, the main crystallization event starts shortly below the liquidus temperature, resulting in a rapid increase in viscosity.

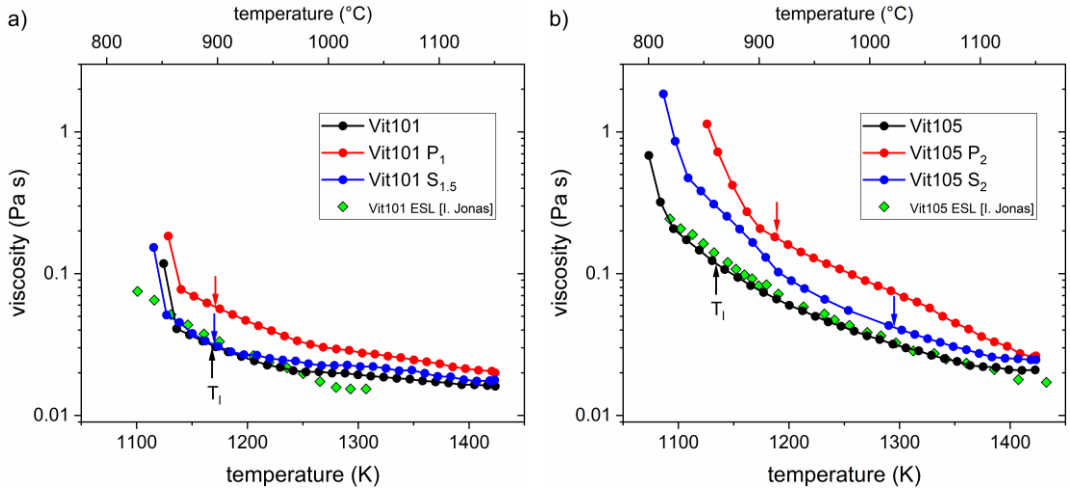

Figure 4.18: High-temperature viscosity as measured in rotating concentric cylinder experiments. The green diamonds represent viscosity reference values from ESL measurements of Vit101 and Vit105 (data taken from Ref. [245]). The DTA liquidus temperature T_l of each composition is indicated by an arrow. **a)** Vit101 alloys. **b)** Vit105 alloys.

While for Vit101 $S_{1.5}$ and Vit105 S_2 additional in-situ synchrotron X-ray diffraction experiments upon cooling during levitation are available to resolve the crystallization behavior, these experiments could not be performed for the P-containing alloys due to the scarce synchrotron beamtime. Therefore, it cannot completely be ruled out that the steeper increase in viscosity upon cooling results from crystallization. An earlier onset of crystallization of the primary phase could possibly be invisible by calorimetric methods (DTA), if the percentage of enthalpy of fusion is very small.

With the viscosity data having been presented, some additional comments on the high-temperature viscosity measurements should be made, especially regarding crucible reactions and the purity of the measurement environment. The presented measurements were all performed in Sigrafine® R6710 [246] isostatically pressed graphite with a very low porosity, reducing the infiltration of the crucible by the melt. Earlier works of Way et al. [62] and Evenson [63] et al. revealed the formation of a passivating ZrC layer at the interface between the melt and the crucible. The diffusion length through such a layer was estimated to be around 1.85 µm for a measurement of 8 h [208]. The formation of a ZrC layer was also confirmed by SEM investigations of Schroers et al. [247] and Choi-Yim et al. [248]. The invariance of the viscosity measurement results throughout different measurement runs over many hours finally proofs the suitability of the chosen crucible material for the analysis of Zr- and or Ti-containing alloys. Related experiments on different alloy compositions, which are not part of this work, showed that this invariance is not always given, and that the selection of an adequate crucible material is an important task in Couette viscosity measurements.

Another important factor is the purity of the measurement environment, considering that the reactive melt is kept at high temperatures for several hours. In the case of a contamination of the gas atmosphere with oxygen, an influence on the viscosity data could be suspected. This risk is minimized by manufacturing the crucible shafts out of titanium, which is kept at high temperatures during the measurement, acting as an oxygen getter. For Vit101 and Vit105, the solidified sample material was cut out of the crucible after the measurement and suction cast into rods with a diameter of 5 mm. The DSC analysis of both samples proved them to be amorphous and display the same heat flow scan as high-purity reference samples. Hence, the GFA of the samples was not deteriorated by the Couette viscosity measurements.

In the context of the strong-fragile transition observed in Vitreloy 1 [62], Way et al. reported a difference in viscosity between initially crystalline and initially amorphous samples. The crystalline material showed a lower viscosity upon heating, before, above a certain threshold temperature, the same viscosity was observed. This difference was attributed to the absence of a pronounced short- and medium-range order in the crystalline sample. We also performed viscosity measurements on initially crystalline and initially amorphous Vit105 samples, however no difference in viscosity was observed.

The presence of an easy to detect strong-to-fragile transition by simple viscosity measurements seems to be limited to the Vitreloy 1 alloy composition. Possibly, a similar transition might occur in Vit105 as well, however the measurements could have been started above the critical threshold temperature or the achievable undercooling was insufficient to re-establish the high-viscosity strong liquid. Indications for a strong-to-fragile transition, derived from the kinetic fragility behavior at high and low temperatures, will be discussed in Chapter 4.7.

The last comment regarding the viscosity measurements of the Vit101 and Vit105 alloy families concerns the flow behavior of the alloys during casting. During sample production, a pronounced difference in the flow behavior between the base alloys and their S-containing modifications was observed. The S-bearing alloys tend to show a much better filling of the mold, when using the same casting parameters. Considering that viscosity is almost equivalent, or even higher, for the S-containing alloys in comparison to the base alloys, the improved mold filling behavior could result from a decreased surface tension. However, surface tension in reactive melts at elevated temperatures is difficult to measure and access to adequate methods is limited (e.g. the oscillating drop method on levitating droplets). In Ref. [249], Mills and Su report on the effects of a contamination with surface active elements on the surface tension of metallic melts. There they find that sulfur (and oxygen), even at such low concentrations as 50 ppm, can cause a 25% decrease in surface tension. Furthermore, surface tension measurements of the S-containing alloy composition $Ti_{60}Zr_{15}Cu_{17}S_8$ are presented in the doctoral thesis of Alexander Kuball [129], where an unusually low surface tension around 0.95 N/m is reported, while S-free alloys typically show values around 1.5 N/m [250]. Hence, the improved mold filling behavior of the S-containing alloys is more than likely caused by a reduced surface tension due to this surface-active element.

4.6 In-situ Synchrotron X-ray Scattering

In this chapter, the results of the in-situ synchrotron X-ray scattering experiments that were performed at DESY in Hamburg and ESRF in Grenoble are presented and discussed. In the first section, the crystallization behavior of the alloys upon heating an amorphous as-cast sample are shown. In the second one, the crystallization behavior upon cooling from the liquid state during electrostatic levitation (ESL) is analyzed. In the final section of this chapter, the calculated total scattering structure functions, S(Q), and the reduced pair distribution functions (PDF), G(r), are displayed. Structural differences of the alloys are discussed, as well as the temperature evolution of the analyzed quantities.

4.6.1 Crystallization Behavior upon Heating

The crystallization behavior of amorphous metals upon heating is the decisive property limiting processing methods like thermoplastic forming or the characterization of the supercooled liquid state. The time and temperature dependence of this process was already discussed in Chapter 4.3, however without looking into the structural changes in the material during the process. After the discovery of the Vit101 and Vit105 alloy compositions, significant efforts were made to analyze and understand the crystallization behavior of these alloys [241,242,251], using different ex-situ techniques like transmission electron microscopy (TEM), atom probe tomography (APT), small-angle neutron scattering (SANS), and laboratory X-ray diffraction, in combination

with differential scanning calorimetry (DSC). These experiments clearly showed a decomposition of the alloys prior to crystallization and then the formation of nanocrystals (roughly with a size of 2 nm) in an amorphous matrix. However, the ex-situ nature of the applied methods, in particular the fact that samples were thermally treated by DSC and could only then be analyzed, made it difficult to determine the exact sequence of phases during crystallization. With access to the rather new in-situ synchrotron X-ray diffraction experiments, the focus here lies on the determination of the sequence of crystallization and a determination of the phases.

In the following, the integrated scattering intensity I(Q) of the experiments on the PETRAIII high-resolution beamline P02.1 at DESY are presented. Figure 4.19 and Fig 4.20 are constructed in the same way, showing the intensity I(Q) for the Vit101 alloys and the Vit105 alloys, respectively. In the center of each plot, selected diffraction patterns at different temperatures during heating with a constant rate of 0.333 K/s are shown. The patterns are color-coded from blue to red for increasing temperatures and the temperatures are written next to the pattern. In the right window, the corresponding DSC scan with the same heating rate is given as a temperature reference. Here, it can also be seen that the diffraction patterns have been selected in accordance with the crystallization events visible in the DSC scan. In the left window, a magnification of the main diffraction peak in the Q-range between 2 and 3.5 Å is shown. All recorded patterns for the stated temperature range are displayed on top of each other, again with a color-coding from blue to red for increasing temperatures. Here, the exact sequence of the growth of the diffraction peaks can be observed.

The crystalline phases that develop during the heating process are indicated in the center window. The simulated diffraction patterns (obtained from PowderCell [229]) are displayed below the experimental data where the crystalline phase can first be indicated. The corresponding phase is written directly next to the pattern. Due to compositional deviations from the ideal crystalline phase, e.g. due to a substitution with different atom species, the diffraction peaks do not always perfectly coincide with the simulated peaks. However, the phases that fit best and are most likely have been selected.

Figure 4.19 shows the diffraction patterns for a) Vit101, b) Vit101 P_1 and c) Vit101 $S_{1.5}$. The DSC scans already indicate that the crystallization sequence in Vit101 and Vit101 P_1 is the same, with both alloys showing three peaks, while Vit101 $S_{1.5}$ only shows two distinct crystallization events. However, the first crystallization event upon heating seems to be the same for all three compositions and it does not lead to clearly visible Bragg diffraction peaks, which would indicate a fully crystalline structure. This is in good agreement with TEM studies by Glade et al. which found that Vit101 samples that were heated up to 748 K show nanocrystals with a size of 2 to 3 nm in an amorphous matrix [242]. However, they could not clearly identify the primary phase from their electron diffraction patterns. The small size of the crystals also explains why SEM and/or EDX investigations are not feasible to determine the crystalline phases.

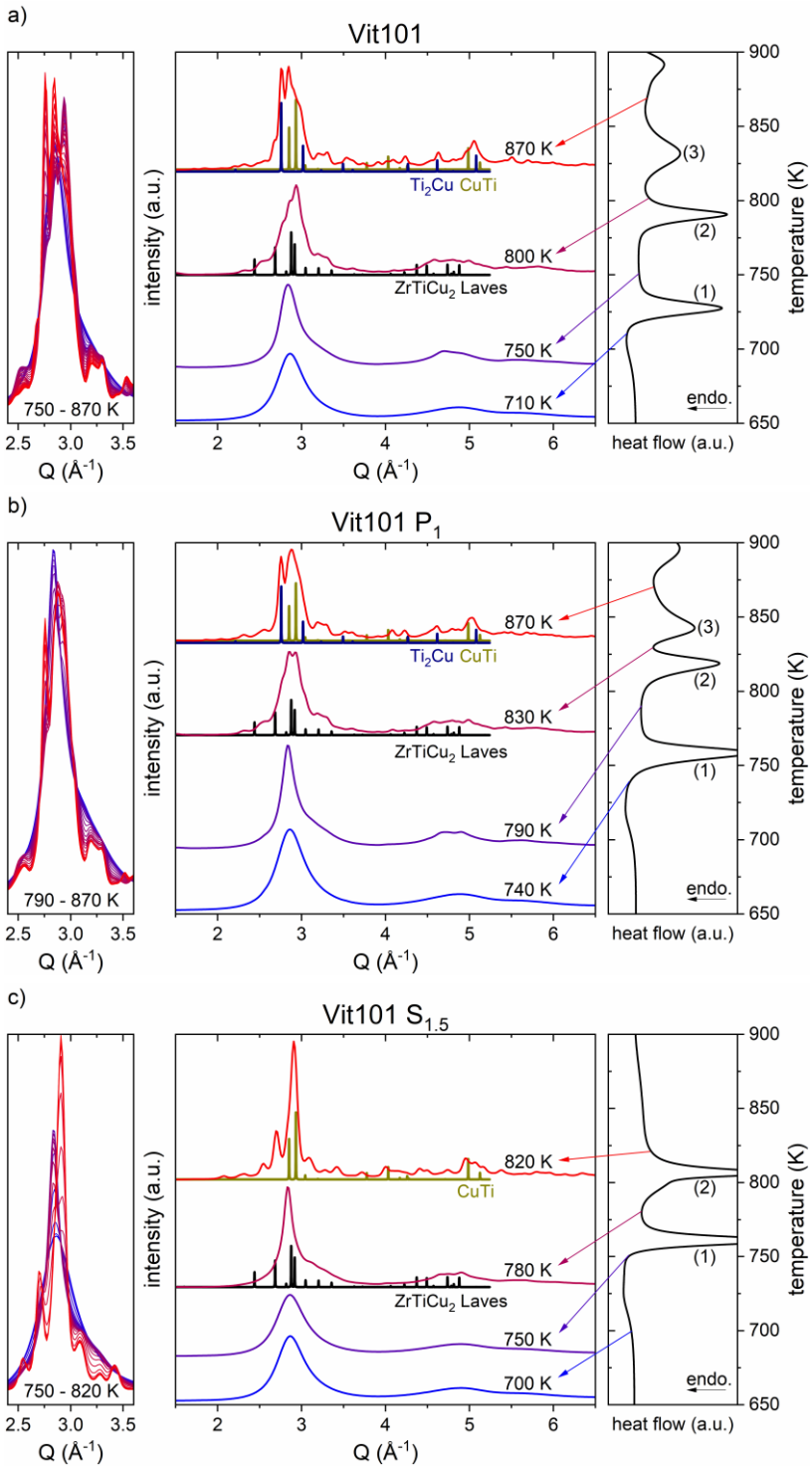

Figure 4.19: In-situ synchrotron X-ray diffraction patterns of the Vit101 alloys upon heating an amorphous sample with 0.333 K/s. A DSC scan with the same heating rate is shown as a temperature reference and the temperature of the patterns is indicated. The development of the main peak is shown on the left side.

The in-situ synchrotron X-ray diffraction experiments suggest that the primary crystallizing phase is a $ZrTiCu_2$ Laves phase. Especially the diffraction pattern of Vit101 $S_{1.5}$ at 780 K reinforces this assumption. The broad diffraction peaks of the nanocrystals resemble the shape of the calculated diffraction pattern of the $ZrTiCu_2$ Laves phase. However, one crystallization event is not necessarily related to the crystallization of a single phase but can also correspond to the formation of multiple phases. When heating Vit101 $S_{1.5}$ to higher temperatures (820 K), the diffraction peaks of the Laves phase become clearly visible. Additionally, diffraction peaks corresponding to the tetragonal CuTi phase arise. The space groups and the lattice parameters of all indicated phases can be found in Table A3 in the appendix.

In Vit101 and Vit101 P_1, the same $ZrTiCu_2$ Laves phase can clearly be indicated in the diffraction patterns after the second crystallization peak (800 K and 830 K, respectively). Hence, this crystallization event might correspond to the growth of the nanocrystals and the crystallization of the remaining matrix. The formation of the CuTi phase can already be assumed at the end of the second crystallization event and becomes clearly visible during the third crystallization peak. After the third crystallization event at 870 K, diffraction peaks corresponding to the tetragonal Ti_2Cu phase are also present. For Vit101, the second and the third crystallization event are rather clearly separated in the DSC scan, while this separation is not so clear in the Vit101 P_1 alloy. Hence, diffraction peaks of the CuTi phase are already visible in Vit101 P_1 before the formation of the $ZrTiCu_2$ Laves phase is completed.

The in-situ X-ray diffraction experiments show a distinct difference in the crystallization behavior of Vit101 $S_{1.5}$ and of Vit101/Vit101 P_1. The addition of sulfur seems to hamper the formation of the Ti_2Cu phase and stabilizes the supercooled liquid region. The primary crystallizing phase however remains unchanged. Similarly, sulfur was also found to hamper the formation of the Ti_2Cu/Ni phase in Ti-based BMGs [9].

The phases observed during crystallization fit rather well to the expected phases based on the alloy composition. The $ZrTiCu_2$ Laves phase displays a nominal composition of 25 at% Zr and Ti, and 50 at% Cu and the CuTi phase is compositionally close to the alloy composition. The remaining Ti can then be found in the Ti-rich Ti_2Cu phase. In general, Cu atom position are likely to be also occupied by the topologically similar Ni atoms. Furthermore, the chemical composition of the Laves phase is also a subject to change as the fixed atom positions can be occupied by other atom species up to a certain degree, also causing slight changes to the lattice constants of the structure. The metastable $ZrTiCu_2$ Laves phase was first reported in Ref. [252] and then described in more detail in Refs. [253] and [254]. It is a hexagonal $MgZn_2$-type intermetallic phase. The corresponding ternary phase diagram for the Cu-Ti-Zr system can be found in Ref. [255].

Figure 4.20 shows the diffraction patterns for a) Vit105, b) Vit105 P_2 and c) Vit105 S_2. At a first glance, the crystallization sequence in the DSC signal seems to be the same for Vit105 P_2 and Vit105 S_2, while Vit105 shows an additional shoulder on the low-temperature side of the principal crystallization peak. However, analyzing the

diffraction patterns, slight differences between Vit105 P_2 and Vit105 S_2 can be observed, and Vit105 shows a completely different crystallization behavior.

The phase separation and crystallization behavior of amorphous Vit105 upon heating and annealing was previously investigated by Johnson and coworkers [241,243]. They used small-angle neutron scattering (SANS), transmission electron microscopy (TEM), laboratory XRD, and DSC. Their efforts showed that Vit105 decomposes on the nanometer scale, which then induces nanocrystallization. This event is correlated with the first exothermic event in the DSC scan, drastically reducing the stability of the SCL region. They further conclude that the thermal parameter ΔT_x is not correlated with the GFA for alloys that display phase separation.

Based on our diffraction measurements, we can only identify structural changes and no clear primary crystallization in Vit105 during the exothermic shoulder on the low-temperature side of the principal crystallization peak. The inset in Fig. 4.20 a) shows that only a sharpening of the second amorphous halo in the diffraction pattern is observed, however, the possibly forming nanocrystals are so small that no clear Bragg diffraction patterns appear. The nature of the first exothermic shoulder will be discussed later in this chapter, when the results of isothermal experiments are presented. The shoulder is immediately followed by a more pronounced crystallization event, where the formation of tetragonal Zr_2Ni crystals is observed. The Zr_2Ni phase remains the dominant one, accounting for all detected Bragg peaks. This fits well to the composition of Vit105, when Ni and Cu are both considered to occupy the Ni sites, due to their topological similarity, and Al and Ti are not considered separately.

Vit105 P_2 shows a very different crystallization sequence, as displayed in Fig. 4.20 b). During the single, sharp crystallization event, the formation of three different crystalline phases is observed at the same time. These are identified as the tetragonal Zr_2Ni, the tetragonal Zr_2Cu, and the cubic CuZr phase. As for all other identified phases, their space groups and the lattice parameters can be found in Table A3 in the appendix.

The crystallization sequence of Vit105 S_2 is shown in Fig. 4.20 c). While the DSC trace looks similar to the one of the P-containing alloy, the primary crystallizing phase and the final diffraction pattern after crystallization are slightly different. At the onset of crystallization, first, the formation of a ZrTiNi Laves phase is detected. While this observation is not too obvious from the crystallization experiments with a constant heating rate, the isothermal experiments shown in Fig. 4.21 b) confirm this observation and will be discussed later. The hexagonal ZrTiNi Laves phase has the same space group as the previously described $ZrTiCu_2$ Laves phase, however, displays slightly different lattice parameters and different atomic species occupy the atom sites in the lattice. This lattice structure can be formed by different atomic compositions, with one possible composition being $Ti_{45}Zr_{38}Ni_{17}$ [256]. As mentioned before, other compositions can be achieved by an occupation of the lattice sites by different atom species. During the same crystallization event, the subsequent formation of the tetragonal Zr_2Ni and Zr_2Cu phase are observed, as is also true for Vit105 P_2.

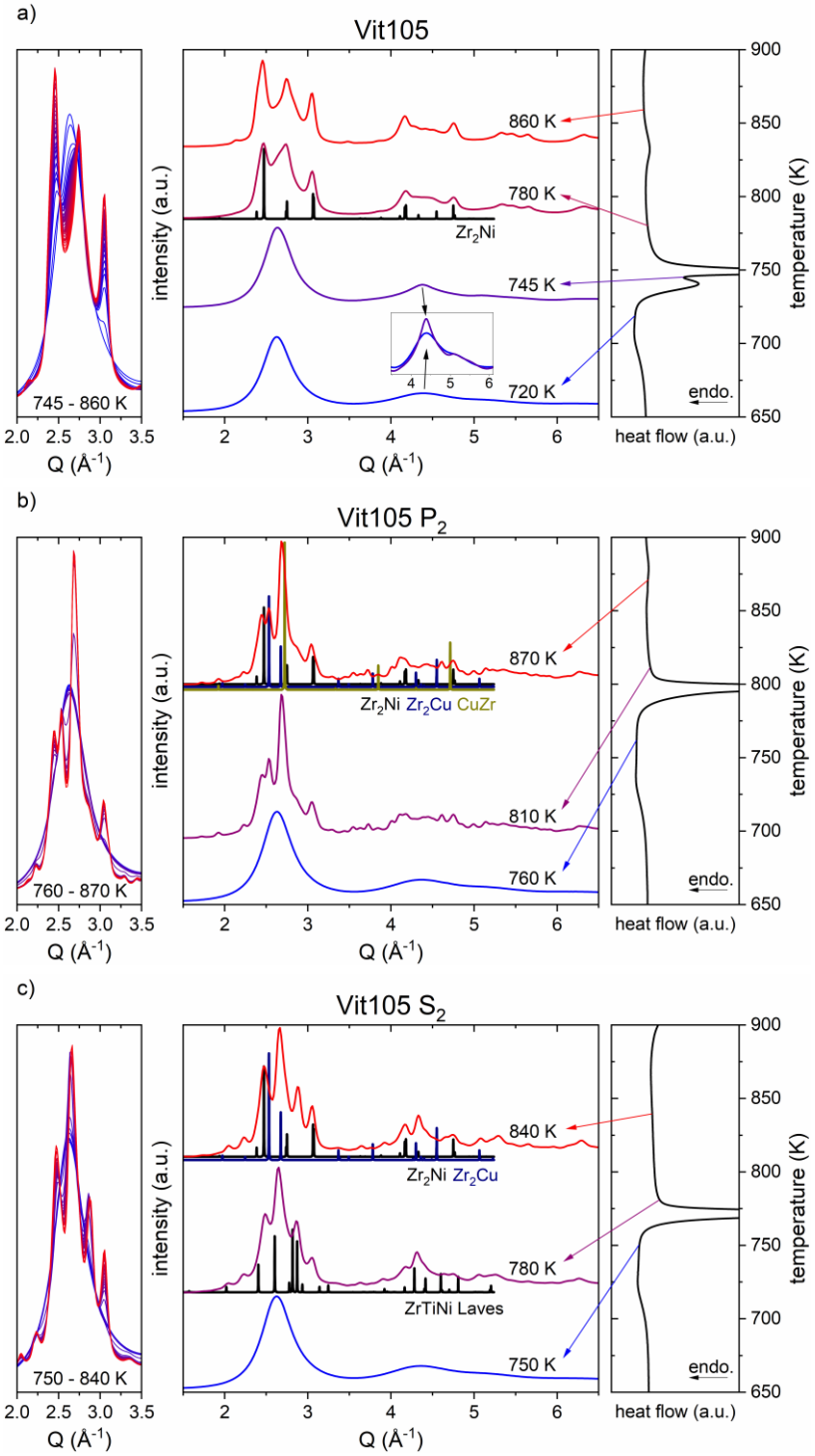

Figure 4.20: In-situ synchrotron X-ray diffraction patterns of the Vit105 alloys upon heating an amorphous sample with 0.333 K/s. A DSC scan with the same heating rate is shown as a temperature reference and the temperature of the patterns is indicated. The development of the main peak is shown on the left side.

Comparing the results of the crystallization experiments, the phosphorus in Vit105 P_2 prevents the formation of the ZrTiNi Laves phase that forms in Vit105 S_2 and hampers the formation of Zr_2Ni which forms in Vit105, thus considerably extending the supercooled liquid region. Therefore, ΔT_x in Vit105 P_2 is extended by 40 K in comparison to Vit105 and by 23 K to Vit105 S_2. In general, the addition of both, S and P, hampers the onset of crystallization and extends the supercooled liquid region in comparison to the base alloy.

Diffraction patterns of isothermal annealing experiments are presented in Fig. 4.21. The samples were heated with a rate of 2 K/s from room temperature to the annealing temperature and then annealed for the displayed time. The diffraction patterns are color-coded from blue to red for increasing time. In the center of each plot, selected diffraction patterns at different times are displayed and the final diffraction pattern after heating the sample to 820 K is shown in black as a reference. In the right window, the corresponding isothermal DSC measurement is given as a time reference. In the bottom window, all recorded patterns for the observed time range are displayed on top of each other, again with a color-coding from blue to red for increasing times. The exact sequence of the growth of the diffraction peaks can be observed and additionally the calculated diffraction pattern of the primary crystalline phase is shown.

Figure 4.21 b) shows the isothermal crystallization sequence of Vit105 S_2 at 733 K. In the DSC measurement, only a single exothermic event is visible, and the diffraction patterns also indicate the formation of a single phase. The patterns correspond well to the ZrTiNi Laves phase that was previously introduced in Fig. 4.20 c). Hence, the isothermal experiments confirm the ZrTiNi Laves phase as primary crystallizing phase in Vit105 S_2. Only after subsequent heating of the sample up to 820 K, the formation of the tetragonal Zr_2Ni and Zr_2Cu phase are observed, resulting in the same diffraction pattern as obtained from the experiments with a constant heating rate.

In contrast, Vit105 shows a very different crystallization behavior, as displayed in Fig. 4.21 a) for an annealing temperature of 713 K. In isothermal experiments, the shoulder on the low-temperature side of the principal crystallization peak in the DSC scan can be clearly separated from the main peak, as visible in the in the DSC measurement on the right side. The diffraction patterns up to an annealing time of 400 s show no diffraction peaks, indicating an amorphous sample even though the first exothermic event was already completed. This observation coincides well with the results of Johnson and coworkers [241,243] where the first exothermic event corresponds only to chemical decomposition and the beginning of nanocrystallization. The second exothermic event visible in the DSC trace clearly corresponds to the formation of tetragonal Zr_2Ni crystals.

In order to further elucidate the first event, the calculated structure function S(Q) of Vit105 during the first 400 s of isothermal annealing at 713 K is displayed in Fig. 4.22 a). With increasing annealing time, the position of the first sharp diffraction peak (FSDP), Q_1, moves to larger Q-values, and the height and sharpness of the second peak, Q_2, increases drastically. As will be discussed later (see Eq. 4.1), the quantity

$[1/Q_1]^3$ relates to the sample volume, and is displayed as a function of time in Fig. 4.22 b), together with the height of Q_2. The change in $[1/Q_1]^3$ indicates a denser packing and the sharpening of Q_2 indicates an ordering of the structure. For a profound understanding of the phenomenon, extensive in-situ studies with other methods, including small-angel neutron or X-ray scattering to resolve decomposition effects, and high-resolution TEM, would be necessary.

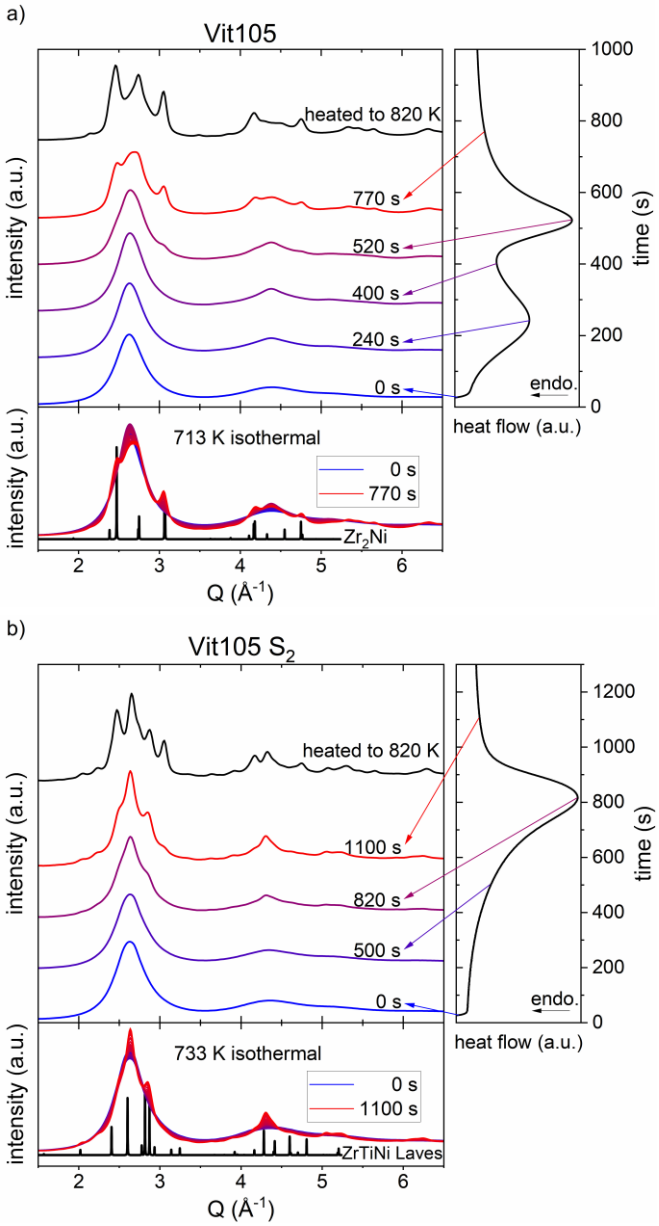

Figure 4.21: In-situ synchrotron X-ray diffraction patterns of **a)** Vit105 and **b)** Vit105 S_2 during isothermal annealing. On the right side, the DSC heat flow signal of the same isothermal measurement is shown as a reference, and at the bottom a superposition of all patterns is shown.

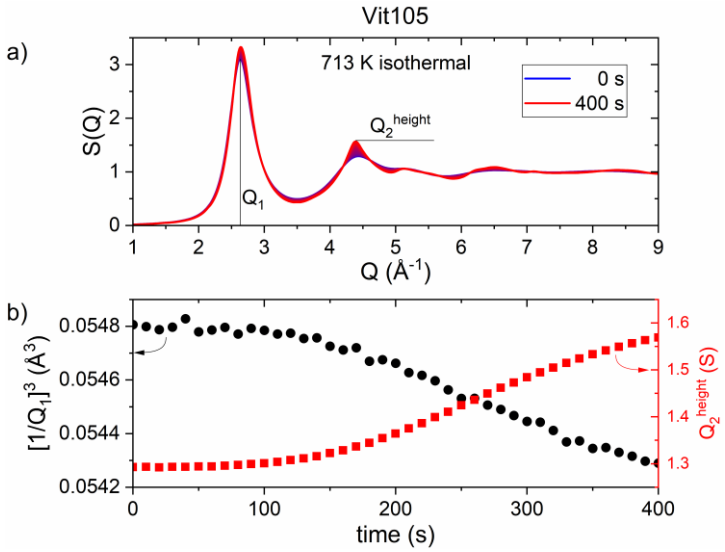

Figure 4.22: a) Structure function S(Q) of Vit105 during the first 400 s of isothermal annealing at 713 K (from blue to red). **b)** Structural volume $[1/Q_1]^3$ (black dots), and height of the second peak Q_2 (red squares), as indicated by the black lines in a).

4.6.2 Crystallization Behavior upon Cooling during Levitation

The crystallization behavior of metallic liquids upon cooling is the decisive property limiting glass formation, and hence determining the glass-forming ability (GFA) of the alloy. While calorimetric cooling experiments provide valuable information, they cannot resolve the exact crystallization sequence, nor detect the crystalline phases that are forming. Ex-situ diffraction experiments on partially crystalline and crystalline samples produced with different cooling rates are very time-consuming and often leave questions unanswered.

In this section, two highly sophisticated experimental techniques, namely in-situ synchrotron X-ray diffraction, and electrostatic levitation (ESL), are combined in order to determine the sequence of crystallization and the crystalline phases that form. The combination of these techniques offers access to a valuable dataset that cannot be obtained by any other technique. In this experimental setup (as described in Chapter 3.5.2) diffraction patterns can be recorded during the free cooling of a sample without the interference of heterogeneous crystallization due to the containerless ESL processing.

Samples of the alloy compositions Vit101 $S_{1.5}$ and Vit105 S_2 were processed at the beamline ID11 at ESRF in Grenoble in 2018, in collaboration with the Institute of "Materials Physics in Space" of the DLR. Additionally, raw measurement data for

Vit101 and Vit105 from previous experiments at DESY in 2011, using the same experimental ESL setup, were kindly provided by Dr. Fan Yang from the Institute of "Materials Physics in Space". This data was newly evaluated in the same way as the recent ESRF data and was used as reference to investigate the influence of the minor additions of sulfur.

Figure 4.23 exemplarily shows the heating and melting process of a crystalline sample, in this case Vit105 S_2, as well as the temperature profile of an ESL processing cycle. For all other alloys, only the diffraction patterns upon cooling are shown later on.

The left panel of Fig. 4.23 shows in-situ synchrotron X-ray diffraction patterns upon heating and melting with a color-coding from blue to red for increasing temperatures. In the center panel, a DTA heating curve of a crystalline sample is displayed as a temperature reference and the dots with the arrows indicate the temperature of the shown diffraction patterns. The right panel shows a single heating and cooling cycle of the ESL experiment, where the left flank of the temperature profile corresponds to the diffraction patterns during heating, as again indicated by the color-coded dots. The right flank relates to the free cooling of the sample, which will be discussed later. On the bottom of the right panel, the heating and cooling rate of the experiment is given on the same time scale, with the maximum cooling rate reaching around -30 K/s. The inset shows the temperature profile of the complete experiment, where five heating and cooling cycles were performed.

The diffraction pattern at 960 K in Fig. 4.23 results from a sample that crystallized previously upon cooling in the ESL, as the critical cooling rate could not be reached. This pattern is different from the pattern obtained after heating an initially amorphous sample, as displayed in Fig. 4.20 c), and hence, different crystalline phases form when crystallization occurs during cooling or upon heating an initially amorphous sample. The crystalline phases observed at 960 K are indicated later in Fig. 4.26 b). Furthermore, this structural difference explains the difference in the DTA melting curves between amorphous and crystalline samples upon heating that were displayed earlier in Fig. 4.5. Initially amorphous samples show an earlier onset of melting in the form of a pre-peak than crystalline samples.

Upon further heating, melting begins at the melting point (T_m^{xtal} = 1065 K) and at 1070 K the intensity of the diffraction peaks already begins to decrease. The melting event is also visible in the ESL temperature profile, where a short isothermal temperature plateau can be seen. After the main melting peak, at 1110 K, the diffraction peaks are already much less pronounced and at 1255 K, right below the liquidus temperature, the sample is almost melted completely, and only a weak diffraction peak is visible, as indicated by the circle. 15 K higher, a completely amorphous liquid structure can be identified.

This observation is in good agreement with the previously discussed DTA melting curves (compare to Fig. 4.5). The remaining crystalline phase up to 1255 K confirms the observed shoulder in the DTA scan and validates its interpretation as the end of the melting event. The low intensity of the remaining peak further confirms that only

a small percentage of the sample remains crystalline to such high temperatures. This melting shoulder at high temperatures is the main difference between Vit105 and Vit105 S_2 in their DTA scans and should therefore result from a sulfur-stabilized phase that does not form in the Vit105 base alloy. The implications of this phase on the crystallization behavior upon cooling, and hence on the GFA, are discussed in the context of Fig. 4.26.

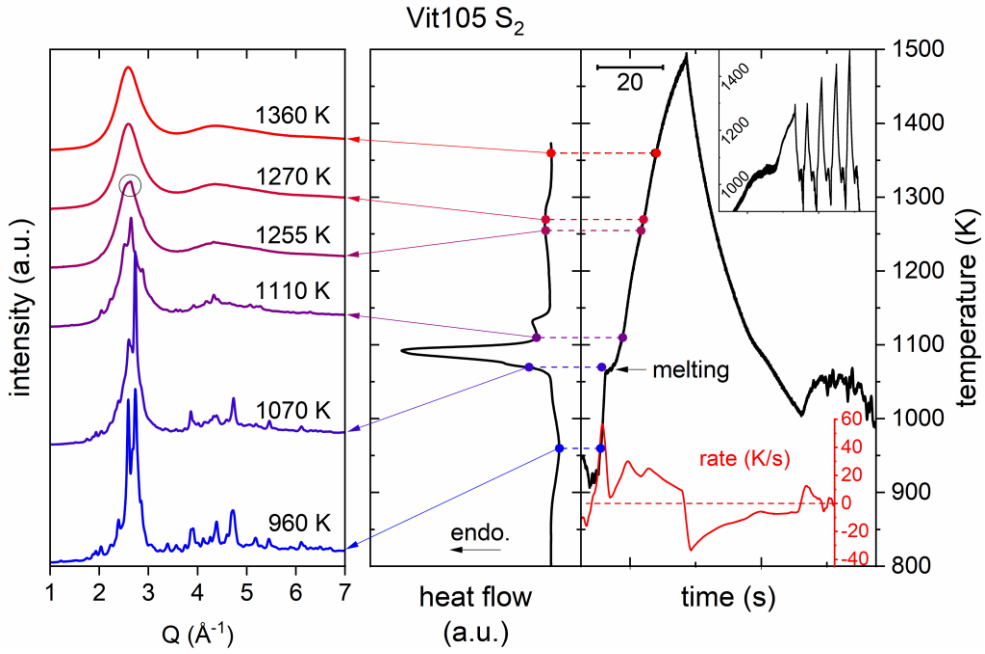

Figure 4.23: Heating and melting of a crystalline Vit105 S_2 sample. The left panel shows in-situ synchrotron X-ray diffraction patterns during electrostatic levitation (ESL). The other panels serve as a temperature reference, with the center one showing a DTA heating curve and the right one displaying the corresponding heating and cooling cycle during the ESL experiments. On the bottom, the heating and cooling rate is also indicated. The inset shows the temperature profile of the whole ESL experiment.

Figures 4.24 and 4.26 show the intensity I(Q) of a single representative free cooling experiment for the Vit101 alloys and the Vit105 alloys, respectively. In the main window of each plot, selected diffraction patterns at different temperatures during free cooling are shown. The patterns are color-coded from red to blue for decreasing temperatures and the temperatures are written next to the pattern. In the right window, the corresponding ESL temperature profile is displayed. The calculated diffraction patterns of the growing crystalline phases are shown directly below the experimental diffraction pattern.

Figure 4.24 a) shows the diffraction patterns of Vit101. Free cooling starts at a maximum temperature of 1400 K, and the sample remains fully amorphous down to 950 K, thus 220 K below the liquidus temperature. Crystallization starts right after, at a temperature of 945 K and occurs in a very narrow time and temperature region.

The primary crystallizing phase can clearly be identified as the $ZrTiCu_2$ Laves phase. The same phase is observed as primary crystallizing phase upon heating amorphous samples. After the formation of the Laves phase, the temperature of the sample increases rapidly up to a value of 1100 K due to recalescence. During this event, the crystal structure of the sample changes abruptly and a single tetragonal CuTi phase is formed. Considering that in the CuTi structure dedicated Cu atom positions might also be occupied by Ni and that Ti atom positions might be occupied by Zr atoms, the nominal compositions of Vit101 can be written as $(Cu/Ni)_{55}(Ti/Zr)_{45}$, which fits well to the CuTi composition.

It is interesting to note that the final diffraction pattern after crystallization upon cooling is different from the pattern upon heating an initially amorphous sample (as previously also mentioned for Vit105 S_2). When crystallizing an amorphous sample upon heating, not only the CuTi phase, but also a Ti_2Cu phase and remains of the $ZrTiCu_2$ Laves phase, are obtained. The reason for this can be found in the atomic mobility of the system at the temperature range of crystal formation. While the crystals are formed at around 1100 K upon cooling, the crystals during the heating process form in a temperature range between 700 K and 850 K, and thus in a range with significantly lower atomic mobility. Therefore, a non-equilibrium microstructure is conserved, that also causes a premature onset of melting in the DTA scan, lowering the melting temperature of initially amorphous samples in comparison to the crystalline structure formed upon slow cooling from the equilibrium liquid. This discussion is not only valid for the Vit101 alloy, but also for the other investigated alloy compositions (also compare to the DTA scans in Fig. 4.5).

In Fig. 4.24 b), the same experimental data is shown for Vit101 $S_{1.5}$. Here, first, but very minor, diffraction peaks become visible at much higher temperatures, starting at 1095 K. At 1070 K, two weak peaks are visible in an otherwise amorphous liquid. With the only compositional difference between the alloys being 1.5 at% S, it stands to reason that this primary crystallizing phase is triggered by the sulfur. The nature of this phase is discussed later, also taking EDX analyses of the sample into account. However, after the formation of the primary phase, no formation of a Laves phase is observed. The sulfur seems to suppress the formation of the Laves phase. Furthermore, the formation of the CuTi phase does not seem to be triggered by the primary phase, thus explaining the improved GFA of the Vit101 $S_{1.5}$ alloy in comparison to Vit101.

In general, both Vit101 and Vit101 $S_{1.5}$ show similar diffraction patterns in the final crystalline state, being dominated by a CuTi phase. In Vit101 $S_{1.5}$ the CuTi phase forms directly from the liquid state, whereas in Vit101 a $ZrTiCu_2$ Laves phase is formed first.

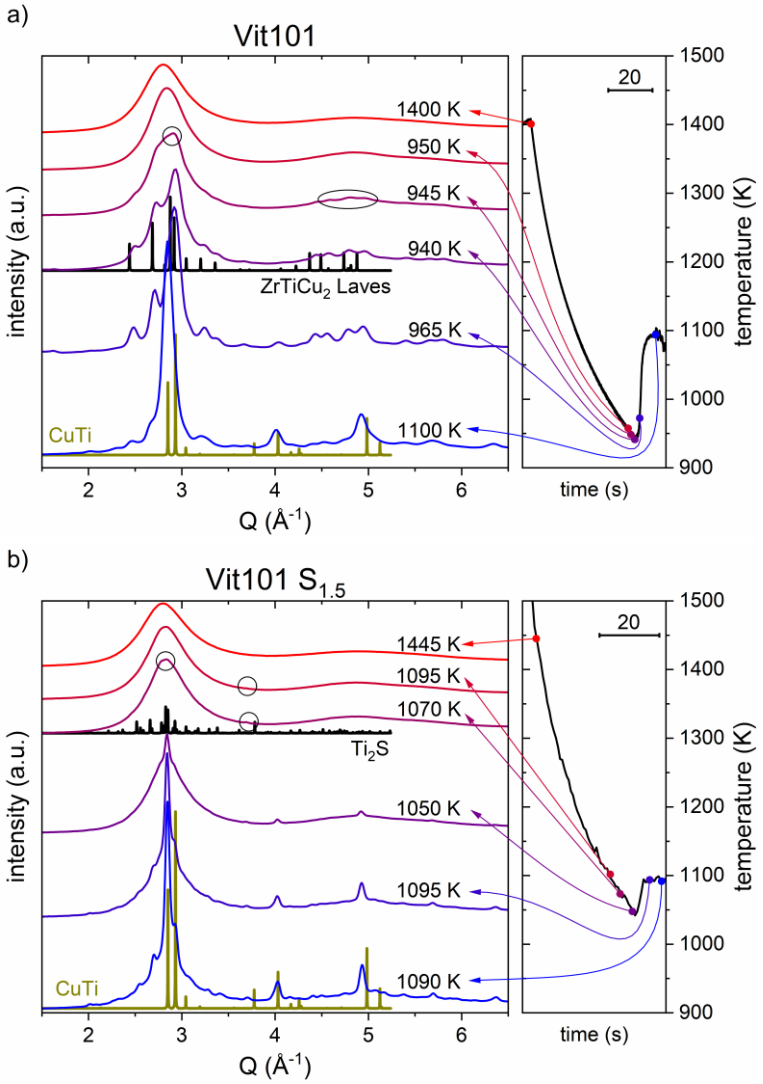

Figure 4.24: In-situ synchrotron X-ray diffraction patterns of **a)** Vit101 and **b)** Vit101 $S_{1.5}$ for free-cooling of a liquid sample during electrostatic levitation (ESL). The temperature profile of the cooling process is shown on the right and the temperature of the displayed diffraction patterns is indicated.

A SEM image from backscattered electrons (BSE) of the Vit101 $S_{1.5}$ sample after processing in ESL is shown in Fig. 4.25 a). The observed microstructure in the polished cross-section corresponds to the final diffraction pattern in Fig. 4.24 b), as the same cooling protocol was applied. A fine patterned microstructure with few large, needle-like structures (black) is visible. EDX analysis of the matrix region, marked by the yellow box (# 1), results in a composition of $Cu_{47}Ti_{33}Zr_{11}Ni_8S_1$, which is close to the nominal composition and also fits well to the compositional ratio of $(Cu/Ni)_{55}(Ti/Zr)_{45}$ that was previously related to the diffraction pattern of the CuTi phase. The black region (# 2) displays a composition of $Cu_4Ti_{58}Zr_{10}Ni_2S_{26}$, hence a very S-rich phase. Not considering Cu and Ni and grouping the chemically similar elements Ti and Zr,

the composition can be simplified to $(Ti/Zr)_{72}S_{28}$ or $Ti_{69}S_{31}$ if Zr is also not taken into account.

The structure of the metal-rich TiS phases in the binary system was first investigated by Owens et al. [257,258] and they found great structural similarities between the Ti_2S phase and the Ti_8S_3 phase, even though they show a different crystal system. In fact, the calculated diffraction patterns of both phases look almost alike. The basic structural information of the phases can be found in Table A3 in the appendix.

In the case of Vit101 $S_{1.5}$, both Ti_2S and Ti_8S_3 could be the primary crystallizing phase, based on the diffraction patterns as well as the EDX analysis. The simulated diffraction pattern of the orthorhombic Ti_2S phase is shown underneath the measured diffraction pattern of Vit101 $S_{1.5}$ at 1070 K in Fig. 4.24 b). The Ti_2S phase has a rather complex unit cell with 12 Ti_2S units per unit cell (36 atoms). Furthermore, it is a very weak scatterer and the assembly of the peaks resembles the shape of the amorphous halo. Hence, the phase is difficult to observe in XRD measurements and might even be present in otherwise fully amorphous samples. This phenomenon is observed in TiCuNiS alloys, where a "black" phase is visible in SEM in an amorphous matrix, even though the laboratory XRD measurements show no diffraction peaks. This observation is discussed in detail in the doctoral thesis of Alexander Kuball [129]. In this study, the main structural signature of the Ti_2S phase in the XRD patterns is a very minor peak at $Q = 3.7$ Å^{-1}, which is indicated by a black circle. This hump remains visible and unchanged even after the formation of the much stronger CuTi diffraction peaks.

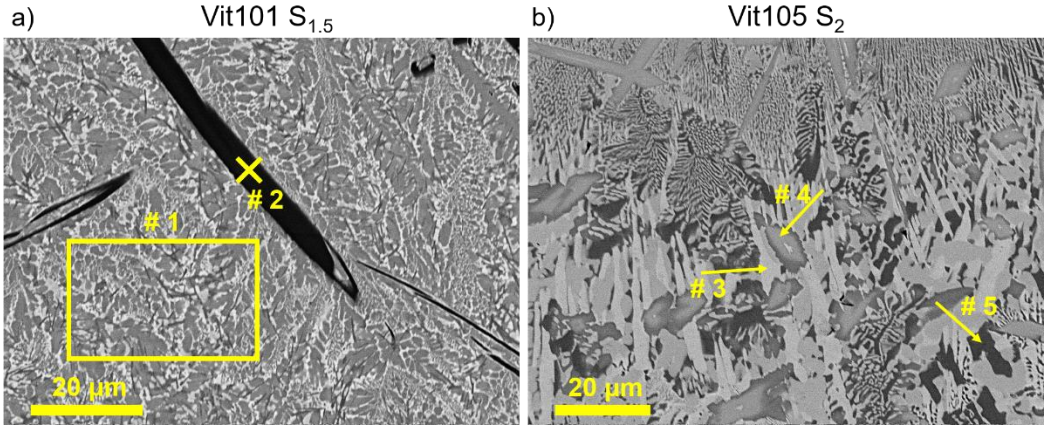

Figure 4.25: SEM images of the processed ESL samples. **a)** Vit101 $S_{1.5}$ and **b)** Vit105 S_2. The yellow markers indicate where EDX measurements were performed and compositions can be found in the main text.

The XRD diffraction patterns during free ESL cooling of Vit105 starting at 1450 K are shown in Fig. 4.26 a). The sample stays amorphous till 960 K, thus reaching an undercooling of 175 K below the liquidus temperature. Crystallization begins at 945 K, where initially only a deformation of the main amorphous diffraction halo is visible (black circle). With the onset of the recalescence, the final diffraction pattern begins

to form immediately, not allowing to determine a clear sequence of phases. The observed peaks can be correlated with a mixture of three crystalline phases, namely the cubic CuZr, the tetragonal Zr_2Cu, and the hexagonal Zr. As for Vit101, the observed diffraction pattern of Vit105 upon cooling is very different from the pattern formed upon heating an amorphous sample, where a single Zr_2Ni structure is observed.

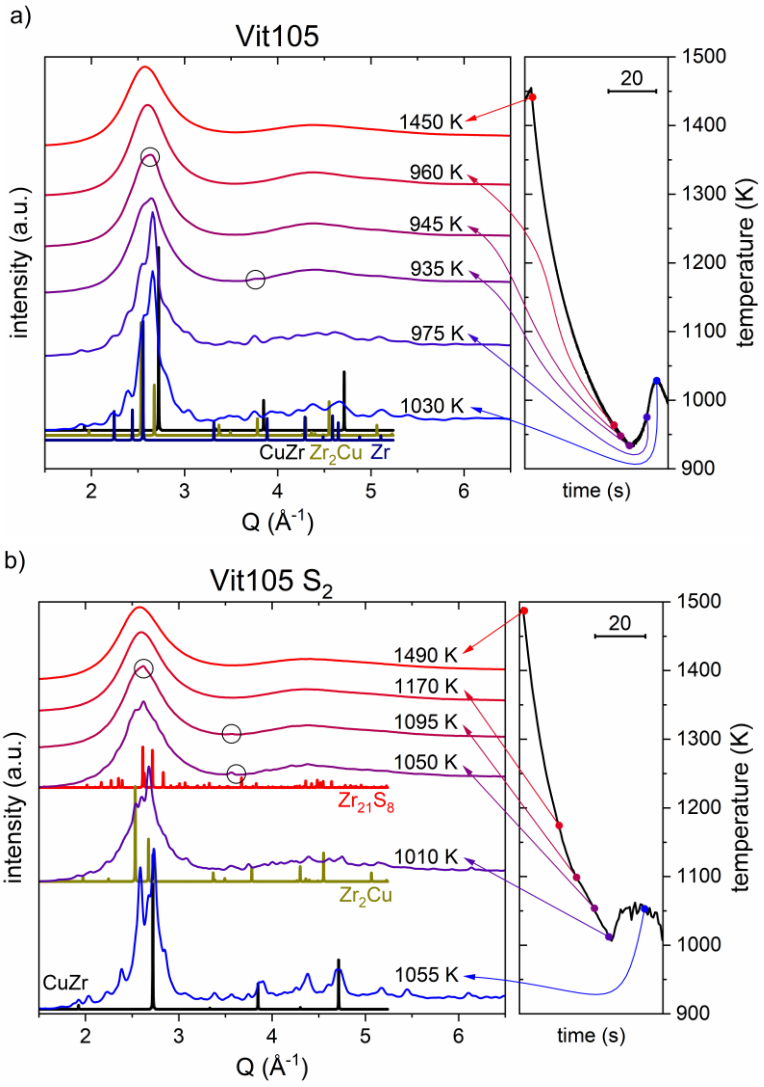

Figure 4.26: In-situ synchrotron X-ray diffraction patterns of **a)** Vit105 and **b)** Vit105 S_2 for free-cooling of a liquid sample during electrostatic levitation (ESL). The temperature profile of the cooling process is shown on the right and the temperature of the displayed diffraction patterns is indicated.

The diffraction data for Vit105 S_2 is displayed in Fig. 4.26 b). As for Vit101 $S_{1.5}$, first but minor diffraction peaks become visible at much higher temperatures of 1095 K. Below, at 1050 K, small, hump-like diffraction peaks are visible on the amorphous background diffraction signal, indicating a minor fraction of small crystalline particles

in the melt. Again, it seems plausible that a sulfur-containing phase is formed initially, as the sulfur also causes a drastic increase of the liquidus temperature. This should be the same phase that remains crystalline up to high temperatures in the heating experiment from Fig. 4.23. Regarding the diffraction pattern, this phase could possibly be tetragonal $Zr_{21}S_8$. Right after the formation of this phase, the formation of the tetragonal Zr_2Cu phase is triggered and the maximum undercooling before the recalescence is much smaller than in Vit105. Hence, the ZrS phase acts as a nucleating agent and reduces the GFA of Vit105 S_2 in comparison to the base alloy. Finally, an additional cubic CuZr phase is formed, which is visible in the final diffraction pattern.

In summary, a Zr_2Cu and a CuZr phase form in both alloys. However, in Vit105 S_2 crystallization is triggered earlier, likely by a ZrS phase, e.g. $Zr_{21}S_8$. This explains the reduced GFA of Vit105 S_2 and is contrary to the effect of sulfur in the Vit101 system, where the primary crystallization of Ti_2S does not trigger the crystallization of the remaining liquid.

The cross-sectional BSE SEM image of the ESL-processed Vit105 S_2 sample is shown in Fig. 4.25 b). As for the other sample, a fine patterned microstructure is visible. EDX measurements were performed in three differently shaded regions, indicated by yellow arrows. Point # 3 corresponds to a composition of $Zr_{59}Cu_{22}Ni_{10}Al_5Ti_4$, which is not too far off from the nominal composition, but without sulfur. Phase # 4 however displays a high concentration of 13 at% sulfur ($Zr_{61}Cu_7Ni_6Al_{11}Ti_2S_{13}$), but the measured composition cannot clearly be assigned to a binary ZrS compound that could be responsible for the primary crystallization. The darkest phase in BSE contrast at point # 5 contains a low amount of Zr and has a composition of $Zr_{38}Cu_{15}Ni_{16}Al_{16}Ti_{14}$. The Zr to (Cu/Ni) ratio of almost 1-1 of this phase suggests that it might be the CuZr structure observed in the diffraction patterns.

4.6.3 Structural Differences and Temperature Evolution

In this final section of Chapter 4.6, the total scattering structure functions, S(Q), and the reduced pair distribution functions (PDF), G(r), that were calculated from the previously discussed scattering intensities, I(Q), are presented. These quantities are analyzed in the glassy, the supercooled liquid, and the liquid state, focusing on the structural differences between the alloys and their temperature dependence. In the end, the results are discussed in the context of the structure-fragility concept of Wei et al. [79].

An overview of the quantities I(Q), S(Q), and G(r), for the six investigated alloy compositions at 350 K is presented in Fig. 4.27, with the Vit101 alloys shown on the left and the Vit105 alloys on the right. Figure 4.27 a) and b) show I(Q) in the full measurement range of the detector from 0 to 16 $Å^{-1}$. The main diffraction peak, as well as the second peak and a shoulder on its right side are clearly visible.

In the panels c) and d) of Fig. 4.27, S(Q) is displayed and the peak positions that are used in the discussion later on are indicated by arrows. Q_1 is the position of the main

peak, Q_2 is the second peak at higher Q-values and $Q_2^{shoulder}$ is the position of its shoulder, which is more pronounced in the Vit101 alloys than in the Vit105 alloys. A shoulder on the second peak is typically attributed to icosahedral short-range order (SRO). For perfect icosahedral SRO in metallic glasses, Sachdev and Nelson calculated the ratio between the first two peak positions Q_2/Q_1 to be 1.71 and the one between the position of the shoulder and the first peak $Q_2^{shoulder}/Q_1$ to be 2.04 [259]. These results were later also confirmed by experiments of Kelton et al. on electrostatically levitated melts [260]. The peak positions and the corresponding ratios for our alloys are given in Table 4.7. The ratios Q_2/Q_1 and $Q_2^{shoulder}/Q_1$ for all compositions are close to the theoretical values and clearly indicate icosahedral SRO. For the Vit101 alloys, the values are 1.72 and about 1.97, and for the Vit105 alloys they are 1.68 and about 1.95. These values and the clearly visible second shoulder in the Vit101 alloys imply that the Vit101 alloys show an even more pronounced icosahedral SRO than the Vit105 alloys.

The total scattering structure functions show almost no differences between the base alloy and the ones with minor additions. S(Q) and the difference in S(Q) between the base alloy and the modified ones are additionally shown in the appendix in Fig. A2. This indicates that the minor additions do not significantly change the structure at ambient temperature but rather effect the crystallization behavior and the temperature dependence of different quantities.

Figure 4.27 e) and f) show the PDF, G(r), of all six alloy compositions. G(r) can roughly be read as a histogram indicating the probability of finding an atom in a certain distance to a reference atom. It must be kept in mind that the PDF represents an average over all pairs of atoms in the sample, where the atomic form factors of all these atom species are also very different (compare to Chapter 3.5.1).

A magnification of the first peak of G(r), r_1, which corresponds to the average, weighted nearest neighbor distance, is shown in the inset. The dashed lines indicate the bond length for different pairs of atoms, calculated from the atomic radii of the atoms in a glassy structure [90]. A comparison between the Vit101 and Vit105 alloys shows that the average nearest neighbor distance in Vit105 is larger, due to the high proportion of large Zr atoms. The same qualitative information can already by gained from the S(Q) patterns, where the peaks in the Fourier space are shifted to lower Q-values.

For the Vit101 alloys in the inset in Fig. 4.27 e), it can be seen that the first peak best corresponds to the bond length of a Cu-Ti atom connection, whereas the Cu-Cu bond length is slightly shorter and the Cu-Zr and Ti-Ti bond length are slightly larger than the measured average nearest neighbor distance. This observation fits very well to the nominal alloy composition ($Cu_{47}Ti_{34}Zr_{11}Ni_8$), where Cu-Ti connections are most likely to occur. In case of the Vit105 alloys (Fig. 4.27 f)), the maximum of the first peak fits very well to the Zr-Zr bond length. This observation fits well to the fact that Zr is the main constituent element with 52.5 at% and that Zr also displays the highest atomic form factor [261] and hence the highest diffraction intensity of the elements in

Vit105. Furthermore, a pronounced shoulder in the first peak of G(r) is visible at lower r-values. The r-value of the shoulder fits well to the Zr-Cu atom connection, which is also identical to the Zr-Ni atom connection, as Cu and Ni are topologically equivalent. Hence, the average nearest neighbor distance in Vit105 is dominated by Zr-Zr and Zr-Cu/Ni atom connections.

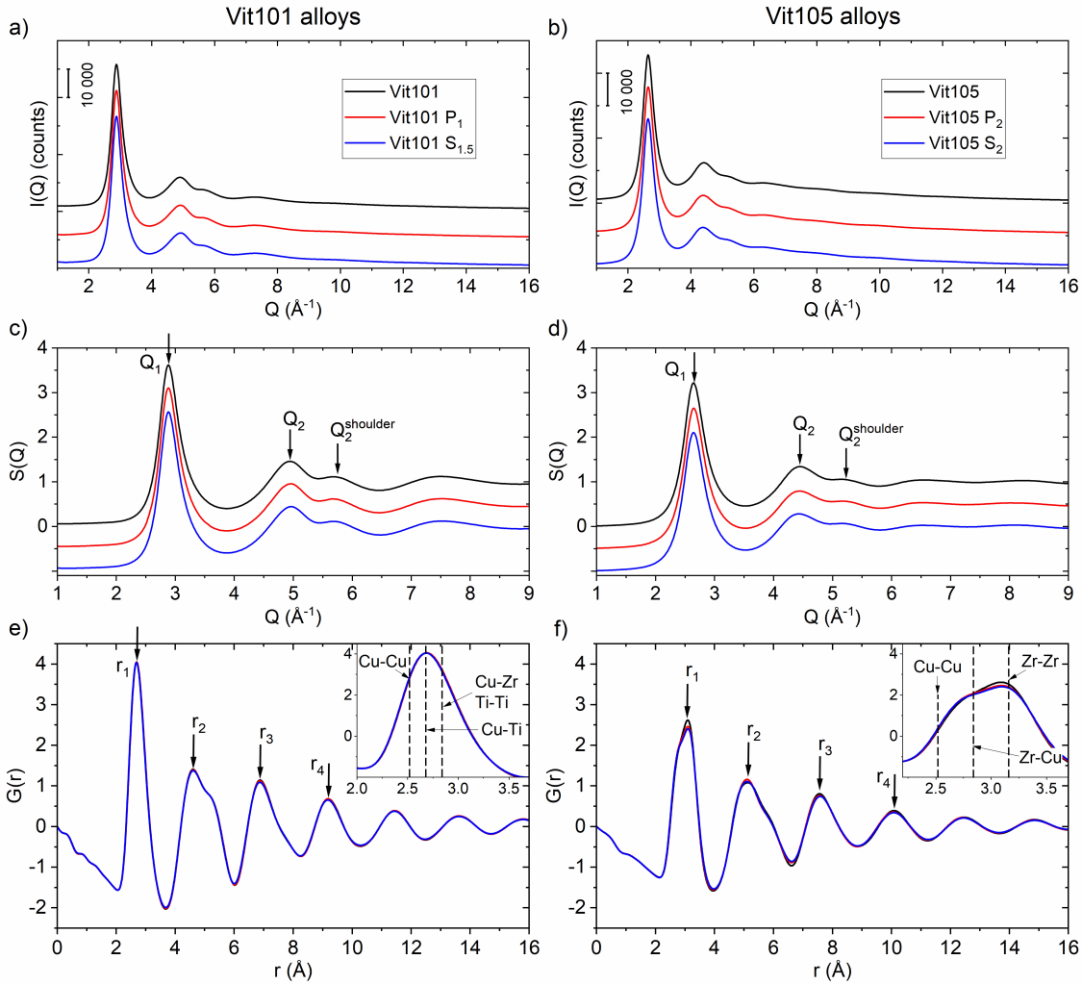

Figure 4.27: Overview of the data obtained from the synchrotron X-ray scattering experiments at 350 K. The Vit101 alloys are shown on the left and the Vit105 alloys on the right. **a)** and **b)** Scattering intensity I(Q), **c)** and **d)** Structure function S(Q), (vertically shifted), **e)** and **f)** Reduced pair distribution function G(r).

Table 4.7: Peak positions in S(Q) at 350 K and ratios.

Alloy	Q_1 [Å^{-1}] (350 K)	Q_2 [Å^{-1}] (350 K)	$Q_2^{shoulder}$ [Å^{-1}] (350 K)	Q_2/Q_1	$Q_2^{shoulder}/Q_1$
Vit101	2.883	4.945	5.685	1.72	1.97
Vit101 P_1	2.883	4.963	5.655	1.72	1.96
Vit101 $S_{1.5}$	2.884	4.974	5.685	1.72	1.97
Vit105	2.643	4.447	5.145	1.68	1.95
Vit105 P_2	2.647	4.439	5.170	1.68	1.95
Vit105 S_2	2.643	4.430	5.170	1.68	1.96

The total scattering structure functions, S(Q), from the in-situ heating and electrostatic levitation experiments are depicted in Fig. 4.28. During the heating experiments, amorphous samples were heated till crystallization occurred and during the ESL experiments, liquid samples were cooled until solidification (compare to Chapters 4.6.1 and 4.6.2). In this way, the maximum accessible temperature range for liquid and amorphous structures could be investigated, still resulting in a temperature gap between the high- and the low-temperature measurements due to crystallization. The S(Q) patterns are color-coded from red to blue for decreasing temperatures and magnifications of the first sharp diffraction peak (FSDP) and the second diffraction peak are shown in the insets. The patterns for Vit101 $S_{1.5}$ are shown in Fig. 4.28 a) and in b) for Vit105 S_2. The same depiction for Vit101 and Vit105 is given in Fig. A3 in the appendix, where also the low-temperature S(Q) patterns for Vit101 P_1 and Vit105 P_2 are provided (ESL experiments were not conducted on the P-containing alloys).

For all alloys, it is evident that the FSDP shifts to lower Q-values for increasing temperatures, indicating a temperature expansion of the structure. The position of the FSDP, Q_1, and the implications of its change with temperature will be discussed in the context of Fig. 4.29. Furthermore, upon heating, the peak intensity decreases, and the width of the peaks increases. Two effects are responsible for this phenomenon: a decreasing structural order and increasing atomic vibrations. Comparing the S(Q) patterns at low temperatures in the glassy state and at high temperatures in the liquid state, especially in the second diffraction peak clear differences are visible. The structure at low temperatures is more ordered and the shoulder indicating icosahedral SRO at around 5.75 Å^{-1} (for Vit101 $S_{1.5}$) is much more pronounced. This artefact becomes blurred out in the liquid state, indicating less structural order. Additionally, increasing atomic vibrations at high temperatures are responsible for the widening of the peaks. This phenomenon is described by the Debye-Waller factor [222], which accounts for decreasing scattering intensity due to thermal fluctuations which is then

observed as diffuse scattering. Ultimately, thermal fluctuations also cause disorder, as the atoms oscillate around their equilibrium position.

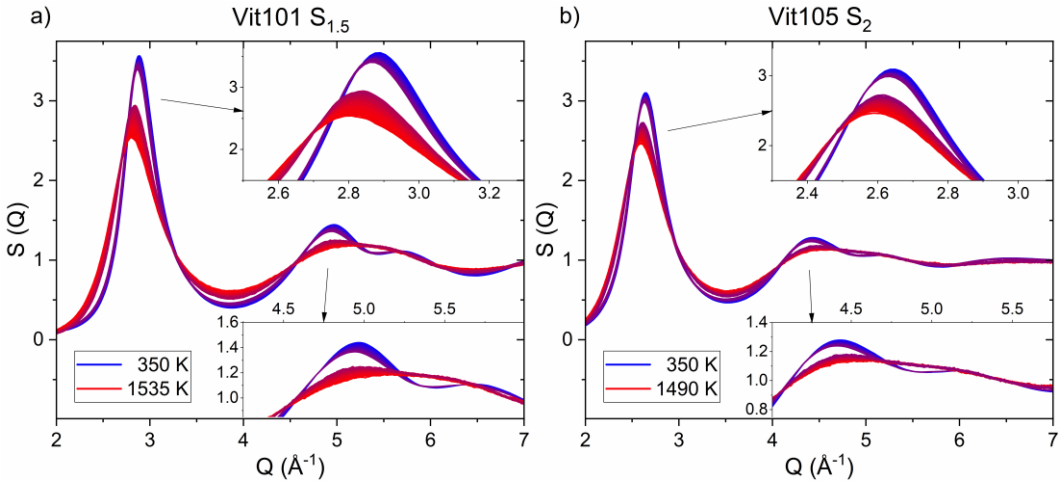

Figure 4.28: Total scattering structure functions, S(Q), from in-situ heating and electrostatic levitation experiments. The curves are color-coded from red to blue (hot to cold) and magnifications of the first and second peak are shown in the insets. **a)** Vit101 $S_{1.5}$ and **b)** Vit105 S_2.

The temperature evolution of the position of the FSDP, Q_1, was used to calculate the quantity $(Q_1(350K)/Q_1)^3$ as a function of temperature, as shown in Fig. 4.29. Following the argumentation of Yavari et al., the third power of the inverse of Q_1, normalized to Q_1 at a reference temperature T_{ref} in the glassy state, relates to the volume coefficient of thermal expansion, γ_{th}, according to [262]:

$$\left(\frac{Q_1(T_{ref})}{Q_1(T)}\right)^3 = \frac{V(T)}{V(T_{ref})} = 1 + \gamma_{th}\left(T - T_{ref}\right), \tag{4.1}$$

where V is the sample volume. This correlation holds true in the glassy state, but does not work in general in the SCL state [263–266]. The volume coefficient of thermal expansion, in the glassy state, γ_{th}^{glass}, resulting from this analysis is given in Table 4.8.

Figure 4.29 displays $(Q_1(350K)/Q_1)^3$, and hence the sample volume as a function of temperature over the whole measurement range for all alloys. The peak position of Q_1 at the reference temperature of 350 K used for normalization is given in Table 4.7. The Vit101 alloys are shown in Fig. 4.29 a) and the Vit105 alloys in b). The filled squares result from the low-temperature measurements which were performed in a resistive Linkam furnace and the dots result from the high-temperature measurements in the ESL. The gap between the datapoints is inevitable and is caused by crystallization. The data show, that within one alloy family a very similar thermal expansion coefficient is observed in the glassy state, which is roughly 4.0×10^{-5} K^{-1} for the Vit101 alloys and 3.3×10^{-5} K^{-1} for the Vit105 alloys (compare to Table 4.8).

At the glass transition, an increase in the slope can be noticed, indicating a larger coefficient of thermal expansion, as would also be expected from the classical volume-temperature curve (compare to Fig 2.1). The calorimetric glass transition temperature T_g is indicated by an arrow as a reference. Please note, that especially for the Vit105 alloys, a slight decrease in slope can be noted before the onset of the glass transition. This decrease in the thermal expansion coefficient is associated with the volume relaxation of the as-cast sample, which partly compensates thermal expansion. In the supercooled liquid state, the slope of the volume curve fits very well to the slope measured at high temperatures in the equilibrium liquid state. The liquidus temperature T_l is also indicated by an arrow.

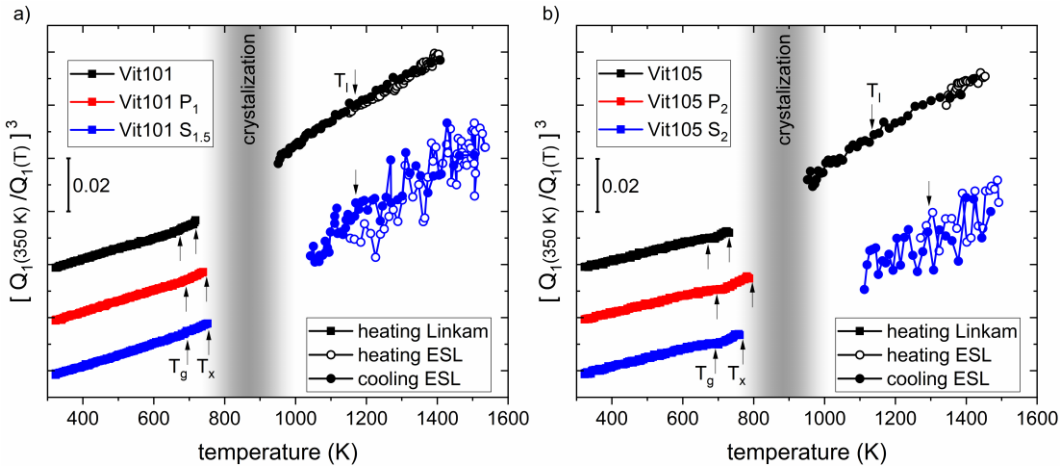

Figure 4.29: "Sample volume" in terms of $(Q_1(350K)/Q_1)^3$, as a function of temperature. The position of the FSDP, Q_1, is used to calculate the sample volume. The low-temperature data were measured in a Linkam furnace and the high-temperature data in ESL. Characteristic temperatures are indicated by arrows. **a)** Vit101 alloys, **b)** Vit105 alloys.

From the data presented in Fig. 4.29, it can be seen that the scatter in the datapoints for the Vit101 $S_{1.5}$ and the Vit105 S_2 alloy is significantly larger than for the other measurements. These two alloys were measured at the ESRF in Grenoble, whereas all other samples were measured at DESY in Hamburg, using a different detector. A comparison of the data quality is presented in Fig. 4.30, where S(Q) is shown in a) and G(r) in b). In the S(Q) data, a much stronger noise is observed in the measurements from ESRF, especially at higher Q-values. This noise explains the scatter in the datapoints for Vit101 $S_{1.5}$ and Vit105 S_2 in Fig. 4.29.

The maximum usable Q-range in the ESRF measurements is roughly $Q = 9$ Å^{-1} whereas the DESY data is usable up to $Q = 16$ Å^{-1}. Due to this limited Q-range, the transformation to obtain G(r) for the ESRF data is rather questionable. A small Q-range causes features like shoulders of the peaks to vanish, as was recently shown by Gross et al. [93] and also blurs out the peak shape, as can be observed in Fig. 4.30 b). Consequently, an evaluation of G(r) of the ESRF ESL data is not reasonable as

the exact peak positions are strongly affected by the limited Q-range. Nevertheless, the G(r) curves of Vit101 $S_{1.5}$ and Vit105 S_2 measured at ESRF are still shown in Fig. A4 c) and d) in the appendix.

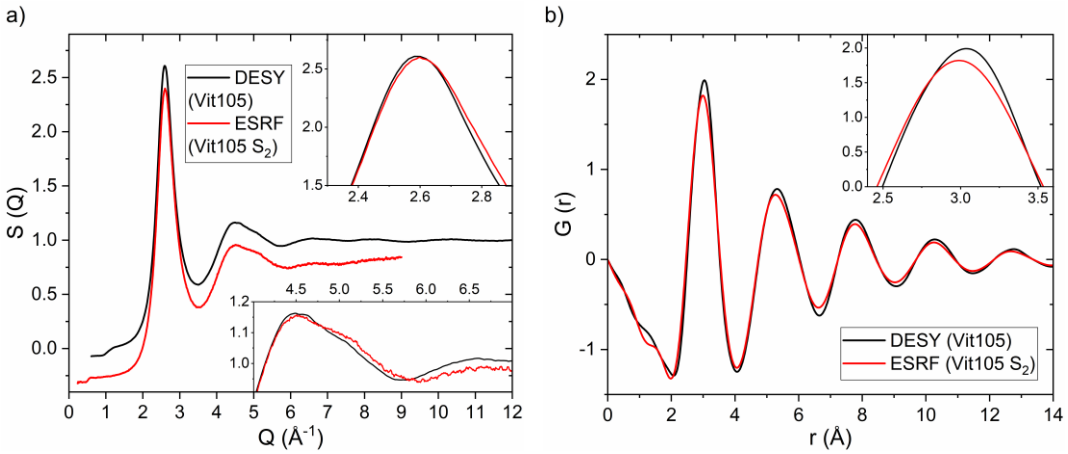

Figure 4.30: Comparison of the data quality of ESL synchrotron X-ray diffraction experiments at DESY (black) and ESRF (red). **a)** S(Q) and **b)** G(r).

For Vit101 and Vit105, the pair distribution function, G(r), was calculated for the low- and high-temperature measurements and is shown in Fig. 4.31 a) and b). The same color-coding as for the S(Q) data in Fig. 4.28 was used. The low-temperature data for the alloys with minor additions of P and S are depicted in Fig. A4 a) to d) in the appendix.

The insets in Fig. 4.31 show a magnification of the second peak, r_2, which represents the average weighted second nearest neighbor distance. For both alloys, a splitting of the second peak can be observed, which is typically caused by different second nearest neighbor distances of different prevailing structural units, as was also observed in various metallic liquids [93,267,268]. Molecular dynamics simulations reveal that the peak splitting is caused by distinct connection styles of the structural units, or atomic clusters, that determine the second nearest neighbor distance [107,269].

The position of the observed sub-peaks can be used to calculate the most likely connection schemes. The atomic clusters can typically share one to four atoms, as previously visualized in Fig. 2.9 c) on page 26. For simple topological considerations, the second nearest neighbor distance decreases if more atoms are shared. The second nearest neighbor distance, r_2, for different connection schemes is related to the observed average nearest neighbor distance, r_1, or rather the average bond length, as follows: 2 r_1 for a 1-atom connection, $\sqrt{3}$ r_1 for a 2-atom connection, $\sqrt{(3/8)}$ r_1 for a 3-atom connection, and $\sqrt{2}$ r_1 for a 4-atom connection [107,270]. The value of r_1 is obtained from the peak position of the first peak in G(r) and corresponds to the bond length of the Cu-Ti connection in the case of Vit101 and the Zr-Zr connection for Vit105, for the reasons discussed in the context of Fig. 4.27.

The different possible values for r_2, calculated according to the considerations above, are depicted as dashed lines in the insets in Fig. 4.31. For Vit101, two different connection schemes can clearly be identified in the low-temperature data: the two-atom connection scheme corresponding to the main peak and the one-atom connection corresponding to the shoulder. A certain amount of three-atom connections might also be present but are not dominant. In the case of Vit105, the three-atom connection scheme is prevailing, and the shoulder also corresponds to the one-atom connection. The three-atom connection scheme in Vit105 is a further indicator for icosahedral SRO, as the icosahedral cluster with 20 triangular faces facilitates three-atom connections (face-sharing) [107].

At elevated temperatures in the equilibrium liquid, the peaks in G(r) become more smeared out for the same reasons as discussed in the context of S(Q) in Fig. 4.28. The structure at high temperatures is less ordered and the cluster connection schemes are less defined. As already pointed out, increasing atomic vibrations at high temperatures are responsible for the blurring of the peaks.

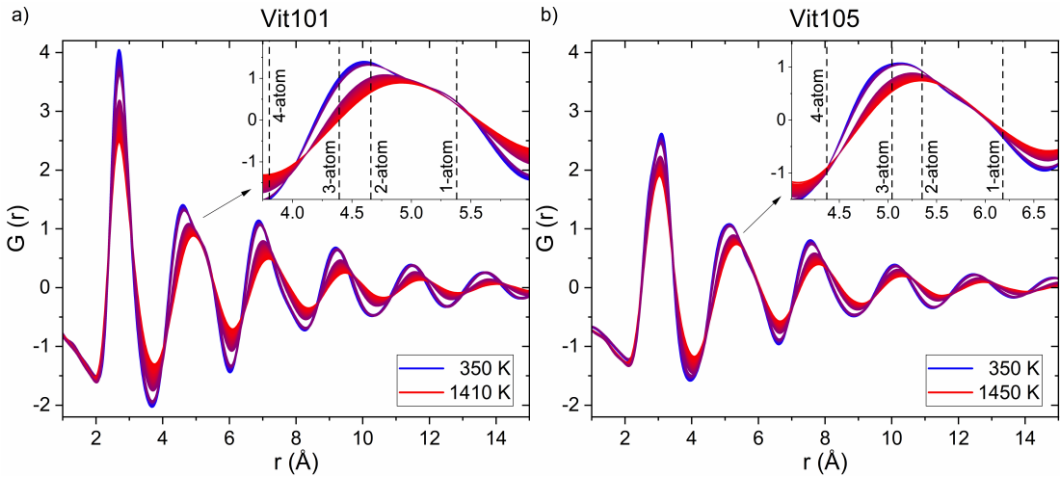

Figure 4.31: The pair distribution functions, G(r), from in-situ heating and electrostatic levitation experiments at different temperatures. The curves are color-coded from red to blue (hot to cold). The insets show a magnification of the second peak, r_2, which represents the average weighted second nearest neighbor distance. Calculated values for r_2 for different cluster connection schemes are depicted as dashed lines. **a)** Vit101 and **b)** Vit105.

The evolution of the peak positions with temperature of all peaks in G(r) was evaluated. For r_1, which corresponds to the average weighted nearest neighbor distance, the peak position normalized to the one at 350 K is depicted in Fig. 4.32 for all investigated alloys. The same information for r_3 and r_4 is presented in the same form in Fig. A5 in the appendix and discussed later in the context of the structure-fragility concept [79]. The values of r_1, r_3, and r_4 at 350 K used for the normalization are given in Table 4.8.

As shown in Fig. 4.32 a), in the case of the Vit101 alloys, r_1 increases linearly with temperature throughout the glassy state to the point where relaxation effects interfere with the thermal expansion behavior. An arrow indicates T_g', the temperature where the system enters the supercooled liquid state from a structural point of view [65] and is noted in Table 4.8. This temperature corresponds to the onset temperature of the SCL region as measured in a DSC scan [79]. In the SCL state, the slope of r_1 with temperature becomes negative, and in the case of Vit101, where high-temperature structural data is available, follows the same course as in the stable liquid.

The same information for the Vit105 alloys is displayed in Fig. 4.32 b). Here, the slope of r_1 with temperature is already negative in the glassy state, indicating a decreasing bond length with increasing temperature. At a first glance, this behavior seems unphysical, but is commonly observed in metallic glasses. However, this phenomenon might be explained by a decreasing coordination number upon heating [271,272]. Ding et al. additionally discussed the influence of the asymmetry of the shape of the first peak [273], which might also explain the abnormal peak shift. Recently, Sukhomlinov and Müser [274,275] showed that the mean bond length increases with temperature if the skewness of the first peak of the radial distribution function is taken into account.

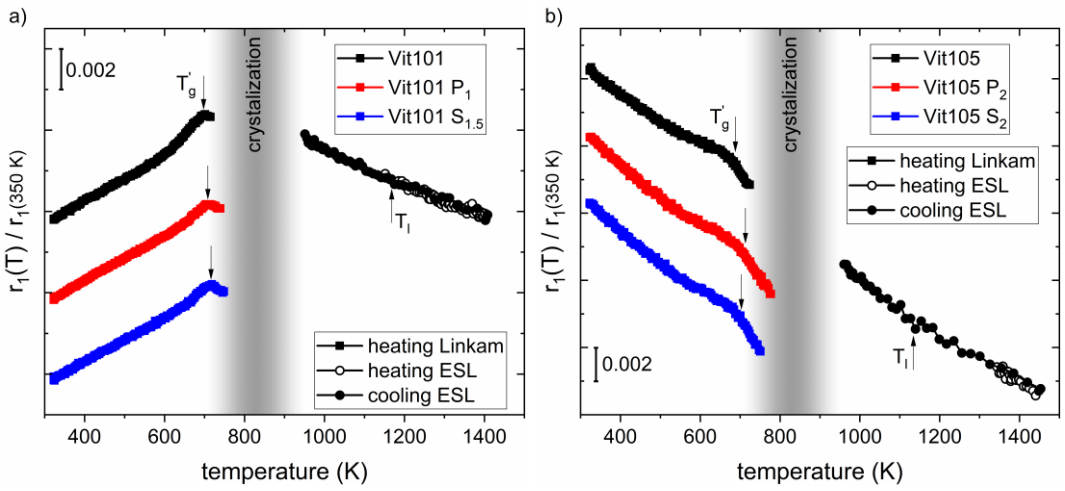

Figure 4.32: Average weighted nearest neighbor distance, r_1, obtained from the first peak position of G(r), as a function of temperature. r_1 is normalized to its value at 350 K and characteristic temperatures are indicated by arrows. The low-temperature data were measured in a Linkam furnace and the high-temperature data in ESL. **a)** Vit101 alloys, **b)** Vit105 alloys.

Table 4.8: Structural characteristics obtained from the in-situ synchrotron x-ray diffraction experiments.
Volume coefficient of thermal expansion in the glassy state, γ_{th}^{glass}; Temperature where the system enters the supercooled liquid state from a structural point of view, T_g'; Positions of the first, third, and fourth peak in G(r) at 350 K, r_1, r_3, and r_4; and the structural fragility parameter, $m_{str}^{V\,4\text{-}3}$, at low temperatures in the SCL region and at high temperatures in the stable liquid.

Alloy	γ_{th}^{glass} [10^{-5} K^{-1}]	T_g'[K]	r_1 [Å] (350 K)	r_3 [Å] (350 K)	r_4 [Å] (350 K)	$m_{str}^{V4\text{-}3}$ (low T)	$m_{str}^{V4\text{-}3}$ (high T)
Vit101	3.9	699	2.69	6.88	9.19	0.0093	0.0898
Vit101 P_1	4.1	708	2.69	6.87	9.18	0.0015	
Vit101 $S_{1.5}$	4.2	716	2.68	6.87	9.18	0.0129	
Vit105	3.3	688	3.09	7.56	10.08	0.0196	0.0510
Vit105 P_2	3.2	713	3.09	7.57	10.06	0.0287	
Vit105 S_2	3.3	703	3.10	7.58	10.08	-0.0079	

The temperature evolution of G(r) can also be used to assess the fragility of metallic glass-forming systems. Wei et al. developed a correlation linking the fragility to the following structural metric [79]:

$$\delta = -\frac{\Delta V_{4-3}(T)}{\Delta V_{4-3}(T_g')} = -\frac{V_{4-3}(T) - V_{4-3}(T_g')}{V_{4-3}(T_g')}, \tag{4.2}$$

$$V_{4-3}(T) = \frac{4}{3}\pi\,[r_4(T)^3 - r_3(T)^3]\,, \tag{4.3}$$

where δ can be understood as the temperature-induced structural dilatation on the length scale of around three to four atomic diameters, which corresponds to the medium-range order (MRO) length scale (~1 nm). $V_{4\text{-}3}(T)$ is the volume corresponding to a spherical volume shell between the fourth and the third peak position in G(r), hence r_4 and r_3. T_g' is the temperature where the system enters the supercooled liquid state from a structural point of view. The structural fragility parameter $m_{str}^{V\,4\text{-}3}$ is then defined as [79]:

$$m_{str}^{V\,4-3} = \left.\frac{d\,\delta}{d(T_g'/T)}\right|_{T=T_g'}, \tag{4.4}$$

hence, the slope of δ plotted over T_g'/T at $T=T_g'$. Consequently, the kinetic fragility or the temperature induced change in viscosity is related to structural changes on the MRO length scale. This assumption fits well into the concept of dense-packed clusters with a size of around 1 nm that cause the viscous slowdown due to aggregation of said structural units [65].

The concept of the structure-fragility relation is also applied to the alloys investigated in this work. The underlying data, hence, the temperature-induced peak shift of r_3 and r_4 in G(r) is shown in Fig. A5 in the appendix. Only the datapoints in the SCL state are taken into account, which are the points above T_g'. Depending on the alloy composition, only a very limited amount of datapoints is available, before crystallization starts. Figure 4.33 a) shows a magnification of these points for Vit101 $S_{1.5}$ for r_3 and r_4. The black open symbols correspond to the raw data where a certain amount of scatter is present. The resulting δ-values are displayed as black open squares in Fig. 4.33 b). In order to reduce scatter in the δ-values, the r_3 and r_4 data is smoothed using a Savitzky-Golay filter with a five point window, leading to the red datapoints shown in Fig. 4.33 a). Using these points, the δ-values shown in red in Fig. 4.33 b) are obtained, drastically reducing the scatter. At the same time, the linear fit of the datapoints remains the same before and after smoothing, proving the applicability of this procedure. The r_3 and r_4 data of all samples was smoothed like this before calculating the δ-values.

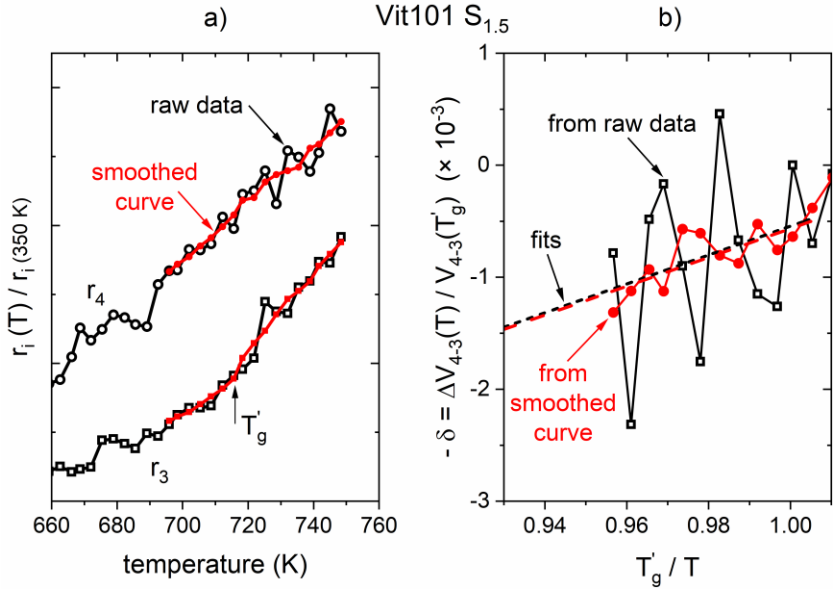

Figure 4.33: Smoothing procedure for the r_3 and r_4 datapoints in the SCL region in the case of Vit101 $S_{1.5}$. **a)** r_3 and r_4 raw datapoints (black) and smoothed datapoints (red). **b)** Resulting δ-values for the raw and smoothed datapoints. The linear fit remains the same while the scatter of the datapoints is significantly reduced.

Figure 4.34 a) and b) show the δ-values of the six investigated alloy compositions in the SCL region upon heating, calculated according to Eq. 4.2. The data is displayed on an inverse T_g'-scaled temperature scale. With increasing length of the SCL region, more datapoints could be obtained. The solid lines in the color of the datapoints are linear fits defining the structural fragility parameter $m_{str}^{V\,4\text{-}3}$ according to Eq. 4.4, and the obtained values can be found in Table 4.8. The kinetically rather fragile $Pt_{42.5}$ alloy ($Pt_{42.5}Cu_{27}Ni_{9.5}P_{21}$, D*=15.3) [24] is shown as a reference. In comparison to this reference, both, the Vit101 alloys and the Vit105 alloys, show a rather weak dependence of δ with temperature, indicating a stronger fragility behavior. It should be noted that the δ-values are only available in a short temperature interval in the case of the Vit101 alloys due to the onset of crystallization and show some kind of deviation from a linear behavior for the Vit105 alloys. Consequently, the structure-fragility correlation should be interpreted with caution in this case.

The structural fragility parameters, $m_{str}^{V\,4\text{-}3}$, obtained from the data in Fig. 4.34 a) and b), are included in the correlation found by Wei et al. [79] in Fig. 4.34 c). $m_{str}^{V\,4\text{-}3}$ is plotted on the ordinate, whereas the kinetic fragility index, m, (compare to the values in Table 4.6) is plotted on the abscissa. The reference data from Wei et al. is shown in light grey, the Vit101 alloys are shown as filled points, and the Vit105 alloys as open symbols. These datapoints result from measurements in the low-temperature SCL region.

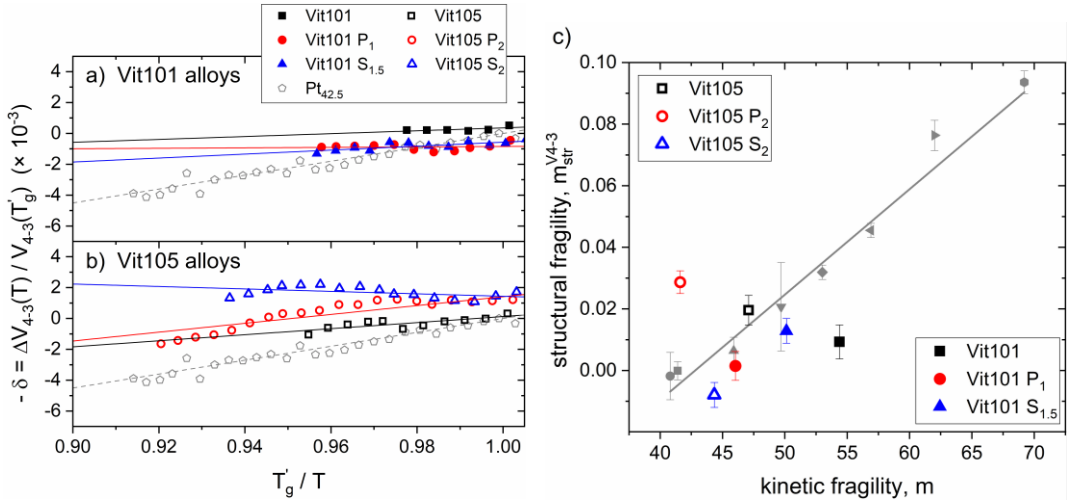

Figure 4.34: a) Vit101 alloys and **b)** Vit105 alloys: Structural dilatation on the MRO length scale in terms of δ, calculated according to Eq. 4.2. The data is shown over inverse temperature, normalized to T_g'. The solid lines in the color of the datapoints are linear fits defining the structural fragility parameter $m_{str}^{V\,4\text{-}3}$ according to Eq. 4.4. The datapoints for $Pt_{42.5}$ are shown as a reference [79]. **c)** Correlation between the structural fragility parameter, $m_{str}^{V\,4\text{-}3}$ and the kinetic fragility index, m. The grey reference points are taken from Refs. [24,79] and represent Zr- and Pt-based BMGs.

The graph shows, that the new data roughly follows the correlation, while especially Vit101 and Vit105 P_2 display a slightly larger offset. In the case of Vit101, the deviation is most likely caused by the extremely short SCL region, not permitting a long enough measurement range to obtain reliable data. In the case of Vit105 P_2, the observed slope of δ as a function of inverse temperature is steeper than expected by the structure-fragility correlation. The δ-values show some kind of S-shape, deviating from the expected linear behavior in the SCL region. This artefact is either caused by scatter in the raw data or by a beginning decomposition of the system, as was previously discussed in Chapter 4.4 in the context of the isothermal viscosity measurements in the SCL region. Nevertheless, the overall trend of the structure-fragility correlation in the SCL region can be validated by our measurements.

In the case of Vit101 and Vit105, the pair distribution function, G(r), is also available at high temperatures in the stable liquid. The structural dilatation on the MRO length scale, δ, of these two systems at high temperatures is depicted in Fig. 4.35 a), together with the previously shown low-temperature data. The linear fit to the high-temperature ESL data is displayed as a dashed line and the resulting slope, corresponding to the structural fragility parameters, $m_{str}{}^{V\,4\text{-}3}$, is written into the figure. The observed slope in Vit101 ($m_{str}{}^{V\,4\text{-}3} \approx 0.09$) is significantly steeper than in Vit105 ($m_{str}{}^{V\,4\text{-}3} \approx 0.05$), indicating a more fragile behavior in the liquid state. This tendency is in good agreement with the more fragile behavior of Vit101 in the SCL region around T_g. Furthermore, for both compositions, the slope in the stable liquid is much steeper than in the SCL region.

Figure 4.35 b) shows the same depiction as 4.34 c), hence the correlation between the structural fragility parameter, $m_{str}{}^{V\,4\text{-}3}$ and the kinetic fragility index, m. However, here the values for Vit101 and Vit105 at high temperatures in the stable liquid are included. The obtained $m_{str}{}^{V\,4\text{-}3}$-values are indicated by horizontal arrows and the fitting uncertainty is represented by the shaded area around the arrows. Following the correlation by Wei et al. [79] (grey line), a kinetic fragility index for the high-temperature liquid can be predicted. For Vit101 this value is roughly m = 69, which corresponds to D* = 11.3; and for Vit105 it is m = 58, and D* = 14.3.

Following the observations and argumentations by Stolpe et al. [65] on the structure-fragility correlation in the presence of a strong-to-fragile (SF) liquid-liquid transition (LLT), the difference in structural fragility at high and low temperatures could indicate such a transition. However, in our work, the high- and low-temperature datapoints are separated by crystallization and a possible transition cannot directly be observed in the measurements. The GFA of the investigated alloys is simply not high enough to cool the liquid sample into the glassy state during the ESL experiments, and hence crystallization takes place and prohibits the measurement of a continuous dataset. The possible existence of a LLT in the investigated alloys is further discussed in Chapter 4.7, based on the combined viscosity data at high and low temperatures. Additionally, the structural fragility data at high temperatures is combined with the observations made from viscosity measurements.

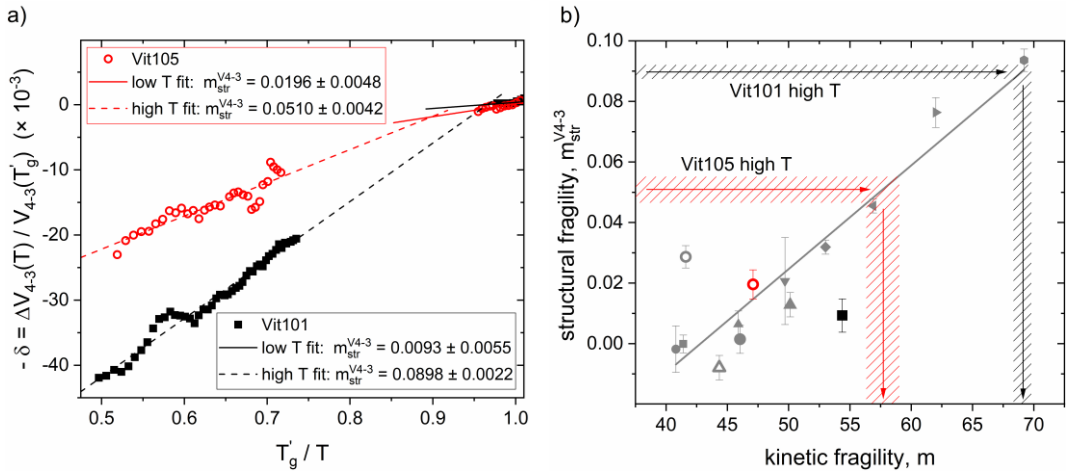

Figure 4.35: a) Structural dilatation on the MRO length scale in terms of δ in the stable liquid and the SCL state, shown over inverse temperature, normalized to T_g'. Linear fits define the structural fragility parameter $m_{str}^{V\,4\text{-}3}$ for Vit101 and Vit105. **b)** Correlation between the structural fragility parameter, $m_{str}^{V\,4\text{-}3}$ and the kinetic fragility index, m, for the high-temperature stable liquid state. The obtained $m_{str}^{V\,4\text{-}3}$-values for Vit101 and Vit105 and the predicted values for m are indicated by the shaded areas and arrows. The previously shown low-temperature data is displayed as reference.

4.7 Summary and Discussion

All of Chapter 4 was dedicated to a thorough analysis on the influence of minor additions of sulfur (S) and phosphorus (P) on the Cu-Ti-based bulk metallic glass-forming alloy Vit101 and the Zr-based alloy Vit105, both of which are highly interesting candidates for industrial applications. Different experimental results, including the thermodynamic properties, low- and high-temperature viscosity, crystallization behavior upon heating and cooling, as well as structural data, were presented and discussed individually. In this Chapter, a short summary of the most important findings is presented and cross-connections between the different sections are discussed. Further conclusions, especially regarding thermal stability, glass-forming ability (GFA), kinetic fragility at low and high temperatures, and the implications in terms of a possible strong-to-fragile (SF) liquid-liquid transition (LLT) are presented.

Minor additions of S and P in Vit101 and Vit105 – a first summary

DSC scans on Vit101 and Vit105 alloys with minor additions of S and P showed a significant enhancement of the thermal stability in terms of the SCL region upon heating. In the case of Vit101, both modified systems display a roughly 15 K longer SCL region than the base alloys, and for Vit105 the SCL region was extended by 28 K

with the addition of S and by 40 K with P. These findings already indicate an enhanced thermoplastic formability of the modified alloys, as will be evaluated in Chapter 6. In all cases, the glass transition temperature is raised by around 20 K due to the additions.

An analysis of the critical casting thickness, and hence the GFA, showed that for Vit101 S-additions increase the critical thickness from 5 mm to 6 mm and P-additions leave it unchanged. In the Vit105 system, S-additions decrease the critical thickness from initially 8 mm to 6 mm, and P-additions lower it to even 3 mm. Surprisingly, the critical casting thickness of the Vit101 alloys remains unchanged if industrial grade Zr and Ti are used. For both, Vit105 and Vit105 S_2 made from industrial grade materials, the critical casting thickness is reduced to 5 mm, and therefore the same as for the Vit101 alloys.

Three-point beam bending tests revealed that minor additions in the Vit101 system cause an embrittlement. The same effect is observed for Vit105 P_2, whereas the Vit105 S_2 alloy shows the same amount of ductility as the base alloy, combined with a slight increase in hardness, reaching a value of around 530 HV, and strength, reaching a value of around 2800 MPa.

In summary it can be said, that minor additions allow for distinct modifications of an alloy without completely changing the characteristics of the alloy family. Most modifications result in a tradeoff between different properties, e.g. an extended SCL region can go along with a reduced GFA. The most important characteristic values of the investigated alloy compositions are summarized in Table A1 (Vit101 alloys) and in Table A2 (Vit105 alloys) in the appendix in the form of a datasheet.

Thermal stability and crystallization behavior upon heating

The thermal stability of amorphous alloys in the low-temperature regime around the glass transition is the decisive property determining the processing window for thermoplastic forming regarding time and temperature. It is defined by a complex interplay between kinetics, driving forces for crystallization and the primary crystallizing phase.

A simple DSC scan can already provide a first idea of the thermal stability in terms of the length of the SCL region, and a better overview is provided by the TTT diagram, as presented in Chapter 4.3 in Fig. 4.9. From these results we learn that minor additions of S and P significantly enhance the thermal stability of the investigated alloys. In the case of the Vit101 alloys, the time till the onset of crystallization at an isothermal temperature of $1.1 \times T_g$ is roughly three times longer in Vit101 P_1 and Vit101 $S_{1.5}$ than in Vit101. For Vit105 S_2 the time to crystallization is also three times longer as for Vit105 and for Vit105 P_2 it is even eight times.

From a kinetic point of view, the enhanced stability of the SCL region in the modified alloy compositions is reasonable. Both, Vit101 and Vit105 are kinetically more fragile than their modified counterparts, hence, their viscosity drops more rapidly when

exceeding the glass transition temperature (compare to Fig. 4.14). Especially for the Vit105 alloys, the length of the SCL region directly correlates with the kinetic fragility of the alloy, with the kinetically strongest alloy, Vit105 P_2, showing the longest SCL region. Upon heating, viscosity, and at the same time the atomic mobility of the system, drops less quickly, hampering the onset of the crystallization process.

The driving force for crystallization is represented by the Gibbs free energy difference, $\Delta G^{l\text{-}x}$, between the liquid and the crystal, as depicted in Fig. 4.8 e) and f). The value at the fictive temperature, T_{fic}, for each composition is noted in Table 4.4. A higher value of $\Delta G^{l\text{-}x}$ indicates a higher driving force for crystallization and hence a tendency for a decreased thermal stability of the SCL region. Accordingly, for both alloy systems, the alloy with the longest SCL region (Vit101 $S_{1.5}$ and Vit105 P_2) features the lowest $\Delta G^{l\text{-}x}$-value. Furthermore, the Vit101 alloys all display higher $\Delta G^{l\text{-}x}$-values than the Vit105 alloys and at the same time show a much smaller SCL region.

The last factor determining thermal stability is the interfacial energy between the liquid and the primary crystallizing phase, and hence the nature of the primary crystallizing phase plays a crucial role. The interfacial energy itself is difficult to measure and an indirect assessment as done in Ref. [202] is difficult and not possible in our case. It requires a complete TTT diagram at low and high temperatures that then can be fitted with a Johnson-Mehl-Avrami-Kolmogorov equation (Eq. 2.25), where the interfacial energy results as a fitting parameter. While in our case we do not have access to the necessary dataset, structural in-situ diffraction data is available and the different primary crystallizing phases upon heating were identified in Chapter 4.6.1.

In the case of the Vit101 alloys, the primary crystallizing phase remains unchanged with the minor additions. Most likely, a $ZrTiCu_2$ Laves phase forms initially upon heating in all three compositions. For the Vit105 alloys, drastic changes can be observed when S and P are added. The Vit105 base alloy shows clear indications of phase separation and decomposition on the nanometer scale before the formation of a Zr_2Ni phase is observed. In this case, the thermal stability of the system is limited by the decomposition. In Vit105 S_2, a ZrTiNi Laves phase can be identified as primary crystallizing phase and no previous phase separation is detected, thus extending the thermal stability of the system. The addition of P in the case of the Vit105 P_2 alloy also suppresses the formation of the Laves phase, further extending the SCL region.

In general, the increase in thermal stability in the alloys with minor additions is well in line with the effect of the minor additions on the kinetics (kinetic fragility) and the driving force for crystallization ($\Delta G^{l\text{-}x}$). Furthermore, in the case of Vit105, the suppression of phase separation significantly increases the thermal stability in the systems with minor additions in comparison to the base alloy.

Glass-forming ability – different influencing factors

The same factors influencing thermal stability in the low-temperature SCL region also determine the GFA of the alloy when quenching the melt, however in a different temperature region than discussed before. Basically, the GFA depends on the thermal stability against crystallization throughout the whole temperature range between the liquidus temperature and the glass transition. The critical point for the GFA of an alloy and hence its critical cooling rate is the position of the tip of the so-called crystallization nose (see Chapter 2.1.5), which needs to be bypassed upon cooling.

Regarding kinetics and atomic mobility, viscosity in the liquid state is the decisive property that could be measured within this work. While viscosity data is not available throughout the whole temperature range due to beginning crystallization, the Couette viscosity measurements around the liquidus temperature provide a good first insight. In general, the Vit105 alloys show a three times higher viscosity at their liquidus temperature than the Vit101 alloys, providing one reason for the better GFA of Vit105 in comparison to Vit101. The viscosity of Vit105 at T_l is roughly 100 mPa s, and hence more than one order of magnitude higher than the one of most pure metals, but similar to the viscosity of Fe-based BMGs [48]. The course of viscosity throughout the complete temperature range and its implications on the kinetic fragility of the system are discussed in the next section.

The discussion concerning the driving force for crystallization remains similar to the one for thermal stability. The decisive quantity determining ΔG^{l-x} upon cooling below T_l is the difference in entropy between the liquid and the crystal, ΔS^{l-x}, as it determines the slope of the ΔG^{l-x}-curve. For the Vit101 alloys, Vit101 $S_{1.5}$ is the alloy with the longest SCL region and at the same time the highest GFA, which is in good agreement with its lower driving force for crystallization in comparison to Vit101 and Vit101 P_1. In the case of the Vit105 alloys, these correlations do not hold true. Even though Vit105 P_2 shows the lowest ΔG^{l-x}-values, it possesses the lowest GFA. Hence, the reduced GFA is most likely caused by a change in the primary crystallizing phase and a reduced nucleation barrier.

The final component influencing the GFA is the primary crystallizing phase and the interfacial energy between the liquid and that crystal. A change in the alloy composition, e.g. by minor additions, can alter the phase that first forms upon cooling. In this work, the structure of the primary phases which forms during the cooling process could be investigated by in-situ synchrotron X-ray diffraction experiments in an electrostatic levitator, resulting in a valuable and hard to get dataset.

In the Vit101 system, the addition of 1.5 at% S suppresses the formation of the $ZrTiCu_2$ Laves phase that forms in unmodified Vit101. In the Vit101 $S_{1.5}$ alloy, first the formation of a very small amount of a Ti-S phase is observed. However, this phase does not trigger the crystallization of the remaining liquid and rather suppresses the Laves phase. Therefore, an increased GFA of the remaining liquid phase could be observed. Minor additions of small metalloid atoms are often found to improve the

GFA, as they supposedly tighten the structure of the melt [10] and sulfur might act in a similar way. It might as well be, that isolated Ti-S crystals are present in an otherwise completely amorphous structure when Vit101 $S_{1.5}$ samples with a large diameter are produced. These artifacts could be a possible explanation for the embrittlement of the Vit101 $S_{1.5}$ samples in comparison to Vit101.

In the Vit105 system, minor additions of S and P reduce the GFA and P even acts as poison for the GFA, reducing the critical casting thickness from at least 8 mm to 3 mm. As no ESL synchrotron diffraction data are available for Vit105 P_2, the author can only speculate that P triggers the formation of crystalline metal-phosphide particles that act as heterogeneous nucleation sites. If their fraction is small, they might not even be visible in the DTA heat flow signal and their presence could possibly explain the rather steep increase in melt viscosity (compare to Fig. 4.18 b)) before falling below the nominal liquidus temperature.

In the case of Vit105 S_2, the formation of a S-containing phase (possibly $Zr_{21}S_8$) upon cooling can be verified by the ESL synchrotron measurements. Additionally, a shoulder is visible in the DTA curves, significantly increasing the liquidus temperature. The effects of this S-stabilized phase are also visible in the high-temperature viscosity measurements, where a kink in the viscosity curve is visible at around 1200 K (compare to Fig. 4.16 b)). This phase causes a premature onset of crystallization and decreases the GFA of the Vit105 S_2 alloy composition.

Viscosity, kinetic fragility, and liquid-liquid transition

In this work, viscosity was measured by two different techniques in two different temperature regimes: by three-point beam bending (3PBB) in a thermomechanical analyzer (TMA) at low temperatures around the glass transition, and by Couette rotating cylinder rheometry at high temperatures in the stable liquid. Before, both datasets were discussed individually and are now combined with the purpose of describing the course of viscosity over the full temperature range. Due to crystallization, a temperature gap of at least 400 K divides the high- and the low-temperature data. Within this gap, viscosity can only be estimated by different viscosity models (compare to Chapter 2.1.4) that are fitted to the data.

In total, six different fitting procedures were applied to the datasets of the six investigated alloys. Within the main text of this work, the dataset for Vit105 S_2 is examined as an example and presented in detail, while the results for all other alloys can be found in the appendix. Figure 4.36 shows the viscosity fits for Vit105 S_2, where the viscosity datapoints from 3PBB TMA measurements at low temperatures and from Couette measurements at high temperatures are displayed (black squares) over inverse temperature. Here, the large temperature gap between the measurements becomes apparent. The horizontal dashed line indicates a viscosity of 10^{12} Pa s, representing the kinetic glass transition at T_g*. The slope of the fitting curve at this temperature is given by the m-fragility index (Eq. 2.11) and defines the fragility of the system.

Figure 4.36 a) displays three different Vogel-Fulcher-Tammann (VFT) fits according to Eq. 2.9. The VFT fit to the low-temperature data (VFT fit low T, blue line) corresponds to the fit previously shown in Fig. 4.13. Here, the infinite temperature limit of viscosity η_0, was fixed at 3.558×10^{-5} Pa s due to the lack of datapoints at high temperatures. This procedure resulted in an m-fragility index of 44.3, indicating a kinetically strong liquid behavior. The red line indicates the VFT fit only to the high-temperature data (VFT fit high T), where viscosity in the low-temperature regime was pinned at $T_g^* = 684$ K and a value of 10^{12} Pa s, in agreement with the results from the low-temperature fit. The η_0-value remains fixed at 3.558×10^{-5} Pa s and an m-fragility of 79.1 is obtained, indicating a much more fragile behavior. The exact same fitting procedure was previously applied in several publications on the topic of strong-to-fragile (SF) liquid-liquid transitions (LLT) [48,65,66] and is therefore reproduced here and discussed in the next paragraphs. The last curve displayed in Fig. 4.36 a) (dashed grey line) corresponds to a VFT fit of all datapoints over the whole temperature range. For this fit, the η_0-value is left free as a fitting parameter, resulting in a much smaller value of 0.024×10^{-5} Pa s. All fitting parameters and characteristic values are written down in Table 4.9.

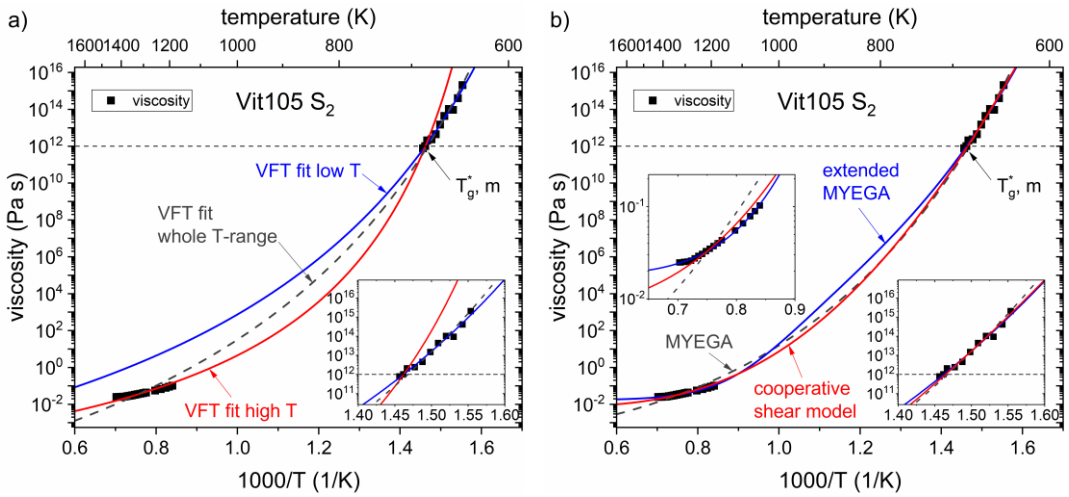

Figure 4.36: Viscosity fits for Vit105 S_2. Viscosity datapoints from 3PBB TMA measurements at low temperatures and from Couette measurements at high temperatures are displayed (black squares) over inverse temperature. The horizontal dashed line indicates a viscosity of 10^{12} Pa s, representing the kinetic glass transition at T_g^*. **a)** Three different VFT fits, one only on the low-temperature data (blue), one on the high-temperature data (red), and one on all datapoints (dashed grey). **b)** MYEGA fit (dashed grey), extended MYEGA fit (blue), and fit according to the cooperative shear model (red).

In the case of the VFT fit over the whole temperature range, it is clearly visible that the fitting equation does not well describe the course of viscosity at high temperatures, while it follows the datapoints at low temperatures rather well (compare to the inset in Fig. 4.36 a)). The slope of the VFT fit at high temperatures is too steep and an unphysically low η_0-value is obtained. If the η_0-value is fixed to 3.558×10^{-5} Pa s, the quality of the fit is even worse, proving that the VFT equation is not adequate to describe the course of viscosity over the whole temperature range in the investigated system.

On the other hand, when the low- and the high-temperature data is fitted individually, a distinctly different kinetic fragility behavior is observed, with a stronger one at low temperatures and a more fragile one at high temperatures. The same phenomenon is observed in a variety of metallic glass-forming liquids, including Zr-based alloys [62–65], Fe-based alloys [48,66], and La-based alloys [59,70]. Typically, the observed kinetic crossover is explained by a strong-to-fragile (SF) liquid-liquid transition (LLT), as is also further discussed in Refs. [60,61,64,67,276]. In our case, the very same phenomenon of a kinetically strong low-temperature liquid and a fragile high-temperature liquid is observed in all six alloy compositions, as shown in Fig. A6 in the appendix. These findings indicate a SF crossover somewhere in the temperature range that is obscured by crystallization. However, without additional data in the non-accessible temperature region, no further proof can be given. Furthermore, other viscosity models can be fitted to the data that better describe the observed behavior without necessarily introducing a SF LLT, as will be discussed now.

Table 4.9: Viscosity fitting parameters of Vit105 S_2 for the fits shown in Fig. 4.36.

	VFT		VFT low T	VFT high T	VFT whole range	Cooperative shear model		
D*			22.3 ±1.7	9.9 ±0.1	24.4 ±3.3	n		1.25
T_0	[K]		430.3 ±11	541.7 ±1.8	434.4 ±17	T_g*	[K]	682.9
η_0	[10^{-5}Pa s]		3.558 [1)]	3.558 [1)]	0.024	η_0	[10^{-5}Pa s]	698.3
m			44.3	79.1	51.4	m		49.5
T_g*	[K]		684.0	684.0	681.4			

MYEGA			Extended MYEGA					
			High T, fragile liquid			Low T, strong liquid		
B	[K]	1270.7	W_1	[K^{-1}]	20.18	W_2	[10^{-4} K^{-1}]	9.86
C	[K]	1481.4	C_1	[K]	12092	C_2	[K]	1526.8
η_0	[10^{-5}Pa s]	4.097	η_0	[10^{-5}Pa s]	1703			
m		52.0	m		186.0	m		44.7
T_g*	[K]	681.5	T_g*	[K]	967.2	T_g*	[K]	683.9

[1)] fixed for fitting

Figure 4.36 b) displays fits of three other viscosity models to the high- and low-temperature data of Vit105 S_2. The fit according to the MYEGA (Mauro, Yue, Ellison, Gupta, Allan) equation (Eq. 2.13) is shown as dashed grey line. The model is said to provide physically reasonable values for the infinite temperature limit of viscosity η_0, which in this case is obtained as 4.1×10^{-5} Pa s and is close to the values used for the VFT fits. The fitting results show that the low-temperature viscosity behavior is indeed following the datapoints quite well and an m-fragility value of 52.0 is obtained, indicating a rather strong liquid behavior. At high temperature however, the slope of the fitting function is too steep, not representing the real measurement data. This behavior is similar to the problems experienced with the VFT equation.

The next fitting function applied to the viscosity data is the cooperative shear model (Eq. 2.15) which was developed by Demetriou et al. in 2006 [56]. They report that their model fits especially Newtonian viscosity data better than the VFT law. The fitting results in Fig. 4.36 b) (red line) follow the datapoints very well. Especially at high temperatures, it agrees much better with the data than the VFT and the MYEGA fits. The m-fragility value is found to be 49.5, according to Eq. 2.16, and hence very similar to the one from the MYEGA fit. All fitting parameters are found in Table 4.9.

The cooperative shear model fits the viscosity data very well over the whole temperature range. It does not indicate the presence of a LLT anywhere in-between the high- and the low-temperature measurements. It is interesting to note that the infinite temperature limit of viscosity η_0, as obtained from the fit to the cooperative shear model, is around 7 mPa s, and hence two orders of magnitude higher than the value obtained from the MYEGA equation and assumed for the VFT fits. While this value is rather high, it still seems reasonable for a densely packed, highly viscous bulk metallic glass-forming liquid, where the infinite temperature limit might well be much higher than in one-component monoatomic liquids.

The last model fitted to the viscosity data is the extended MYEGA model [59]. It was developed by Mauro and coworkers in 2010, and accounts for a strong and a fragile contribution in metallic glass-forming systems that display a SF transition. The fit to the extended MYEGA model from Eq. 2.17 is drawn as blue curve in Fig. 4.36 b). The fit perfectly follows the datapoints at high and low temperatures, representing especially the course of viscosity at high temperatures better than all previously applied models.

In order to ease the discussion of the strong and the fragile contribution in this five-parameter model, both are plotted individually in Fig. 4.37. The complete extended MYEGA fit is shown in black, the kinetically strong low-temperature contribution in blue, and the fragile high-temperature contribution in red. The horizontal dashed line indicates a viscosity value of 10^{12} Pa s, hence the threshold value for the kinetic glass transition. As discussed in Ref. [59], the strong and the fragile liquid phase would obviously display two different glass transition temperatures, where only the glass transition region of the low-temperature strong liquid is experimentally accessible.

Both temperatures are given in Table 4.9, together with the m-fragility values and the fitting parameters. Based on this model, the hypothetical glass transition of the fragile phase would occur at much higher temperatures (967 K) than the one of the strong phase (684 K). Given that both liquids possess the same composition, a change in the kinetic glass transition temperature of 283 K seems unphysical and calls the extended MYEGA model into question. For the fragile phase, the viscosity curve would show a much steeper increase, resulting in an m-fragility index of 186, in comparison to the value of 44.7 for the strong liquid. At this point it should be mentioned, that the course of the strong liquid part of the extended MYEGA model almost perfectly coincides with the VFT fit of the low-temperature data, which is displayed as a dashed grey line.

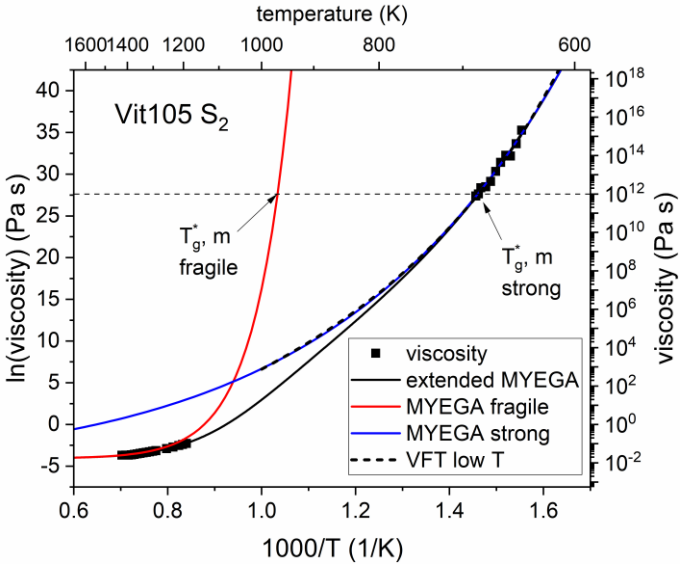

Figure 4.37: Extended MYEGA viscosity fit for Vit105 S_2. The fitting function (black line) consists of two parts, a fragile high-temperature contribution (red), and a strong low-temperature contribution (blue). The VFT fit to the low-temperature data is shown as a reference (dashed line).

While the extended MYEGA model, which incorporates the aspect of a SF transition, perfectly fits the viscosity data, it can still not be seen as proof for a such a LLT, especially when taking into account the difference in glass transition temperature between the two phases. The cooperative shear model describes the measured viscosity data almost equally well and does not consider a LLT. Proof for a LLT can only be provided in systems where it can directly be observed, as e.g. in the BMG Vit106a [65], and where the transition is not obscured by crystallization. However, it can be concluded that the viscosity behavior of metallic glass-forming liquids cannot be represented by the simple VFT equation over the whole temperature range, and that more elaborate models, like the cooperative shear model or the extended MYEGA model, are necessary. With these models, the viscosity of BMGs can be described from the high-temperature stable liquid down to below the glass transition, providing

valuable datasets, e.g. for the modelling and simulation of flow during casting processes or thermoplastic forming.

All the information that is presented for Vit105 S_2 in Fig. 4.36 and in Table 4.9 can be found in the appendix for all six investigated alloys. Figure A6 shows the three different VFT fits, Fig. A7 shows the fits to the MYEGA equation, the extended MYEGA equation, and the cooperative shear model. All obtained fitting parameters and characteristic values are given in Table A4.

An additional remark regarding the Vit105 S_2 high-temperature viscosity data needs to be discussed. Earlier, in Fig. 4.18 b), a change in the slope of the viscosity measurement at around 1200 K was reported. The ESL synchrotron X-ray experiments confirmed that a S-stabilized crystalline phase forms prior to the onset of the main crystallization event. These observations agree well with the observation of a melting shoulder in the DTA, shifting the liquidus temperature upwards. Consequently, the change in slope in the viscosity measurements and the increased viscosity at lower temperatures is almost certainly caused by the beginning crystallization of this phase. Therefore, the viscosity datapoints below 1200 K were not considered for fitting, as only the behavior of the liquid should be described.

The same line of thought might also be true for the two P-containing alloys. The high temperature viscosity of these alloys shows a steeper increase upon cooling than their counterparts. However, no clear signature of a melting shoulder in the DTA scans can be found and ESL synchrotron X-ray crystallization experiments for these alloys could not be performed due to time constraints during the beamtime. Hence, an unambiguous statement regarding the possible influence of crystallization upon the course of viscosity in the high-temperature liquid of the P-containing alloys cannot be provided.

Structure-fragility correlation

In Chapter 4.6.3, the structure-fragility correlation was mainly discussed regarding fragility at low temperatures in the SCL region around the glass transition. For the stable high-temperature liquid of Vit101 and Vit105, only the structural fragility parameter $m_{str}{}^{V\,4\text{-}3}$ was determined and a prediction for the corresponding kinetic m-fragility index was made. The correlation found by Wei et al. [79] suggests values of m = 69 for Vit101 and m = 58 for Vit105. However, when looking at the m-fragility values from the high-temperature VFT fit from this chapter, Vit101 displays a value of m = 93 and Vit105 of m = 81 (compare to Table A4 in the appendix), and hence much higher than expected from the structure-fragility correlation.

Moreover, as discussed earlier, the strong and the fragile liquid phase should display two different glass transition temperatures. For the VFT fitting of the high-temperature data, this cannot be considered, as no reasonable estimation of the glass transition temperature of the fragile liquid is available. When considering an increased T_g-value for the fragile liquid, as proposed by the extended MYEGA model, an even

higher m-fragility would be obtained, resulting in a clear offset from the structure-fragility correlation. However, for Vit101 and Vit105, the kinetic glass transition temperature, T_g*, of the fragile high-temperature phase would need to shift between 80 and 90 K to lower temperatures in order to obtain a high-temperature VFT fit with the same m-fragility as predicted by the structure-fragility correlation. While this shift is rather large, it still seems more likely than the 283 K shift obtained from the extended MYEGA model. Of all the applied viscosity models, only the extended MYEGA model provides an estimation of the course of viscosity in the fragile liquid and gives a value for T_g*. In this model, m-fragility values for the high-temperature fragile liquid of m = 239 for Vit101 and m = 135 for Vit105 are obtained. These values however are completely off the chart in the structure-fragility correlation.

It stands to reason that the structure-fragility correlation, found for the low-temperature SCL region, cannot directly be transferred to the structure and fragility behavior in the high-temperature stable liquid. The general tendencies for less and more fragile liquids are however apparent in the structural data. This observation was also confirmed by the results of Stolpe et al. [65], where the structure-fragility correlation at high temperatures loosely matches to the fragility data based on viscosity measurements. In all applied fitting models in this work, Vit101 displays a more fragile behavior than Vit105, which is also found true in the structural fragility parameter. Consequently, the structure data can still be used as an indicator for the kinetic fragility behavior at high temperatures.

Chapter 5

Thermoplastic Forming

In the following chapter, results from thermoplastic bulk deformation experiments of different alloys, as well as powder consolidation experiments are presented and discussed. The deformation experiments are evaluated regarding the formability of the alloys and deformation maps are derived and related to the material properties. Furthermore, amorphous powder is consolidated, producing larger amorphous structures by this additive manufacturing process and the performance of the samples is evaluated.

In this chapter, the focus is not laid upon the Vit101 and Vit105 alloys with minor additions, discussed in the previous chapter, but rather on the thermoplastic forming of bulk metallic glasses in general. The findings from this chapter and the previous one are than combined in Chapter 6, where the influence of minor additions on the thermoplastic formability of Vit101 and Vit105 is discussed.

5.1 Bulk Forming

Among all metallic materials, only amorphous metals can be thermoplastically formed like polymers, providing a unique advantage over other metals. The possibilities of thermoplastic forming allow for an easy shaping of parts after the production of the amorphous wrought material. Complex shapes or elaborate surface patterns can be realized in a single processing step. In order to exploit these possibilities, a profound knowledge about the material, its properties, and the ideal processing conditions are crucial. Most of the properties discussed in Chapter 4 provide valuable information in order to assess the thermoplastic formability of an alloy in advance. The formability is mainly influenced by viscosity and the time- and temperature-dependent crystallization behavior, which can be summarized in terms of a TTT diagram and supplemented by additional information on the primary crystallizing phases.

In this chapter, first, the thermoplastic formability of 12 different BMGs is assessed in a simple deformation experiment with a constant heating rate (compare to Section 3.6.1). Based on these findings, two alloys are selected for further experiments, resulting in time-temperature-deformation (TTD) diagrams. Finally, the thermoplastic formability of BMGs is discussed and related to the material properties quantified beforehand.

5.1.1 TPF Experiments with a Constant Heating Rate

Thermoplastic deformation experiments upon heating with a constant rate of 0.333 K/s and a pressing force of 500 N were performed on 12 different alloy compositions. Given an initial sample diameter of 3 mm, this results in a pressing stress of 70 MPa. The used alloys are listed in Table 5.1 and are taken from different alloy families, including Zr-, Cu-, Fe-, Ni-, Pt-, and Au-based alloys. In general, alloys with a pronounced SCL region were selected, as this is a first indicator for a high formability. The experimental results for one single alloy are visualized exemplarily for AMZ4 ($Zr_{59.3}Cu_{28.8}Al_{10.4}Nb_{1.5}$) in Fig. 5.1. The same set of experiments was performed for all mentioned compositions and detailed results can be found in the Bachelor thesis of Oliver Kruse which was handed in in August 2019.

Figure 5.1 shows the travel of the piston of the TPF machine (a), the viscosity of the material during a scan (b), and the heat flow of a DSC scan (c), all as a function of temperature. The travel of the piston corresponds to the deformation of the sample, as recorded by the TPF machine. At the beginning of the experiment, the undeformed sample has a length of 7 mm, as visualized by the model rod and the photo on the left. Upon heating, the sample deforms under the load of the TPF piston. Here, we determine the deformation temperature T_{deform} for a pressing stress of 70 MPa using tangents on the deformation curve. This onset of deformation corresponds quite well to the end of the glass transition region, as can be seen in the DSC scan. For higher pressing stresses, T_{deform} would obviously shift to lower temperatures. After the experiment, the sample shows the shape of a flat disc (photo on the right side) and the actual height of the sample is measured. The right axis of Fig. 5.1 a) shows the deformation of the sample in %, calculated according to the equation: $\varphi = \ln(h_1/h_0)$, where h_0 is the initial height of the sample and h_1 the deformed height. The horizontal dashed blue line indicates the true final deformation, calculated from the final sample thickness. A deformation of 193% is observed for AMZ4. It can also be seen that the deformation calculated by the travel of the piston does not completely coincide with the observed maximum deformation. The travel measurement in the TPF machine is not sufficiently exact to allow for an accurate measurement of the final sample height.

Figure 5.1 b) shows the viscosity of the alloy during a TMA scan with the same heating rate as the TPF experiments and Fig. 5.1 c) shows the corresponding DSC scan. The dashed line in the viscosity plot indicates the VFT fit, as obtained from isothermal measurements from Ref. [184]. The datapoints from the scan approach the VFT fit when the glass transition temperature is reached. Upon heating, the viscosity decreases down to a minimum value just before crystallization begins. The crystallization temperature detected in the TMA scan is indicated as T_x^{TMA} and for AMZ4 a minimum viscosity of 1.6×10^8 Pa s is measured. It can be seen, that the deformation of the sample stops completely when crystallization begins. In this depiction, the importance of the length of the SCL region stands out. Considering that deformation starts at the end of the glass transition, a longer SCL region allows for a

larger processing window, where higher deformation temperatures are reached, and viscosity drops to lower values.

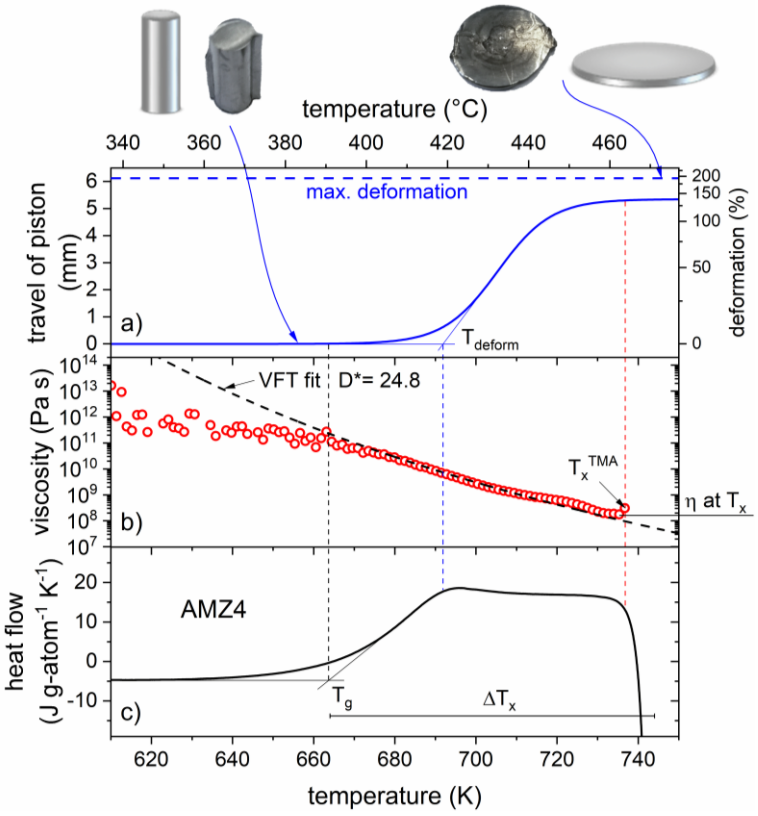

Figure 5.1: TPF deformation experiment with a constant heating rate. **a)** Travel of the TPF piston in mm and the corresponding sample deformation in %. The true final deformation is indicated by the dashed blue line. The sample before and after the deformation experiment is shown above the plot. **b)** Viscosity as measured in a TMA scan together with a VFT viscosity fit [184]. The minimum viscosity at T_x^{TMA} is indicated. **c)** DSC scan with the same heating rate, where T_g and ΔT_x are shown.

The results of the TPF deformation experiments with a constant heating rate for all alloy compositions are summarized in Table 5.1. The values for the glass transition temperature, T_g, and the length of the SCL region, ΔT_x, originate from own DSC measurements (and therefore sometimes deviate slightly from earlier literature values). The liquidus temperatures, T_l are taken from literature. The D*-values are taken from literature if indicated or result from own measurements. The viscosity values at T_x are the lowest values measured in the TMA scans. They are not the values calculated from the VFT fits, as often decomposition or nano-crystallization cause a deviation from the fit to higher viscosity values, especially in the high-temperature regime around T_x. In the last column, references for original work on the alloy and TMA viscosity measurements are given.

Table 5.1: TPF bulk deformation experiments with a constant heating rate. T_g, glass transition temperature; ΔT_x, length of the SCL region; T_l, liquidus temperature; D*, fragility parameter; η at T_x, viscosity value at T_x; φ, deformation in %, calculated according to $\varphi = \ln(h_1/h_0)$. The alloys are sorted by their maximum deformation.

Alloy	Composition [at%]	T_g [K]	ΔT_x [K]	T_l [K]	D*	η at T_x [Pa s]	φ [%]	Ref.
Pt42	$Pt_{42.5}Cu_{27}Ni_{9.5}P_{21}$	514	75	874	15.3 [a]	5.0×10^5	**281**	[24,154]
Au49	$Au_{49}Cu_{26.9}Si_{16.3}Ag_{5.5}Pd_{2.3}$	396	60	644	21.1 [a]	1.7×10^7	**238**	[68,277]
ZrAg	$Zr_{48}Cu_{36}Al_8Ag_8$	685	96	1143	24.1 [a]	6.0×10^7	**233**	[278,279]
AMZ3	$Zr_{60.8}Cu_{28.8}Al_{10.4}$	658	81	1180	~ 25	1.3×10^8	**205**	[280,281]
AMZ4	$Zr_{59.3}Cu_{28.8}Al_{10.4}Nb_{1.5}$	663	80	1203	24.8 [a]	1.6×10^8	**190**	[184]
FeMo PCB	$Fe_{67.5}Mo_{7.5}P_{10}C_{10}B_5$	753	80	1338	20.1	1.4×10^8	**180**	[282]
Ni69	$Ni_{69}Cr_{8.5}Nb_3P_{16.5}B_3$	668	48	1153	14.9 [a]	2.0×10^8	**167**	[24,49]
AMZ4 $Zr^{(705)}$	$Zr^{(705)}{}_{60.8}Cu_{28.8}Al_{10.4}$	673	71	1196	25.6 [a]	2.0×10^8	**165**	[250,283]
Vit106a	$Zr_{58.5}Cu_{15.6}Ni_{12.8}Al_{10.3}Nb_{2.8}$	679	75	1140	24.1 [a]	5.5×10^8	**165**	[250,284, 285]
CuTi	$Cu_{47}Ti_{33}Zr_{11}Ni_6Sn_2Si_1$	689	67	1140	~ 25	6.9×10^8	**155**	[134,143]
Vit101 Sn_2	$Cu_{45}Ti_{34}Zr_{11}Ni_8Sn_2$	681	64	1150	25.3 [a]	8.0×10^8	**143**	[250]
iRon	$Fe_{67}Mo_6Ni_{3.5}Cr_{3.5}P_{12}C_{5.5}B_{2.5}$	714	39	1267	21.3 [a]	1.3×10^{10}	**20**	[66]

[a] value taken from Refs. in the last column

The results in Table 5.1 clearly show a strong correlation between the maximum sample deformation φ and the minimum viscosity at T_x. As the Pt42 alloy has a very low viscosity of 5×10^5 Pa s at T_x, it reaches a deformation of 281 %, which corresponds to a final sample thickness of only 0.42 mm for an initially 7 mm high sample. Samples of the Cu-based alloy CuTi for example only reach a maximum deformation of 155 % (1.49 mm final sample thickness), and the minimum viscosity at T_x is 6.9×10^8 Pa s, and hence roughly three orders of magnitude higher than in Pt42.

The other material properties listed in the table do not show a direct correlation with deformability. However, when only one property is changed in a system, a direct influence of said property can be observed. For example in the AMZ4 system, the deformation in pure AMZ4 is much larger (190%) than in the industrial grade version AMZ4 $Zr^{(705)}$ (165%). The main difference between the systems is that the SCL region is about 10 K shorter in the industrial grade alloy, and hence a higher viscosity value is detected at T_x, as both alloys show almost the same kinetic fragility (change of viscosity with temperature).

It should be emphasized that especially ΔT_x alone does not correlate with the deformability, even though the length of the SCL region is often considered as the key indicator for the formability. However, a correlation with deformability is found for the quantity $\Delta T_x/T_g$, as will be discussed in the context of Fig. 5.6 a) on page 151. The normalization to T_g basically scales the length of the SCL region to the intrinsic softening temperature of the system and by this makes them comparable. It should further be mentioned, that viscosity at the calorimetric T_g is not always exactly 10^{12} Pa s, e.g. the Pt42 alloy shows a much lower viscosity already at T_g [24]. Hence, the sole knowledge of T_g, T_x, and D* is insufficient to describe the complete course of viscosity as a function of temperature, as it does not account for these offsets. A profound discussion of the influence of different material properties on the formability of metallic glasses can be found in Chapter 5.1.3 in the context of Fig. 5.8.

For the isothermal deformation experiments presented in the next chapter, only two of the alloys from Table 5.1 were selected, namely AMZ4 and FeMoPCB. These are the two alloys with the best compromise between deformability and industrial applicability, as they show a sufficiently high GFA and do not contain precious metals.

5.1.2 Isothermal TPF Experiments

The goal of the isothermal TPF experiments is to construct a time-temperature-deformation (TTD) diagram which allows to indicate the optimum processing conditions for TPF regarding time and temperature. While the previous experiments with a constant heating rate only evaluate the deformation during a single trajectory through the time-temperature processing space, the isothermal experiments can sample the whole processing region. It should be noted, that distinct experiments were performed for different pressing times at the same temperature. Even though the TPF machine records its piston movement, the previous experiments showed that this measurement deviates significantly from the real sample thickness. Hence, it is not sufficient to simply record deformation as a function of time for a single temperature. Furthermore, the onset of crystallization should be determined as a function of pressing time subsequent to the experiments and ex-situ XRD measurements were necessary. In order to keep all results comparable, the exact same sample geometry (rod with d = 3 mm and l = 7 mm) and pressing force (500 N) as before was used for the isothermal TPF experiments.

Before performing the TPF experiments, for both alloys, viscosity was measured by TMA scans and by isothermal measurements in order to obtain a VFT fit. Figure 5.2 displays viscosity as a function of temperature for AMZ4 (a) and FeMoPCB (b). The black squares represent equilibrium viscosity values and are fitted by the VFT equation (Eq. 2.9, dashed line). The resulting fitting parameters are written down in the figure. The red circles represent viscosity as measured by a TMA scan and above the glass transition they coincide well with the VFT fit. On the bottom, a DSC scan with the same heating rate (0.333 K/s) is shown as a temperature reference. The data for AMZ4 in Fig. 5.2 a) is taken from our publication [184].

The grey shaded box in Fig. 5.2 marks the TPF processing region. The previous experiments showed that deformation for the used samples and under the applied pressing conditions starts at viscosities of around 10^{10} Pa s, which corresponds roughly to the end of the glass transition region. Hence, the TPF processing region is defined by a viscosity below 10^{10} Pa s and down to the minimum value reached before the beginning of crystallization.

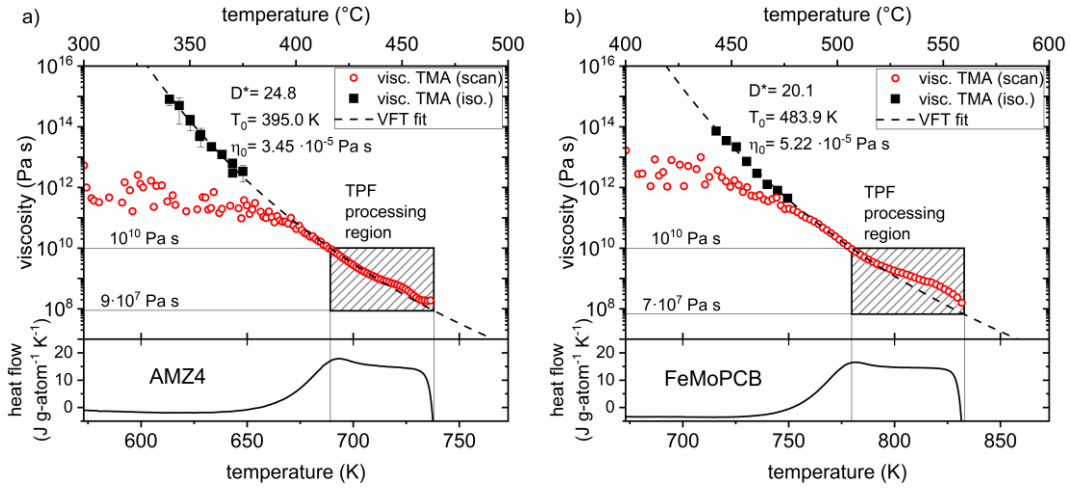

Figure 5.2: Viscosity as a function of temperature. The black squares represent equilibrium viscosity values as measured in TMA and are fitted by the VFT equation (Eq. 2.9, dashed line). The resulting fitting parameters are written down in the figure. The red circles represent viscosity as measured in a TMA scan and above the glass transition they coincide well with the VFT fit. On the bottom, a DSC scan with the same heating rate (0.333 K/s) is shown as a temperature reference. The TPF processing region between a viscosity of 10^{10} Pa s and the onset of crystallization is marked by the shaded area. **a)** Viscosity of AMZ4, figure and caption adapted from Ref. [184], and **b)** viscosity of FeMoPCB.

Various temperatures within the defined TPF processing region are chosen for the experiments and different samples are pressed for increasing times. Each set of samples pressed at the same temperature is than analyzed by X-ray diffraction in order to determine if the sample remained amorphous. Figure 5.3 shows the diffraction patterns for AMZ4 (a) pressed at 455 °C (728 K), and for FeMoPCB (b) pressed at 550 °C

(823 K). In the case of AMZ4, the sample set at 455 °C could be investigated by synchrotron X-rays, undoubtedly proving that the samples remain amorphous during the TPF process up to a time of 125 s at this temperature. Only for the sample pressed for 135 s, first signs of structural ordering, indicating crystallization, become apparent in the synchrotron diffractogram. In the case of FeMoPCB, laboratory XRD patterns are shown. For this alloy, the signal-to-noise ratio in the diffractograms is fairly high due to fluorescence caused by the use of Cu K_α radiation on Fe-based samples [195]. Still, first Bragg peaks are visible in the sample pressed for 160 s, as indicated by the circle. The photo above the graph shows the deformed and amorphous samples after TPF.

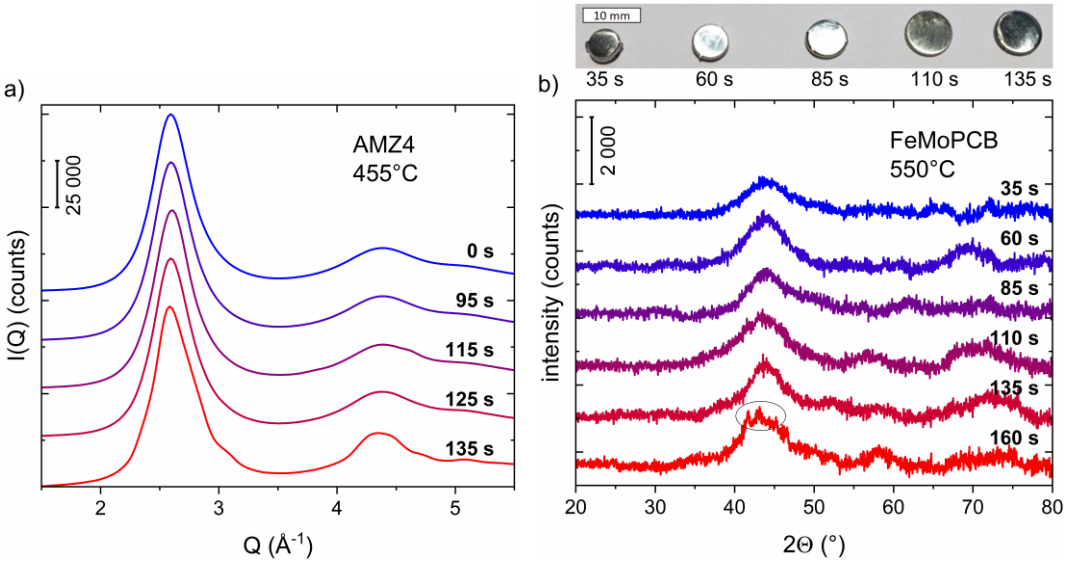

Figure 5.3: X-ray diffraction patterns for a set of consecutive samples pressed at the same temperature for increasing times. **a)** Synchrotron X-ray diffraction patterns for AMZ4, thermoplastically deformed at 455 °C (728 K) for times up to 135 s. Only the last sample shows evidence for a beginning crystallization. **b)** Laboratory XRD patterns for FeMoPCB, pressed at 550 °C (823 K) for times up to 160 s. The circle indicates upcoming Bragg peaks in the sample pressed for 160 s. Above the graph, a photo of the deformed and amorphous samples after TPF is displayed.

All samples from the isothermal TPF experiments are displayed in an isothermal TTT diagram in Fig. 5.4, according to their processing parameters. AMZ4 is shown in Fig. 5.4 a) and the crystallization times are taken from Ref. [184]; FeMoPCB is shown in Fig. 5.4 b). Samples that remained amorphous are indicated by green dots and samples that show first indications for crystallization are indicated by red circles. The crystallization times for the 1 %, 50 %, and 99 % transformation are indicated by the black symbols.

For both alloys, the crystallization times from the TTT diagram coincide rather well with the results from the TPF experiments. It must be mentioned that the

temperature control in the TPF is by far less accurate than in the DSC and that it is challenging to calibrate the temperature [230]. Furthermore, the temperature distribution throughout the sample is not completely homogeneous as the sample is heated by conduction through the Cu pistons. Hence, small deviations of the TPF results from the TTT diagram have to be expected.

In the case of AMZ4, crystallization in the TPF samples can be detected when roughly the 50 % crystallization time of the TTT diagram is passed. It should be noted that the sample at 455 °C and 135 s is labeled as crystalline based on the synchrotron XRD pattern, while the onset of crystallization is not yet clearly visible in the laboratory XRD. Hence, the red circle at 455 °C is shifted slightly to shorter times in comparison to other TPF temperatures. For FeMoPCB, first signs of crystallization can be detected at shorter times in relation to the TTT diagram, roughly between the 1 % and the 50 % transformation time.

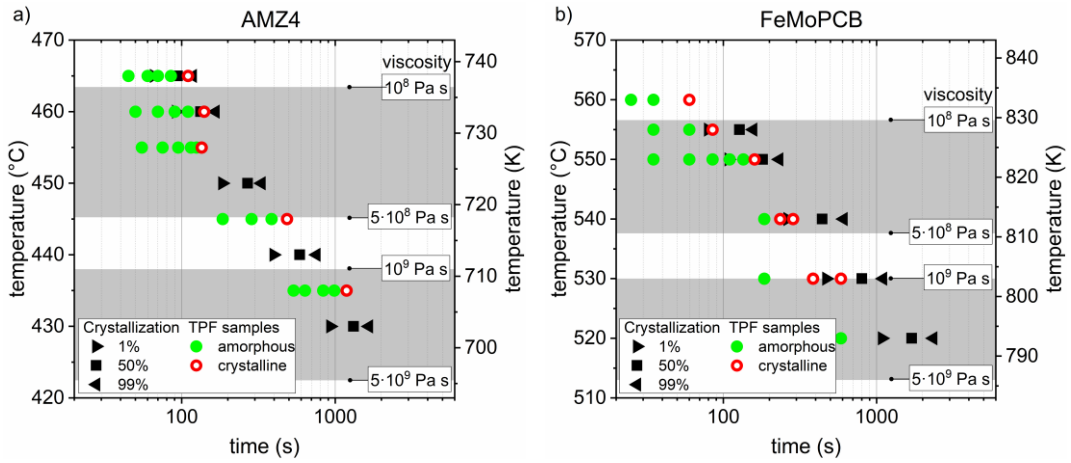

Figure 5.4: Isothermal time-temperature-transformation (TTT) diagrams for **a)** AMZ4 and **b)** FeMoPCB in the TPF temperature range. The black symbols indicate the 1 % (▶), the 50 % (■), and the 99 % (◀) crystallization transformation in the DSC. All TPF samples that were prepared and analyzed are indicated according to their processing conditions (temperature and time). Samples that stayed amorphous are depicted as green dots and samples that began to crystallize are depicted as red circles. Viscosity values calculated from the VFT fits in Fig. 5.2 are given for four temperatures as indicated by the blunt arrows. The grey shaded areas indicate a change of viscosity of half an order of magnitude. (Crystallization times and viscosities for AMZ4 are taken from Ref. [184]).

The grey shaded areas in Fig. 5.4 indicate a change of viscosity of half an order of magnitude. The temperatures at which viscosities of 10^8, 5×10^8, 10^9, and 5×10^9 Pa s are expected according to the VFT fits in Fig. 5.2 are indicated by the blunt arrows. Comparing AMZ4 and FeMoPCB, it can be seen that the crystallization times are very similar within the same viscosity region. Hence, both alloys display a similar TPF processing region regarding time and viscosity.

In the next step, for each sample the deformation during the TPF experiment is calculated according to the equation: $\varphi = \ln(h_1/h_0)$, where h_0 is the initial height of the sample and h_1 the deformed height after the experiment. From this data, a time-temperature-deformation (TTD) diagram for the thermoplastic forming of AMZ4 and FeMoPCB is constructed, as displayed in Fig. 5.5 a) and b).

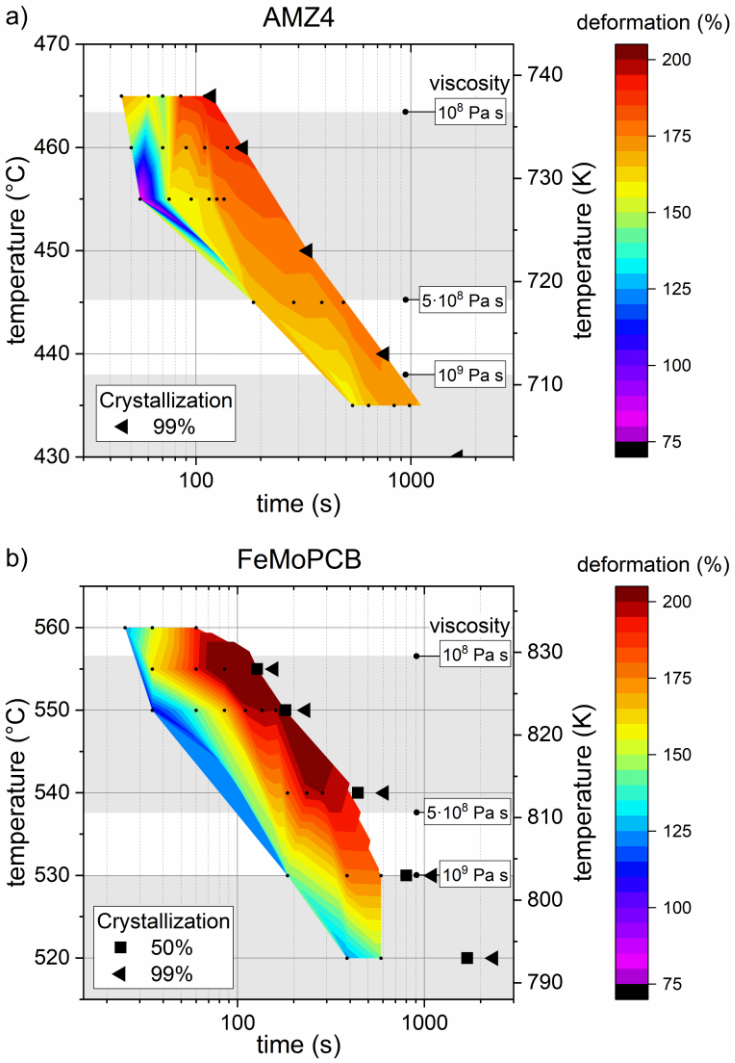

Figure 5.5: Time-temperature-deformation (TTD) diagrams for the thermoplastic forming of **a)** AMZ4 and **b)** FeMoPCB. The deformation during isothermal TPF experiments is visualized in a color-filled contour plot, where dark red indicates a deformation above 200 %. The deformation map is embedded in the TTT diagrams from Fig. 5.4 and the prepared samples are indicated by black dots. Crystallization and viscosity values are displayed in the same way as before.

The deformation during the isothermal TPF experiments is visualized in a color-filled contour plot, where dark red indicates a deformation above 200 % and purple a deformation of 75 %. The deformation map is embedded in the TTT diagrams from Fig. 5.4 and the prepared samples are indicated by black dots. Crystallization and viscosity values are displayed in the same way as before.

When comparing the two alloys, FeMoPCB displays a larger deformation than AMZ4, with the maximum reaching a value of 215 % at 555 °C and 85 s. The maximum value for AMZ4 is 195 % at 465 °C and 110 s. In this comparison, the kinetically more fragile alloy, FeMoPCB, shows a larger decrease in viscosity throughout a SCL region of similar length, thus explaining the better formability.

For both systems, the largest deformation is reached at high temperatures, just below the nominal crystallization temperature from DSC. Hence, the drop in viscosity at higher temperatures overcompensates the decreasing crystallization times, indicating that TPF should be performed at the upper end of the experimentally accessible temperature range. This finding coincides with the observations Pitt et al. made for $Zr_{35}Ti_{30}Cu_{8.25}Be_{26.75}$ and other alloys [168].

In our experimental setup, processing temperatures that require processing times much shorter than one minute are not feasible anymore. Such experiments were performed, but mostly resulted in the crystallization of the sample. At such high temperatures, the outer parts of the sample can already start to crystallize before the whole sample is heated homogeneously and starts to deform in the center. For TPF experiments at high temperatures, a different experimental setup becomes necessary, where the sample can be heated fast and homogeneously. In fact, Johnson et al. demonstrated that crystallization can be beaten by millisecond heating and processing [169]. They use a rapid capacitive discharge method where the sample is heated by the ohmic heat of a millisecond current pulse and heating rates of 10^6 K/s can be achieved. Later, Kaltenboeck et al. demonstrated the feasibility of this technique for near-net shaping of a fine precision part, when the sample can be heated to the ideal TPF processing range at viscosities below 10^4 Pa s at high temperatures [170].

The existence of this ideal processing window at high temperatures also explains why both sample alloys demonstrate a higher deformability in the isothermal experiments than in the ones with a constant heating rate. For a large thermoplastic deformation, it is advantageous to reach the upper limit of the accessible temperature region as fast as possible, in order to deform the sample at the lowest viscosity for the longest amount of time possible, rather than deforming for longer times at higher viscosities.

5.1.3 Formability

In this chapter, the results of the thermoplastic deformation experiments with a constant heating rate and under isothermal conditions are discussed in reference to the material properties of the alloys that were quantified beforehand. A quantity describing the thermoplastic formability based on the thermophysical properties of the system is derived and compared to the experimental deformation data.

In 2008, Schroers first described the formability of BMGs in their SCL state [172]. He argued that the most accurate and easiest way to experimentally assess the thermoplastic formability of an alloy is through TPF experiments with a constant heating rate, as were also performed in this work. These experiments circumvent issues with an exact absolute temperature measurement that is necessary due to the strong dependence of viscosity and crystallization time on temperature. Furthermore, a TPF experiment at a single isothermal temperature would not be representative as formability is also temperature dependent (compare to the TTD diagrams in Fig. 5.5).

In theory, the formability of a BMG in the SCL region is defined by the maximum strain, ε_{max}, the sample can experience before crystallization. The strain rate, $\dot{\varepsilon}$, for Newtonian behavior can be written as:

$$\dot{\varepsilon} = \sigma / 3\eta \,, \tag{5.1}$$

where σ is the flow stress and η the temperature dependent viscosity. ε_{max} for isothermal conditions now results from the integration of the strain rate between 0 s and the crystallization time t_c [172]:

$$\varepsilon_{max} = \int_0^{t_c} \dot{\varepsilon}\, \mathrm{d}t = \int_0^{t_c} \frac{\sigma}{3\eta}\, \mathrm{d}t = \sigma \frac{t_c}{3\eta} = \sigma\, F^{iso} \,. \tag{5.2}$$

The quantity relating the maximum strain to the applied stress is the isothermal formability F^{iso}:

$$F^{iso}(T) = \frac{t_c(T)}{3\,\eta(T)}, \tag{5.3}$$

where both, crystallization time and viscosity, are strongly temperature dependent. In Ref. [168], Pitt et al. discuss that the slope of F^{iso} with temperature is always positive, confirming that the highest formability is observed at the highest temperatures where crystallization can still be avoided.

In order to calculate the formability parameter for constant heating experiments, F^{scan}, Eq. 5.2 and 5.3 can be adapted [172]:

$$F^{scan}(\dot{T}) = \frac{1}{3\dot{T}} \int_{T_g(\dot{T})}^{T_x(\dot{T})} \frac{1}{\eta(T)} \mathrm{d}T = \frac{1}{3\dot{T}} \int_{T_g(\dot{T})}^{T_x(\dot{T})} \frac{1}{\eta_0} \exp\left(\frac{-D^* T_0}{T - T_0}\right) \mathrm{d}T \,, \tag{5.4}$$

where $\dot{T}$ is the applied heating rate of the scan and T_g and T_x are the heating rate dependent glass transition and crystallization temperature, respectively. The temperature dependent viscosity η(T) can be expressed in terms of the VFT equation (Eq. 2.9). The formability during a scan strongly depends on the heating rate, mainly through the influence of the heating rate on the crystallization temperature. In this work however, a constant heating rate of 0.333 K/s was used for all experiments.

The discussed reflections regarding formability are in perfect agreement with the theoretical background of viscosity measurements with a parallel plate rheometer. Parallel plate rheometry is commonly used for BMGs in the SCL region, e.g. by Bakke et al. [286]. There, the flow behavior of a sample between two pistons is used to calculate viscosity and hence, the experimental setup is almost identical to the TPF setup used for our experiments. The theoretical background of parallel plate rheometry was first described by Dienes and Klemm in 1946 [287], where the viscosity, η, can be calculated from the slope of a $1/h^4$ vs time curve, according to:

$$\frac{1}{h^4} = \frac{8\pi F}{3\,\eta\,V^2}\, t + C \,, \tag{5.5}$$

where h is the sample height (or the plate separation), F is the pressing force, V the sample volume, t the time, and C an integration constant. This formulation is valid for the case where the sample does not completely fill the space between the pressing plates, as is also true for the TPF setup. The value of $1/h^4$ can be interpreted as a measure of the maximum strain, ε_{max}, and the quantities F and V are kept constant during all our experiments, resulting in the following formulation:

$$\varepsilon_{max} \sim \frac{1}{h^4} = \frac{8\pi F}{V^2} \frac{t}{3\eta} = const \cdot F^{iso} \,. \tag{5.6}$$

Hence, the maximum strain only depends on the quantity $t/(3\eta)$, which corresponds to the previously defined isothermal formability F^{iso}.

This furthermore implies that the TPF deformation experiments can also be used to calculate the viscosity of a sample, which however is only true to a certain degree. As discussed before, the travel measurement of the piston in the TPF machine is not sufficiently exact to allow for an accurate measurement of the final sample height. Hence, the viscosity values calculated from these experiments are located in the right order of magnitude but are by far not exact.

In his original work on the formability of BMGs in the SCL region upon heating with a constant rate, Schroers derived several quantities that correlate with the

experimentally observed deformation [172]. The best correlation was found for the so-called S parameter, which is defined as $S = \Delta T_x/(T_l\text{-}T_g)$, and a good correlation was also observed for $\Delta T_x/T_g$. These quantities are calculated as well for our deformation experiments with a constant heating rate and are depicted over the experimental deformation in % in Fig. 5.6 (compare to Table 5.1 for the experimental results). The goal of the experiments in this work is to assess if the reported correlations are universal, and hence hold true for a different experimental setup and different alloys.

Figure 5.6 a) shows a rather good correlation for $\Delta T_x/T_g$ with the deformation, where the coefficient of determination for a linear fit is $R^2 = 0.82$. The correlation found for S, as shown in Fig. 5.6 b) is slightly worse, with $R^2 = 0.72$. The material properties needed to calculate these two predictive quantities can be easily obtained from a DTA measurement. Hence, a quick first prediction of the general formability of a BMG can be made from a single DTA scan.

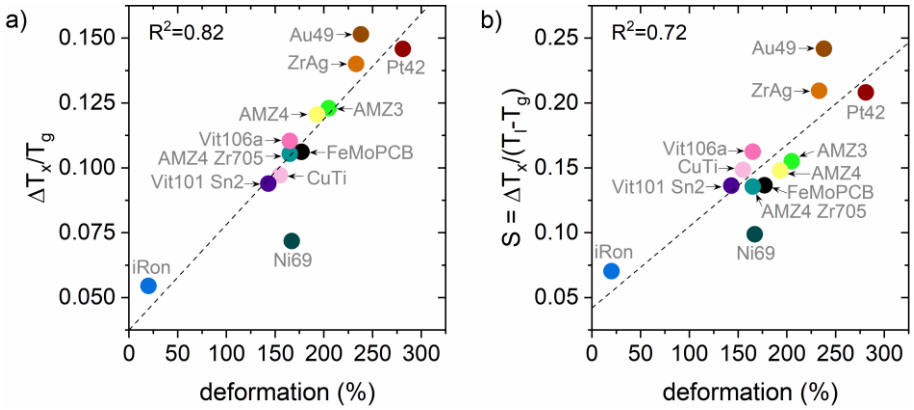

Figure 5.6: Correlations obtained from the TPF experiments with a constant heating rate (Table 5.1). The dashed lines represent linear fits to the datapoints. **a)** Correlation between $\Delta T_x/T_g$ and the experimental thermoplastic deformation in %. **b)** Correlation between $S = \Delta T_x/(T_l\text{-}T_g)$ and the deformation.

While the correlation of $\Delta T_x/T_g$ and S with the deformation is reasonable, some outliers are still observed (e.g. Ni69), making it desirable to define a quantity with a better correlation that still is somewhat easy to measure. A single TMA 3PBB viscosity scan does not require more experimental efforts than a DTA measurement. Such a viscosity measurement results in a dataset that easily allows to obtain the minimum viscosity of the system right before the onset of crystallization at T_x, as noted in Table 5.1. The correlation of $\eta(T_x)$ with the deformation is displayed in Fig. 5.7 a). While not a linear correlation is observed on this logarithmic viscosity scale, no more outliers from the general trend are found. The grey dotted line corresponds to a quadratic fit that is only intended to guide the eye. Hence, a single viscosity measurement allows for a good prediction of the achievable thermoplastic deformation.

Finally, also the theoretical formability parameter for a temperature scan, F^{scan}, is calculated for all investigated alloys, according to Eq. 5.4. For each alloy, the inverse of the VFT equation was plotted and numerically integrated from T_g to T_x, resulting in the displayed values. A linear fit to the datapoints shows a very good correlation between F^{scan} and the deformation with a coefficient of determination of $R^2 = 0.94$. This stunning correlation emphasizes the validity of the theoretical formability concept. The correlation between formability and deformation in the original work of Schroers was not as strong as in our work. However, there, viscosity data for the sample alloys was obtained from different literature sources, while in our work all viscosity measurements were performed with the same experimental setup in our group (including the data from cited sources). This emphasizes the necessity for careful and consistent measurements under defined and constant conditions.

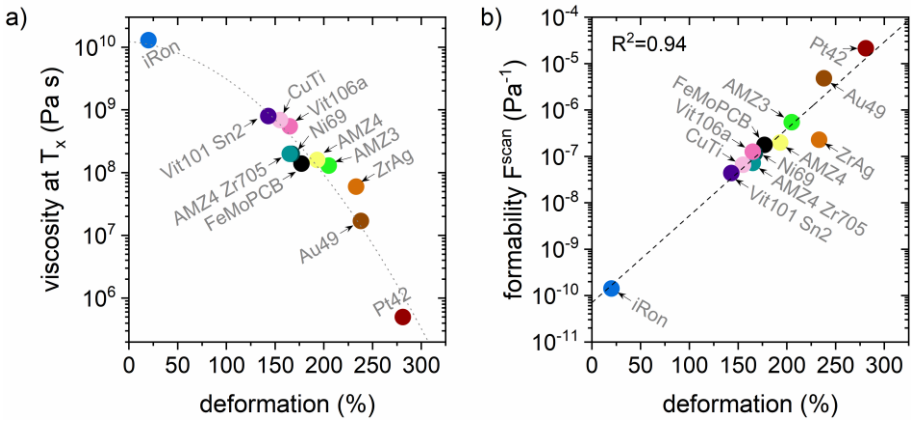

Figure 5.7: Correlations obtained from the TPF experiments with a constant heating rate (Table 5.1). **a)** Correlation between the viscosity at T_x, and the experimental thermoplastic deformation. The grey dotted line corresponds to a quadratic fit that is only intended to guide the eye. **b)** Correlation between the formability F^{scan} according to Eq. 5.4 and the deformation. The dashed line is a linear fit to the data.

While the formability F^{scan} in this case was calculated from VFT fits that can only reliably be obtained from labor-intensive isothermal equilibrium viscosity measurements, the viscosity information for the relevant temperature interval contained in the VFT fits can also be extracted from a single TMA 3PBB viscosity scan. In this case, the course of the viscosity scan can be used for a VFT fit of the temperature region between T_g and T_x without a significant deviation from the VFT fit based on the isothermal measurements. The resulting calculation of F^{scan} according to Eq. 5.4 yields very similar values, not challenging the found correlation. Hence, a single TMA viscosity scan can be sufficient to assess the formability F^{scan} of a BMG. However, it should be mentioned that a TMA scan with an excellent data quality is necessary, where especially at higher temperatures, approaching T_x, no measurement artifacts e.g. due to the TMA deflection limit are observed.

Commonly, the length of the SCL region, ΔT_x, is interpreted as an indicator of the thermoplastic formability, however the deformation experiments in this work showed no direct correlation. As discussed before, the formability during a scan is mainly determined by the minimum viscosity that can be reached before crystallization occurs, $\eta(T_x)$. Consequently, in order to better understand the important influence of the other material properties on the formability during a scan, their influence on viscosity is visualized in Fig. 5.8.

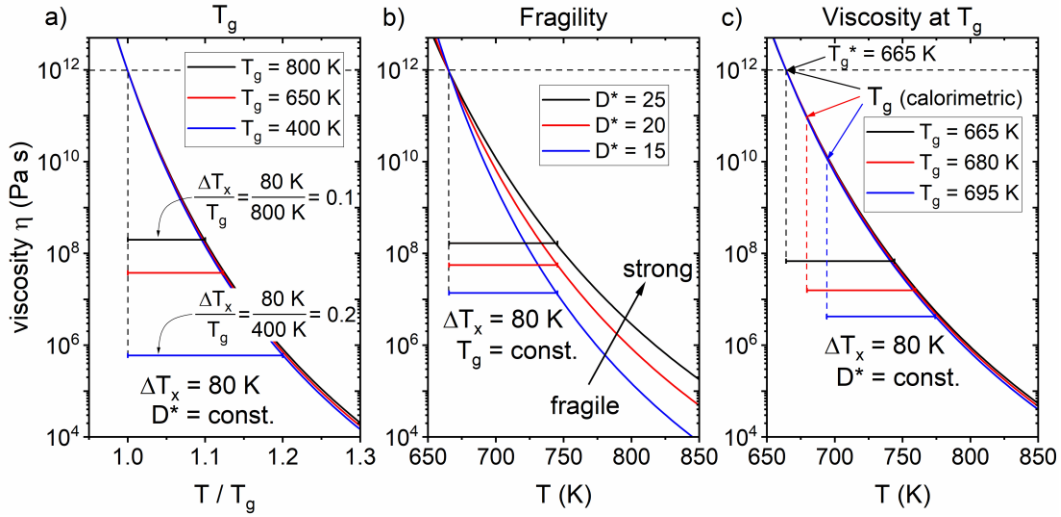

Figure 5.8: Influence of **a)** the glass transition temperature T_g, **b)** the kinetic fragility, and **c)** the viscosity at T_g, on the viscosity at the onset of crystallization. A lower viscosity at the end of the SCL region (at T_x) causes a higher thermoplastic formability. For all systems, the value of ΔT_x is constant, in order to visualize the influence of the other properties on the formability.

Figure 5.8 a) shows the hypothetical influence of the glass transition temperature, T_g, on the minimum viscosity. Three systems with the same ΔT_x value of 80 K and the same kinetic fragility of D*= 20, are displayed over a T_g-scaled temperature axis. The alloy with the lowest T_g reaches lower viscosity values than the alloys with higher glass transition temperatures. A simple calculation is shown within the plot to visualize the effect of T_g. On the T_g-scaled axis, a lower T_g value causes the corresponding SCL region to be larger and therefore lower viscosity values are reached, given the same fragility. Hence, the sole length of the SCL region cannot account for the influence of the intrinsic temperature of the system on the formability. The T_g-scaling however, corrects for this influence which explains the good correlation of $\Delta T_x/T_g$ with the formability. Accordingly, the excellent formability of the Pt42 and Au49 alloy (compare to Table 5.1) are based on their low T_g-values.

In Fig. 5.8 b), the influence of the kinetic fragility on the viscosity above the glass transition is visualized. Given the same T_g and the same ΔT_x, the more fragile systems

with a lower D*-value reach a much lower viscosity at the onset of crystallization and hence show a better thermoplastic formability.

Finally, the influence of the viscosity at the calorimetric glass transition temperature, T_g, is depicted in Fig. 5.8 c). In theory, a viscosity of 10^{12} Pa s is assumed at the glass transition temperature, leading to the definition of the kinetic glass transition temperature, T_g* [19]. Some alloys, however, show much lower viscosity values at their calorimetric glass transition temperature (measured by DSC), leading to a temperature offset of many degrees between T_g and T_g*. In the case of the Pt42 alloy for example, T_g and T_g* are 16 K apart [24]. Figure 5.8 c) shows three systems with the same values of ΔT_x, T_g*, and D*, where only the viscosity at T_g (calorimetric) differs. Obviously, the alloy with the lowest viscosity at T_g also shows the lowest viscosity at T_x, and hence the highest thermoplastic formability.

In a last step, also the isothermal formability, F^{iso}, corresponding to the TTD diagram experiments from Chapter 5.1.2 is calculated according to Eq. 5.3. The temperature-dependent values of F^{iso} for AMZ4, FeMoPCB and Pt42 are displayed in Fig. 5.9 a) as symbols with connecting lines. Formability is shown over temperature scaled to T_g. The data for AMZ4 (black) and FeMoPCB (red) results from the TTT and viscosity measurements from this work (Fig. 5.2 and 5.4) and the Pt42 data is calculated from our previous work [202] and serves as a reference. Note that the formability axis has a break between the Pt42 and FeMoPCB data.

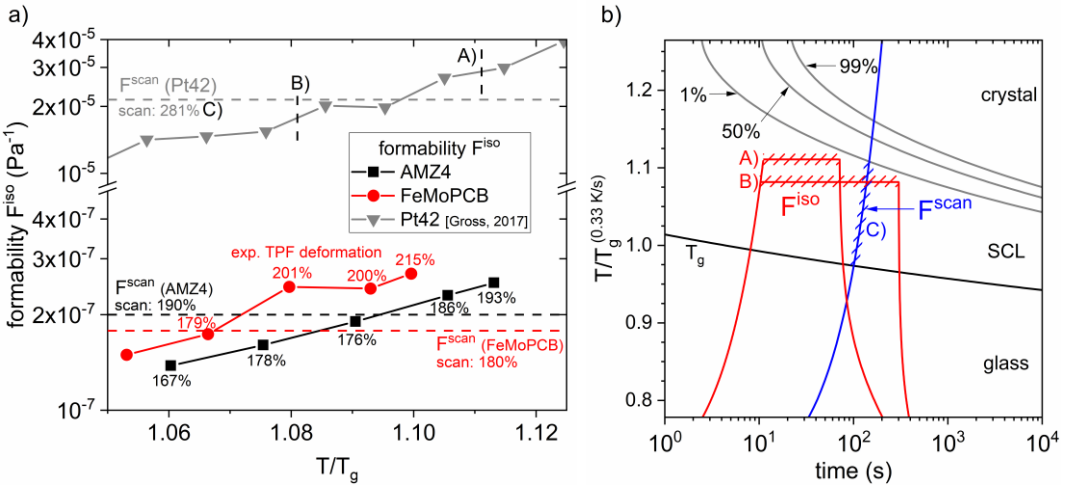

Figure 5.9: a) Isothermal formability, F^{iso}, displayed over T_g-scaled temperature. Data for AMZ4 (black), FeMoPCB (red), and Pt42 (grey) is shown. For each formability datapoint, the experimentally obtained TPF deformation is noted in %. The dashed lines indicate the values of the formability parameter for constant heating, F^{scan} and the corresponding experimental deformation is also noted. **b)** TTT diagram for Pt42 [202] with three different TPF processing routes: A) and B), isothermal pressing at different temperatures; C), TPF during a scan with constant heating rate. The corresponding formability values are also indicated in Fig. a).

For AMZ4 and FeMoPCB, next to each formability datapoint, the experimentally obtained TPF deformation from the isothermal experiments is noted in % (compare to the TTD diagrams in Fig. 5.5). It can be seen, that the isothermal formability values for both alloys follow the trends found in the deformation experiments. In total, FeMoPCB displays a higher formability than AMZ4. For both alloys, a deformation of around 200 % with our experimental conditions roughly corresponds to a value of $F^{iso} = 2.5 \times 10^{-7}$ Pa^{-1}. The results also confirm the findings of Pitt et al. that the highest formability is observed at the highest temperatures where crystallization can still be avoided [168].

The dashed lines in Fig. 5.9 a) indicate the values of the formability parameter for constant heating, F^{scan}, as previously calculated, on the same scale. For all alloys, the formability during a scan lies among the values of F^{iso}, whereas the maximum formability upon isothermal processing exceeds the formability during a scan. This is in good agreement with the measured TPF deformation values that are written next to the dashed lines indicating F^{scan}. It can clearly be seen that the formability of Pt42 significantly exceeds the one of the other two alloys.

The corresponding temperature protocols for different processing conditions are visualized in the TTT diagram in Fig. 5.9 b). The displayed TTT diagram is the one for the Pt42 alloy (taken from Ref. [202]), shown on the same temperature scale as the formability. Three different processes named A), B), and C) are shown and the corresponding formability is indicated in Fig. 5.9 a) using the same letters. A) and B) correspond to isothermal temperature protocols. The sample is initially heated quickly to the desired processing temperature, then pressed for a time shorter than the crystallization time at that temperature (shaded area), and then rapidly cooled. As discussed before, the resulting formability for A) is higher than for B), as the decreased viscosity at higher temperatures overcompensates the shorter processing time. C) visualizes thermoplastic deformation during a scan with a constant heating rate. Deformation takes place in the shaded area between T_g and T_x. While rather high temperatures and hence low viscosities are reached during the scan, only a short amount of pressing time is associated to this temperature region. Therefore, the overall formability during a scan stays below the values achievable during isothermal pressing.

5.2 Powder Consolidation

One of the main trends in the last years in the metal industry are additive manufacturing techniques. These techniques promise a completely new bottom-up approach to produce parts with geometries and properties that were inconceivable with conventional technologies. One strategy is for example selective laser melting, where the energy of a laser is used to melt and fuse metal powders at precisely defined spots. This technology is also applicable to amorphous metal powders, where the intrinsically high cooling rates of the process allow to obtain amorphous parts with complex geometries [187–189].

An alternative approach to additive manufacturing of amorphous metals is the consolidation of amorphous powder by thermoplastic forming. In this two-step process, the production process of an amorphous pre-material and the forming of the final part can be decoupled. The idea behind this is to overcome part size limitations induced by the high necessary cooling rates in casting processes. In the SCL region, the amorphous powder particles are supposed to flow into the desired mold shape and fuse with the neighboring particles, forming a monolithic sample.

Within the scope of a research project funded by the Industrielle Gemeinschaftsforschung (IGF, Vorhaben Nr. 19291 N) the applicability of a powder consolidation process was investigated for three different alloy compositions, namely AMZ4, FeMoPCB, and CuTi (compare to Table 5.1). The results of the investigations on AMZ4 powder were published in the article *Consolidation of amorphous powder by thermoplastic forming and subsequent mechanical testing* in the journal Materials and Design in 2018 [184]. Hence, this chapter is strongly based on the results presented in this article and figures and captions are adapted from there.

In the following, the results of the thermoplastic consolidation experiments of amorphous AMZ4 powder are presented. The insights from the experiments on the FeMoPCB and CuTi powder are qualitatively equivalent and will only be discussed briefly in the end. The experiments are based on the knowledge obtained from the bulk deformation experiments, where the TPF processing window was defined and deformation diagrams were drafted. The consolidated powder samples were analyzed regarding their density, their amorphous structure, and their mechanical performance. In the end, the lessons learned from the powder consolidation experiments are collated with experiments on the thermoplastic surface bonding of amorphous bulk samples.

5.2.1 Density and Amorphous Structure

The thermoplastic powder consolidation experiments show that amorphous powder can be pressed into dense samples. Figure 5.10 a) shows such a sample in the shape of a rectangular beam. The shiny sample surface results from an exact reproduction of the surface of the polished steel punches that are used for pressing. An optical micrograph of the polished sample cross section is depicted in Fig. 5.10 b). The remaining porosity is below the detection level of optical microscopy. Only some sharp-edged triple points between three powder particles can still be detected. This sample was pressed with 50 MPa at 460 °C for 70 s and hence in the ideal TPF processing region where the largest deformation was observed in the bulk TPF experiments. A synchrotron X-ray diffractogram of the beam confirming its amorphous structure is shown in Fig. 5.10 c).

While the beam-shaped samples are convenient for subsequent mechanical tests, e.g. by three-point bending (3PB), they cannot visualize the idea behind an additive manufacturing process where more complex geometries are of interest. In a first attempt, small cup-shaped structures were pressed from amorphous powder, as

displayed in Fig. 5.10 d). Here it can be seen that the powder particles can be thermoplastically formed into more complex shapes, given an adequate pressing mold. Figure 5.10 e) displays an optical micrograph of the polished sample cross section together with a magnification of the area in the red frame. As before, an optically dense sample can be obtained. However, the achievable complexity of a part in this process is limited by the complexity of the pressing mold, similar to casting applications. Furthermore, in our case the installation space of the mold in-between the pistons of the TPF devise is limited and does not allow for more complex pressing molds.

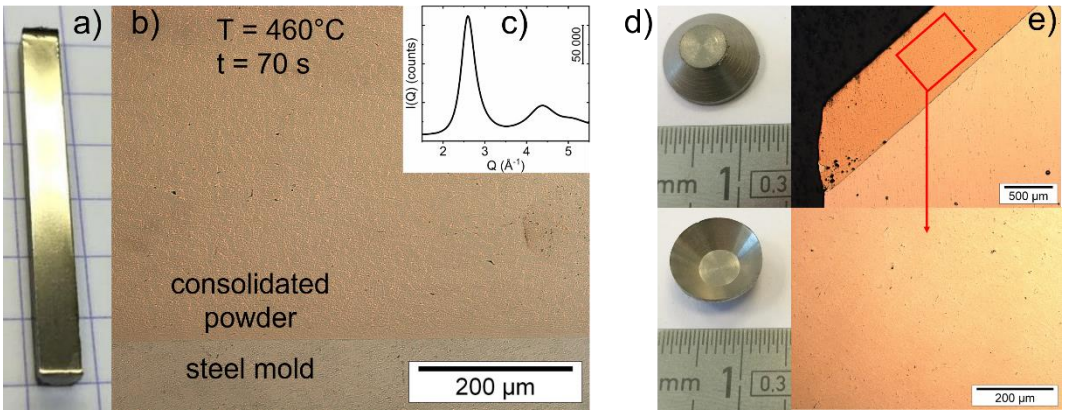

Figure 5.10: **a)** As-pressed AMZ4 powder sample. **b)** Optical micrograph of a polished cross section. The sample was pressed at 460 °C for 70 s and no measurable porosity can be detected. [Fig. a), b), and caption taken from Ref. [184]]. **c)** Synchrotron XRD of the cross section. **d)** Image of an as-pressed cup-shaped sample with increased geometrical complexity. **e)** Optical micrograph of a polished cross section and magnification of the area in the red frame.

5.2.2 Mechanical Performance

In a first step, the Vickers hardness of different samples was measured on polished cross sections and the experiments show that dense samples reach the hardness of as-cast bulk samples (466.9 HV5) [184].

Densely compacted beam shaped samples, as shown in Fig. 5.10 a), were used for mechanical three-point bending flexural tests (3PB). The resulting stress-strain curves are depicted in Fig. 5.11 and two sample groups with a different mechanical performance are visible. The black filled symbols represent samples fracturing around 600 MPa and the red open symbols samples fracturing around 300 MPa. All samples show a purely elastic deflection until fracture occurs (indicated by the arrow) and multiple samples pressed with the same experimental parameters were tested to account for a statistical distribution of the results. The samples displayed in black were processed at 460 °C for 60 s to 70 s and a maximum fracture stress of $\sigma_{f,max}$ = 650 MPa could be reached at a strain of 0.85 %. The determined elastic modulus in

bending is E = 75 GPa which is equivalent to the elastic modulus of bulk samples. The samples shown in red show a lower fracture stress of roughly 300 MPa and were pressed at 450 °C for 100 s to 120 s, indicating that these process parameters are not ideal and result in a decreased mechanical performance [184].

The inset Fig. 5.11 shows a 3PB curve of an as-cast bulk sample with the same geometry and the dashed line marks the maximum fracture stress of the consolidated powder samples. Cast bulk samples reach a fracture stress of 2600 MPa, and thus four times higher than the best powder samples. Additionally, they display a significant plastic deformability before fracture.

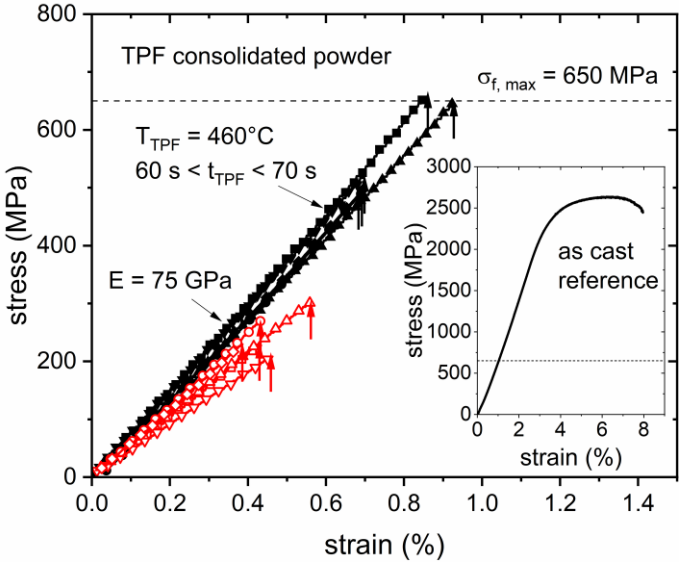

Figure 5.11: Stress-strain curves from three-point bending flexural tests. Two different groups of samples can be observed: samples fracturing around 300 MPa (red open symbols) and samples fracturing around 600 MPa (black filled symbols). The samples with the highest strength were pressed at 460 °C for 60 s to 70 s. The inset shows the stress strain curve of an as-cast bulk sample with the same sample geometry. Figure and caption taken from Ref. [184].

Figure 5.12 shows SEM images of the fracture surfaces of the 3PB powder samples. In Fig. 5.12 a), the surface of a sample fracturing at 270 MPa (red open circles in Fig. 5.11) is displayed. Both, unconnected powder particles and particles with transgranular fracture can be seen, indicating an embrittlement of the particles during the consolidation process. Figure 5.12 b) shows the fracture surface of the sample fracturing at 650 MPa (black filled squares in Fig. 5.11). Here, intergranular fracture can be observed, where vein patterns on the interface between the powder particles are visible, which indicates that an intrinsically ductile joint has formed between the particles [184].

The powder samples showing transgranular fracture and a smooth fracture surface through the particles imply that the initially ductile material experienced an

embrittlement in the TPF process. The initially ductile nature of AMZ4 can be observed in the 3PB curve in the inset in Fig. 5.11. In amorphous bulk material, embrittlement is typically a consequence of relaxation [126,175–177] or beginning crystallization [178–180]. Both phenomena can occur during the TPF process. A heat treatment above T_g for an excessive amount of time causes nanocrystallization which at the beginning is not yet visible in XRD measurements. A relaxed sample state is obtained if the sample is not cooled sufficiently fast from the SCL, resulting in a fictive temperature below the critical fictive temperature for embrittlement [116].

In contrast, the powder samples that show intergranular fracture with vein patterns on the fracture interfaces and reach a fracture stress of 650 MPa do not show any sign of relaxation or crystallization. Vein patterns are characteristic for a ductile fracture behavior in BMGs [112,152,288]. The SEM images also show that the powder particles are not well connected on the edges between multiple powder particles, but only on the larger surface contact areas. Even though no porosity is visible in a polished cross section, the poorly connected edges of the particles can act as crack initiators and facilitate catastrophic fracture. In total, the fracture strength of the sample is limited by the strength and amount of the well-connected interface between the powder particles. In comparison to bulk samples, the fracture strength of the powder samples is still four times lower. In order to obtain consolidated samples with a higher mechanical performance, different approaches are conceivable.

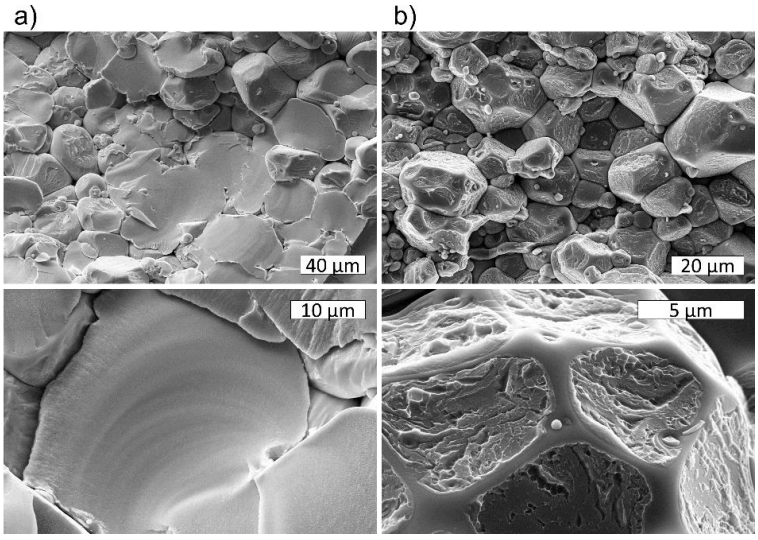

Figure 5.12: SEM images of the fracture surfaces of compacted powder beams. **a)** Transgranular fracture at a maximal stress of 270 MPa and **b)** intergranular fracture at 650 MPa. Figure and caption taken from Ref. [184].

First, a significantly higher pressing stress could be applied in a different experimental setup, causing a higher contact force between the particles and especially the edges. Furthermore, the interface connection problem could be caused by oxide layers on the surface of the AMZ4 powder [164]. Zr-based alloys will always form oxide layers on

the surface due to the high affinity of zirconium to oxygen, however it might intensify the surface connection if a shear-type force is implemented in the pressing procedure that could break up the surface oxide layer [289]. Another approach could be to use non-globular and rather flaky powder particles that might cause a better connection between the particles [164].

As a side note it should be mentioned that TPF experiments with amorphous AMZ4 bulk material were performed in the exact same experimental setup as the powder consolidation experiments. As-cast beams were pressed at the same temperatures and for the same times in the powder pressing molds, thus preventing a deformation of the sample. Subsequent mechanical tests on these beams showed no difference in mechanical strength and ductility in comparison to as-cast samples. Consequently, the cooling conditions after the TPF process do not cause a fictive temperature below the critical fictive temperature. Hence, it can be concluded that the inferior mechanical performance of the consolidated powder samples results from the weak particle interfaces and is not caused by the thermal protocol of the TPF process.

In summary, the powder consolidation experiments confirm the findings regarding formability presented in Chapter 5.1.3. The powder samples with the best mechanical performance are obtained when pressing them at the upper limit of the AMZ4 TPF processing window and for times shorter than the onset of crystallization, thereby avoiding an embrittlement. Hence the processing region with the highest formability results in the most intense bonding of the powder particles. The higher ability to flow enables a larger deformation of the powder particles which might also facilitate breaking up the surface oxide layer.

Within the scope of the IGF project on the thermoplastic consolidation of amorphous powder, two more alloy compositions were investigated. Amorphous powder out of FeMoPCB and CuTi were also consolidated by TPF and then mechanically tested. However, the disillusioning results found for AMZ4 also apply to these alloys. While dense samples can be obtained, their mechanical strength in 3PB lies far below the values of as-cast bulk material. For both alloy compositions, the best samples do not exceed fracture strength values of 500 MPa. While for the Fe-based alloy, surface oxides might not play such an important role as for the Zr-containing compositions, the intrinsically brittle nature of the alloy composition causes the particles to break in a transgranular manner.

Based on these findings regarding the weak surface bonding of the powder particles which does not allow TPF consolidated samples to reach the strength of cast bulk material, additional experiments were dedicated to the thermoplastic bonding behavior of BMGs. The results of these experiments and their implications are presented in the next section.

5.2.3 Thermoplastic Joining of Bulk Samples

Developing a bonding and joining technology for a new engineering material is a crucial step on the way to a widespread use. The experiments on the thermoplastic consolidation of amorphous powder demonstrated that the formation of samples with the same mechanical performance as as-cast bulk samples is not yet possible. The limiting factor in the process is the strength of the interface between the powder particles. In order to evaluate the general feasibility of a thermoplastic bonding process of BMGs in our experimental setup (in a high-purity Ar atmosphere), TPF consolidation experiments with bulk samples were performed.

In a first step, two short AMZ4 beams are laid on top of each other in the shape of a cross and pressed at 450 °C for 10 s, 20 s, and 30 s. The obtained samples are shown in Fig. 5.13 a) and no detectable joint strength is obtained. Both sample sides show a perfect tight fit, however without a bonding of the surfaces. Figure 5.13 b) shows a magnification of the sample contact area during the TPF process. The thermoplastic deformation of both surfaces results in a smooth and shiny surface with a mirror like finish. The possibility to use thermoplastic forming of metallic glasses to produce atomically smooth surfaces was presented earlier by Kumar et al. [290].

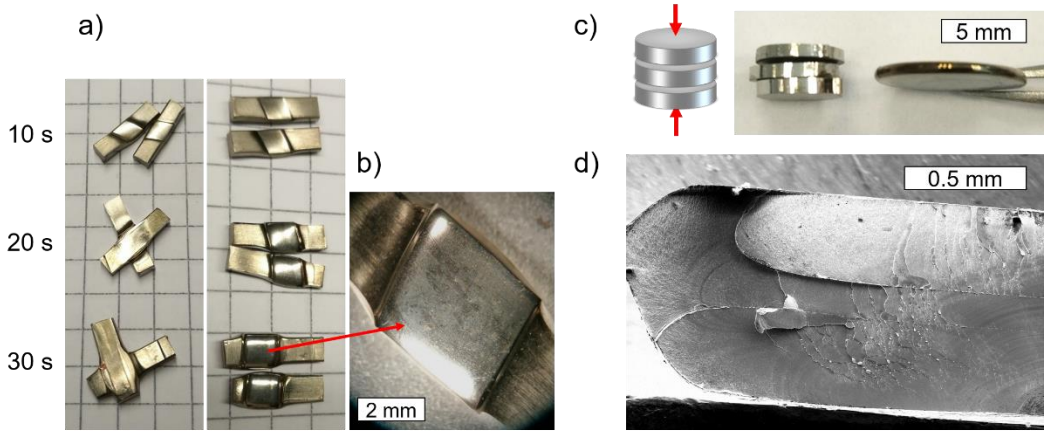

Figure 5.13: Thermoplastic surface bonding experiments with bulk amorphous AMZ4 samples. All samples were pressed with a force of 1000 N. **a)** Two beams were laid on top of each other in the shape of a cross and pressed at 450 °C for 10, 20, and 30 s. The samples can easily be taken apart again after the experiment. **b)** Magnification of the contact area in the TPF process. **c)** Schematic and photographic illustration of a TPF bonding experiment of three stacked discs. The samples were pressed at 465 °C for 60 s. **d)** SEM image of the fracture surface of the pressed disc after TPF. The initial disc surfaces are still visible in the fracture surface.

Efforts regarding the joining of BMGs in their SCL region are also found in literature. Kuo et al. demonstrated that the thermoplastic joining of BMGs in their SCL region is generally possible [291], however relies on a long-range diffusion bonding. The

underlying diffusion kinetics are similar to the crystallization kinetics in the SCL, thus making it challenging to avoid crystallization during the bonding process. Furthermore, surface oxide layers on the highly reactive Zr-based alloys act as additional diffusion barriers. These observations are in good agreement with our results from the powder consolidation experiments, where a surface bonding of the particles is shortly after followed by embrittlement due to nanocrystallization.

Later, Schroers and coworkers published a study on the joining of BMGs in air [289] where they propose a thermoplastic method to join BMGs and also include a mechanism to explain their findings. They argue that the inevitable surface oxide layers hamper the long-range diffusion bonding and that breaking these oxide layers is a necessary condition to allow for a fast and intense bonding of the surfaces. When two BMG surfaces are strongly deformed and shear occurs in-between the surfaces, the oxide layers break and allow pristine BMG material to flow to the surface during the thermoplastic deformation, where this material than forms a metallurgical bond. This process is schematically depicted in Fig. 5.14 a). They found that the strength of the joint is directly proportional to the amount of strain the material experiences, as shown in Fig. 5.14 b). While their findings are based on TPF experiments in air, the results match astonishingly well with our observations in a high-purity Ar atmosphere. Hence, the initial surface oxide layer (even after polishing the samples) is enough to prohibit a metallurgical bond. We can conclude that the samples depicted in Fig. 5.13 a) experienced a strain below the critical value to break these surface oxides and hence no bonding is observed.

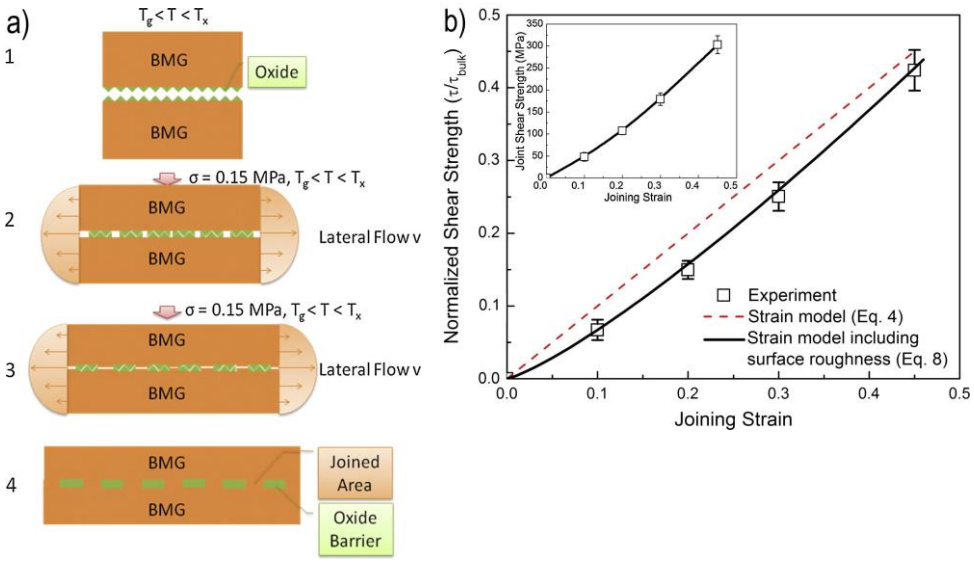

Figure 5.14: a) Schematic depiction of the BMG TPF joining mechanism in air. **b)** Joint shear strength over TPF joining strain. Taken from Ref. [289].

In a second approach, the findings of Schroers et al. regarding the joining of BMGs are taken into account and a simple experimental setup for our TPF device is conceived. Three thin BMG discs are stacked on top of each other and are then thermoplastically pressed as depicted in Fig. 5.13 c). As the samples are heated by Cu-pistons from top and bottom, the outer discs will first start to deform, and their deformation causes shear on the interfaces between them and the inner disc. All discs and the interfaces in-between experience a large strain, complying with the necessary conditions for a bonding of the surfaces. The final shape of such a pressed sample can be seen on the right side of the image. From the outside, the sample appears well joined and no signs of the individual discs are visible.

Similar to the results presented in Ref. [291], also on a polished cross-section in SEM no visible interface can be detected. However, when the joint disc is forcefully broken in half, the fracture surface clearly reveals the former surfaces of the individual discs, as can be seen in Fig. 5.13 d). Hence, the initial surfaces still act as weak spots, deteriorating the mechanical properties and facilitating fracture. Again, this is in agreement with the findings of Schroers at al. who observe a maximum shear strength of joint samples of close to half the value of bulk samples. The joint always remains the weak spot and the full strength of the bulk material is not reached.

In the end, the same phenomenon determines the bond strength in the consolidated powder samples. At the particle surfaces where the largest strain is experienced, the surface oxide layers break and a metallurgical bond is obtained, whereas on the less deformed edges of the particles the oxide layer stays intact and no bond is obtained, significantly reducing the mechanical strength of the samples.

5.3 Summary and Conclusions

The chapter on thermoplastic forming is dedicated to a description and discussion of the formability of BMGs and the implications of formability on processing techniques for amorphous metals. Formability is experimentally assessed by two different approaches, first, TPF experiments with a constant heating rate, and second, isothermal experiments. For both cases, formability is also calculated from previously measured material properties and found to perfectly coincide with the experimental deformation results. The highest formability is obtained at the highest temperatures that can be reached while still avoiding crystallization. The determined ideal processing window for TPF is then used for consolidation experiments on amorphous powder, where dense amorphous samples can be pressed. Their mechanical performance however falls significantly behind the one of as-cast bulk samples, as inevitable surface oxide layers hamper a metallurgical bonding of the powder particle surfaces.

The bulk TPF experiments with a constant heating rate show that the obtained deformation varies strongly between different alloys. A correlation between deformation and the two parameters $\Delta T_x/T_g$ and $S = \Delta T_x/(T_l\text{-}T_g)$, which can simply

be calculated from a single calorimetric measurement, is observed. An even stronger correlation with deformation is found for two quantities that can be obtained from a single TMA viscosity scan. First, the viscosity just before T_x, and second, the formability F^{scan}, as calculated according to Eq. 5.4. This also verifies the validity of the theoretical concept behind the formability F^{scan}, which can be calculated from the viscosity data in the temperature range between T_g and T_x.

The isothermal deformation experiments on AMZ4 and FeMoPCB demonstrate that the highest deformation is reached at the upper limit of the accessible temperature processing window, where crystallization can still be avoided. The experimental time-temperature-deformation (TTD) diagrams for both alloys are displayed in Fig. 5.5. These results align well with the theoretical temperature-dependent formability calculated from isothermal crystallization times and viscosity values.

Finally, the findings regarding the highest formability and hence the ideal TPF processing region are transferred and applied to TPF powder consolidation experiments with AMZ4 powder. The powder can be consolidated into dense and amorphous samples and these samples reach the hardness of as-cast samples and one quarter of their strength under flexural load. The drastically reduced mechanical strength is most likely caused by an insufficient bonding of the powder particles due to surface oxide layers. Given these limitations, still a process window for thermoplastic consolidation of powder can be defined solely based on the isothermal crystallization times and viscosity. Amorphous powder should be consolidated at the highest temperatures possible where crystallization can still be avoided in the experimental setup.

Joining experiments on bulk samples show that a metallurgical bonding of surfaces is partly possible, but that the initial surfaces still acts as a weak spot and that the full strength of the bulk material cannot be reached. The strength of the joint correlates with the surface strain during thermoplastic joining. Against this background, a limitation of the strength of consolidated powder samples to roughly 25 % of the strength of bulk material seems reasonable. Only parts of the powder particle surfaces experience a sufficiently large strain during the consolidation process, resulting in an already weakened bonding, while the edges of the deformed powder particles remain almost without strain during consolidation and do not contribute to the strength of the joint at all.

While the thermoplastic powder consolidation and joining experiments do not raise hope for this technology as a candidate for the additive manufacturing of amorphous parts, further techniques have been evaluated in the meantime. In a joint IGF research project between the chair of Metallic Materials at Saarland University and the chair of Production Engineering at the University of Duisburg-Essen, experiments on the additive manufacturing of amorphous parts by selective laser melting (SLM) are performed. First promising results were published in Ref. [292]. Amorphous SLM parts reach much higher strength values than TPF consolidated ones, as can be seen in Fig. 5.15 a) where three-point bending (3PB) curves are shown. While the SLM parts do

not yet display plasticity in bending, they surpass a strength of 2 GPa, almost reaching the values of as-cast bulk material. Typical SLM samples printed from AMZ4 powder are shown in Fig. 5.15 b). This promising additive manufacturing method for amorphous parts will be pursued in future projects.

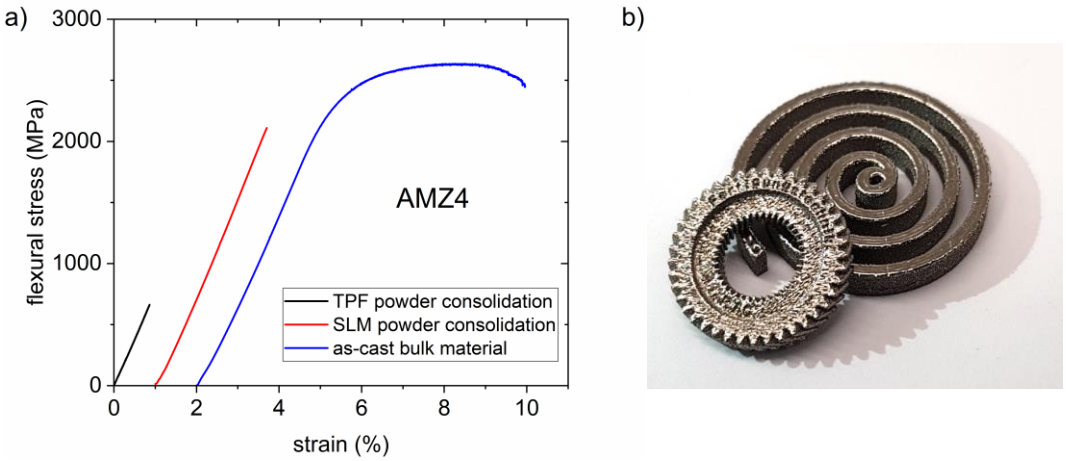

Figure 5.15: **a)** Flexural 3PB stress-strain diagram for AMZ4 produced by TPF powder consolidation, SLM, and as-cast bulk material. **b)** Photograph of SLM samples printed from AMZ4 powder.

Chapter 6

Influence of Minor Additions on the Thermoplastic Formability

The lessons learned in the previous two chapters are combined in this one. The six alloy compositions that were thoroughly investigated in Chapter 4 are now used for thermoplastic deformation experiments, following the evaluation methods used in Chapter 5. Consequently, the influence of minor additions of S and P on the thermoplastic deformation behavior and the formability of Vit101 and Vit105 is presented and discussed. Both, experiments with a constant heating rate and isothermal experiments at different temperatures, leading to time-temperature-deformation (TTD) diagrams, are performed. It can be shown that the minor additions cause a drastic increase of thermoplastic formability which is in accordance with the observed changes in the thermophysical properties.

The TPF experiments on the Vit101 and Vit105 alloys were performed in collaboration with Cristo Paulo and in the framework of his master thesis. More detailed experimental results, e.g. XRD and DSC measurements of the TPF samples, can be found in his thesis [293]. Additionally, oxidation experiments on the six alloy compositions can be found there.

6.1 Formability upon Constant Heating

The thermoplastic formability upon constant heating is evaluated in the same way as discussed in Chapter 5.1.1. The averaged deformation curves obtained from several measurements for the six investigated alloys are depicted in Fig. 6.1, together with the corresponding TMA viscosity scans and the DSC scans. The results for the Vit101 alloys are shown in Fig. 6.1 a)-c) and the ones for the Vit105 alloys in d)-f). The base alloys are always shown in black, the P-containing alloys in red, and the S-containing alloys in blue.

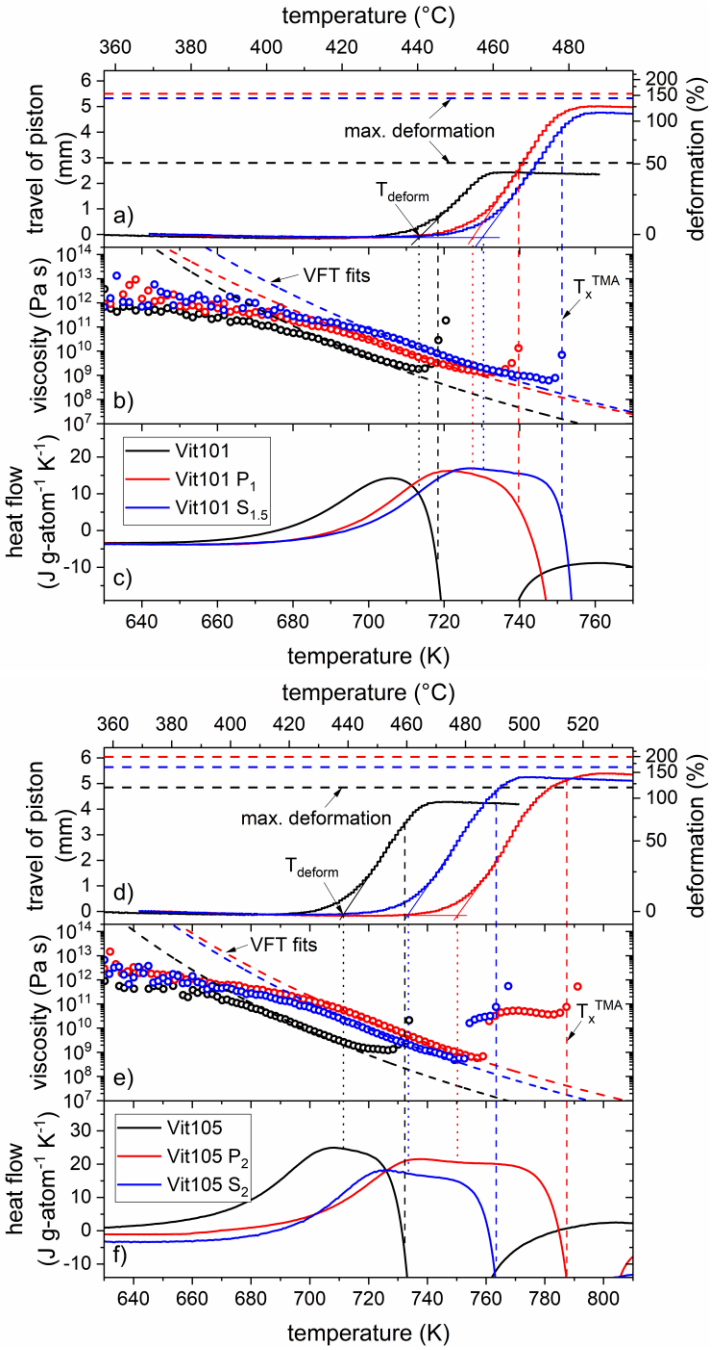

Figure 6.1: TPF deformation experiments with a constant heating rate. **a)-c)** Vit101 alloys and **d)-f)** Vit105 alloys. In each case, the upper panel shows the travel of the TPF piston in mm and the corresponding sample deformation in %. The true final maximal deformation is indicated by the dashed horizontal lines. The center panel displays viscosity as measured in TMA scans together with the VFT viscosity fits. The onset of crystallization in the TMA measurement is indicated by a dashed line as T_x^{TMA}. The bottom panel shows DSC scans with the same heating rate.

Figure 6.1 a) and d) show the travel of the piston of the TPF machine as a function of temperature, corresponding to the deformation of the sample which is displayed on the right-hand side axis (deformation $\varphi = \ln(h_1/h_0)$, where h_0 is the initial height of the sample and h_1 the deformed height). The horizontal dashed lines indicate the true final deformation, calculated from the final sample thickness. The numerical values can be found in Table 6.1. In the case of the Vit101 alloys, the minor additions significantly increase the maximum deformation. While Vit101 only shows a value of around 50 %, both modified versions of the alloy reach roughly 150 %. A similar trend is observed for Vit105 (118 %), where the S-containing alloy reaches 164 % and the P-containing alloy even 199 %. Additionally, the deformation temperature, T_{deform}, for a pressing stress of 70 MPa is determined by tangents on the deformation curve and indicated by dotted lines. Similar to the shift in T_g caused by the minor additions, also the deformation temperature increases in comparison to the base alloys.

Figure 6.1 b) and e) show viscosity as a function of temperature on the same temperature scale. The datapoints correspond to TMA scans with the same heating rate as the TPF experiments (0.333 K/s) and the dashed lines are the VFT fits obtained from the isothermal TMA measurements (compare to Fig. 4.13). The onset of crystallization in the TMA measurements, T_x^{TMA}, is indicated by a vertical dashed line. It should be noted that in the case of Vit105 P_2 and Vit105 S_2 the viscosity in the TMA scan jumps up before the onset of crystallization due to the deflection limit of the TMA device. Finally, the corresponding DSC scans for all alloys are depicted in Fig. 6.1 c) and f).

Besides the true final deformation, φ, in %, all other relevant material properties for different correlations with the deformation are given in Table 6.1.

Table 6.1: TPF bulk deformation experiments with a constant heating rate. T_g, glass transition temperature; ΔT_x, length of the SCL region; T_l, liquidus temperature; D*, VFT fragility parameter; $\Delta T_x/T_g$; $S = \Delta T_x/(T_l-T_g)$, S-formability parameter; η at T_x, viscosity values at T_x; F^{scan}, formability parameter for a constant heating rate; φ, deformation in %, calculated according to $\varphi = \ln(h_1/h_0)$.

Alloy	T_g [K]	ΔT_x [K]	T_l [K]	D*	$\Delta T_x/T_g$	S	η at T_x [Pa s]	F^{scan} [Pa^{-1}]	φ [%]
Vit101	674	44	1168	16.2	0.066	0.090	1.82×10^{9}	1.02×10^{-8}	**51**
Vit101 P_1	691	58	1171	20.8	0.084	0.121	1.3×10^{9}	6.89×10^{-8}	**154**
Vit101 $S_{1.5}$	695	60	1170	18.3	0.087	0.127	6.1×10^{8}	8.22×10^{-8}	**143**
Vit105	671	60	1134	20.3	0.089	0.129	1.22×10^{9}	3.84×10^{-8}	**118**
Vit105 P_2	696	100	1189	24.8	0.144	0.203	6.0×10^{7}	5.94×10^{-7}	**199**
Vit105 S_2	692	77	1295	22.3	0.112	0.128	1.6×10^{8}	1.48×10^{-7}	**164**

Figure 6.2 shows how the TPF deformation results with a constant heating rate for the Vit101 and Vit105 alloys align with the correlations previously presented in the Figs. 5.6 and 5.7. The grey datapoints and the dashed lines are a reproduction of these figures and are displayed as a reference. The correlation with $\Delta T_x/T_g$ is shown in Fig. 6.2 a), the one with $S = \Delta T_x/(T_l\text{-}T_g)$ in b), the one with the viscosity η at T_x in c), and the one with the formability parameter for a constant heating rate, F^{scan}, in d).

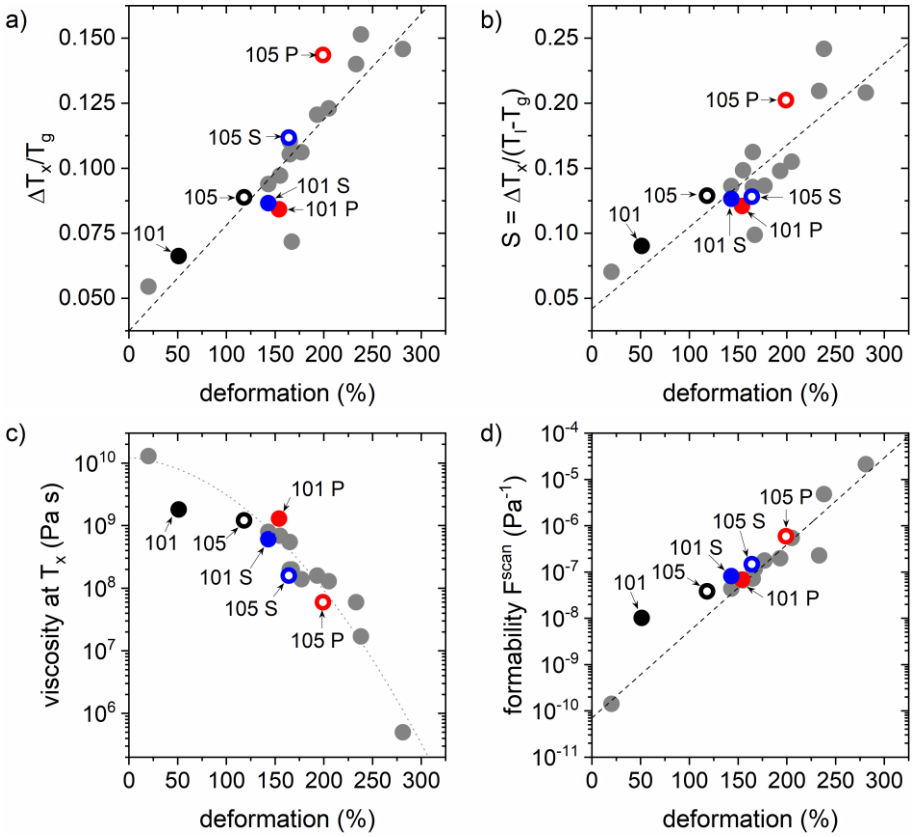

Figure 6.2: Correlations obtained from the TPF experiments with a constant heating rate (Table 6.1). Correlation between the experimental thermoplastic deformation in % and **a)** $\Delta T_x/T_g$, **b)** $S = \Delta T_x/(T_l\text{-}T_g)$, **c)** the viscosity at T_x, and **d)** the formability F^{scan} according to Eq. 5.4. The grey datapoints are reference points previously shown in Figs. 5.6 and 5.7, together with the corresponding linear fits. The Vit101 alloys are shown as filled dots and the Vit105 alloys as hollow circles.

In Fig. 6.2, the newly obtained results for the Vit101 alloys are shown as filled dots and the ones for the Vit105 alloys as hollow circles and the alloy corresponding to each datapoint is written into the figure. In general, it can be seen that the new results align well with the previously presented correlations and no significant outliers are observed. Only for Vit101, the measured deformation is lower than predicted by the calculated F^{scan} value. Possibly, this effect is caused by the very short SCL region,

where the sample does not reach the metastable equilibrium in the SCL sufficiently fast and no stable deformation regime is reached in the TPF experiment.

6.2 Formability in Isothermal Experiments

In the second part of this chapter, the formability of the Vit101 and Vit105 alloys in isothermal deformation experiments is evaluated (compare to Chapter 5.1.2). The main outcome of these experiments are time- and temperature-dependent deformation maps. Together with all the results from the thermophysical characterization in Chapter 4, time-temperature-deformation (TTD) diagrams can be constructed, equivalent to the ones for AMZ4 and FeMoPCB which were presented in Fig. 5.5. Besides the deformation behavior of the alloys, these TTD diagrams include the temperature-dependent equilibrium viscosity, which was measured in TMA experiments, as well as the isothermal crystallization times that were previously displayed in the TTT diagrams.

Figure 6.3 shows the TTD diagrams for a) Vit101, b) Vit105, c) Vit101 P_1, d) Vit105 P_2, e) Vit101 $S_{1.5}$, and f) Vit105 S_2. The deformation during the isothermal TPF experiments is visualized in a color-filled contour plot which is embedded in a TTT diagram. The same color-scale is chosen for all six alloys and dark red indicates a deformation above 190 % and purple a deformation of 10 %. These deformation maps result from more than 150 single TPF experiments and each single experiment is indicated by a small black dot at the corresponding temperature and time. Only samples that were found to be XRD amorphous after the TPF experiment are used for this depiction. Samples that crystallized due to longer processing times are left out. It should be mentioned that the displayed processing time is the pressing time when the isothermal temperature is reached. Based on measurements with thermocouples inside the samples, this corresponds to the total pressing time minus a 15 s heating period.

The grey shaded areas in Fig. 6.3 indicate a change of viscosity of half an order of magnitude. The viscosity values according to the VFT fits (compare to Fig. 4.13) are given in the figure and the corresponding temperatures are indicated by the blunt arrows. It can be seen that the viscosity values in the experimental TPF region are rather different for the investigated alloys. Additionally, the crystallization times from the TTT diagrams (compare to Fig. 4.9) are also displayed. The black square indicates the 50 % crystallization transformation at the given temperature and the black triangle stands for the 99 % transformation.

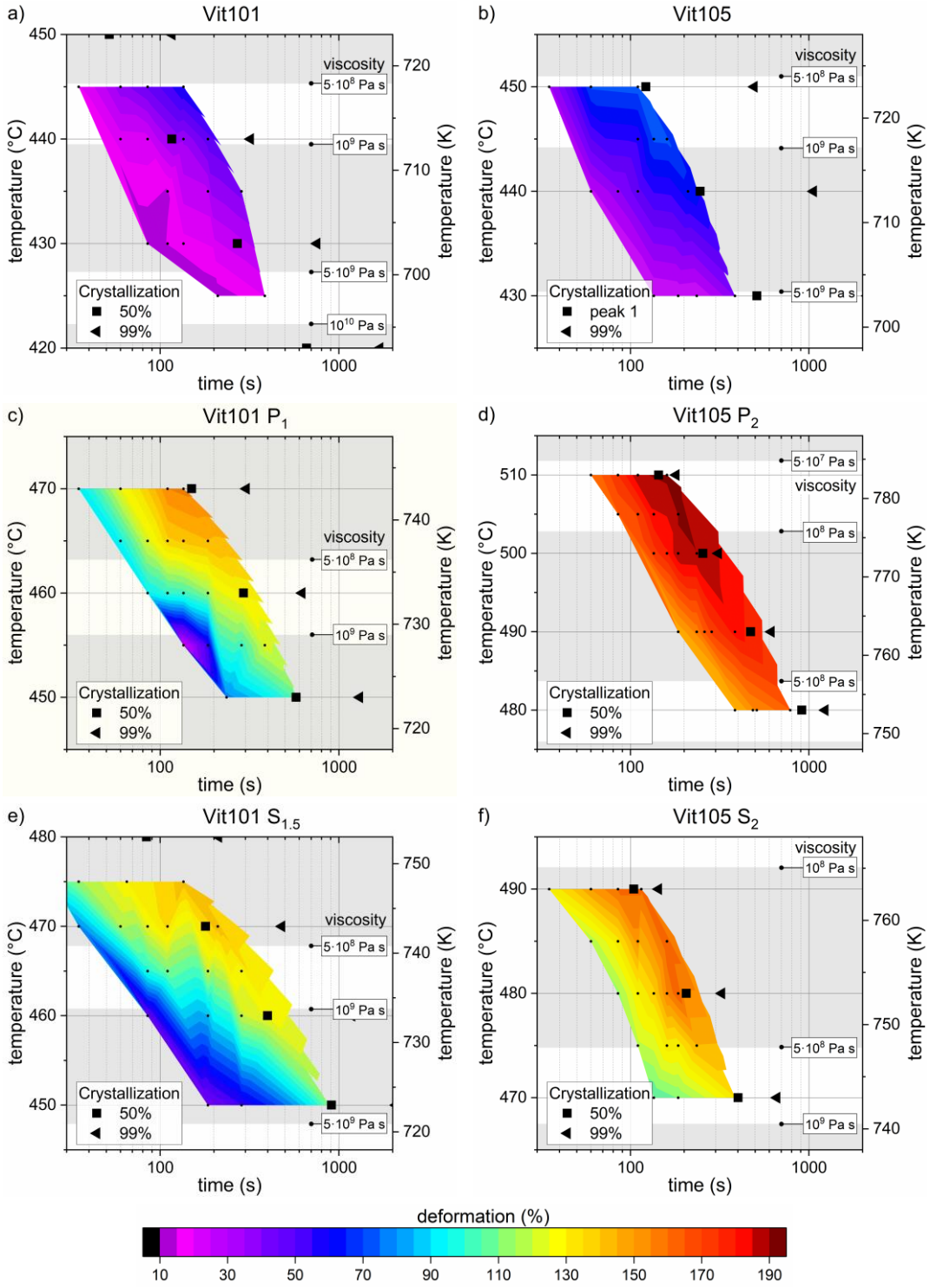

Figure 6.3: Time-temperature-deformation (TTD) diagrams for the thermoplastic forming of **a)** Vit101, **b)** Vit105, **c)** Vit101 P_1, **d)** Vit105 P_2, **e)** Vit101 $S_{1.5}$, and **f)** Vit105 S_2.

In all cases, XRD amorphous samples could be obtained for processing times reaching roughly the 50 % crystallization transformation times from the TTT diagrams for a given temperature. First, a beginning nanocrystallization upon heating from the glassy state is difficult to detect in laboratory XRD measurements. When looking into the in-situ synchrotron X-ray diffraction patterns upon heating (compare to Fig. 4.19 and 4.20), it can be seen that sharp and clear diffraction peaks only become visible after a significant percentage of the crystallization enthalpy has been released. Especially in the case of the Vit101 alloys and the unmodified Vit105 composition, the first peak in the DSC measurements does not lead to clear XRD diffraction peaks. The isothermal in-situ synchrotron X-ray diffraction experiments on Vit105 S_2 further show that clear diffraction peaks are only visible after times far beyond the 1 % crystallization time (compare to Fig. 4.21). Second, already minor deviations of the real sample temperature in the TPF machine from the measured temperature can account for a significant change in the isothermal crystallization time, due to its strong temperature dependence. Temperature differences of ± 3 K could possibly occur in the used TPF device, even after a careful temperature calibration [230].

The TTD diagrams in Fig. 6.3 show tremendous differences in the thermoplastic deformation behavior of the Vit101 and Vit105 alloys and their modifications. Both base alloys (a) Vit 101 and b) Vit105) display a very limited sample deformation around roughly 60 %, even in the high-temperature region with the largest formability.

In the case of the Vit101 alloys, the achievable deformation can be increased to around 150 % for both Vit101 P_1 and Vit101 $S_{1.5}$. The maximum deformation is reached at temperatures around 5 K below the crystallization temperature in a scan with 0.333 K/s and for pressing times of roughly 120 s. Longer processing times result in crystalline samples. For the Vit105 alloys, the differences in formability between the different alloy modifications is even more pronounced. The maximum deformation observed is 70 % for Vit105, 160 % for Vit105 S_2 and even above 190 % for Vit105 P_2. With almost 200 % of deformation, the P-containing alloy is amongst the non-precious metal containing BMGs with the highest formability.

When the fragility of the alloys is considered, it is apparent that the alloys with a higher kinetic fragility parameter D* allow for a larger thermoplastic deformation, even though this seems counterintuitive at a first glance. In the case of the Vit105 alloys, the achievable deformation increases monotonically with D*. This observation can be explained if not only the implications of D* on the temperature dependence of viscosity are considered, but also the effects of the kinetics on the crystallization behavior. The length of the SCL region also increases with D* for the Vit105 alloys, overcompensating the slower decrease in viscosity upon heating (also compare to Fig. 5.8). Therefore, lower viscosity values can be reached in the stronger alloys before the onset of crystallization is observed.

When comparing the maximum deformations in the isothermal experiments and the scans with a constant heating rate, similar deformation values are reached for all alloys but Vit105. In the case of Vit105, a maximum deformation of almost 120 % is reached

in the deformation scan, while the isothermal experiments reach a maximum deformation of 70 % for XRD amorphous samples. This difference can be explained by the uncommon isothermal crystallization behavior of Vit105 (compare to the in-situ synchrotron XRD patterns in Fig. 4.21 a)). The first exothermal event in the DSC scan corresponds to the formation of a structure that still seems to be partly amorphous and hence capable of thermoplastic deformation. The formability potential of this structure is exhausted during the deformation scan. In the isothermal experiments however, deformation is only considered for fully amorphous samples, and hence the formability of this partially amorphous structure is not exhausted. In Fig. 6.3 b) it can also be seen that fully amorphous samples after deformation are only obtained up to the first crystallization peak (black square), and not beyond.

Finally, the isothermal formability, F^{iso}, is calculated for the six alloys depicted in Fig. 6.3 according to Eq. 5.3. The results are presented in Fig. 6.4 in the style of Fig. 5.9, where formability is shown over temperature scaled to T_g. The small grey dots represent the formability values for AMZ4 and are shown as a reference. The results for the Vit101 alloys are shown in Fig. 6.4 a) and the ones for Vit105 in b). The vertical dashed lines represent the highest temperature at which deformation experiments for the TTD diagrams (Fig. 6.3) were performed and the horizontal dashed lines indicate the corresponding formability values.

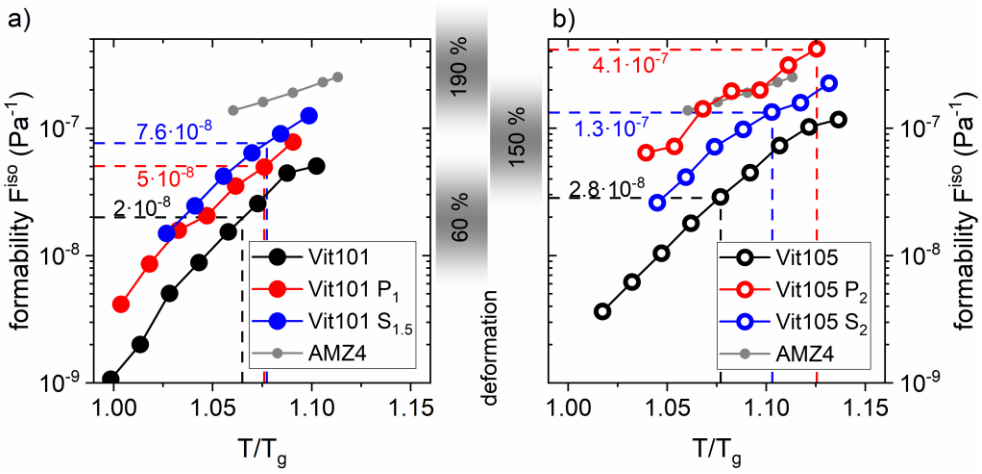

Figure 6.4: Isothermal formability, F^{iso}, displayed over T_g-scaled temperature for the **a)** Vit101 alloys and **b)** Vit105 alloys, both on the same axis. The values for AMZ4 from Fig. 5.9 are shown as grey dots as a reference. The dashed lines indicate the highest temperature and the corresponding formability at which deformation experiments for the TTD diagrams (Fig. 6.3) were performed (and feasible). The grey shaded areas in the center roughly indicate which formability values correspond to which deformation in our TPF experiments.

The calculated formabilities at the maximum deformation temperatures agree well and consistently with the observed deformation in the TPF experiments. In the case of the Vit101 alloys, both compositions with minor additions show a similar and

increased formability in comparison to the base alloy. For the Vit105 alloys, the formability increases drastically from Vit105, over Vit105 S_2, to Vit105 P_2. The P-containing composition displays a formability that is almost equivalent to the one of AMZ4. And indeed, the observed maximum deformation in the isothermal TPF experiments is around 190 % for both alloys.

Based on the TPF deformation values of the six investigated alloys, a rough estimate on the correlation between isothermal formability and deformation is given by the grey shaded areas in the center of Fig. 6.4. This correlation of cause depends on the experimental TPF conditions, e.g. pressing stress, sample volume, and the geometric quantity used for the calculation of the deformation, and hence is limited to our experimental setup. We can observe that a deformation of around 190 % is obtained for a formability of around $F^{iso} \approx 3\times10^{-7}$ Pa^{-1}. 150 % can be reached for a formability of $F^{iso} \approx 8\times10^{-8}$ Pa^{-1}, and 60 % for $F^{iso} \approx 2\times10^{-8}$ Pa^{-1}.

In summary it can be claimed that the effects of minor alloying that are found in the thermophysical characterization of the alloys in Chapter 4 can also be observed during the thermoplastic deformation experiments. The correlation between the thermoplastic formability and the thermophysical properties of an alloy that were described in Chapter 5.1 also hold true for differences between the alloys caused by minor additions. Hence, minor additions can be used to significantly alter and fine-tune the thermoplastic deformation behavior. Especially the strong effect of minor additions on the length of the SCL region allows for large changes in formability. The isothermal crystallization times can be extended while the change in kinetic fragility and hence viscosity is much less pronounced.

Chapter 7

Summary, Conclusions, and Outlook

The main focus of this work was to investigate the thermophysical properties and the structure of the bulk metallic glass-forming alloys Vit101 and Vit105, and to elucidate the influence of minor additions of phosphorus and sulfur in these systems. In a second step, the results were linked to findings on the thermoplastic deformation behavior of BMGs. In this chapter, a short summary is presented, followed by some general concluding remarks about the cross connections between the different chapters. For a more detailed summary of the different topics, the reader is referred to the final section of each individual chapter. In the end, an outlook regarding further work on the effects of minor additions in BMGs is provided.

7.1 Summary and Conclusions

After the discovery of sulfur as a main constituent element in bulk metallic glass-forming alloys in 2016 in our group [7], the question arose if minor additions of sulfur could also enhance the properties of known alloy compositions, especially with respect to their thermoplastic formability. Additionally to sulfur (S), also its neighboring element in the periodic table, phosphorus (P), was considered for these experiments. For two well-known BMG alloys with a high relevance for industrial applications, namely Vit101 ($Cu_{47}Ti_{34}Zr_{11}Ni_8$) and Vit105 ($Zr_{52.5}Cu_{17.9}Ni_{14.6}Al_{10}Ti_5$), their initially low thermal stability upon heating was increased by minor additions of P and S, and the following compositions were selected for an in-depth investigation: Vit101 P_1 ($Cu_{46.53}Ti_{33.66}Zr_{10.89}Ni_{7.92}P_1$), Vit101 $S_{1.5}$ ($Cu_{46.3}Ti_{33.5}Zr_{10.8}Ni_{7.9}S_{1.5}$), Vit105 P_2 ($Zr_{51.45}Cu_{17.54}Ni_{14.31}Al_{9.8}Ti_{4.9}P_2$), and Vit105 S_2 ($Zr_{51.45}Cu_{17.54}Ni_{14.31}Al_{9.8}Ti_{4.9}S_2$).

Furthermore, experiments on the thermoplastic forming (TPF) of different BMGs were performed, using an approach with a constant heating rate as well as isothermal TPF experiments. For both cases, formability was also calculated from previously measured material properties and found to perfectly coincide with the experimental deformation results. Based on these findings, thermoplastic forming was also used to consolidate amorphous powder into dense and amorphous samples. In the end, TPF experiments were also performed on the different Vit101 and Vit105 alloys, linking the results of the alloy characterization to the thermoplastic deformation behavior.

Vit101 and Vit105, and the Influence of Minor Additions of P and S

All experiments performed on these compositions were presented in Chapter 4 of this work and a first summary on these findings can be found in Chapter 4.7. DSC scans of the modified alloy compositions showed a significant enhancement of the thermal stability in terms of the supercooled liquid (SCL) region upon heating. For Vit101, the modified systems show a roughly 15 K longer SCL region than the base alloys, and for Vit105 the SCL region was extended by 28 K with the addition of S and by 40 K with P. In terms of critical casting thickness, and hence glass-forming ability (GFA), the experiments showed that for Vit101 S-additions increase the critical thickness from 5 mm to 6 mm and P-additions leave it unchanged. In the Vit105 system, S-additions decrease the critical thickness from initially 8 mm to 6 mm, and P-additions lower it to even 3 mm. Three-point beam bending tests revealed that minor additions in the Vit101 system cause an embrittlement. The same effect is observed for Vit105 P_2, whereas the Vit105 S_2 alloy shows the same amount of ductility as the base alloy.

The most important characteristic values of the investigated alloy compositions are summarized in Table A1 (Vit101 alloys) and in Table A2 (Vit105 alloys) in the appendix in the form of a datasheet.

When looking closer into the thermal stability and the crystallization behavior upon heating, the constructed TTT diagrams reveal that the modified alloy compositions display an at least three times longer time till the onset of crystallization in isothermal experiments. The thermal stability in terms of the SCL region correlates with the kinetic fragility of the alloys, with the kinetically stronger modified alloys showing a longer SCL region. Furthermore, for both alloy systems, the alloys with the longest SCL region (Vit101 $S_{1.5}$ and Vit105 P_2) feature the lowest $\Delta G^{l\text{-}x}$-value, which indicates a lower driving force for crystallization and hence a tendency for an increased thermal stability. Finally, the thermal stability is also influenced by the interfacial energy between the liquid and the primary crystallizing phase. The in-situ synchrotron X-ray diffraction experiments revealed the primary crystallizing phases for all alloy compositions. In the case of the Vit101 alloys, the primary crystallizing phase upon heating remains unchanged with the minor additions. For the Vit105 alloys however, the observed phase separation in the base alloy is suppressed by the minor additions and different primary phases are formed upon heating.

Regarding the GFA of the different compositions, the thermal stability against crystallization throughout the whole temperature range is of importance, which can best be visualized by the position of the tip of the so-called crystallization nose in a TTT diagram which needs to be bypassed upon cooling. The GFA is determined by kinetic and thermodynamic aspects. The kinetics of the alloys can be assessed by the viscosity in the liquid state, which was measured in this work. Within one alloy family, the alloys show relatively similar results, indicating that the differences in GFA are not caused by kinetics. In terms of driving force for crystallization, the calculated values cannot explain the changes in GFA. Hence, the differences are most likely

caused by a change in the primary crystallizing phase and a shift in nucleation barrier due to a different interfacial energy between the liquid and the competing crystal.

In this work, the structure of the primary phases which forms during the cooling process could be investigated by in-situ synchrotron X-ray diffraction experiments in an electrostatic levitator, resulting in a valuable and hard to get dataset. In the Vit101 system, the addition of 1.5 at% S suppresses the formation of the $ZrTiCu_2$ Laves phase that forms in unmodified Vit101.

In the Vit105 system, minor additions of S and P reduce the GFA and P even acts as poison for the GFA, reducing the critical casting thickness from at least 8 mm to 3 mm. In the case of Vit105 S_2, the formation of a S-containing phase (possibly $Zr_{21}S_8$) upon cooling can be verified by the ESL synchrotron measurements. The effects of this S-stabilized phase are also visible in the high-temperature viscosity measurements, where a kink in the viscosity curve is visible at around 1200 K. This phase causes a premature onset of crystallization and decreases the GFA of the Vit105 S_2 alloy composition.

A complete picture of the kinetic fragility behavior of the alloys can be obtained when the viscosity datapoints from the three-point beam bending (3PBB) experiments at low temperatures around the glass transition, and by Couette rotating cylinder rheometry at high temperatures in the stable liquid are combined. However, due to crystallization, a temperature gap of at least 400 K divides the high- and the low-temperature data and within this gap, viscosity can only be estimated by different viscosity models.

When a Vogel-Fulcher-Tammann (VFT) fit is used to describe viscosity based on the low-temperature data, a kinetically strong liquid behavior is found. A VFT fit only to the high-temperature data however indicates a much more fragile behavior. This observation was also made in a variety of metallic glass-forming liquids, and is commonly interpreted as an indication for a strong-to-fragile (SF) liquid-liquid transition (LLT). However, without additional data in the non-accessible temperature region, no further proof can be given.

Besides the VFT model, other models can be used to describe viscosity over the whole temperature range. Within this work, the MYEGA model, the extended MYEGA model, and the cooperative shear model were applied. While the MYEGA model experiences the same difficulties as the VFT model, the cooperative shear model fits the viscosity data very well over the whole temperature range, and does not necessarily indicate the presence of a LLT anywhere in-between the high- and the low-temperature measurements. The extended MYEGA model, which incorporates the existence of a SF transition, also perfectly fits the viscosity data, however indicating a rather unphysically large offset between the kinetic glass transition temperature of the strong and the fragile liquid. In the end, proof for a LLT can only be provided in systems where it can directly be observed, as e.g. in the BMG Vit106a [65], and where the transition is not obscured by crystallization. However, it can be concluded that the viscosity behavior of metallic glass-forming liquids cannot be represented by the

simple VFT equation over the whole temperature range, and that more elaborate models, like the cooperative shear model or the extended MYEGA model, are necessary. With these models, the viscosity of BMGs can be described from the high-temperature stable liquid down to below the glass transition, providing valuable datasets, e.g. for the modelling and simulation of flow during casting processes or thermoplastic forming.

The results of the in-situ synchrotron XRD experiments were not only used to assess the crystallization behavior, but also to reveal structural differences and the temperature evolution of structural features in the alloys. The S(Q) patterns imply that the investigated alloys possess a pronounced icosahedral SRO. The shift of the first sharp diffraction peak (FSDP) in S(Q) was used to estimate the thermal expansion behavior in the glassy state. The pair distribution function, G(r), was calculated for all patterns and the shape of the second peak was used to estimate the dominant cluster connection schemes. Finally, the G(r) data was used to estimate the fragility of the alloys according to the structure-fragility correlation by Wei et al. [79]. The results of this work imply that the structure-fragility correlation, found for the low-temperature SCL region, by tendency also applies to the high-temperature stable liquid. However, the correlation cannot directly be applied to calculate accurate fragility values from the structural data.

Thermoplastic Forming of BMGs

The thermoplastic formability of twelve alloys was first assessed by TPF deformation experiments with a constant heating rate. A correlation between the sample deformation and different parameters was established. The strongest correlation with deformation was found for the thermoplastic formability F^{scan}, which can be calculated from the viscosity data in the temperature range between T_g and T_x, hence verifying the validity of the underlying theoretical concept. Out of the twelve alloys, two were chosen for isothermal deformation experiments, namely AMZ4 ($Zr_{59.3}Cu_{28.8}Al_{10.4}Nb_{1.5}$) and FeMoPCB ($Fe_{67.5}Mo_{7.5}$ $P_{10}C_{10}B_5$). The experiments showed that the highest deformation is reached at the upper limit of the accessible temperature processing window, where crystallization can still be avoided.

The findings of these experiments were then transferred to thermoplastic consolidation experiments of amorphous AMZ4 powder. The best consolidation results are obtained when the powder is pressed at the highest temperatures possible where crystallization can still be avoided. The powder can be consolidated into dense and amorphous samples and these samples reach the hardness of as-cast samples and one quarter of their strength under flexural load. The drastically reduced mechanical strength is most likely caused by an insufficient bonding of the powder particles due to surface oxide layers. Joining experiments on bulk samples confirmed that a metallurgical bonding of surfaces is partly possible, but that the initial surfaces still acts as a weak spot.

Finally, TPF experiments on the Vit101 and Vit105 alloys and their modifications proved that the effects of minor alloying that are found in the thermophysical characterization of the alloys also affect their formability.

Conclusions

In conclusion it can be said, that minor additions allow for distinct modifications of an alloy without completely changing the characteristics of the alloy family. Properties like the density, the elastic modulus, or the hardness remain mostly unchanged. However, especially the properties connected to the kinetics of the system, e.g. the length of the SCL region, the kinetic fragility, as well as the crystallization behavior, and hence GFA, can be changed drastically by minor additions of an element. Regarding the thermoplastic formability of the alloys, the thermal stability and the viscosity are the decisive factors, both of which are largely influenced by minor additions. Therefore, the formability of BMGs is a property that is highly sensitive to modifications by minor additions. This can impressively be confirmed by the thermoplastic deformation experiments on the Vit101 and Vit105 alloys and their modifications.

Most modifications of the alloys result in a tradeoff between different properties: An increased thermoplastic formability for example can go along with a reduced GFA, or a mechanical embrittlement. Therefore, minor additions should not necessarily be seen as a universal tool to improve the properties of BMGs, but rather as a simple way to fine-tune a wide variety of properties to the desired use case.

The processing technique of thermoplastic forming was found to be applicable for many different BMGs. A good knowledge of the thermophysical properties of an alloy, especially viscosity and crystallization times, is sufficient to predict the formability without having to perform TPF experiments. Furthermore, the adequate processing conditions regarding temperature and time can already be indicated, allowing for quick and easy processing of BMGs by thermoplastic forming.

7.2 Outlook

The results of this work demonstrated the possibilities minor additions, especially with sulfur and phosphorus, offer for the modification of alloy properties. In our original publication on the discovery of sulfur-bearing BMGs [7], besides Vit101 and Vit105, one more alloy system was introduced where minor additions of sulfur improve the thermal stability, namely $Ni_{62}Nb_{38}$. In this case, sulfur also increases the critical casting thickness, however, causes a severe embrittlement of the alloy. Due to the embrittlement, an industrial relevance for structural applications is not given. Further investigations however showed that minor additions of phosphorus have a strong positive effect on the thermal stability, the critical casting thickness, and also the mechanical properties. The preliminary findings on the NiNbP alloy system are briefly presented here and lay the basis for further research on this promising BMG system.

A detailed characterization of the NiNbP BMGs can in the future be found in the master thesis of Markus Kipper, which will be handed in in the fourth quarter of 2019.

Figure 7.1 a) shows DSC scans with a heating rate of 0.333 K/s for the $Ni_{62}Nb_{38-x}P_x$ system, from x = 0 to 3. The glass transition temperature, T_g, and the crystallization temperature, T_x, are indicated by arrows. The binary alloy $Ni_{62}Nb_{38}$ displays a T_g of 915 K and a T_x of 957 K, while the compositions $Ni_{62}Nb_{36}P_2$ displays a T_g of 924 K and a T_x of 977 K. Consequently, minor additions of 2 % of P increase the length of the SCL region from 42 K to 53 K. Higher concentrations of P cause a destabilization of the SCL region. Based on these results, an S-formability parameter of 0.09 can be calculated for $Ni_{62}Nb_{36}P_2$, which would roughly predict a deformation of 75 % in our experimental setup and confirm the general feasibility for thermoplastic forming. Besides the positive effect on the thermal stability, the critical casting thickness can be increased by 50 % from 2 mm for the binary $Ni_{62}Nb_{38}$ to 3 mm for $Ni_{62}Nb_{36}P_2$.

A stress-strain curve of the $Ni_{62}Nb_{36}P_2$ alloy in a three-point bending flexural test is displayed in Fig. 7.1 b) and the characteristic values are written into the plot. The inset shows an X-ray diffractogram proving the amorphous nature of the 3PB sample. The alloy shows an extraordinary mechanical strength of around 4600 MPa and even first beginnings of plastic deformation can be seen in bending. It outperforms all common engineering materials regarding strength. Furthermore, in first wear tests it shows an extraordinary wear resistance.

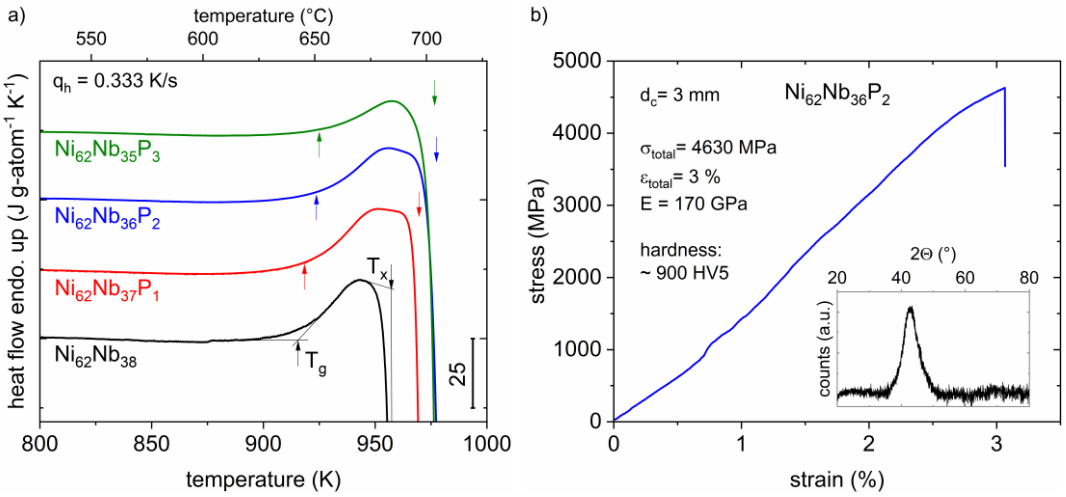

Figure 7.1: NiNbP alloys: NiNb BMG with minor additions of P. **a)** DSC scans with a heating rate of 0.333 K/s for $Ni_{62}Nb_{38-x}P_x$ alloys with increasing P content. T_g and T_x are indicated by arrows. **b)** Stress-strain curve of the $Ni_{62}Nb_{36}P_2$ alloy in a three-point bending flexural test. The characteristic values are written into the plot. The inset shows an X-ray diffractogram proving the amorphous nature of the 3PB sample.

In the future, the $Ni_{62}Nb_{36}P_2$ alloy could be a promising candidate for industrial applications where small parts must bear extreme mechanical stresses or have to resist abrasive wear. Due to their high T_g, they can even be used for applications at elevated temperatures.

Regarding the investigated Vit101 and Vit105 alloys, future work could be dedicated to the influence of much cheaper industrial grade raw materials on the alloy properties. In other sulfur-bearing alloys, we found no detrimental effect of industrial grade raw materials on the glass-forming ability, e.g. in the $Ti_{40}Zr_{35}Cu_{17}S_8$ alloy [9]. Preliminary experiments suggest similar results for the here investigated alloys, especially in the Vit101 alloy family. Minor additions of sulfur might counter negative effects of raw materials with a higher oxygen content.

On the way to an industrial processing of the Vit101 and Vit105 alloys, not only the price of the raw materials is of importance, but also an adequate technological solution for a serial production of parts. In the last two years, an automated die-casting machine, specifically tailored to the needs of BMGs, was conceived and built in our research group and the machine will be taken into operation shortly. A short description of the concept can be found in the doctoral thesis of Alexander Kuball [129]. For a simulation of this die-casting process, viscosity as a function of temperature throughout the whole temperature range from the stable liquid to the glass is of great importance. Therefore, the viscosity measurements from this work and the corresponding fits, e.g. with the cooperative shear model, will come to use. A reliable mold design based on simulations and prior to the mold fabrication is one of the main future challenges for an industrial casting process.

Similar to this die-casting machine, also a TPF machine for an industrial-scale process should be developed. The main requirements for this include a fast and well-controlled process. The pressing needs to happen in a protective gas environment, the machine needs a magazine within the TPF chamber, pressing force and piston travel should be well controlled. The key to exploit the maximum formability of an alloy is a fast and well controlled temperature control, either by conduction heating, or by alternative heating methods, e.g. capacitive discharge or induction heating. This machine could be dedicated to a micro-scale structuring of functional surfaces or a blow molding process where complex, hollow shapes can be realized. Like this, amorphous feedstock material from the newly developed die-casting machine can be further processed and the next step towards a widespread industrial use of BMGs could be taken.

Appendix

Table A1: Properties of the Vit101 family.

			Vit101	**Vit101 P_1**	**Vit101 $S_{1.5}$**
			$Cu_{47}Ti_{34}Zr_{11}Ni_8$	$Cu_{46.53}Ti_{33.66}Zr_{10.89}Ni_{7.92}P_1$	$Cu_{46.3}Ti_{33.5}Zr_{10.8}Ni_{7.9}S_{1.5}$
Glass trans. temp.	T_g	[K] (0.333 K/s)	674.0	690.5	694.5
Crystalliz. temp.	T_x	[K] (0.333 K/s)	718.7	748.7	754.7
SCL region	ΔT_x	[K] (0.333 K/s)	44.7	58.2	60.2
Melting temp.	T_m	[K]	1 067	1 036	1 049
Temp. of fusion	T_f	[K]	1 139	1 146	1 144
Liquidus temp.	T_l	[K]	1 168	1 171	1 170
Crystalliz. enthalpy	ΔH_x	[kJ g-atom^{-1}]	7.46	7.98	6.97
Enthalpy of fusion	ΔH_f	[kJ g-atom^{-1}]	11.3	11.4	10.0
Entropy of fusion	ΔS_f	[J g-atom^{-1} K^{-1}]	9.92	9.95	8.74
Kauzmann temp.	T_K	[K]	553	577	599
Molar mass	M	[g g-atom^{-1}]	60.87	60.57	60.43
Critical thickness	d_c	[mm]	5	5	6
VFT parameters	D^*		16.19	20.76	18.26
	T_0	[K]	466.86	435.53	460.90
	η_0	[10^{-5} Pa s]	4.419	4.395	4.374
	m		54.38	46.03	50.12
	T_g^*	[K]	667.6	675.6	684.3
	$G_{\tau-\eta}$	[MPa]	-	1.12	1.24
Density	ρ	[kg m^{-3}]	6 890	-	-
Yield strength	$\sigma_y^{0.2}$	[MPa]	2 900	2 040	2 240
Strain to fracture	ε_f	[%]	5.5	2.15	2.35
Elastic modulus	E^{3PB}	[GPa]	108	103	105
Hardness	HV		576	588	590
Thermal expansion	γ^{glass}	[10^{-5} K^{-1}]	3.9	4.1	4.2
c_p fitting param.	a	[$\times 10^{-3}$ J g-atom^{-1} K^{-2}]	5.9616	2.8887	1.7231
	b	[$\times 10^{6}$ J g-atom^{-1} K]	7.8161	10.1619	10.8112
	c	[$\times 10^{-3}$ J g-atom^{-1} K^{-2}]	-0.1549	-1.9621	-3.2852
	d	[$\times 10^{-6}$ J g-atom^{-1} K^{-3}]	6.9447	8.5986	10.3694

Table A2: Properties of the Vit105 family.

			Vit105	**Vit105 P_2**	**Vit105 S_2**
			$Zr_{52.5}Cu_{17.9}Ni_{14.6}Al_{10}Ti_5$	$Zr_{51.45}Cu_{17.54}Ni_{14.31}Al_{9.8}Ti_{4.9}P_2$	$Zr_{51.45}Cu_{17.54}Ni_{14.31}Al_{9.8}Ti_{4.9}S_2$
Glass trans. temp.	$\mathbf{T_g}$	[K] (0.333 K/s)	671.4	695.7	691.9
Crystalliz. temp.	$\mathbf{T_x}$	[K] (0.333 K/s)	731.1	795.6	769.3
SCL region	$\mathbf{\Delta T_x}$	[K] (0.333 K/s)	59.7	99.9	77.4
Melting temp.	$\mathbf{T_m}$	[K]	1 055	1 068	1 057
Temp. of fusion	$\mathbf{T_f}$	[K]	1 095	1 089	1 093
Liquidus temp.	$\mathbf{T_l}$	[K]	1 134	1 189	1 295
Crystalliz. enthalpy	$\mathbf{\Delta H_x}$	[kJ g-atom^{-1}]	5.24	4.82	5.86
Enthalpy of fusion	$\mathbf{\Delta H_f}$	[kJ g-atom^{-1}]	8.8	6.9	8.7
Entropy of fusion	$\mathbf{\Delta S_f}$	[J g-atom^{-1} K^{-1}]	8.04	6.34	7.96
Kauzmann temp.	$\mathbf{T_K}$	[K]	591	634	603
Molar mass	$\mathbf{M}$	[g g-atom^{-1}]	72.93	72.09	72.11
Critical thickness	$\mathbf{d_c}$	[mm]	8	3	6
VFT parameters	$\mathbf{D^*}$		20.33	24.76	22.34
	$\mathbf{T_0}$	[K]	433.11	416.3	430.31
	$\mathbf{\eta_0}$	[10^{-5} Pa s]	3.585	3.567	3.558
	$\mathbf{m}$		47.09	41.6	44.34
	$\mathbf{T_g^*}$	[K]	665.6	688.5	684.1
	$\mathbf{G_{\tau\text{-}\eta}}$	[MPa]	3.22	3.55	2.27
Density	$\mathbf{\rho}$	[kg m^{-3}]	6 660	-	-
Yield strength	$\mathbf{\sigma_y^{0.2}}$	[MPa]	2 600	2 510	2 770
Strain to fracture	$\mathbf{\varepsilon_f}$	[%]	6.1	3.0	5.2
Elastic modulus	$\mathbf{E^{3PB}}$	[GPa]	89	94	92
Hardness	**HV**		506	538	527
Thermal expansion	$\mathbf{\gamma^{glass}}$	[10^{-5} K^{-1}]	3.3	3.2	3.3
c_p fitting param.	$\mathbf{a}$	[$\times 10^{-3}$ J g-atom^{-1} K^{-2}]	6.1935	3.2428	3.8825
	$\mathbf{b}$	[$\times 10^{6}$ J g-atom^{-1} K]	7.2205	9.3593	9.2005
	$\mathbf{c}$	[$\times 10^{-3}$ J g-atom^{-1} K^{-2}]	-0.8554	-3.2134	1.1879
	$\mathbf{d}$	[$\times 10^{-6}$ J g-atom^{-1} K^{-3}]	6.7032	10.9324	5.1906

Table A3: Crystalline phases identified in the diffraction patterns.

Phase	Crystal System	Space Group		Lattice Parameters [Å]	Reference
CuTi	tetragonal	129	P4/nmm	a=3.115 c=5.899	[294]
CuZr	cubic	221	Pm-3m	a=3.263	[295]
Ti_2Cu	tetragonal	139	I4/mmm	a=2.944 c=10.786	[296]
Ti_2S	orthorhombic	58	Pnnm	a=11.35 b=14.06 c=3.32	[257,297]
Ti_8S_3	monoclinic	12	C2/m	a=32.69 b=3.327 c=19.36	[258]
Zr	hexagonal	194	$P6_3/mmc$	a=3.232 c=5.148	[298]
Zr_2Cu	tetragonal	139	I4/mmm	a=3.22 c=11.18	[299]
Zr_2Ni	tetragonal	140	I4/mcm	a=6.483 c=5.267	[300]
$Zr_{21}S_8$	tetragonal	87	I4/m	a=16.88 c=3.42	[301]
$ZrTiCu_2$ Laves	hexagonal	194	$P6_3/mmc$	a=5.151 c=8.244	[302]
ZrTiNi Laves	hexagonal	194	$P6_3/mmc$	a=5.222 c=8.559	[256,303]

Table A4: Fitting parameters for the viscosity fitting functions.

		Vit101	Vit101 P_1	Vit101 $S_{1.5}$	Vit105	Vit105 P_2	Vit105 S_2
VFT low T							
D*		16.19	20.76	18.26	20.33	24.76	22.34
T_0	[K]	466.86	435.53	460.90	433.11	416.3	430.31
η_0	[10^{-5} Pa s]	4.419	4.395	4.374	3.585	3.567	3.558
m		54.38	46.03	50.12	47.09	41.6	44.34
T_g*	[K]	667.4	675.4	684.1	665.4	688.4	684.0
VFT high T							
D*		8.05	8.70	7.70	9.60	10.61	9.95
T_0	[K]	549.93	548.73	568.06	530.87	537.83	541.75
η_0	[10^{-5} Pa s]	4.419	4.395	4.374	3.585	3.567	3.558
m		92.89	87.19	96.44	81.33	75.18	79.08
T_g*	[K]	667.4	675.4	684.1	665.4	688.4	684.0
VFT whole range							
D*		13.42	17.17	11.67	15.59	22.74	24.38
T_0	[K]	498.29	473.79	525.23	476.60	445.13	434.39
η_0	[10^{-5} Pa s]	0.394	0.134	0.654	0.310	0.046	0.024
m		69.38	60.69	75.45	62.80	52.38	51.37
T_g*	[K]	665.2	671.5	680.1	660.8	684.9	681.4
MYEGA							
B	[K]	295.26	578.81	204.42	524.72	1231.37	1270.65
C	[K]	2349.6	1945.0	2659.7	1962.0	1507.7	1481.4
η_0	[10^{-5} Pa s]	72.10	27.08	116.27	42.39	6.075	4.097
m		68.63	60.64	73.29	60.96	51.90	52.02
T_g*	[K]	665.5	672.0	680.8	661.8	685.3	681.5
Coop. shear model							
n		1.705	1.464	1.800	1.409	1.167	1.248
T_g*	[K]	666.86	673.56	682.15	664.18	687.05	682.86
η_0	[10^{-5} Pa s]	945.4	890.6	1037.6	992.9	724.2	698.3
m		61.84	55.20	64.33	53.46	47.13	49.50

(continued)

Table A4: Fitting parameters for the viscosity fitting functions.

		Vit101	Vit101 P_1	Vit101 $S_{1.5}$	Vit105	Vit105 P_2	Vit105 S_2
Ext. MYEGA							
High T, fragile liquid							
W_1	[K^{-1}]	942.05	0.2168	0.7888	0.4679	0.0129	20.184
C_1	[K]	15000	6154	6932	7542	4036	12092
η_0	[10^{-5} Pa s]	1560	1175	1360	1081	400	1703
m		239.06	122.26	139.10	134.73	86.49	185.99
T_g*	[K]	920.3	791.1	767.2	872.1	805.8	967.2
Low T, strong liquid							
W_2	[10^{-4} K^{-1}]	19.932	1.732	0.7401	7.977	0.6430	9.856
C_2	[K]	1946.4	501.8	0.0	1368.4	0.0	1526.8
m		54.11	31.33	19.75	45.03	22.60	44.70
T_g*	[K]	668.1	675.4	684.2	665.4	688.2	683.9

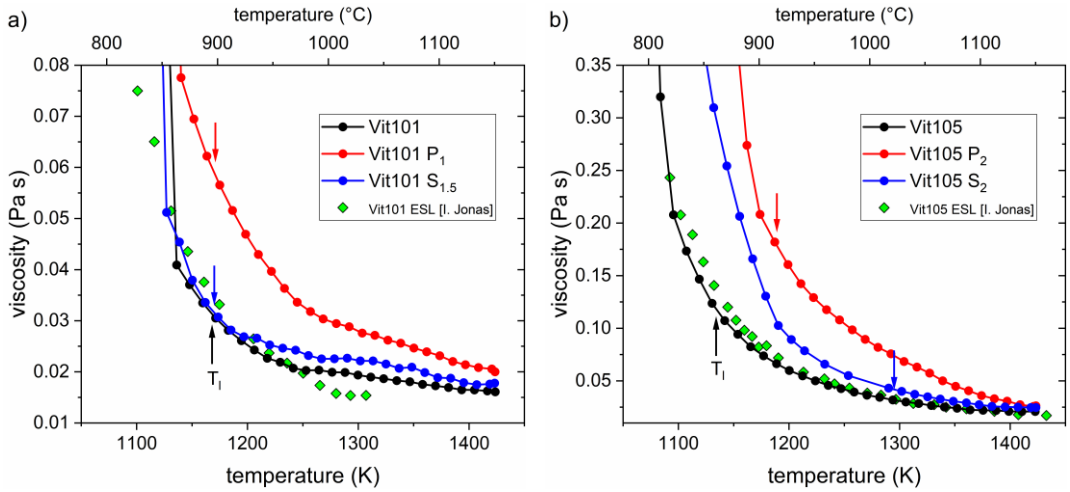

Figure A1: High-temperature viscosity as measured in rotating concentric cylinder experiments. The green diamonds represent viscosity reference values from ESL measurements of Vit101 and Vit105 (data taken from Ref. [245]). The liquidus temperature T_l (from DTA) of each composition is indicated by an arrow. **a)** Vit101 alloys. **b)** Vit105 alloys.

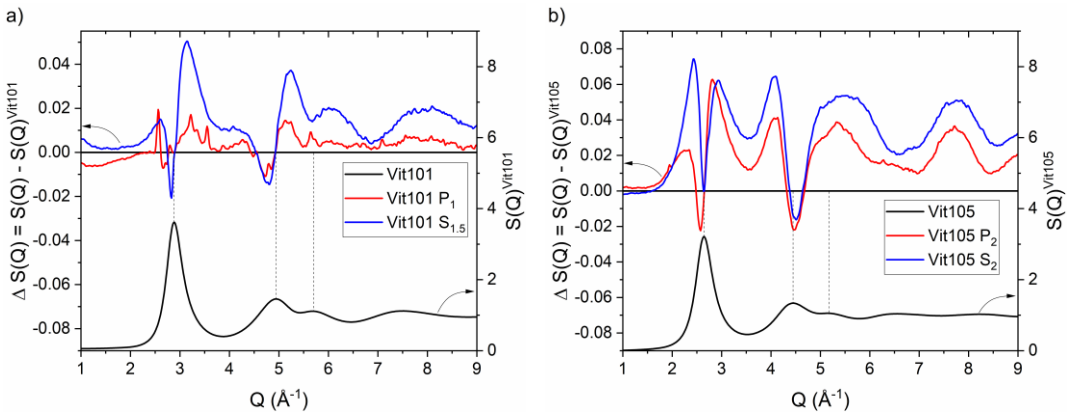

Figure A2: S(Q) and the difference between the base alloy and the modified ones. **a)** Vit101 alloys, **b)** Vit105 alloys. The lower part shows S(Q) of the base alloy, and the upper part shows the difference to the alloys with minor additions, ΔS(Q).

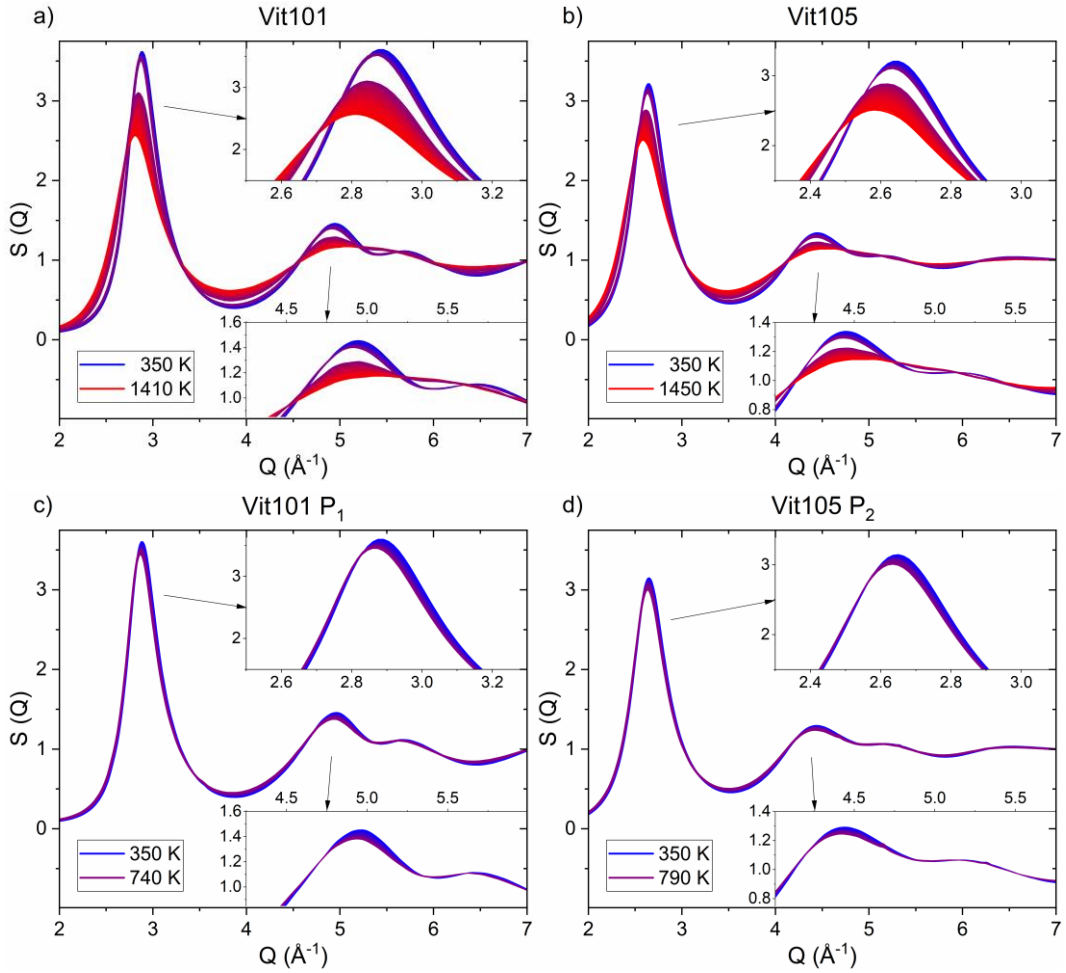

Figure A3: Total scattering structure functions, S(Q), from in-situ heating and electrostatic levitation experiments. The curves are color-coded from red to blue (hot to cold) and magnifications of the first and second peak are shown in the insets. **a)** Vit101, **b)** Vit105, **c)** Vit101 P_1, and **d)** Vit105 P_2.

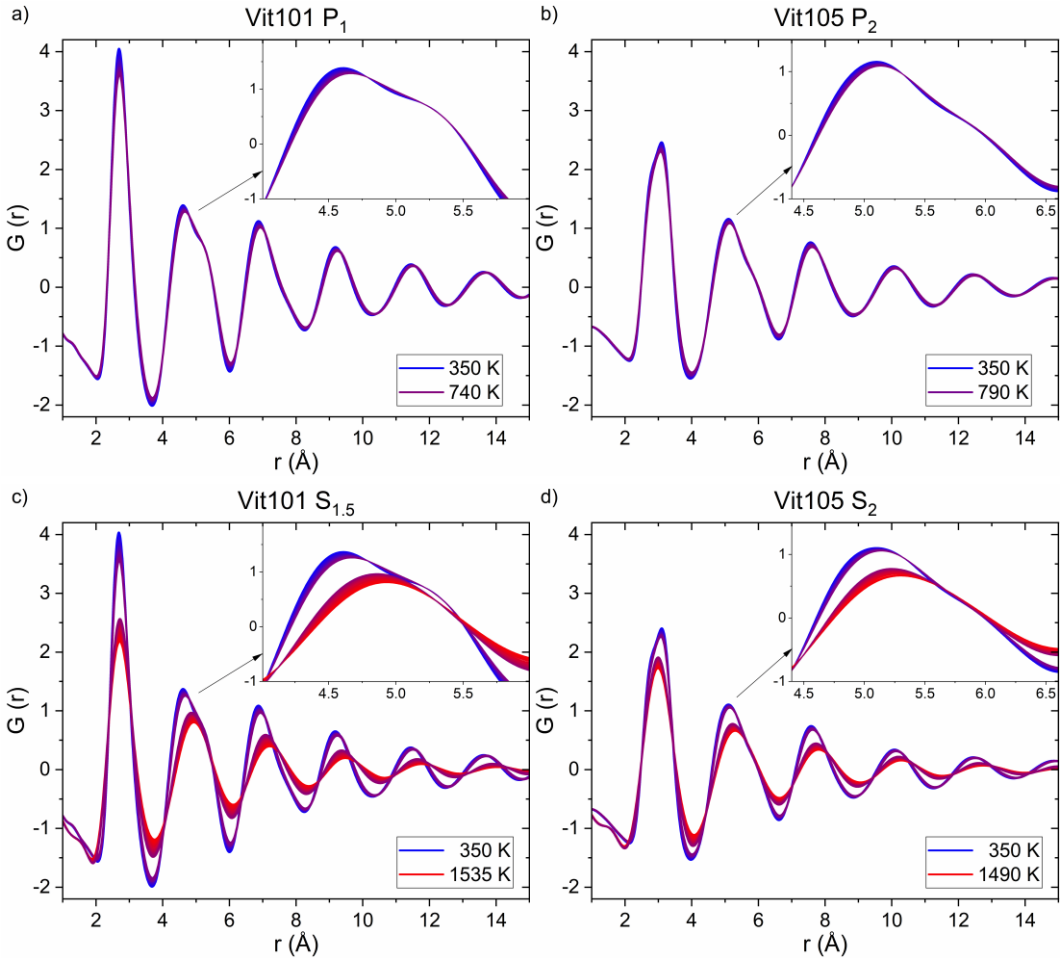

Figure A4: The pair distribution functions, G(r), at different temperatures. The curves are color-coded from red to blue (hot to cold). The insets show a magnification of the second peak, r_2, which represents the average weighted second nearest neighbor distance. **a)** Vit101 P_1, **b)** Vit105 P_2, **c)** Vit101 $S_{1.5}$, and **d)** Vit105 S_2.

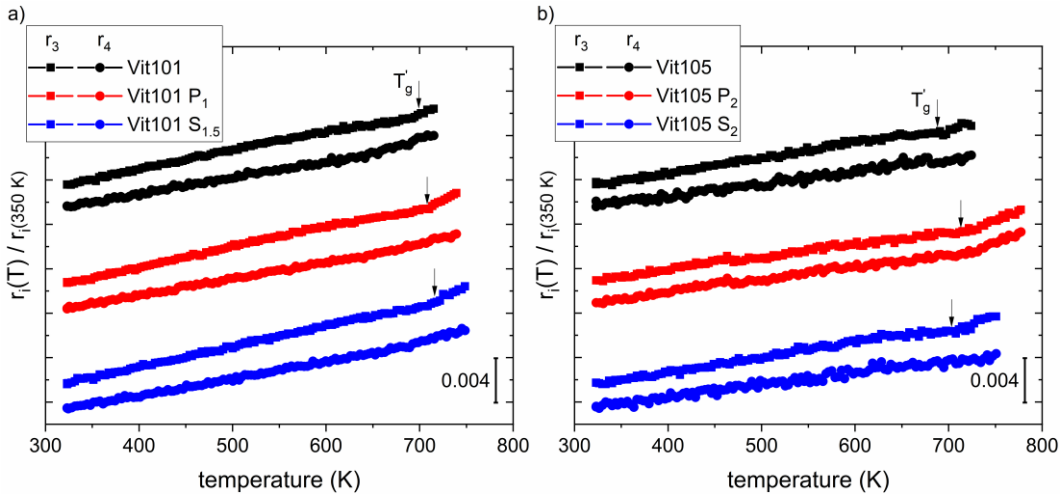

Figure A5: Position of the third and fourth peak in G(r), r_3, and r_4, as a function of temperature. Values are normalized to the ones at 350 K and characteristic temperatures are indicated by arrows. **a)** Vit101 alloys, **b)** Vit105 alloys.

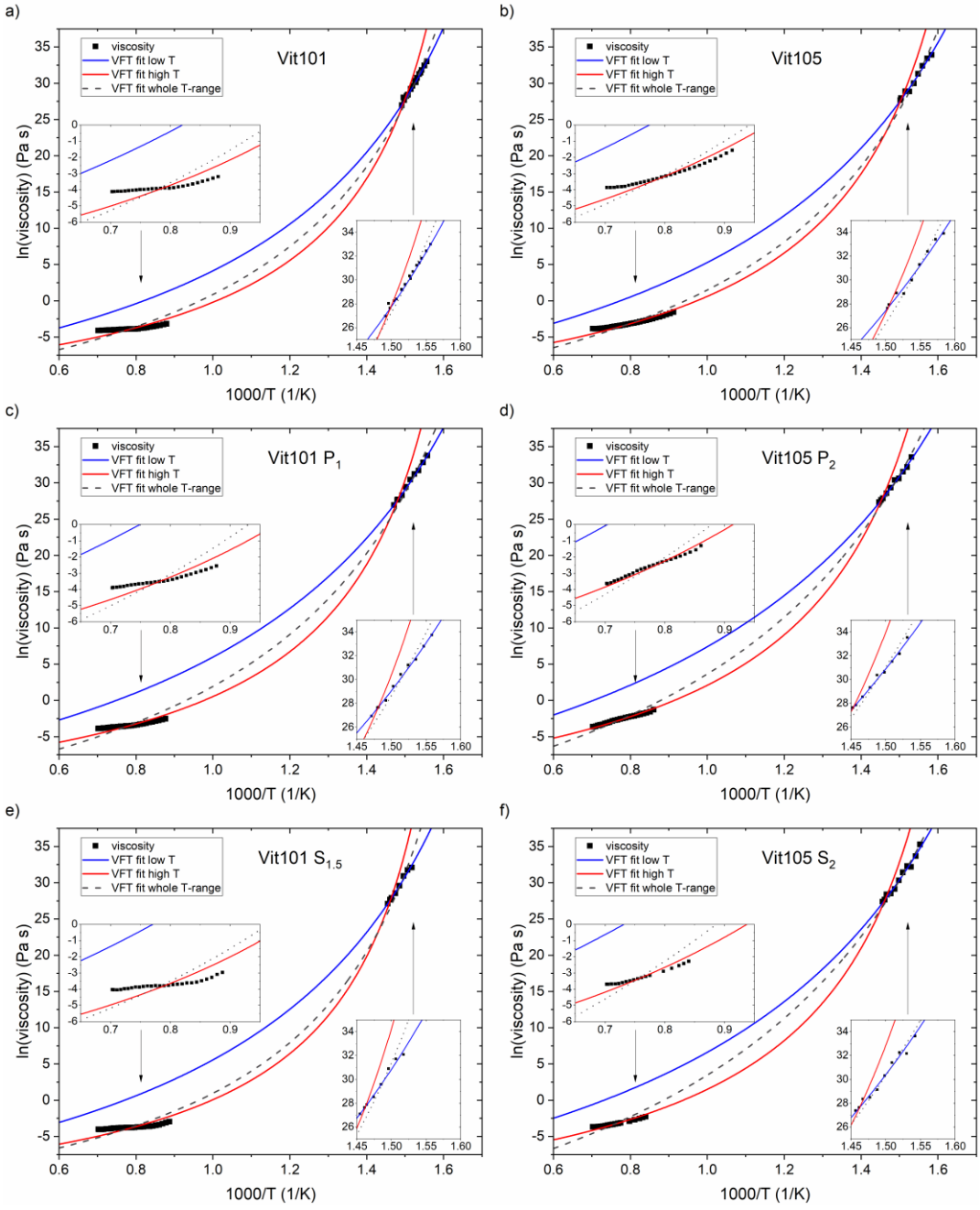

Figure A6: VFT viscosity fits for **a)** Vit101, **b)** Vit105, **c)** Vit101 P_1, **d)** Vit105 P_2, **e)** Vit101 $S_{1.5}$, and **f)** Vit105 S_2. Viscosity datapoints from 3PBB TMA measurements at low temperatures and from Couette measurements at high temperatures are displayed (black squares) over inverse temperature. Three different VFT fits are shown for each composition: one only on the low-temperature data (blue), one on the high-temperature data (red), and one on all datapoints (dashed grey). The insets show a magnification of the high-temperature and the low-temperature region.

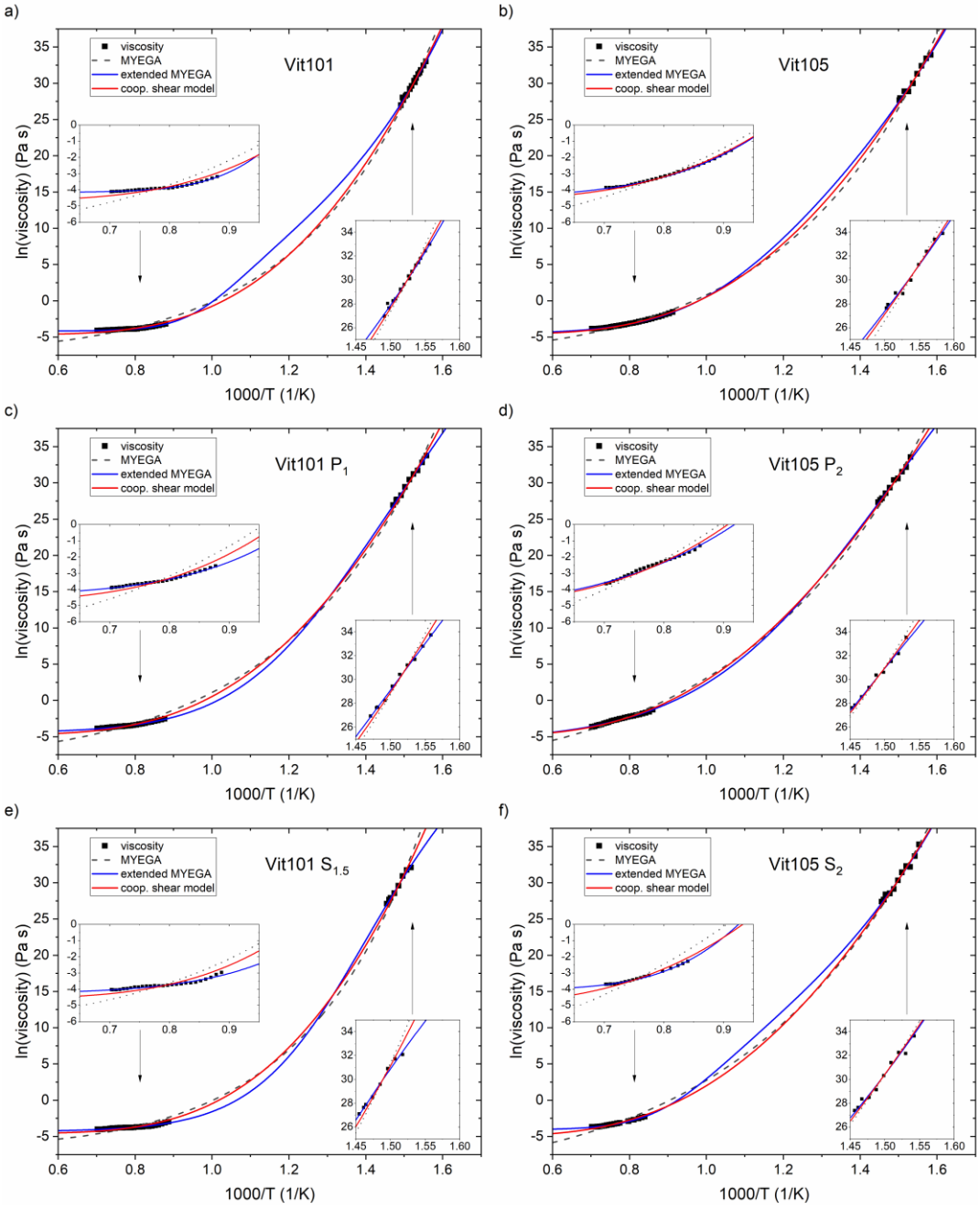

Figure A7: Viscosity fits for **a)** Vit101, **b)** Vit105, **c)** Vit101 P_1, **d)** Vit105 P_2, **e)** Vit101 $S_{1.5}$, and **f)** Vit105 S_2. Viscosity datapoints from 3PBB TMA measurements at low temperatures and from Couette measurements at high temperatures are displayed (black squares) over inverse temperature. Three different fitting functions are shown for each composition: a fit to the MYEGA equation (dashed grey), one to the extended MYEGA equation (blue), and one to the cooperative shear model (red). The insets show a magnification of the high-temperature and the low-temperature region.

Copyright Permissions

Figure	Reference	License
2.4	[19]	4640651152559
2.5	[48]	4640660082976
2.8 a)	[103]	4640660376114
2.8 b); 2.9 a)	[105]	4640660708109
2.9 b), c)	[107]	CC BY 4.0
2.10 a), b); 2.11	[112]	4640670008899
2.10 c)	[113]	4640670155506
2.12	[7]	CC BY-NC-ND 4.0 (own work)
2.13 a)-d)	[159]	4640670796101
2.13 e), f)	[160]	4640671363027
2.13 g)-i)	[162]	4640680031000
3.7; 3.8	[208]	4640680175493
3.10	[214]	4640680375272
5.2; 5.10; 5.11; 5.12	[184]	CC BY-NC-ND 4.0 (own work)
5.14	[289]	4644190219245

References

[1] W. Klement, R.H. Willens, P. Duwez, Non-crystalline Structure in Solidified Gold–Silicon Alloys, Nature. 187 (1960) 869–870. doi:10.1038/187869b0.

[2] A.J. Drehman, A.L. Greer, D. Turnbull, Bulk Formation of a Metallic Glass: $Pd_{40}Ni_{40}P_{20}$, Appl. Phys. Lett. 41 (1982) 716–717. doi:10.1063/1.93645.

[3] A. Inoue, K. Kita, T. Zhang, T. Masumoto, An Amorphous $La_{55}Al_{25}Ni_{20}$ Alloy Prepared by Water Quenching, Mater. Trans. JIM. 30 (1989) 722–725. doi:10.2320/matertrans1989.30.722.

[4] A. Inoue, T. Nakamura, N. Nishiyama, T. Masumoto, Mg-Cu-Y Bulk Amorphous Alloys with High Tensile Strength Produced by a High-Pressure Die Casting Method, Mater. Trans. JIM. 33 (1992) 937–945. doi:10.2320/matertrans1989.33.937.

[5] A. Peker, W.L. Johnson, A highly processable metallic glass: $Zr_{41.2}Ti_{13.8}Cu_{12.5}Ni_{10}Be_{22.5}$, Appl. Phys. Lett. 63 (1993) 2342–2344. doi:10.1063/1.110520.

[6] A. Inoue, T. Zhang, N. Nishiyama, K. Ohba, T. Masumoto, Preparation of 16 mm Diameter Rod of Amorphous $Zr_{65}Al_{7.5}Ni_{10}Cu_{17.5}$ Alloy, Mater. Trans. JIM. 34 (1993) 1234–1237. doi:10.2320/matertrans1989.34.1234.

[7] A. Kuball, O. Gross, B. Bochtler, R. Busch, Sulfur-bearing metallic glasses: A new family of bulk glass-forming alloys, Scr. Mater. 146 (2018) 73–76. doi:10.1016/j.scriptamat.2017.11.011.

[8] A. Kuball, B. Bochtler, O. Gross, V. Pacheco, M. Stolpe, S. Hechler, R. Busch, On the bulk glass formation in the ternary Pd-Ni-S system, Acta Mater. 158 (2018) 13–22. doi:10.1016/j.actamat.2018.07.039.

[9] A. Kuball, O. Gross, B. Bochtler, B. Adam, L. Ruschel, M. Zamanzade, R. Busch, Development and characterization of titanium-based bulk metallic glasses, J. Alloys Compd. 790 (2019) 337–346. doi:10.1016/j.jallcom.2019.03.001.

[10] W.H. Wang, Roles of minor additions in formation and properties of bulk metallic glasses, Prog. Mater. Sci. 52 (2007) 540–596. doi:10.1016/j.pmatsci.2006.07.003.

[11] X.H. Lin, W.L. Johnson, W.K. Rhim, Effect of Oxygen Impurity on Crystallization of an Undercooled Bulk Glass Forming Alloy, Mater. Trans. JIM. 38 (1997) 473–477. doi:10.2320/matertrans1989.38.473.

[12] X.H. Lin, W.L. Johnson, Formation of Ti–Zr–Cu–Ni bulk metallic glasses, J. Appl. Phys. 78 (1995) 6514–6519. doi:10.1063/1.360537.

[13] A. Kuball, O. Gross, B. Bochtler, R. Busch, Konstruktionswerkstoff fuer hochfeste Kleinteile, Konstr. - Zeitschrift Für Produktentwicklung Und Ingenieur-Werkstoffe, VDI Fachmedien GmbH Co. KG. (2018) 5–7.

[14] M. Telford, The case for bulk metallic glass, Mater. Today. 7 (2004) 36–43. doi:10.1016/S1369-7021(04)00124-5.

[15] C.T. Moynihan, A.J. Easteal, M.A. Bolt, J. Tucker, Dependence of the Fictive Temperature of Glass on Cooling Rate, J. Am. Ceram. Soc. 59 (1976) 12–16. doi:10.1111/j.1151-2916.1976.tb09376.x.

[16] C.A. Angell, Glass-Formers and Viscous Liquid Slowdown since David Turnbull: Enduring Puzzles and New Twists, MRS Bull. 33 (2008) 544–555. doi:10.1557/mrs2008.108.

[17] M.H. Cohen, G.S. Grest, Liquid-glass transition, a free-volume approach, Phys. Rev. B. 20 (1979) 1077–1098. doi:10.1103/PhysRevB.20.1077.

[18] W. Kauzmann, The Nature of the Glassy State and the Behavior of Liquids at Low Temperatures., Chem. Rev. 43 (1948) 219–256. doi:10.1021/cr60135a002.

[19] C.A. Angell, Formation of Glasses from Liquids and Biopolymers, Science (80-.). 267

(1995) 1924–1935. doi:10.1126/science.267.5206.1924.

[20] D. Turnbull, M.H. Cohen, Free-Volume Model of the Amorphous Phase: Glass Transition, J. Chem. Phys. 34 (1961) 120–125. doi:10.1063/1.1731549.

[21] J.H. Gibbs, E.A. DiMarzio, Nature of the Glass Transition and the Glassy State, J. Chem. Phys. 28 (1958) 373–383. doi:10.1063/1.1744141.

[22] R. Busch, Y.J. Kim, W.L. Johnson, Thermodynamics and kinetics of the undercooled liquid and the glass transition of the $Zr_{41.2}Ti_{13.8}Cu_{12.5}Ni_{10}Be_{22.5}$ alloy, J. Appl. Phys. 77 (1995) 4039–4043. doi:10.1063/1.359485.

[23] D. Turnbull, Kinetics of Heterogeneous Nucleation, J. Chem. Phys. 18 (1950) 198–203. doi:10.1063/1.1747588.

[24] O. Gross, B. Bochtler, M. Stolpe, S. Hechler, W. Hembree, R. Busch, I. Gallino, The kinetic fragility of Pt-P- and Ni-P-based bulk glass-forming liquids and its thermodynamic and structural signature, Acta Mater. 132 (2017) 118–127. doi:10.1016/j.actamat.2017.04.030.

[25] J.W. Christian, Solidification and Melting, in: Theory Transform. Met. Alloy., Elsevier, 2002: pp. 623–701. doi:10.1016/B978-008044019-4/50019-2.

[26] W.L. Johnson, Thermodynamic and kinetic aspects of the crystal to glass transformation in metallic materials, Prog. Mater. Sci. 30 (1986) 81–134. doi:10.1016/0079-6425(86)90005-8.

[27] C.A. Angell, K.L. Ngai, G.B. McKenna, P.F. McMillan, S.W. Martin, Relaxation in glassforming liquids and amorphous solids, J. Appl. Phys. 88 (2000) 3113. doi:10.1063/1.1286035.

[28] T. Egami, Structural Relaxation in Metallic Glasses, Ann. N. Y. Acad. Sci. 371 (1981) 238–251. doi:10.1111/j.1749-6632.1981.tb55664.x.

[29] O. Gross, Precious metal based bulk glass-forming liquids : development, thermodynamics, kinetics and structure, Dissertation, Saarland University, 2018. doi:10.22028/D291-27993.

[30] A. van den Beukel, J. Sietsma, The glass transition as a free volume related kinetic phenomenon, Acta Metall. Mater. 38 (1990) 383–389. doi:10.1016/0956-7151(90)90142-4.

[31] I.M. Hodge, Enthalpy relaxation and recovery in amorphous materials, J. Non. Cryst. Solids. 169 (1994) 211–266. doi:10.1016/0022-3093(94)90321-2.

[32] G. Williams, D.C. Watts, Non-symmetrical dielectric relaxation behaviour arising from a simple empirical decay function, Trans. Faraday Soc. 66 (1970) 80. doi:10.1039/tf9706600080.

[33] M.D. Ediger, C.A. Angell, S.R. Nagel, Supercooled Liquids and Glasses, J. Phys. Chem. 100 (1996) 13200–13212. doi:10.1021/jp953538d.

[34] A. Einstein, Ueber die von der molekularkinetischen Theorie der Waerme geforderte Bewegung von in ruhenden Fluessigkeiten suspendierten Teilchen, Ann. Phys. 322 (1905) 549–560.

[35] G. Tarjus, D. Kivelson, Breakdown of the Stokes–Einstein relation in supercooled liquids, J. Chem. Phys. 103 (1995) 3071–3073. doi:10.1063/1.470495.

[36] U. Geyer, W.L. Johnson, S. Schneider, Y. Qiu, T.A. Tombrello, M.P. Macht, Small atom diffusion and breakdown of the Stokes–Einstein relation in the supercooled liquid state of the $Zr_{46.7}Ti_{8.3}Cu_{7.5}Ni_{10}Be_{27.5}$ alloy, Appl. Phys. Lett. 69 (1996) 2492–2494. doi:10.1063/1.117716.

[37] J.Q. Wang, Y. Shen, J.H. Perepezko, M.D. Ediger, Increasing the kinetic stability of bulk metallic glasses, Acta Mater. 104 (2016) 25–32. doi:10.1016/j.actamat.2015.11.048.

[38] S. Arrhenius, Ueber die Reaktionsgeschwindigkeit bei der Inversion von Rohrzucker

durch Saeuren, Zeitschrift Fuer Phys. Chemie. 4U (1889). doi:10.1515/zpch-1889-0416.

[39] H. Vogel, Das Temperaturabhaengigkeitsgesetz der Viskositaet von Fluessigkeiten, Phys. Z. 22 (1921) 645–646.

[40] G.S. Fulcher, Analysis of Recent Measurements of the Viscosity of Glasses, J. Am. Ceram. Soc. 8 (1925) 339–355. doi:10.1111/j.1151-2916.1925.tb16731.x.

[41] G. Tammann, W. Hesse, Die Abhaengigkeit der Viscositaet von der Temperatur bei unterkuehlten Fluessigkeiten, Zeitschrift Für Anorg. Und Allg. Chemie. 156 (1926) 245–257. doi:10.1002/zaac.19261560121.

[42] S. V Nemilov, Correlation of crystallization character of glass melts with the temperature dependence of their viscosity and the degree of spatial structural connectiveness, Glas. Phys. Chem.(Engl. Transl.). 21 (1995) 91–96.

[43] R. Busch, J. Schroers, W.H. Wang, Thermodynamics and Kinetics of Bulk Metallic Glass, MRS Bull. 32 (2007) 620–623. doi:10.1557/mrs2007.122.

[44] Z. Evenson, S. Raedersdorf, I. Gallino, R. Busch, Equilibrium viscosity of Zr–Cu–Ni–Al–Nb bulk metallic glasses, Scr. Mater. 63 (2010) 573–576. doi:10.1016/j.scriptamat.2010.06.008.

[45] R. Busch, W. Liu, W.L. Johnson, Thermodynamics and kinetics of the $Mg_{65}Cu_{25}Y_{10}$ bulk metallic glass forming liquid, J. Appl. Phys. 83 (1998) 4134. doi:10.1063/1.367167.

[46] M. Frey, R. Busch, W. Possart, I. Gallino, On the thermodynamics, kinetics, and sub-T g relaxations of Mg-based bulk metallic glasses, Acta Mater. 155 (2018) 117–127. doi:10.1016/j.actamat.2018.05.063.

[47] J.H. Na, M.D. Demetriou, W.L. Johnson, Fragility of iron-based glasses, Appl. Phys. Lett. 99 (2011) 161902. doi:10.1063/1.3651763.

[48] B. Bochtler, O. Gross, R. Busch, Indications for a fragile-to-strong transition in the high- and low-temperature viscosity of the $Fe_{43}Cr_{16}Mo_{16}C_{15}B_{10}$ bulk metallic glass-forming alloy, Appl. Phys. Lett. 111 (2017) 261902. doi:10.1063/1.5013108.

[49] J.H. Na, M.D. Demetriou, M. Floyd, A. Hoff, G.R. Garrett, W.L. Johnson, Compositional landscape for glass formation in metal alloys., Proc. Natl. Acad. Sci. U. S. A. 111 (2014) 9031–6. doi:10.1073/pnas.1407780111.

[50] C.A. Angell, Spectroscopy simulation and scattering, and the medium range order problem in glass, J. Non. Cryst. Solids. 73 (1985) 1–17. doi:10.1016/0022-3093(85)90334-5.

[51] R. Boehmer, C.A. Angell, Correlations of the nonexponentiality and state dependence of mechanical relaxations with bond connectivity in Ge-As-Se supercooled liquids, Phys. Rev. B. 45 (1992) 10091–10094. doi:10.1103/PhysRevB.45.10091.

[52] C.A. Angell, Liquid Fragility and the Glass Transition in Water and Aqueous Solutions, Chem. Rev. 102 (2002) 2627–2650. doi:10.1021/cr000689q.

[53] G. Adam, J.H. Gibbs, On the Temperature Dependence of Cooperative Relaxation Properties in Glass-Forming Liquids, J. Chem. Phys. 43 (1965) 139. doi:10.1063/1.1696442.

[54] A.K. Doolittle, Studies in Newtonian Flow. II. The Dependence of the Viscosity of Liquids on Free-Space, J. Appl. Phys. 22 (1951) 1471–1475. doi:10.1063/1.1699894.

[55] J.C. Mauro, Y. Yue, A.J. Ellison, P.K. Gupta, D.C. Allan, Viscosity of glass-forming liquids, Proc. Natl. Acad. Sci. 106 (2009) 19780–19784. doi:10.1073/pnas.0911705106.

[56] M.D. Demetriou, J.S. Harmon, M. Tao, G. Duan, K. Samwer, W.L. Johnson, Cooperative Shear Model for the Rheology of Glass-Forming Metallic Liquids, Phys. Rev. Lett. 97 (2006) 065502. doi:10.1103/PhysRevLett.97.065502.

[57] A.S. Argon, Plastic deformation in metallic glasses, Acta Metall. 27 (1979) 47–58. doi:10.1016/0001-6160(79)90055-5.

[58] W.L. Johnson, M.D. Demetriou, J.S. Harmon, M.L. Lind, K. Samwer, Rheology and

Ultrasonic Properties of Metallic Glass-Forming Liquids: A Potential Energy Landscape Perspective, MRS Bull. 32 (2007) 644–650. doi:10.1557/mrs2007.127.

[59] C. Zhang, L. Hu, Y. Yue, J.C. Mauro, Fragile-to-strong transition in metallic glass-forming liquids, J. Chem. Phys. 133 (2010) 014508. doi:10.1063/1.3457670.

[60] R. Busch, I. Gallino, Kinetics, Thermodynamics, and Structure of Bulk Metallic Glass Forming Liquids, JOM. 69 (2017) 2178–2186. doi:10.1007/s11837-017-2574-5.

[61] K.F. Kelton, Kinetic and structural fragility—a correlation between structures and dynamics in metallic liquids and glasses, J. Phys. Condens. Matter. 29 (2017) 023002. doi:10.1088/0953-8984/29/2/023002.

[62] C. Way, P. Wadhwa, R. Busch, The influence of shear rate and temperature on the viscosity and fragility of the $Zr_{41.2}Ti_{13.8}Cu_{12.5}Ni_{10.0}Be_{22.5}$ metallic-glass-forming liquid, Acta Mater. 55 (2007) 2977–2983. doi:10.1016/j.actamat.2006.12.032.

[63] Z. Evenson, T. Schmitt, M. Nicola, I. Gallino, R. Busch, High temperature melt viscosity and fragile to strong transition in Zr–Cu–Ni–Al–Nb(Ti) and $Cu_{47}Ti_{34}Zr_{11}Ni_8$ bulk metallic glasses, Acta Mater. 60 (2012) 4712–4719. doi:10.1016/j.actamat.2012.05.019.

[64] S. Wei, F. Yang, J. Bednarcik, I. Kaban, O. Shuleshova, A. Meyer, R. Busch, Liquid–liquid transition in a strong bulk metallic glass-forming liquid, Nat. Commun. 4 (2013) 2083. doi:10.1038/ncomms3083.

[65] M. Stolpe, I. Jonas, S. Wei, Z. Evenson, W. Hembree, F. Yang, A. Meyer, R. Busch, Structural changes during a liquid-liquid transition in the deeply undercooled $Zr_{58.5}Cu_{15.6}Ni_{12.8}Al_{10.3}Nb_{2.8}$ bulk metallic glass forming melt, Phys. Rev. B. 93 (2016) 014201. doi:10.1103/PhysRevB.93.014201.

[66] B. Bochtler, O. Gross, I. Gallino, R. Busch, Thermo-physical characterization of the $Fe_{67}Mo_6Ni_{3.5}Cr_{3.5}P_{12}C_{5.5}B_{2.5}$ bulk metallic glass forming alloy, Acta Mater. 118 (2016) 129–139. doi:10.1016/j.actamat.2016.07.031.

[67] S. Hechler, B. Ruta, M. Stolpe, E. Pineda, Z. Evenson, O. Gross, A. Bernasconi, R. Busch, I. Gallino, Microscopic evidence of the connection between liquid-liquid transition and dynamical crossover in an ultraviscous metallic glass former, Phys. Rev. Mater. 2 (2018) 085603. doi:10.1103/PhysRevMaterials.2.085603.

[68] I. Gallino, D. Cangialosi, Z. Evenson, L. Schmitt, S. Hechler, M. Stolpe, B. Ruta, Hierarchical aging pathways and reversible fragile-to-strong transition upon annealing of a metallic glass former, Acta Mater. 144 (2018) 400–410. doi:10.1016/j.actamat.2017.10.060.

[69] S. Lan, Y. Ren, X.Y. Wei, B. Wang, E.P. Gilbert, T. Shibayama, S. Watanabe, M. Ohnuma, X.L. Wang, Hidden amorphous phase and reentrant supercooled liquid in Pd-Ni-P metallic glasses, Nat. Commun. 8 (2017) 14679. doi:10.1038/ncomms14679.

[70] W. Xu, M.T. Sandor, Y. Yu, H.-B. Ke, H.-P. Zhang, M.-Z. Li, W.-H. Wang, L. Liu, Y. Wu, Evidence of liquid–liquid transition in glass-forming $La_{50}Al_{35}Ni_{15}$ melt above liquidus temperature, Nat. Commun. 6 (2015) 7696. doi:10.1038/ncomms8696.

[71] S. Wei, M. Stolpe, O. Gross, W. Hembree, S. Hechler, J. Bednarcik, R. Busch, P. Lucas, Structural evolution on medium-range-order during the fragile-strong transition in $Ge_{15}Te_{85}$, Acta Mater. 129 (2017) 259–267. doi:10.1016/j.actamat.2017.02.055.

[72] K.N. Lad, N. Jakse, A. Pasturel, Signatures of fragile-to-strong transition in a binary metallic glass-forming liquid, J. Chem. Phys. 136 (2012) 104509. doi:10.1063/1.3692610.

[73] C. Zhou, L. Hu, Q. Sun, J. Qin, X. Bian, Y. Yue, Indication of liquid-liquid phase transition in CuZr-based melts, Appl. Phys. Lett. 103 (2013) 171904. doi:10.1063/1.4826487.

[74] C. Zhou, L. Hu, Q. Sun, H. Zheng, C. Zhang, Y. Yue, Structural evolution during fragile-to-strong transition in CuZr(Al) glass-forming liquids, J. Chem. Phys. 142 (2015) 064508. doi:10.1063/1.4907374.

[75] P. Gallo, K. Amann-Winkel, C.A. Angell, M.A. Anisimov, F. Caupin, C. Chakravarty,

E. Lascaris, T. Loerting, A.Z. Panagiotopoulos, J. Russo, J.A. Sellberg, H.E. Stanley, H. Tanaka, C. Vega, L. Xu, L.G.M. Pettersson, Water: A Tale of Two Liquids, Chem. Rev. 116 (2016) 7463–7500. doi:10.1021/acs.chemrev.5b00750.

[76] V. V. Vasisht, S. Saw, S. Sastry, Liquid–liquid critical point in supercooled silicon, Nat. Phys. 7 (2011) 549–553. doi:10.1038/nphys1993.

[77] G.N. Greaves, M.C. Wilding, S. Fearn, D. Langstaff, F. Kargl, S. Cox, Q. V. Van, O. Majerus, C.J. Benmore, R. Weber, C.M. Martin, L. Hennet, Detection of First-Order Liquid/Liquid Phase Transitions in Yttrium Oxide-Aluminum Oxide Melts, Science (80-.). 322 (2008) 566–570. doi:10.1126/science.1160766.

[78] H. Tanaka, R. Kurita, H. Mataki, Liquid-Liquid Transition in the Molecular Liquid Triphenyl Phosphite, Phys. Rev. Lett. 92 (2004) 025701. doi:10.1103/PhysRevLett.92.025701.

[79] S. Wei, M. Stolpe, O. Gross, Z. Evenson, I. Gallino, W. Hembree, J. Bednarcik, J.J. Kruzic, R. Busch, Linking structure to fragility in bulk metallic glass-forming liquids, Appl. Phys. Lett. 106 (2015). doi:10.1063/1.4919590.

[80] K.F. Kelton, A.L. Greer, eds., Nucleation in Condensed Matter - Applications in Materials and Biology, 1st ed., Pergamon Materials Series, 2010. https://www.sciencedirect.com/bookseries/pergamon-materials-series/vol/15.

[81] R.W. Cahn, P. Haasen, Physical Metallurgy - vol 1, Phys. Metall. 1 (1996) 1042.

[82] D.R. Uhlmann, A kinetic treatment of glass formation, J. Non. Cryst. Solids. 7 (1972) 337–348.

[83] W.L. Johnson, J.H. Na, M.D. Demetriou, Quantifying the origin of metallic glass formation, Nat. Commun. 7 (2016) 10313. doi:10.1038/ncomms10313.

[84] A. Gebert, J. Eckert, L. Schultz, Effect of oxygen on phase formation and thermal stability of slowly cooled $Zr_{65}Al_{7.5}Cu_{17.5}Ni_{10}$ metallic glass, Acta Mater. 46 (1998) 5475–5482. doi:10.1016/S1359-6454(98)00187-6.

[85] J.J. Wall, C.T. Liu, W.-K. Rhim, J.J.Z. Li, P.K. Liaw, H. Choo, W.L. Johnson, Heterogeneous nucleation in a glass-forming alloy, Appl. Phys. Lett. 92 (2008) 244106. doi:10.1063/1.2948861.

[86] D. Granata, E. Fischer, V. Wessels, J.F. Loeffler, Fluxing of Pd-Si-Cu bulk metallic glass and the role of cooling rate and purification, Acta Mater. 71 (2014) 145–152. doi:10.1016/j.actamat.2014.03.008.

[87] D. Turnbull, Under what conditions can a glass be formed?, Contemp. Phys. 10 (1969) 473–488. doi:10.1080/00107516908204405.

[88] Z.P. Lu, Y. Li, S.C. Ng, Reduced glass transition temperature and glass forming ability of bulk glass forming alloys, J. Non. Cryst. Solids. 270 (2000) 103–114. doi:10.1016/S0022-3093(00)00064-8.

[89] A.L. Greer, Confusion by design, Nature. 366 (1993) 303–304. doi:10.1038/366303a0.

[90] K.J. Laws, D.B. Miracle, M. Ferry, A predictive structural model for bulk metallic glasses., Nat. Commun. 6 (2015) 8123. doi:10.1038/ncomms9123.

[91] D.B. Miracle, A structural model for metallic glasses, Nat. Mater. 3 (2004) 697–702. doi:10.1038/nmat1219.

[92] R. Busch, E. Bakke, W.L. Johnson, On the Glass Forming Ability of Bulk Metallic Glasses, Mater. Sci. Forum. 235–238 (1997) 327–336. doi:10.4028/www.scientific.net/MSF.235-238.327.

[93] O. Gross, N. Neuber, A. Kuball, B. Bochtler, S. Hechler, M. Frey, R. Busch, Signatures of structural differences in Pt–P- and Pd–P-based bulk glass-forming liquids, Commun. Phys. 2 (2019) 83. doi:10.1038/s42005-019-0180-2.

[94] A. Inoue, Stabilization of Supercooled Liquid and Opening-up of Bulk Glassy Alloys., Proc. Japan Acad. Ser. B Phys. Biol. Sci. 73 (1997) 19–24. doi:10.2183/pjab.73.19.

[95] A. Inoue, T. Zhang, T. Masumoto, Al-La-Ni Amorphous Alloys with a Wide Supercooled Liquid Region, Mater. Trans. JIM. 30 (1989) 965–972.

[96] J.L. Finney, Bernal's road to random packing and the structure of liquids, Philos. Mag. 93 (2013) 3940–3969. doi:10.1080/14786435.2013.770179.

[97] J.D. Bernal, A Geometrical Approach to the Structure Of Liquids, Nature. 183 (1959) 141–147. doi:10.1038/183141a0.

[98] J.D. Bernal, J. Mason, Packing of Spheres: Co-ordination of Randomly Packed Spheres, Nature. 188 (1960) 910–911. doi:10.1038/188910a0.

[99] J.D. Bernal, Geometry of the Structure of Monatomic Liquids, Nature. 185 (1960) 68–70. doi:10.1038/185068a0.

[100] G.S. Cargill, Structure of Metallic Alloy Glasses, in: Solid State Phys. - Adv. Res. Appl., 1975: pp. 227–320. doi:10.1016/S0081-1947(08)60337-9.

[101] J.L. Finney, Modelling the structures of amorphous metals and alloys, Nature. 266 (1977) 309–314. doi:10.1038/266309a0.

[102] P.H. Gaskell, A new structural model for transition metal–metalloid glasses, Nature. 276 (1978) 484–485. doi:10.1038/276484a0.

[103] A. Hirata, L.J. Kang, T. Fujita, B. Klumov, K. Matsue, M. Kotani, A.R. Yavari, M.W. Chen, Geometric Frustration of Icosahedron in Metallic Glasses, Science (80-.). 341 (2013) 376–379. doi:10.1126/science.1232450.

[104] F.C. Frank, J.S. Kasper, Complex alloy structures regarded as sphere packings. I. Definitions and basic principles, Acta Crystallogr. 11 (1958) 184–190. doi:10.1107/S0365110X58000487.

[105] H.W. Sheng, W.K. Luo, F.M. Alamgir, J.M. Bai, E. Ma, Atomic packing and short-to-medium-range order in metallic glasses, Nature. 439 (2006) 419–425. doi:10.1038/nature04421.

[106] D.B. Miracle, The efficient cluster packing model – An atomic structural model for metallic glasses, Acta Mater. 54 (2006) 4317–4336. doi:10.1016/j.actamat.2006.06.002.

[107] J. Ding, E. Ma, M. Asta, R.O. Ritchie, Second-Nearest-Neighbor Correlations from Connection of Atomic Packing Motifs in Metallic Glasses and Liquids, Sci. Rep. 5 (2015) 17429. doi:10.1038/srep17429.

[108] M.F. Ashby, A.L. Greer, Metallic glasses as structural materials, Scr. Mater. 54 (2006) 321–326. doi:10.1016/j.scriptamat.2005.09.051.

[109] C. Suryanarayana, A. Inoue, Iron-based bulk metallic glasses, Int. Mater. Rev. 58 (2013) 131–166. doi:10.1179/1743280412Y.0000000007.

[110] A.L. Greer, Y.Q. Cheng, E. Ma, Shear bands in metallic glasses, Mater. Sci. Eng. R Reports. 74 (2013) 71–132. doi:10.1016/j.mser.2013.04.001.

[111] F. Spaepen, A microscopic mechanism for steady state inhomogeneous flow in metallic glasses, Acta Metall. 25 (1977) 407–415. doi:10.1016/0001-6160(77)90232-2.

[112] C. Schuh, T. Hufnagel, U. Ramamurty, Mechanical behavior of amorphous alloys, Acta Mater. 55 (2007) 4067–4109. doi:10.1016/j.actamat.2007.01.052.

[113] R.D. Conner, W.L. Johnson, N.E. Paton, W.D. Nix, Shear bands and cracking of metallic glass plates in bending, J. Appl. Phys. 94 (2003) 904–911. doi:10.1063/1.1582555.

[114] M.H. Cohen, D. Turnbull, Molecular Transport in Liquids and Glasses, J. Chem. Phys. 31 (1959) 1164–1169. doi:10.1063/1.1730566.

[115] J. Schroers, W.L. Johnson, Ductile Bulk Metallic Glass, Phys. Rev. Lett. 93 (2004) 255506. doi:10.1103/PhysRevLett.93.255506.

[116] G. Kumar, P. Neibecker, Y.H. Liu, J. Schroers, Critical fictive temperature for

plasticity in metallic glasses, Nat. Commun. 4 (2013) 1536. doi:10.1038/ncomms2546.

[117] J. Ketkaew, W. Chen, H. Wang, A. Datye, M. Fan, G. Pereira, U.D. Schwarz, Z. Liu, R. Yamada, W. Dmowski, M.D. Shattuck, C.S. O'Hern, T. Egami, E. Bouchbinder, J. Schroers, Mechanical glass transition revealed by the fracture toughness of metallic glasses, Nat. Commun. 9 (2018) 3271. doi:10.1038/s41467-018-05682-8.

[118] Y. Yokoyama, Ductility improvement of Zr–Cu–Ni–Al glassy alloy, J. Non. Cryst. Solids. 316 (2003) 104–113. doi:10.1016/S0022-3093(02)01942-7.

[119] M. Stolpe, J.J. Kruzic, R. Busch, Evolution of shear bands, free volume and hardness during cold rolling of a Zr-based bulk metallic glass, Acta Mater. 64 (2014) 231–240. doi:10.1016/j.actamat.2013.10.035.

[120] S. Xie, J.J. Kruzic, Cold rolling improves the fracture toughness of a Zr-based bulk metallic glass, J. Alloys Compd. 694 (2017) 1109–1120. doi:10.1016/j.jallcom.2016.10.134.

[121] Y. Zhang, W.H. Wang, A.L. Greer, Making metallic glasses plastic by control of residual stress, Nat. Mater. 5 (2006) 857–860. doi:10.1038/nmat1758.

[122] S. V. Ketov, Y.H. Sun, S. Nachum, Z. Lu, A. Checchi, a. R. Beraldin, H.Y. Bai, W.H. Wang, D. V. Louzguine-Luzgin, M.A. Carpenter, A.L. Greer, Rejuvenation of metallic glasses by non-affine thermal strain, Nature. 524 (2015) 200–203. doi:10.1038/nature14674.

[123] M.M. Trexler, N.N. Thadhani, Mechanical properties of bulk metallic glasses, Prog. Mater. Sci. 55 (2010) 759–839. doi:10.1016/j.pmatsci.2010.04.002.

[124] J.J. Kruzic, Bulk Metallic Glasses as Structural Materials: A Review, Adv. Eng. Mater. 18 (2016) 1308–1331. doi:10.1002/adem.201600066.

[125] J.J. Kruzic, Understanding the problem of fatigue in bulk metallic glasses, Metall. Mater. Trans. A Phys. Metall. Mater. Sci. 42 (2011) 1516–1523. doi:10.1007/s11661-010-0413-1.

[126] M.E. Launey, R. Busch, J.J. Kruzic, Effects of free volume changes and residual stresses on the fatigue and fracture behavior of a Zr-Ti-Ni-Cu-Be bulk metallic glass, Acta Mater. 56 (2008) 500–510. doi:10.1016/j.actamat.2007.10.007.

[127] Y. Li, S. Zhao, Y. Liu, P. Gong, J. Schroers, How Many Bulk Metallic Glasses Are There?, ACS Comb. Sci. 19 (2017) 687–693. doi:10.1021/acscombsci.7b00048.

[128] A. Kuball, B. Bochtler, O. Gross, R. Busch, Sulfur-containing alloy forming metallic glasses, EP3447158A1, 2017. //patents.google.com/patent/EP3447158A1/.

[129] A. Kuball, Development, Characterization and Processing of a novel Family of Bulk Metallic Glasses: Sulfur-containing Bulk Metallic Glasses, Dissertation, Saarland University, (unpublished), 2019.

[130] A. Guinier, Structure of Age-Hardened Aluminium-Copper Alloys, Nature. 142 (1938) 569–570. doi:10.1038/142569b0.

[131] Z.P. Lu, C.T. Liu, Role of minor alloying additions in formation of bulk metallic glasses: A Review, J. Mater. Sci. 39 (2004) 3965–3974. doi:10.1023/B:JMSC.0000031478.73621.64.

[132] N. Chen, L. Martin, D. V. Luzguine-Luzgin, A. Inoue, Role of Alloying Additions in Glass Formation and Properties of Bulk Metallic Glasses, Materials (Basel). 3 (2010) 5320–5339. doi:10.3390/ma3125320.

[133] H. Choi-Yim, R. Busch, W.L. Johnson, The effect of silicon on the glass forming ability of the $Cu_{47}Ti_{34}Zr_{11}Ni_8$ bulk metallic glass forming alloy during processing of composites, J. Appl. Phys. 83 (1998) 7993–7997. doi:10.1063/1.367981.

[134] E.S. Park, H.K. Lim, W.T. Kim, D.H. Kim, The effect of Sn addition on the glass-forming ability of Cu–Ti–Zr–Ni–Si metallic glass alloys, J. Non. Cryst. Solids. 298 (2002) 15–22. doi:10.1016/S0022-3093(01)01047-X.

[135] A. Kawashima, H. Habazaki, K. Hashimoto, Highly corrosion-resistant Ni-based bulk amorphous alloys, Mater. Sci. Eng. A. 304–306 (2001) 753–757. doi:10.1016/S0921-5093(00)01587-2.

[136] J. Heinrich, R. Busch, F. Mueller, S. Grandthyll, S. Huefner, Role of aluminum as an oxygen-scavenger in zirconium based bulk metallic glasses, Appl. Phys. Lett. 100 (2012) 071909. doi:10.1063/1.3685492.

[137] Y. Zhang, M.X. Pan, D.Q. Zhao, R.J. Wang, W.H. Wang, Formation of Zr-Based Bulk Metallic Glasses from Low Purity of Materials by Yttrium Addition, Mater. Trans. JIM. 41 (2000) 1410–1414. doi:10.2320/matertrans1989.41.1410.

[138] Q. Hu, X.R. Zeng, M.W. Fu, S.S. Chen, J. Jiang, Improvement of the thermoplastic formability of $Zr_{65}Cu_{17.5}Ni_{10}Al_{7.5}$ bulk metallic glass by minor addition of Erbium, Phys. B Condens. Matter. 502 (2016) 68–72. doi:10.1016/j.physb.2016.08.012.

[139] J. Pan, L. Liu, K.C. Chan, Enhanced plasticity by phase separation in CuZrAl bulk metallic glass with micro-addition of Fe, Scr. Mater. 60 (2009) 822–825. doi:10.1016/j.scriptamat.2009.01.032.

[140] N. Nollmann, I. Binkowski, V. Schmidt, H. Rösner, G. Wilde, Impact of micro-alloying on the plasticity of Pd-based bulk metallic glasses, Scr. Mater. 111 (2016) 119–122. doi:10.1016/j.scriptamat.2015.08.030.

[141] J. Pan, K.C. Chan, Q. Chen, N. Li, S.F. Guo, L. Liu, The effect of microalloying on mechanical properties in CuZrAl bulk metallic glass, J. Alloys Compd. 504 (2010) S74–S77. doi:10.1016/j.jallcom.2010.02.064.

[142] N. Neuber, O. Gross, M. Eisenbart, A. Heiss, U.E. Klotz, J.P. Best, M.N. Polyakov, J. Michler, R. Busch, I. Gallino, The role of Ga addition on the thermodynamics, kinetics, and tarnishing properties of the Au-Ag-Pd-Cu-Si bulk metallic glass forming system, Acta Mater. 165 (2019) 315–326. doi:10.1016/j.actamat.2018.11.052.

[143] G.R. Garrett, M.D. Demetriou, J. Chen, W.L. Johnson, Effect of microalloying on the toughness of metallic glasses, Appl. Phys. Lett. 101 (2012) 241913. doi:10.1063/1.4769997.

[144] S. Venkataraman, M. Stoica, S. Scudino, T. Gemming, C. Mickel, U. Kunz, K.B. Kim, L. Schultz, J. Eckert, Revisiting the $Cu_{47}Ti_{33}Zr_{11}Ni_8Si_1$ glass-forming alloy, Scr. Mater. 54 (2006) 835–840. doi:10.1016/j.scriptamat.2005.11.007.

[145] Y. Yokoyama, A. Kobayashi, K. Fukaura, A. Inoue, Oxygen Embrittlement and Effect of the Addition of Ni Element in a Bulk Amorphous Zr-Cu-Al Alloy, Mater. Trans. 43 (2002) 571–574. doi:10.2320/matertrans.43.571.

[146] C.T. Liu, M.F. Chisholm, M.K. Miller, Oxygen impurity and microalloying effect in a Zr-based bulk metallic glass alloy, Intermetallics. 10 (2002) 1105–1112. doi:10.1016/S0966-9795(02)00131-0.

[147] J. Schroers, B. Lohwongwatana, W.L. Johnson, A. Peker, Precious bulk metallic glasses for jewelry applications, Mater. Sci. Eng. A. 449–451 (2007) 235–238. doi:10.1016/j.msea.2006.02.301.

[148] A. Inoue, T. Zhang, Fabrication of Bulky Zr-Based Glassy Alloys by Suction Casting into Copper Mold, Mater. Trans. JIM. 36 (1995) 1184–1187. doi:10.2320/matertrans1989.36.1184.

[149] A. Inoue, T. Zhang, E. Makabe, Production methods of metallic glasses by a suction casting method, JP2930880B2, 1994. //patents.google.com/patent/US5740854A/.

[150] L.H. Liu, J. Ma, C.Y. Yu, X.S. Huang, L.J. He, L.C. Zhang, P.J. Li, Z.Y. Liu, Determination of forming ability of high pressure die casting for Zr-based metallic glass, J. Mater. Process. Technol. 244 (2017) 87–96. doi:10.1016/j.jmatprotec.2017.01.015.

[151] J. Schroers, Processing of Bulk Metallic Glass, Adv. Mater. 22 (2010) 1566–1597. doi:10.1002/adma.200902776.

[152] H.J. Leamy, T.T. Wang, H.S. Chen, Plastic flow and fracture of metallic glass, Metall.

Trans. 3 (1972) 699–708. doi:10.1007/BF02642754.

[153] J.P. Patterson, D.R.H. Jones, Moulding of a metallic glass, Mater. Res. Bull. 13 (1978) 583–585. doi:10.1016/0025-5408(78)90182-4.

[154] J. Schroers, W.L. Johnson, Highly processable bulk metallic glass-forming alloys in the Pt–Co–Ni–Cu–P system, Appl. Phys. Lett. 84 (2004) 3666–3668. doi:10.1063/1.1738945.

[155] J. Schroers, The superplastic forming of bulk metallic glasses, JOM. 57 (2005) 35–39. doi:10.1007/s11837-005-0093-2.

[156] J. Schroers, T. Nguyen, S. O'Keeffe, A. Desai, Thermoplastic forming of bulk metallic glass—Applications for MEMS and microstructure fabrication, Mater. Sci. Eng. A. 449 (2007) 898–902. doi:10.1016/j.msea.2006.02.398.

[157] Y. Saotome, S. Miwa, T. Zhang, A. Inoue, The micro-formability of Zr-based amorphous alloys in the supercooled liquid state and their application to micro-dies, J. Mater. Process. Technol. 113 (2001) 64–69. doi:10.1016/S0924-0136(01)00605-7.

[158] N. Li, W. Chen, L. Liu, Thermoplastic Micro-Forming of Bulk Metallic Glasses: A Review, JOM. 68 (2016) 1246–1261. doi:10.1007/s11837-016-1844-y.

[159] G. Kumar, H.X. Tang, J. Schroers, Nanomoulding with amorphous metals, Nature. 457 (2009) 868–872. doi:10.1038/nature07718.

[160] G. Kumar, A. Desai, J. Schroers, Bulk metallic glass: the smaller the better., Adv. Mater. 23 (2011) 461–76. doi:10.1002/adma.201002148.

[161] Z. Hu, S. Gorumlu, B. Aksak, G. Kumar, Patterning of metallic glasses using polymer templates, Scr. Mater. 108 (2015) 15–18. doi:10.1016/j.scriptamat.2015.06.011.

[162] J. Schroers, T.M. Hodges, G. Kumar, H. Raman, A.J. Barnes, Q. Pham, T.A. Waniuk, Thermoplastic blow molding of metals, Mater. Today. 14 (2011) 14–19. doi:10.1016/S1369-7021(11)70018-9.

[163] J. Schroers, Q. Pham, A. Peker, N. Paton, R. V. Curtis, Blow molding of bulk metallic glass, Scr. Mater. 57 (2007) 341–344. doi:10.1016/j.scriptamat.2007.04.033.

[164] M. Takagi, Y. Kawamura, T. Imura, J. Nishigaki, H. Saka, Mechanical properties of amorphous alloy compacts prepared by different consolidation techniques, J. Mater. Sci. 27 (1992) 817–824. doi:10.1007/BF00554059.

[165] Y. Kawamura, H. Kato, A. Inoue, T. Masumoto, Full strength compacts by extrusion of glassy metal powder at the supercooled liquid state, Appl. Phys. Lett. 67 (1995) 2008–2010. doi:10.1063/1.114769.

[166] Y. Kawamura, H. Kato, A. Inoue, T. Masumoto, Effects of extrusion conditions on mechanical properties in ZrAlNiCu glassy powder compacts, Mater. Sci. Eng. A. 219 (1996) 39–43. doi:10.1016/S0921-5093(96)10437-8.

[167] H.M. Chiu, G. Kumar, J. Blawzdziewicz, J. Schroers, Thermoplastic extrusion of bulk metallic glass, Scr. Mater. 61 (2009) 28–31. doi:10.1016/j.scriptamat.2009.02.052.

[168] E. Bryn Pitt, G. Kumar, J. Schroers, Temperature dependence of the thermoplastic formability in bulk metallic glasses, J. Appl. Phys. 110 (2011) 043518. doi:10.1063/1.3624666.

[169] W.L. Johnson, G. Kaltenboeck, M.D. Demetriou, J.P. Schramm, X. Liu, K. Samwer, C.P. Kim, D.C. Hofmann, Beating Crystallization in Glass-Forming Metals by Millisecond Heating and Processing, Science (80-.). 332 (2011) 828–833. doi:10.1126/science.1201362.

[170] G. Kaltenboeck, T. Harris, K. Sun, T.T. Tran, G. Chang, J.P. Schramm, M.D. Demetriou, W.L. Johnson, Accessing thermoplastic processing windows in metallic glasses using rapid capacitive discharge., Sci. Rep. 4 (2014) 6441. doi:10.1038/srep06441.

[171] G. Kaltenboeck, M.D. Demetriou, S. Roberts, W.L. Johnson, Shaping metallic glasses by electromagnetic pulsing, Nat. Commun. 7 (2016) 10576. doi:10.1038/ncomms10576.

[172] J. Schroers, On the formability of bulk metallic glass in its supercooled liquid state, Acta Mater. 56 (2008) 471–478. doi:10.1016/j.actamat.2007.10.008.

[173] A. Wiest, G. Duan, M.D. Demetriou, L.A. Wiest, A. Peck, G. Kaltenboeck, B. Wiest, W.L. Johnson, Zr–Ti-based Be-bearing glasses optimized for high thermal stability and thermoplastic formability, Acta Mater. 56 (2008) 2625–2630. doi:10.1016/j.actamat.2008.02.001.

[174] P. Gong, S. Wang, Z. Liu, W. Chen, N. Li, X. Wang, K.F. Yao, Lightweight Ti-based bulk metallic glasses with superior thermoplastic formability, Intermetallics. 98 (2018) 54–59. doi:10.1016/j.intermet.2018.04.019.

[175] G. Kumar, D. Rector, R.D. Conner, J. Schroers, Embrittlement of Zr-based bulk metallic glasses, Acta Mater. 57 (2009) 3572–3583. doi:10.1016/j.actamat.2009.04.016.

[176] P. Murali, U. Ramamurty, Embrittlement of a bulk metallic glass due to sub-Tg annealing, Acta Mater. 53 (2005) 1467–1478. doi:10.1016/j.actamat.2004.11.040.

[177] R. Raghavan, P. Murali, U. Ramamurty, On factors influencing the ductile-to-brittle transition in a bulk metallic glass, Acta Mater. 57 (2009) 3332–3340. doi:10.1016/j.actamat.2009.03.047.

[178] R. Raghavan, V. V. Shastry, A. Kumar, T. Jayakumar, U. Ramamurty, Toughness of as-cast and partially crystallized composites of a bulk metallic glass, Intermetallics. 17 (2009) 835–839. doi:10.1016/j.intermet.2009.03.012.

[179] A. Concustell, G. Alcalá, S. Mato, T.G. Woodcock, A. Gebert, J. Eckert, M.D. Baró, Effect of relaxation and primary nanocrystallization on the mechanical properties of $Cu_{60}Zr_{22}Ti_{18}$ bulk metallic glass, Intermetallics. 13 (2005) 1214–1219. doi:10.1016/j.intermet.2005.04.003.

[180] C.J. Gilbert, R.O. Ritchie, W.L. Johnson, Fracture toughness and fatigue-crack propagation in a Zr–Ti–Ni–Cu–Be bulk metallic glass, Appl. Phys. Lett. 71 (1997) 476. doi:10.1063/1.119610.

[181] M. Wakeda, J. Saida, J. Li, S. Ogata, Controlled Rejuvenation of Amorphous Metals with Thermal Processing, Sci. Rep. 5 (2015) 10545. doi:10.1038/srep10545.

[182] N. Ciftci, N. Ellendt, E. Soares Barreto, L. Mädler, V. Uhlenwinkel, Increasing the amorphous yield of FeCoBSiNb powders by hot gas atomization, Adv. Powder Technol. 29 (2018) 380–385. doi:10.1016/j.apt.2017.11.025.

[183] D. Geissler, J. Grosse, S. Donath, D. Ehinger, M. Stoica, J. Eckert, U. Kühn, Granulation of Bulk Metallic Glass Forming Alloys as a Feedstock for Thermoplastic Forming and their Compaction into Bulk Samples, Mater. Sci. Forum. 879 (2016) 589–594. doi:10.4028/www.scientific.net/MSF.879.589.

[184] B. Bochtler, M. Stolpe, B. Reiplinger, R. Busch, Consolidation of amorphous powder by thermoplastic forming and subsequent mechanical testing, Mater. Des. 140 (2018) 188–195. doi:10.1016/j.matdes.2017.11.058.

[185] D. Herzog, V. Seyda, E. Wycisk, C. Emmelmann, Additive manufacturing of metals, Acta Mater. 117 (2016) 371–392. doi:10.1016/j.actamat.2016.07.019.

[186] E. Williams, N. Lavery, Laser processing of bulk metallic glass: A review, J. Mater. Process. Technol. 247 (2017) 73–91. doi:10.1016/j.jmatprotec.2017.03.034.

[187] S. Pauly, L. Löber, R. Petters, M. Stoica, S. Scudino, U. Kühn, J. Eckert, Processing metallic glasses by selective laser melting, Mater. Today. 16 (2013) 37–41. doi:10.1016/j.mattod.2013.01.018.

[188] H.Y. Jung, S.J. Choi, K.G. Prashanth, M. Stoica, S. Scudino, S. Yi, U. Kühn, D.H. Kim, K.B. Kim, J. Eckert, Fabrication of Fe-based bulk metallic glass by selective laser melting: A parameter study, Mater. Des. 86 (2015) 703–708.

doi:10.1016/j.matdes.2015.07.145.

[189] S. Pauly, C. Schricker, S. Scudino, L. Deng, U. Kühn, Processing a glass-forming Zr-based alloy by selective laser melting, Mater. Des. 135 (2017) 133–141. doi:10.1016/j.matdes.2017.08.070.

[190] X.P. Li, M.P. Roberts, S. O'Keeffe, T.B. Sercombe, Selective laser melting of Zr-based bulk metallic glasses: Processing, microstructure and mechanical properties, Mater. Des. 112 (2016) 217–226. doi:10.1016/j.matdes.2016.09.071.

[191] P. Bordeenithikasem, M. Stolpe, A. Elsen, D.C. Hofmann, Glass forming ability, flexural strength, and wear properties of additively manufactured Zr-based bulk metallic glasses produced through laser powder bed fusion, Addit. Manuf. 21 (2018) 312–317. doi:10.1016/j.addma.2018.03.023.

[192] D. Ouyang, W. Xing, N. Li, Y. Li, L. Liu, Structural evolutions in 3D-printed Fe-based metallic glass fabricated by selective laser melting, Addit. Manuf. 23 (2018) 246–252. doi:10.1016/j.addma.2018.08.020.

[193] J.P. Best, Z. Evenson, F. Yang, A.-C. Dippel, M. Stolpe, O. Gutowski, M.T. Hasib, X. Li, J.J. Kruzic, Structural periodicity in laser additive manufactured Zr-based bulk metallic glass, Appl. Phys. Lett. 115 (2019) 031902. doi:10.1063/1.5100050.

[194] H.W. Kui, A.L. Greer, D. Turnbull, Formation of bulk metallic glass by fluxing, Appl. Phys. Lett. 45 (1984) 615–616. doi:10.1063/1.95330.

[195] B.D. Cullity, S.R. Stock, Elements of X-ray diffraction, 3rd ed., Prentice Hall, New York, 2001.

[196] S. Vyazovkin, N. Koga, C. Schick, eds., Handbook of Thermal Analysis and Calorimetry, Volume 6, Recent Advances, Techniques and Applications, 2nd ed., Elsevier Science, 2018.

[197] W. Zielenkiewicz, E. Margas, Theory of Calorimetry, Kluwer Academic Publishers, Dordrecht, 2004. doi:10.1007/0-306-48418-8.

[198] R. Busch, E. Bakke, W.L. Johnson, Viscosity of the supercooled liquid and relaxation at the glass transition of the $Zr_{46.75}Ti_{8.25}Cu_{7.5}Ni_{10}Be_{27.5}$ bulk metallic glass forming alloy, Acta Mater. 46 (1998) 4725–4732. doi:10.1016/S1359-6454(98)00122-0.

[199] Z. Evenson, I. Gallino, R. Busch, The effect of cooling rates on the apparent fragility of Zr-based bulk metallic glasses, J. Appl. Phys. 107 (2010). doi:10.1063/1.3452381.

[200] Y.J. Kim, R. Busch, W.L. Johnson, A.J. Rulison, W.K. Rhim, Experimental determination of a time-temperature-transformation diagram of the undercooled $Zr_{41.2}Ti_{13.8}Cu_{12.5}Ni_{10.0}Be_{22.5}$ alloy using the containerless electrostatic levitation processing technique, Appl. Phys. Lett. 68 (1996) 1057–1059. doi:10.1063/1.116247.

[201] J.F. Loeffler, J. Schroers, W.L. Johnson, Time–Temperature–Transformation Diagram and Microstructures of Bulk Glass Forming $Pd_{40}Cu_{30}Ni_{10}P_{20}$, Appl. Phys. Lett. 77 (2000) 681–683. doi:10.1063/1.127084.

[202] O. Gross, S.S. Riegler, M. Stolpe, B. Bochtler, A. Kuball, S. Hechler, R. Busch, I. Gallino, On the high glass-forming ability of Pt-Cu-Ni/Co-P-based liquids, Acta Mater. 141 (2017) 109–119. doi:10.1016/j.actamat.2017.09.013.

[203] Z. Evenson, On the thermodynamic and kinetic properties of bulk glass forming metallic systems, Dissertation, Saarland University, 2012. doi:10.22028/D291-22851.

[204] O. Kubaschewski, C.B. Alcock, P.J. Spencer, Materials Thermochemistry, 6th ed., 1993.

[205] F.T. Trouton, On the Coefficient of Viscous Traction and Its Relation to that of Viscosity, Proc. R. Soc. London. 77 (1906) 426–440. http://www.jstor.org/stable/92817.

[206] H.E. Hagy, Experimental Evaluation of Beam-Bending Method of Determining Glass Viscosities in the Range 10^8 to 10^{15} Poises, J. Am. Ceram. Soc. 46 (1963) 93–97. doi:10.1111/j.1151-2916.1963.tb11684.x.

[207] NETZSCH-Gerätebau GmbH, User manual TMA 402 F1/F3 Hyperion, 2012.

[208] W. Hembree, B. Bochtler, R. Busch, High-temperature rotating cylinder rheometer for studying metallic glass forming liquids, Rev. Sci. Instrum. 89 (2018) 113904. doi:10.1063/1.5039318.

[209] M. Kehr, W. Hoyer, I. Egry, A New High-Temperature Oscillating Cup Viscometer, Int. J. Thermophys. 28 (2007) 1017–1025. doi:10.1007/s10765-007-0216-9.

[210] R.F. Brooks, A.T. Dinsdale, P.N. Quested, The measurement of viscosity of alloys - a review of methods, data and models, Meas. Sci. Technol. 16 (2005) 354–362. doi:10.1088/0957-0233/16/2/005.

[211] I. Egry, H. Giffard, S. Schneider, The oscillating drop technique revisited, Meas. Sci. Technol. 16 (2005) 426–431. doi:10.1088/0957-0233/16/2/013.

[212] W. Rhim, S.K. Chung, D. Barber, K.F. Man, G. Gutt, A. Rulison, R.E. Spjut, An electrostatic levitator for high-temperature containerless materials processing in 1-g, Rev. Sci. Instrum. 64 (1993) 2961–2970. doi:10.1063/1.1144475.

[213] W.-K. Rhim, K. Ohsaka, P.-F. Paradis, R.E. Spjut, Noncontact technique for measuring surface tension and viscosity of molten materials using high temperature electrostatic levitation, Rev. Sci. Instrum. 70 (1999) 2796–2801. doi:10.1063/1.1149797.

[214] T. Meister, H. Werner, G. Lohoefer, D.M. Herlach, H. Unbehauen, Gain-scheduled control of an electrostatic levitator, Control Eng. Pract. 11 (2003) 117–128. doi:10.1016/S0967-0661(02)00102-8.

[215] T. Kordel, D. Holland-Moritz, F. Yang, J. Peters, T. Unruh, T. Hansen, A. Meyer, Neutron scattering experiments on liquid droplets using electrostatic levitation, Phys. Rev. B. 83 (2011) 104205. doi:10.1103/PhysRevB.83.104205.

[216] I. Egry, G. Lohoefer, I. Seyhan, S. Schneider, B. Feuerbacher, Viscosity and Surface Tension Measurements in Microgravity, Int. J. Thermophys. 20 (1999) 1005–1015. doi:10.1023/A:1022686316437.

[217] D.C. Hofmann, S.N. Roberts, Microgravity metal processing: from undercooled liquids to bulk metallic glasses, Npj Microgravity. 1 (2015) 15003. doi:10.1038/npjmgrav.2015.3.

[218] D.J. Stein, F.J. Spera, New high-temperature rotational rheometer for silicate melts, magmatic suspensions, and emulsions, Rev. Sci. Instrum. 69 (1998) 3398–3402. doi:10.1063/1.1149106.

[219] T.G. Mezger, The rheology handbook: for users of rotational and oscillatory rheometers, 3rd ed., Vincentz Network GmbH & Co KG, 2011.

[220] W. Reimers, A.R. Pyzalla, A.K. Schreyer, H. Clemens, eds., Neutrons and Synchrotron Radiation in Engineering Materials Science, Wiley-VCH Verlag GmbH & Co. KGaA, Weinheim, Germany, 2008. doi:10.1002/9783527621927.

[221] ESRF (European Synchrotron Radiation Facility), What is a synchrotron?, (2019). https://www.esrf.eu/about/synchrotron-science/synchrotron (accessed January 25, 2019).

[222] T. Egami, S.J.. Billinge, Underneath the Bragg Peaks - Structural Analysis of Complex Materials, 2003.

[223] A.-C. Dippel, H.-P. Liermann, J.T. Delitz, P. Walter, H. Schulte-Schrepping, O.H. Seeck, H. Franz, Beamline P02.1 at PETRA III for high-resolution and high-energy powder diffraction, J. Synchrotron Radiat. 22 (2015) 675–687. doi:10.1107/S1600577515002222.

[224] W.A. Peifer, Levitation melting …… A Survey of the State-of-the-Art, J. Met. 17 (1965) 487–493.

[225] M. Basham, J. Filik, M.T. Wharmby, P.C.Y. Chang, B. El Kassaby, M. Gerring, J. Aishima, K. Levik, B.C.A. Pulford, I. Sikharulidze, D. Sneddon, M. Webber, S.S. Dhesi, F. Maccherozzi, O. Svensson, S. Brockhauser, G. Náray, A.W. Ashton, Data Analysis

WorkbeNch (DAWN), J. Synchrotron Radiat. 22 (2015) 853–858. doi:10.1107/S1600577515002283.

[226] J. Filik, A.W. Ashton, P.C.Y. Chang, P.A. Chater, S.J. Day, M. Drakopoulos, M.W. Gerring, M.L. Hart, O. V. Magdysyuk, S. Michalik, A. Smith, C.C. Tang, N.J. Terrill, M.T. Wharmby, H. Wilhelm, Processing two-dimensional X-ray diffraction and small-angle scattering data in DAWN 2, J. Appl. Crystallogr. 50 (2017) 959–966. doi:10.1107/S1600576717004708.

[227] G. Ashiotis, A. Deschildre, Z. Nawaz, J.P. Wright, D. Karkoulis, F.E. Picca, J. Kieffer, The fast azimuthal integration Python library: pyFAI, J. Appl. Crystallogr. 48 (2015) 510–519. doi:10.1107/S1600576715004306.

[228] X. Qiu, J.W. Thompson, S.J.L. Billinge, PDFgetX2 : a GUI-driven program to obtain the pair distribution function from X-ray powder diffraction data, J. Appl. Crystallogr. 37 (2004) 678–678. doi:10.1107/S0021889804011744.

[229] W. Kraus, G. Nolze, POWDER CELL – a program for the representation and manipulation of crystal structures and calculation of the resulting X-ray powder patterns, J. Appl. Crystallogr. 29 (1996) 301–303. doi:10.1107/S0021889895014920.

[230] M. Kelkel, Thermoplastisches Formen Metallischer Massivglaeser, Master thesis, Saarland University, 2016.

[231] Heraeus, AMZ4 Metal Powder - Material datasheet, (2017). https://www.heraeus.com/media/media/group/doc˙group/products˙1/additivemanufacturing/datasheets˙en/Datasheet˙AMZ4.pdf (accessed August 1, 2017).

[232] Heraeus Holding, Heraeus Amorphous Metals, (2018). https://www.heraeus.com/en/group/products˙and˙solutions˙group/amorphous˙metals/home˙amorphous˙metals.aspx (accessed January 9, 2019).

[233] J. Eckert, J.C. Holzer, C.C. Ahn, Z. Fu, W.L. Johnson, Melting behavior of nanocrystalline aluminum powders, Nanostructured Mater. 2 (1993) 407–413. doi:10.1016/0965-9773(93)90183-C.

[234] H.J. Fecht, Synthesis and properties of nanocrystalline metals and alloys prepared by mechanical attrition, Nanostructured Mater. 1 (1992) 125–130. doi:10.1016/0965-9773(92)90064-5.

[235] C.R.M. Wronski, The size dependence of the melting point of particles of tin, Brit. J. Appl. Phys. 18 (1967) 1731–1737.

[236] S. Pogatscher, D. Leutenegger, J.E.K. Schawe, P.J. Uggowitzer, J.F. Löffler, Solid–solid phase transitions via melting in metals, Nat. Commun. 7 (2016) 11113. doi:10.1038/ncomms11113.

[237] M.J. Kaufman, R.D. Shull, Nature of large Ti_4Cu_2O particles formed during annealing of $Cu_{55}Ti_{45}$ metallic glass ribbons, Metall. Trans. A. 17 (1986) 575–581. doi:10.1007/BF02643976.

[238] M.H. Mueller, H.W. Knott, The Crystal Structures of Ti_2Cu, Ti_2Ni, Ti_4Ni_2O and Ti_4Cu_2O, Trans. Metall. Soc. AIME. 227 (1963) 674–678.

[239] R. Busch, The thermophysical properties of bulk metallic glass-forming liquids, JOM. 52 (2000) 39–42. doi:10.1007/s11837-000-0160-7.

[240] T.A.A. Waniuk, R. Busch, A. Masuhr, W.L.L. Johnson, Equilibrium viscosity of the $Zr_{41.2}Ti_{13.8}Cu_{12.5}Ni_{10}Be_{22.5}$ bulk metallic glass-forming liquid and viscous flow during relaxation, phase separation, and primary crystallization, Acta Mater. 46 (1998) 5229–5236. doi:10.1016/S1359-6454(98)00242-0.

[241] A.A. Kündig, J.F. Löffler, W.L. Johnson, Composition Dependence of Phase Separation and Crystallization in Deeply Undercooled Zr-(Ti-)Cu-Ni-Al Alloys, MRS Proc. 644 (2000) L5.6. doi:10.1557/PROC-644-L5.6.

[242] S.C. Glade, J.F. Löffler, S. Bossuyt, W.L. Johnson, M.K. Miller, Crystallization of amorphous $Cu_{47}Ti_{34}Zr_{11}Ni_8$, J. Appl. Phys. 89 (2001) 1573. doi:10.1063/1.1332089.

[243] E. Pekarskaya, J.F. Löffler, W.L. Johnson, Microstructural studies of crystallization of a Zr-based bulk metallic glass, Acta Mater. 51 (2003) 4045–4057. doi:10.1016/S1359-6454(03)00225-8.

[244] C. Way, T. Shaw, P. Wadhwa, R. Busch, Shear rate dependence of viscosity and configurational entropy of the $Zr_{41.2}Ti_{13.8}Cu_{12.5}Ni_{10.0}Be_{22.5}$ metallic glass forming liquid, J. Alloys Compd. 434–435 (2007) 88–91. doi:10.1016/j.jallcom.2006.08.116.

[245] I. Jonas, Thermophysical and structural properties of the equilibrium and undercooled melt of bulk metallic glasses investigated by electrostatic levitation, Dissertation, Saarland University, 2016. doi:10.22028/D291-23228.

[246] SGL Group Sigrafine ff R6710 Datasheet; date accessed: 2018.04.20, Sigrafine ff R6710 Datasheet, (2015). http://www.sglgroup.com/cms/˙common/downloads/products/product-groups/gs/tds/iso/SIGRAFINE˙TDS-R6710˙US.02.pdf (accessed April 20, 2018).

[247] J. Schroers, K. Samwer, F. Szuecs, W.L. Johnson, Characterization of the Interface Between the Bulk Glass Forming Alloy $Zr_{41}Ti_{14}Cu_{12}Ni_{10}Be_{23}$ with Pure Metals and Ceramics, J. Mater. Res. 15 (2000) 1617–1621. doi:10.1557/JMR.2000.0232.

[248] H. Choi-Yim, R. Busch, U. Köster, W.L. Johnson, Synthesis and characterization of particulate reinforced $Zr_{57}Nb_5Al_{10}Cu_{15.4}Ni_{12.6}$ bulk metallic glass composites, Acta Mater. 47 (1999) 2455–2462. doi:10.1016/S1359-6454(99)00103-2.

[249] K.C. Mills, Y.C. Su, Review of surface tension data for metallic elements and alloys: Part 1 – Pure metals, Int. Mater. Rev. 51 (2006) 329–351. doi:10.1179/174328006X102510.

[250] W. Hembree, High temperature rheology of Zr-based bulk metallic glass forming liquids, Dissertation, Saarland University, 2015. doi:10.22028/D291-23174.

[251] J.F. Löffler, S. Bossuyt, S.C. Glade, W.L. Johnson, W. Wagner, P. Thiyagarajan, Crystallization of bulk amorphous Zr–Ti(Nb)–Cu–Ni–Al, Appl. Phys. Lett. 77 (2000) 525–527. doi:10.1063/1.127032.

[252] M.Y. Teslyuk, Intermetallic Compounds with Structure of Laves Phases, Nauk. Moscow. (1969) 1–138.

[253] C.G. Woychik, T.B. Massalski, Phase diagram relationships in the system Cu-Ti-Zr, Zeitschrift Fuer Met. 79 (1988) 149–153.

[254] Y.K. Kovneristyj, A.G. Pashkovskaya, Bulk amorphization of alloys in the intermetallide containing system Ti–Cu–Zr, Amorf.(Stekloobraz) Met, Mater. RAN Int. Metall. M. (1992) p153-157.

[255] T. Velikanova, M. Turchanin, Cu-Ti-Zr (Copper-Titanium-Zirconium), in: Non-Ferrous Met. Syst. Part 3, Springer Berlin Heidelberg, Berlin, Heidelberg, n.d.: pp. 436–464. doi:10.1007/978-3-540-47004-5˙37.

[256] P. Villars, K. Cenzual, eds., $Ti_{45}Zr_{38}Ni_{17}$ (ZrTiNi) Crystal Structure: Datasheet from "PAULING FILE Multinaries Edition – 2012" in SpringerMaterials, (n.d.). https://materials.springer.com/isp/crystallographic/docs/sd˙1803780.

[257] J.P. Owens, B.R. Conrad, N.F. Franzen, The crystal structure of Ti_2S, Acta Crystallogr. 23 (1967) 77–82. doi:10.1107/S0365110X67002154.

[258] J.P. Owens, H.F. Franzen, Preparation and structure determination of Ti_8S_3, Acta Crystallogr. Sect. B Struct. Crystallogr. Cryst. Chem. 30 (1974) 427–430. doi:10.1107/S0567740874002949.

[259] S. Sachdev, D.R. Nelson, Theory of the Structure Factor of Metallic Glasses, Phys. Rev. Lett. 53 (1984) 1947–1950. doi:10.1103/PhysRevLett.53.1947.

[260] K.F. Kelton, G.W. Lee, A.K. Gangopadhyay, R.W. Hyers, T.J. Rathz, J.R. Rogers, M.B. Robinson, D.S. Robinson, First X-Ray Scattering Studies on Electrostatically Levitated Metallic Liquids: Demonstrated Influence of Local Icosahedral Order on the

Nucleation Barrier, Phys. Rev. Lett. 90 (2003) 195504. doi:10.1103/PhysRevLett.90.195504.

[261] P.J. Brown, A.G. Fox, E.N. Maslen, M.A. O'Keefe, B.T.M. Willis, Intensity of diffracted intensities, in: Int. Tables Crystallogr., International Union of Crystallography, Chester, England, 2006: pp. 554–595. doi:10.1107/97809553602060000600.

[262] A.R. Yavari, A. Le Moulec, A. Inoue, N. Nishiyama, N. Lupu, E. Matsubara, W.J. Botta, G. Vaughan, M. Di Michiel, Å. Kvick, Excess free volume in metallic glasses measured by X-ray diffraction, Acta Mater. 53 (2005) 1611–1619. doi:10.1016/j.actamat.2004.12.011.

[263] A.K. Gangopadhyay, M.E. Blodgett, M.L. Johnson, A.J. Vogt, N.A. Mauro, K.F. Kelton, Thermal expansion measurements by x-ray scattering and breakdown of Ehrenfest's relation in alloy liquids, Appl. Phys. Lett. 104 (2014) 191907. doi:10.1063/1.4876125.

[264] N. Mattern, M. Stoica, G. Vaughan, J. Eckert, Thermal behaviour of $Pd_{40}Cu_{30}Ni_{10}P_{20}$ bulk metallic glass, Acta Mater. 60 (2012) 517–524. doi:10.1016/j.actamat.2011.10.032.

[265] J. Bednarcik, S. Michalik, M. Sikorski, C. Curfs, X.D. Wang, J.Z. Jiang, H. Franz, Thermal expansion of a La-based bulk metallic glass: insight from in situ high-energy x-ray diffraction, J. Phys. Condens. Matter. 23 (2011) 254204. doi:10.1088/0953-8984/23/25/254204.

[266] A.K. Gangopadhyay, K.F. Kelton, A re-evaluation of thermal expansion measurements of metallic liquids and glasses from x-ray scattering experiments, J. Chem. Phys. 148 (2018) 204509. doi:10.1063/1.5032319.

[267] X.J. Liu, Y. Xu, X. Hui, Z.P. Lu, F. Li, G.L. Chen, J. Lu, C.T. Liu, Metallic Liquids and Glasses: Atomic Order and Global Packing, Phys. Rev. Lett. 105 (2010) 155501. doi:10.1103/PhysRevLett.105.155501.

[268] X.W. Fang, C.Z. Wang, S.G. Hao, M.J. Kramer, Y.X. Yao, M.I. Mendelev, Z.J. Ding, R.E. Napolitano, K.M. Ho, Spatially Resolved Distribution Function and the Medium-Range Order in Metallic Liquid and Glass, Sci. Rep. 1 (2011) 194. doi:10.1038/srep00194.

[269] S.P. Pan, J.Y. Qin, W.M. Wang, T.K. Gu, Origin of splitting of the second peak in the pair-distribution function for metallic glasses, Phys. Rev. B. 84 (2011) 092201. doi:10.1103/PhysRevB.84.092201.

[270] C.H. Bennett, Serially Deposited Amorphous Aggregates of Hard Spheres, J. Appl. Phys. 43 (1972) 2727–2734. doi:10.1063/1.1661585.

[271] H. Lou, X. Wang, Q. Cao, D. Zhang, J. Zhang, T. Hu, H. -k. Mao, J.-Z. Jiang, Negative expansions of interatomic distances in metallic melts, Proc. Natl. Acad. Sci. 110 (2013) 10068–10072. doi:10.1073/pnas.1307967110.

[272] A.K. Gangopadhyay, M.E. Blodgett, M.L. Johnson, J. McKnight, V. Wessels, A.J. Vogt, N.A. Mauro, J.C. Bendert, R. Soklaski, L. Yang, K.F. Kelton, Anomalous thermal contraction of the first coordination shell in metallic alloy liquids, J. Chem. Phys. 140 (2014) 044505. doi:10.1063/1.4861666.

[273] J. Ding, M. Xu, P.F. Guan, S.W. Deng, Y.Q. Cheng, E. Ma, Temperature effects on atomic pair distribution functions of melts, J. Chem. Phys. 140 (2014) 064501. doi:10.1063/1.4864106.

[274] S. V. Sukhomlinov, M.H. Müser, Determination of accurate, mean bond lengths from radial distribution functions, J. Chem. Phys. 146 (2017) 024506. doi:10.1063/1.4973804.

[275] S. V. Sukhomlinov, M.H. Müser, Anomalous system-size dependence of properties at the fragile-to-strong transition in a bulk-metallic-glass forming melt, Comput. Mater. Sci. 156 (2019) 129–134. doi:10.1016/j.commatsci.2018.09.047.

[276] M. Kobayashi, H. Tanaka, The reversibility and first-order nature of liquid-liquid transition in a molecular liquid, Nat. Commun. 7 (2016). doi:10.1038/ncomms13438.

[277] J. Schroers, B. Lohwongwatana, W.L. Johnson, A. Peker, Gold based bulk metallic glass, Appl. Phys. Lett. 87 (2005) 94–97. doi:10.1063/1.2008374.

[278] Q. Zhang, W. Zhang, A. Inoue, New Cu–Zr-based bulk metallic glasses with large diameters of up to 1.5cm, Scr. Mater. 55 (2006) 711–713. doi:10.1016/j.scriptamat.2006.06.024.

[279] S.S. Riegler, Investigations on the annealing-induced structural changes in the $Zr_{48}Cu_{36}Al_8Ag_8$ bulk metallic glass and their effects on the kinetic and mechanical properties, Master thesis, Saarland University, 2019.

[280] A. Inoue, T. Zhang, T. Masumoto, The structural relaxation and glass transition of La-Al-Ni and Zr-Al-Cu amorphous alloys with a significant supercooled liquid region, J. Non. Cryst. Solids. 150 (1992) 396–400. doi:10.1016/0022-3093(92)90160-L.

[281] D. Wang, H. Tan, Y. Li, Multiple maxima of GFA in three adjacent eutectics in Zr–Cu–Al alloy system – A metallographic way to pinpoint the best glass forming alloys, Acta Mater. 53 (2005) 2969–2979. doi:10.1016/j.actamat.2005.03.012.

[282] W. Zhang, X. Jia, Y. Li, C. Fang, Effects of Mo addition on thermal stability and magnetic properties of a ferromagnetic $Fe_{75}P_{10}C_{10}B_5$ metallic glass, J. Appl. Phys. 115 (2014) 17A768. doi:10.1063/1.4869161.

[283] J. Heinrich, R. Busch, B. Nonnenmacher, Processing of a bulk metallic glass forming alloy based on industrial grade Zr, Intermetallics. 25 (2012) 1–4. doi:10.1016/j.intermet.2012.02.011.

[284] C.C. Hays, J. Schroers, U. Geyer, S. Bossuyt, N. Stein, W.L. Johnson, Glass Forming Ability in the Zr-Nb-Ni-Cu-Al Bulk Metallic Glasses, J. Metastable Nanocrystalline Mater. 8 (2000) 103–108. doi:10.4028/www.scientific.net/JMNM.8.103.

[285] C.C. Hays, J. Schroers, W.L. Johnson, T.J. Rathz, R.W. Hyers, J.R. Rogers, M.B. Robinson, Vitrification and determination of the crystallization time scales of the bulk-metallic-glass-forming liquid $Zr_{58.5}Nb_{2.8}Cu_{15.6}Ni_{12.8}Al_{10.3}$, Appl. Phys. Lett. 79 (2001) 1605–1607. doi:10.1063/1.1398605.

[286] E. Bakke, R. Busch, W.L. Johnson, The viscosity of the $Zr_{46.75}Ti_{8.25}Cu_{7.5}Ni_{10}Be_{27.5}$ bulk metallic glass forming alloy in the supercooled liquid, Appl. Phys. Lett. 67 (1995) 3260–3262. doi:10.1063/1.114891.

[287] G.J. Dienes, H.F. Klemm, Theory and Application of the Parallel Plate Plastometer, J. Appl. Phys. 17 (1946) 458–471. doi:10.1063/1.1707739.

[288] C.A. Pampillo, A.C. Reimschuessel, The fracture topography of metallic glasses, J. Mater. Sci. 9 (1974) 718–724. doi:10.1007/BF00761791.

[289] W. Chen, Z. Liu, J. Schroers, Joining of bulk metallic glasses in air, Acta Mater. 62 (2014) 49–57. doi:10.1016/j.actamat.2013.08.053.

[290] G. Kumar, P.A. Staffier, J. Blawzdziewicz, U.D. Schwarz, J. Schroers, Atomically smooth surfaces through thermoplastic forming of metallic glass, Appl. Phys. Lett. 97 (2010) 101907. doi:10.1063/1.3485298.

[291] P.H. Kuo, S.H. Wang, P.K. Liaw, G.J. Fan, H.T. Tsang, D. Qiao, F. Jiang, Bulk-metallic glasses joining in a supercooled-liquid region, Mater. Chem. Phys. 120 (2010) 532–536. doi:10.1016/j.matchemphys.2009.11.044.

[292] J. Wegner, S. Kleszczynski, M. Frey, S. Hechler, G. Witt, R. Busch, Parameter study about processing Zr-based bulk metallic glass with Laser beam melting, in: Rapid.Tech + FabCon 3.D – Int. Trade Show + Conf. Addit. Manuf., Carl Hanser Verlag GmbH & Co. KG, München, 2018: pp. 343–358. doi:10.3139/9783446458123.022.

[293] Cristo Nsiangango Paulo, Einfluss von Phosphor und Schwefel auf die thermoplastische Verformung und Oxidation von Zr- und Cu-basierten metallischen Glaesern, Master thesis, Saarland University, 2019.

[294] P. Villars, K. Cenzual, eds., CuTi Crystal Structure: Datasheet from "PAULING FILE

Multinaries Edition – 2012" in SpringerMaterials, (n.d.). https://materials.springer.com/isp/crystallographic/docs/sd˙0261228.

[295] P. Villars, K. Cenzual, eds., CuZr Crystal Structure: Datasheet from "PAULING FILE Multinaries Edition – 2012" in SpringerMaterials, (n.d.). https://materials.springer.com/isp/crystallographic/docs/sd˙0450958.

[296] P. Villars, K. Cenzual, eds., Ti_2Cu ($CuTi_2$ rt) Crystal Structure: Datasheet from "PAULING FILE Multinaries Edition – 2012" in SpringerMaterials, (n.d.). https://materials.springer.com/isp/crystallographic/docs/sd˙0260616.

[297] J.L. Murray, The S−Ti (Sulfur-Titanium) system, Bull. Alloy Phase Diagrams. 7 (1986) 156–163. doi:10.1007/BF02881555.

[298] P. Villars, K. Cenzual, eds., α-Zr (Zr rt) Crystal Structure: Datasheet from "PAULING FILE Multinaries Edition – 2012" in SpringerMaterials, (n.d.). https://materials.springer.com/isp/crystallographic/docs/sd˙0455185.

[299] P. Villars, K. Cenzual, eds., $CuZr_2$ Crystal Structure: Datasheet from "PAULING FILE Multinaries Edition – 2012" in SpringerMaterials, (n.d.). https://materials.springer.com/isp/crystallographic/docs/sd˙0310057.

[300] P. Villars, K. Cenzual, eds., $NiZr_2$ (Zr_2Ni) Crystal Structure: Datasheet from "PAULING FILE Multinaries Edition – 2012" in SpringerMaterials, (n.d.). https://materials.springer.com/isp/crystallographic/docs/sd˙0251548.

[301] P. Villars, K. Cenzual, eds., $Zr_{21}S_8$ Crystal Structure: Datasheet from "PAULING FILE Multinaries Edition – 2012" in SpringerMaterials, (n.d.). https://materials.springer.com/isp/crystallographic/docs/sd˙0453427.

[302] P. Villars, K. Cenzual, eds., $ZrTiCu_2$ ($Cu_{1.5}Zr_{0.75}Ti_{0.75}$ hex) Crystal Structure: Datasheet from "PAULING FILE Multinaries Edition – 2012" in SpringerMaterials, (n.d.). https://materials.springer.com/isp/crystallographic/docs/sd˙1124292.

[303] P. Villars, K. Cenzual, eds., ZrTiNi Crystal Structure: Datasheet from "PAULING FILE Multinaries Edition – 2012" in SpringerMaterials, (n.d.). https://materials.springer.com/isp/crystallographic/docs/sd˙0306334.